Solvent Extraction and Mass Transfer Assessment in Novel Extraction Technologies

University of Leeds

School of Chemical and Process Engineering

Submitted in Accordance with the Requirements for the Degree of

Doctor of Philosophy

James Michael John Miller

January 2021

Acknowledgements

I would first like to thank my supervisors Frans Muller and Bruce Hanson for their support and advice over the course of my PhD, without which I would not have been able to submit this thesis.

I would also like to thank the members of the University of Leeds Nuclear Group and those I have shared offices with in G29 and 4th floor chemistry for the chatter and countless pub trips. Diolch Alastair Baker, not only for all your guidance over the past few years, but also for putting up with my constant panicked questioning. Thank you Charlotte (Steve) Parrington for keeping me (somewhat) sane with stupid games, random nonsense and kinder egg toys. A quick thank you to Alex Fells for your help with job hunting and my viva preparations.

Thank you to everyone involved in running the Next Generation Nuclear CDT for giving me the chance to undertake this PhD, and for the amazing help, support and opportunities to grow and travel I've been lucky enough to receive during the program.

Thank you to my family, especially Mum, Dad and Tony, for your endless support all the way through my education. Thanks for all the trips, books, school equipment and patience taken to get me to where I am today. I love you all very much, I hope I've made you all proud.

Last but certainly not least, a massive thank you to Olivia Voyce (and Rusty) for all the encouragement and patience. Thanks for making me laugh and constantly challenging me to be a better person. I love you and without you, none of this would have been possible.

Abstract

An agitated tube reactor (ATR) has been converted from a commercially available flow chemistry reactor into a working solvent extraction contactor. It has been determined that the ATR has potential to be an industrial option for solvent extraction.

Mass transfer coefficients have been calculated for a wide range of agitation frequencies and residence times using Cu(II) extraction by extractant Mextral® 84H. Mass transfer has then been compared to a Taylor-Couette Disc Contactor, and a novel design, presented in this work, called a D-cell contactor.

Varying liquid volume by including an air phase has been shown to improve mass transfer within the ATR. The motion of liquid in the tube at each volume has also been monitored and compared against power per volume and droplet diameter calculations. In most operational parameters, liquid in the ATR is found to bypass agitation, therefore not achieving the expected extraction equilibrium. The volume of unmixed liquid is determined and a mass transfer coefficient for the mixed liquid is calculated. Based on the current design, optimum parameters are found when a tube is half filled and subject to an agitation frequency of 5 Hz. With these operational conditions, the ATR is shown to mix 95% of the fluid and reaches equilibrium within approximately 160 s.

The viability of the ATR as a solvent extractor has been compared against a Taylor-Couette Disc Contactor and a Pulsed Column. It is seen that at 5 Hz, with 50% fill fraction, that the ATR produces a comparable mass transfer coefficient to a pulsed column correlation,[1] as well as other mass transfer coefficients in literature.

List of Publications

The following conference paper was published by the author during the course of the presented work.

J. Miller, B. Hanson and F. Muller, “Design optimisation for solvent extraction in a modified agitated tube reactor”, Waste Management Symposia, March 2019, Phoenix.

Abbreviations

ATR	**A**gitated **T**ube **R**eactor
CAD	**C**omputer **A**ided **D**esign
CCD	**C**harge **C**oupled **D**evice
CFD	**C**omputational **F**luid **D**ynamics
FBRM	**F**ocus **B**eam **R**eflectance **M**easurement
FWHM	**F**ull **W**idth **H**alf **M**aximum
GANEX	**G**roup **A**cti**N**ide **EX**traction
HLW	**H**igh **L**evel **W**aste
HTU	**H**eight of **T**ransfer **U**nit
ID	**I**nternal **D**iameter
ILW	**I**ntermediate **L**evel **W**aste
LES	**L**arge **E**ddy **S**imulation
LEU	**L**ow **E**nriched **U**ranium
MOx	**M**ixed **Ox**ide
OD	**O**uter **D**iameter
PEEK	**P**oly **E**ther **E**ther **K**etone
PUREX	**P**lutonium **U**ranium **R**edox **EX**traction
PVC	**P**oly **V**inyl **C**hloride
RDC	**R**otating **D**isc **C**ontactor
rpm	**R**otations **P**er **M**inute
TBP	**T**ri**B**utyl **P**hosphate
TCC	**T**aylor-**C**ouette **C**ontactor

TCDC	**T**aylor-**C**ouette **D**isc **C**ontactor
TEP	**T**ri**E**thyl **P**hosphate
TGA	**T**hermo**G**ravimetic **A**nalysis
THORP	**TH**ermal **O**xide **R**eprocessing **P**lant
UREX	**UR**anium **EX**traction
UV	**U**ltra-**V**iolet

Nomenclature

A	Absorbance
A_{int}	Interfacial area (m^2)
a	Amplitude (m)
a_{v}	Interfacial area per unit volume ($m^2 \cdot m^{-3}$)
B_{C}	Annular compartment width in a TCDC or D-cell (m)
B_{λ}	Background spectra intensity at wavelength, λ ($W \cdot m^{-2}$)
c	Concentration ($mol \cdot m^{-3}$)
d_{32}	Sauter mean diameter (m)
D_{an}	Annular gap in a TCC (m)
D_{d}	Droplet diameter (m)
D_{h}	Pulsed column hole diameter (m)
D_{I}	Impeller diameter (m)
D_{in}	Inner cylinder diameter in a TCDC (m)
D_{out}	Outer cylinder diameter in a TCDC (m)
D_{d}	Rotor disc diamter in a TCDC (m)
d_{s}	Sample thickness for UV-Vis spectroscopy (m)
E_{K}	Kinetic energy (J)
E_{P}	Potential energy (J)
E_{q}	Chemical reaction enhancement factor
E_{T}	Total energy (J)
F	Molar transfer rate ($mol \cdot s^{-1}$)
f	Agitation frequency (Hz)
G	Total measured light intensity ($W \cdot m^{-2}$)

h	Height (m)
H_C	Compartment height of a TCDC (m)
h_{con}	Contactor height of a TCDC (m)
H_T	Total kinetic coefficient
I	Intensity (W·m^{-2})
K	Dissociation constant (mol·L^{-1})
k	Mass transfer coefficient (m·s^{-1})
L	Referring to the extractant ligand
L_A	Agitator length (m)
L_s	Separator length (m)
M	Referring to the metal ion
m	Mass (kg)
N	Number of moles of a substance (mol)
N_C	Number of compartments in a TCDC
P	Pressure (Pa)
P_w	Power (W)
Q	Flow rate (m^{3}·s^{-1})
q	Mass transfer rate (mol·m^{-3}·s^{-1})
q_3	Probability distribution function
R	Radius (m)
R_λ	Reference intensity at wavelength, λ (W·m^{-2})
S	Partition Coefficient
T	Transmittance
T_{osc}	Period of oscillation (s^{-1})
t	Time: residence or rise time (s)
u	Velocity (m·s^{-1})
u_{sf}	Superficial velocity (m·s^{-1})
V	Volume (m^{3})
V_L	Volume of liquid (m^{3})
x	Molar fraction of solute (mol)

α	Unmixed fraction of liquid in an ATR
ϵ	Molar Extinction coefficient (L·mol^{-1}·cm^{-1})
ζ	Normalised concentration difference $\frac{c_{aq}-c_{eq}}{c_0-c_{aq}}$
η	Ratio of outer to inner cylinder radius in a TCC
θ	Ratio of inner to outer rotational velocities in a TCC
μ	Dynamic viscosity (Pa·s)
ν	Kinematic viscosity (m^2·s^{-1})
ρ	Density (kg·m^{-3})
ϕ	Dispersed phase hold-up
ψ	Sphericity
Ω	Mass transfer resistance (s)
ω	Rotational velocity (s^{-1})

Dimensionless Numbers

N_{P}	Power number
N_{Ta}	Taylor number
N_{We}	Weber number

Subscripts

A	Refers to solute component A
ad	Adsorbed at the interface
aq	Denotes the aqueous phase
c	Denotes a continuous phase
crit	A critical value
eq	Denotes a phase at equilibrium
I	Refers to the Impeller
i	Refers to the interface between phases
in	Refers to the inner cylinder of a TCDC
L	Refers to the ligand
max	A maximum value
org	Denotes the organic phase
out	Refers to the outer cylinder of a TCDC
R	Refers to the rotor disc of a TCDC
T	Total value
λ	Denotes a specific wavelength

Constants

g	Acceleration due to gravity = 9.81 m·s^{-2}
μ_{aq}	Dynamic viscosity of water = 8.90×10^{-4} Pa·s
μ_{org}	Dynamic viscosity of Exxsol™ D80 = 1.68×10^{-3} Pa·s
ρ_{aq}	Density of water = 997.0 kg·m^{-3}
ρ_{org}	Density of Exxsol™ D80 = 798 kg·m^{-3}
σ	Interfacial tension between water and dodecane = 2.54×10^{-2} N·m^{-1}

Contents

CHAPTER 1

Research Focus

Spent fuel reprocessing currently uses the PUREX (Plutonium Uranium Redox EXtraction) solvent extraction process to recover any usable uranium and plutonium from used fuel, subsequently converting it into MOx (Mixed Oxide) fuels.[2] MOx fuels are able to be reused for future power generation or stored for future disposal. Reprocessing also facilitates waste volume reduction by further categorising waste. If left unprocessed all spent fuel, including fuel cladding, is automatically classified as high-level waste (HLW). Separation of the highly radioactive constituents, such as minor actinides or fission products, allows a large portion of the waste to be categorised as intermediate-level waste (ILW).

The United Kingdom has had a long history of reprocessing spent nuclear fuel. Opened in 1964, the Magnox reprocessing plant began reprocessing used fuel from its fleet of Magnox reactors. All Magnox reactors are now shut down and in the process of being decommissioned. The Magnox reprocessing plant is still in operation today, though its lifetime has been extended with its original closure planned in 2019. Operations are expected to be completed in 2021.[3]

Following the next wave of power plants, THORP (THermal Oxide Reprocessing Plant) was opened in 1997 to reprocess new fuels, which consist of metal oxides instead of the pure uranium metal fuel used in Magnox.[4] THORP stopped reprocessing in 2018[5,6] and, at this moment, the UK has no plans to continue reprocessing after the closure of the Magnox reprocessing plant.

Though reprocessing in the UK has been halted, future fuel generation or decommissioning strategies may include new plans to reprocess. As such, a much needed update of solvent extraction technologies used in the nuclear industry is beneficial. Solvent extraction technology in the UK nuclear industry primarily comprises of mixer-settlers and pulsed columns designed in the 1960s. The work presented in this thesis looks to find a modern alternative, primarily testing a novel solvent extraction contactor called the Coflore® agitated tube reactor (ATR). The ATR is a commercially available chemistry flow reactor, constructed by AMTechnology in the United Kingdom.

This thesis explores an ATRs conversion into a solvent extraction contactor, and discusses its overall viability as a replacement to current technology. By researching the solvent extraction capabilities and droplet sizes across a range of residence times, agitation frequencies and liquid volumes, it is hoped that the ideal conditions for mass transfer in the ATR can be found. The mass transfer coefficients of the ATR can then be compared with a lab-scale Taylor-Couette Disc Contactor (also presented in this work) and current nuclear processing equipment.

CHAPTER 2

Introduction and Background

2.1 Nuclear Reprocessing

Nuclear reprocessing is the act of treating spent fuel and extracting useful uranium and plutonium for reuse or easier disposal.[2] Reprocessing uses a solvent extraction method called PUREX which uses a tributyl phosphate (TBP) extractant to separate uranium and plutonium from waste products and minor actinides.[7] Separating waste in this way allows the remaining uranium and plutonium to be reused as MOx fuels, minor actinides (e.g. americium) to be used in other industries and reduces the volume of storage for high-level waste.[2]

Updating equipment in a radioactive environment is a problem unique to the nuclear industry and as such, equipment can often be outdated. Though solvent extraction technology in other industries has been kept up to date, nuclear reprocessing in the United Kingdom, until recently, has made use of equipment designed in the 1960s. With the recent closure of THORP in 2019 and the imminent closure of the Magnox reprocessing plant, there is an opportunity to introduce modern technologies for future reprocessing.

2.1.1 The Nuclear Fuel Cycle

The fuel cycle, shown in Figure 2.1, represents the path of uranium fuel from mining to disposal. Three possible cycles exist, an open, a partially closed and a closed cycle. The decision about which cycle is most beneficial is often made on a country by country basis and can be chosen based on economic or political factors.[8] In practice, most countries are currently using a deferred system in which fuel is placed in interim storage until a decision is made at a later date.

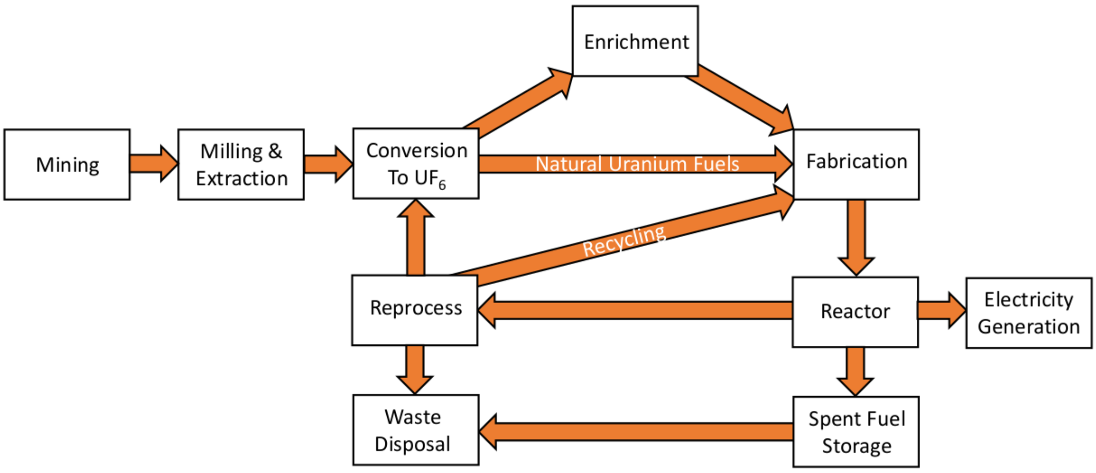

Figure 2.1: *A flow chart of the complete nuclear fuel cycle. The schematic follows uranium from mining, enrichment and fuel fabrication to energy generation, disposal and reprocessing.*[9]

An open fuel cycle, a flow chart of which can be seen in Figure 2.2, uses fuel only once and subsequently disposes of the spent fuel permanently. This is the simplest option, though it does come with difficulties. Once through disposal of materials is unsustainable and limits the industry to the continued supply of natural resources. Disposing of waste without reprocessing generates a far larger quantity of high-level waste, increasing the volume of any disposal facilities designed to store it. There are no countries currently using an open system as storage facilities are not yet available, though the Onkalo spent fuel repository is currently under construction in Finland.

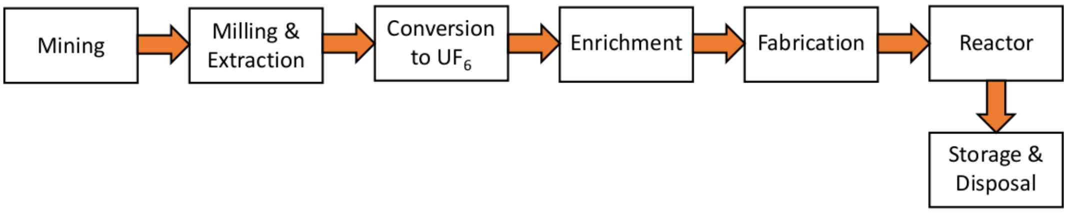

Figure 2.2: *A schematic of the open fuel cycle. In an open cycle, fuel is removed from the reactor and directly disposed.*[10, 11]

A flow diagram for a partially closed cycle is shown in Figure 2.3. Fuel is reprocessed only once and any uranium and plutonium is recycled into MOx fuels. Waste is separated into high, intermediate and low-level categories and disposed through the relevant waste routes. This reduces the volume of high-level waste as it is no longer inclusive of intermediate waste as in the open cycle. The ability to recycle uranium further decreases the need for long term storage as material can be reused. France, India, Japan and the United Kingdom currently operate on a partially closed cycle, however the United Kingdom is in the process of reverting to a deferred cycle with the closure and imminent closure of its THORP and Magnox reprocessing plants respectively.

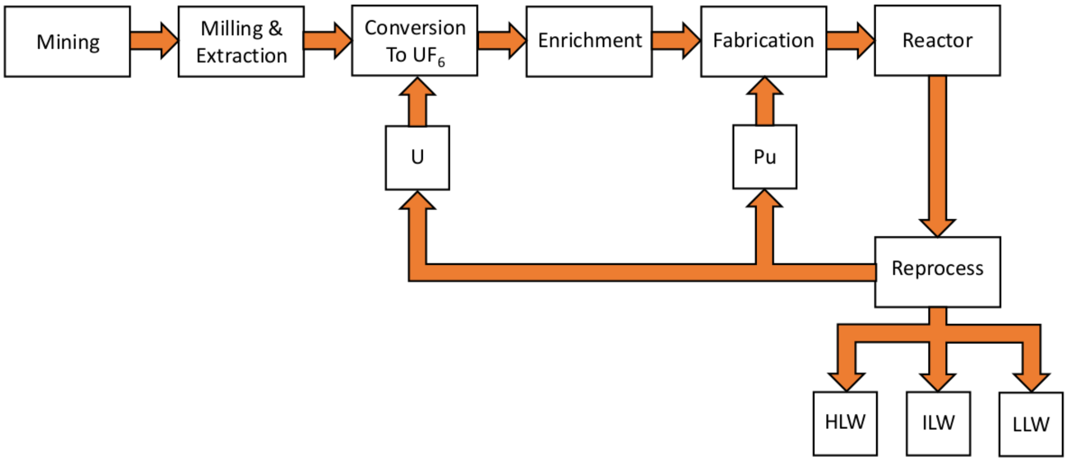

Figure 2.3: *A schematic of the partially closed fuel cycle. A partially closed fuel cycle reprocesses fuel once, recycling uranium and plutonium into MOx fuel. Reprocessing the waste allows it to be separated into high, intermediate and low-level waste, reducing the volume of high-level waste.*[10, 11]

A fully closed cycle requires fast reactors and is therefore not currently implemented by any countries. Reprocessed uranium and plutonium are used to produce fast reactor fuel. Fast reactors use the fissile plutonium and are able to produce more than they consume.[10, 11] Technology is only in the prototyping stages with projects such as Dounreay in the United Kingdom. A flow diagram for a fully closed cycle can be seen in Figure 2.4.

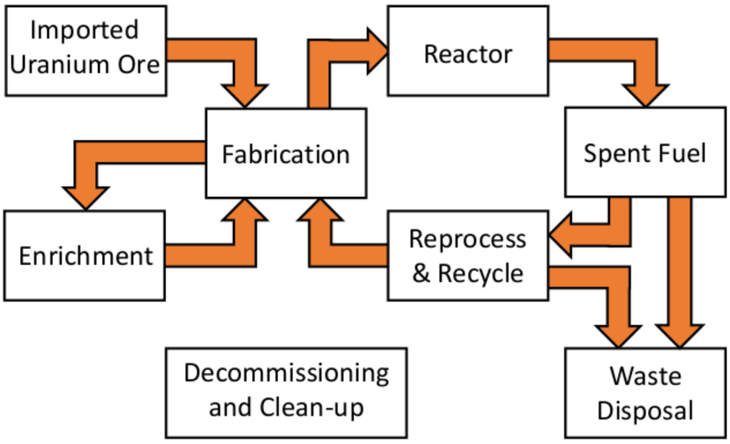

Figure 2.4: *A schematic of the closed fuel cycle. In a closed cycle, fuel is constantly reprocessed. The MOx fuel is reused and the high-level waste is removed and sent to permanent disposal. A fully closed cycle requires a fast reactor and is not currently an available option.*[10, 11] *Prototype fast reactors, such as Dounreay in the United Kingdom, have been developed to try and achieve a fully closed cycle.*

2.2 Overview of Spent Fuel Reprocessing

First developed in 1949,[12] and first used industrially in 1954, reprocessing of spent nuclear fuel is traditionally achieved via the PUREX process.[13] The process was first used in the manufacture of weaponry and as such produces a plutonium waste stream considered a proliferation risk. PUREX remains the only commercially used form of extraction in spent fuel reprocessing.

Once removed from a reactor, spent fuel typically contains around 91% uranium (with less than 1% being usable U^{235}) and approximately 1% plutonium. The remaining volume is made up of minor actinides and fission products.[14] These percentages, which are displayed in a pie chart in Figure 2.5, are representative of spent low-enriched uranium (LEU) fuel irradiated for 45 GWd/t (gigawatt days per metric tonne) and cooled for 5 years.[14] Reprocessing the fuel allows for any left over uranium or plutonium to be converted into MOx fuel to be reused at a later date. In addition, the separation of intermediate and high-level wastes reduces the need for highly engineered materials and facilities for disposal.

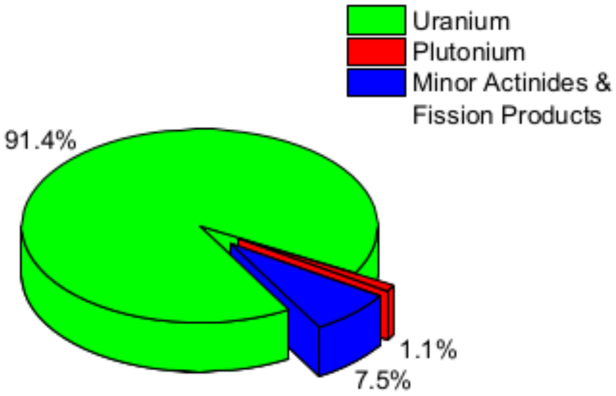

Figure 2.5: *A pie chart displaying a breakdown of spent nuclear fuel components. Approximately 91.4% of the spent fuel is uranium, with less than 1% uranium-235. The other 8.6% is made up from approximately 1.1% plutonium with the remaining volume consisting of minor actinides and fission products. Percentages calculated based on data from the OECD-NEA "Spent Nuclear Fuel Reprocessing Flowsheet."*[14]

2.3 Solvent Extraction

2.3.1 Introduction to Solvent Extraction

Solvent extraction, also known as liquid-liquid extraction, is a technique used extensively in many industries to separate desirable materials from waste products. It involves the use of two immiscible (or partially miscible) liquids, one acting as an extracting solvent, or extractant, and the other acting as a carrier of the desired solute.

Figure 2.6 gives a visual description of the solvent extraction process. Two immiscible liquids in contact are agitated such that one phase is dispersed within the other, creating a dispersed and a continuous phase respectively. Agitating the liquids to form droplets increases the surface area of the interface. Through chemical reaction, diffusion or the relative affinities for a solute to dissolve in a solvent, transfer of a solute between phases can occur. The liquids are left to settle and separate into two distinct layers, after which they can be isolated. The rate at which liquids separate is determined by their relative densities.

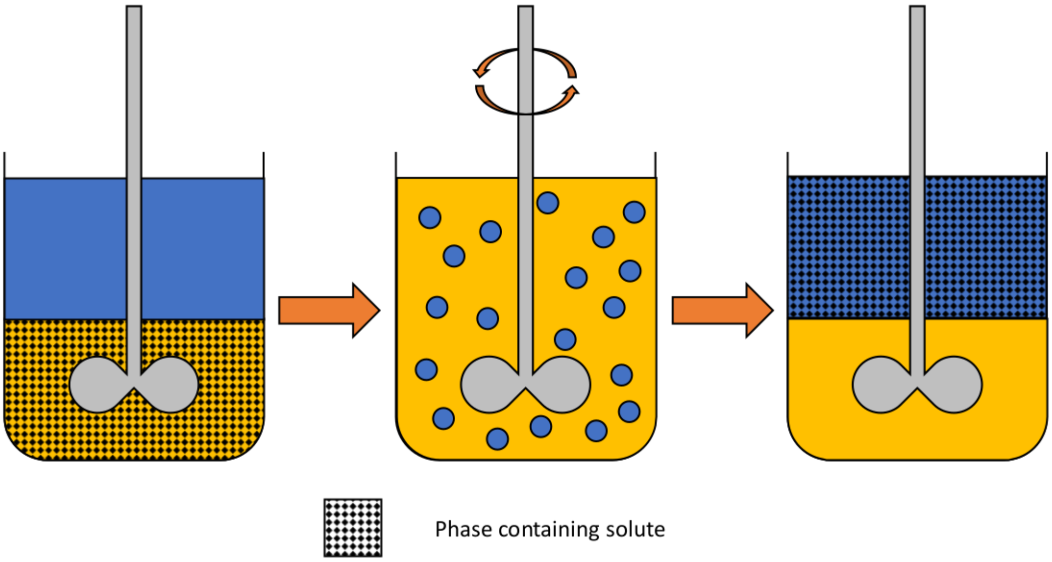

Figure 2.6: *Schematic of Solvent Extraction. The blue and yellow phases represent an organic extractant phase and an aqueous phase respectively. The chequered pattern denotes the phase containing the desired solute. In the left beaker, the solute is in the aqueous phase, while the extractant is in the organic phase. The central beaker shows the two phases being agitated, creating dispersed and continuous phases. The final beaker shows the two phases after separation. The solute has been extracted by the organic phase extractant from the aqueous phase raffinate. In practice, an equilibrium will occur and some solute will remain in the raffinate. Further extraction is possible via mixing with fresh extractant.*

The extent to which a solute is extracted from the carrier is dependent on the liquid-liquid equilibrium of the solute between the two phases. Once an equilibrium has been reached, no net transfer of the solute occurs. The partition coefficient, S, is defined as the ratio of the molar fraction of solute, x, in the organic extractant phase to the molar fraction of solute in the aqueous raffinate.[15] This is shown in Equation 2.1 for a solute being extracted from an aqueous phase into an organic phase. The aqueous and organic phases have been labelled with the subscripts "aq" and "org" respectively. Volume, V, for each phase has been included to account for systems in which the phase volumes are not equal.

$$S = \frac{x_{org}}{x_{aq}} \frac{V_{org}}{V_{aq}} \tag{2.1}$$

The higher the partition coefficient, the higher the achieved extraction. Further extraction can be achieved by repeating the process with fresh extractant and can be repeated until the desired extraction has been reached.

Commonly used in industrial processes, solvent extraction is often used when other separation techniques, such as distillation or crystallisation, are not appropriate.[16] For example, when boiling temperatures of two components are too similar. Solvent extraction has many uses in a range of industries and can be used in both batch (as seen in Figure 2.6) and continuous processes. It is particularly useful in the pharmaceuticals industry because of the diverse range of solvents available, as well as its ability to deal with temperature sensitive materials and processes. Solvent extraction has been used in the extraction of antibiotics and synthetic vitamins,[17] water treatment and desalination,[18] spent nuclear fuel reprocessing[14] and hydrometallurgy.[19] Continuous extraction has been used as part of the PUREX process for spent nuclear fuel since 1947 and has become more popular in the pharmaceuticals industry in recent years as part of the search for greener alternatives to batch processes.[20,21]

2.3.2 Flow Orientations

There are multiple flow orientations to consider when performing solvent extraction. Figure 2.7 shows a schematic for three flow orientations. Each orientation passes through three equipment stages.

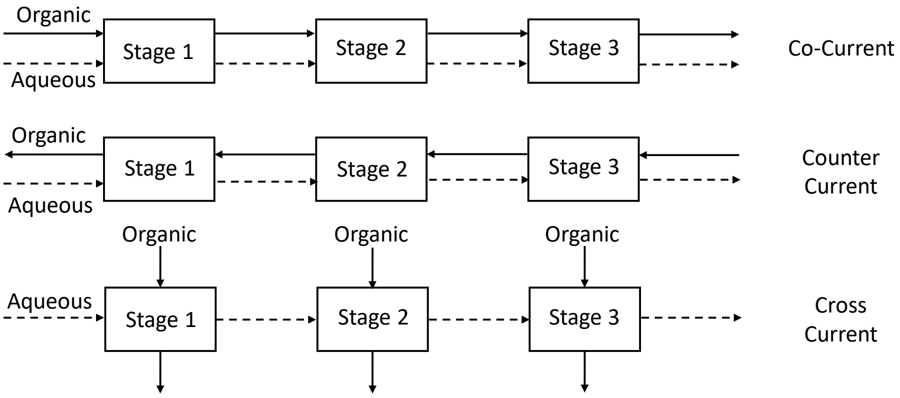

Figure 2.7: *A schematic describing co-current, counter-current and cross-current extraction for multiple extraction stages. Solid and dotted arrows represent organic and aqueous flows respectively. Co-current extraction (top) features two phases, an organic and an aqueous phase, flowing in the same direction through one or more stages. In counter-current extraction (middle), the two phases flow in opposite directions, allowing the phase containing the desired solute to continuously contact fresh extractant. Cross-current extraction (bottom) uses fresh extractant at each stage.*

In co-current flow, both aqueous and organic phases flow in the same direction, beginning at stage 1. Extraction of the solute will continue until an equilibrium is reached.

Counter-current flow, commonly used in nuclear fuel reprocessing, forces the two phases to flow in opposing directions. The aqueous phase will flow from stage 1 to stage 3, whilst the organic phase will begin at stage 3, flowing through to stage 1. The advantage of counter-current over co-current flow is its capability to extract material beyond equilibrium, since the solute carrying phase will continuously meet fresh extractant. This can reduce the amount of extractant needed and create less waste.[20]

Cross-current flow uses fresh extractant at each phase. This has the advantage of being able to extract beyond the equilibrium experienced in co-current flow the solute carrying phase is constant in contact with fresh extractant. When compared with counter-current flow however, a larger volume of extractant will be used.

2.3.3 The PUREX Process

Spent fuel is dissolved into an aqueous phase of 3 M boiling nitric acid and extracted into an organic mixture of 70% TBP (tributyl phosphate) and 20-30% paraffinic hydrocarbon solvent, typically odourless kerosene. Uranyl(VI) nitrate and plutonium(IV) nitrate form neutral complexes with TBP (more detail will be given in Sections 2.5.2) and are extracted into the organic phase. A back-extraction of U(VI) into nitric acid is then performed to further separate it from the Pu(IV). An overview of this process is shown as a flowsheet in Figure 2.8.

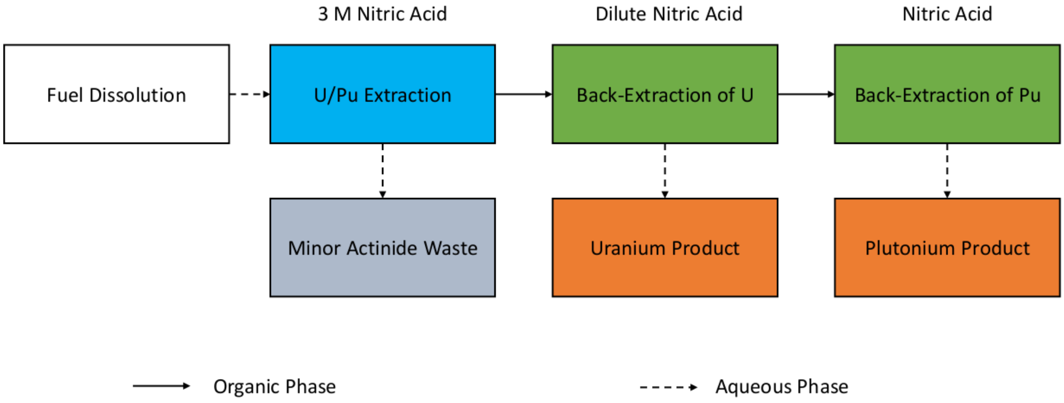

Figure 2.8: *A simplified flowsheet for the PUREX process.*[14, 22] *Solid and dotted arrows denote the flow of organic and aqueous phases respectively. U/Pu are first extracted from the spent fuel solution into an organic phase containing TBP. U and Pu are then separately back-extracted into new aqueous phases.*

The separation of uranium and plutonium streams is considered a proliferation risk, as pure plutonium can be used for nuclear weaponry. As such, recent research has focussed on developing alternative methods. Newer methods, such as UREX,[23] GANEX[24] and advanced PUREX,[25,26] have been heavily developed as alternatives which dilute the purity of the plutonium stream. New methods often focus on extracting some minor actinides, e.g. neptunium, with the plutonium stream to make it less useful for weaponry and reduce the proliferation risk.

2.4 Mass Transfer

2.4.1 Mass Transfer Models

Many studies have tried to explain mass transfer across interfaces. Some common models are the two-film theory, the Higbie penetration model and Dankwerts' surface renewal model.[27]

Two-Film Model

The two-film model is the original model for explaining mass transfer between two phases.[28,29] The model theorises the existence of two steady-state laminar films, one each side of the liquid-liquid interface, which are independent of the turbulences present in the bulk liquids.

Solute concentrations in the bulk liquids are considered homogeneous, as convective mixing will be enough to limit the need for diffusion through the liquid. As such, the laminar films will contain all resistance to mass transfer via diffusion. Concentration difference between the bulk liquid and the film acts as the driving force for mass transfer.

The two-film model is based solely on molecular diffusion across the interface. As such, the rate of mass transfer through the aqueous and organic liquid films can be expressed by Equations 2.2 and 2.3 respectively.[30] Equations 2.2 and 2.3 show the mass transfer rate of a component A, q_A, through an aqueous film and an organic film.

$$q_A = k_{A,aq} a_v (c_{A,aq} - c_{A,aq,i}) \tag{2.2}$$

$$q_A = k_{A,org} a_v (c_{A,org,i} - c_{A,org}) \tag{2.3}$$

Where $\mathrm{k_{A,aq}}$ and $\mathrm{k_{A,org}}$ are the mass transfer coefficients through the aqueous and organic films respectively. The concentration difference in the aqueous and organic films, ($\mathrm{c_{A,aq}}$-$\mathrm{c_{A,aq,i}}$) and ($\mathrm{c_{A,org,i}}$-$\mathrm{c_{A,org}}$) respectively, are the driving forces of mass transfer. If the bulk organic concentration is greater than the interfacial concentration, diffusion will occur, via Fick's law, towards the interface until an equilibrium is reached and the two concentrations are equivalent. The same will occur for the aqueous phase, however in this case diffusion will occur from the interface into the bulk liquid. Figure 2.9 depicts the two-film model of mass transfer for a liquid droplet within a continuous phase.

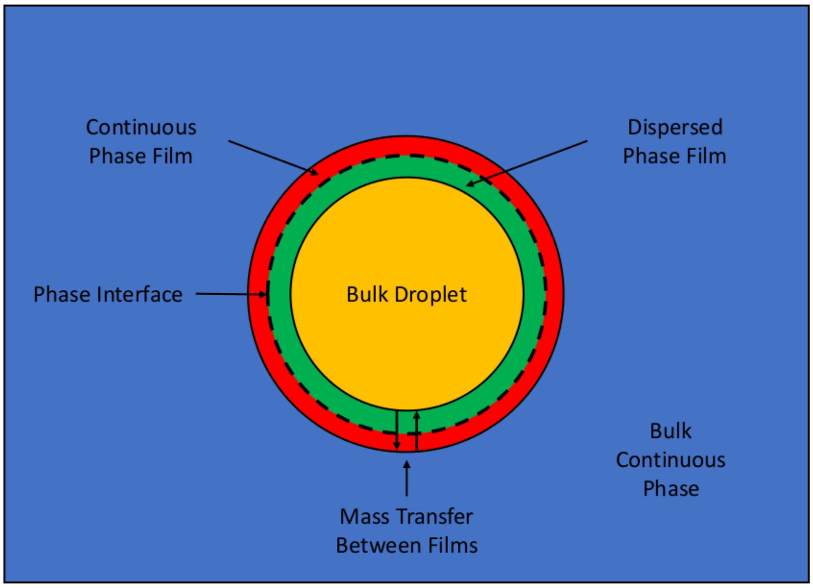

Figure 2.9: *A diagram of the two-film model. Two films, unaffected by bulk turbulences, are modelled around the liquid-liquid interface. The two films are described as containing all resistances to mass transfer.*

Penetration Model

The penetration model, originally introduced by Higbie,[31] is an extension of the two-film model that assumes the elements of the continuous phase are in an unsteady-state.[32] All continuous phase elements that contact the surface are assumed to remain in contact for the same period of time, therefore ignoring the convective effects of eddies in the bulk phase. For a rising droplet, the continuous phase elements will flow over the droplet as seen in Figure 2.10.

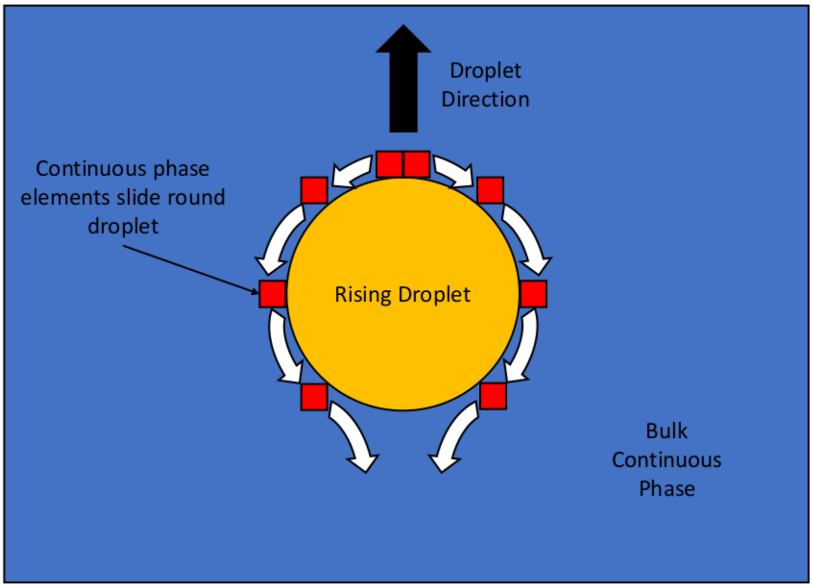

Figure 2.10: *Schematic of the penetration model of mass transfer. Continuous phase elements surrounding a droplet are constantly in an unsteady-state and being renewed. All elements remain in contact with the droplet for the same period of time.*

Mass transfer, much like the two-film theory, is assumed to be diffusive and can be described by Fick's law of diffusion, shown in Equation 2.4.

$$J_A = -D_{AB}\frac{dc_A}{dz} \tag{2.4}$$

Fick's law describes the molar flux of a component A, J_A, based on the concentration gradient of A over distance, z. The diffusivity of component A into component B, D_{AB}, is a coefficient specific to the system and is defined as the ratio of molar flux to concentration gradient.[33]

The aqueous phase mass transfer coefficient can be expressed in terms of the contact time between phases, t_{con}, and the diffusivity as seen in Equation 2.5. This has not been derived here, but a thorough derivation can be found in "Transport Phenomena" by Bird et al.[34]

$$k_{A,aq} = 2\sqrt{\frac{D_{AB}}{\pi t_{con}}} \tag{2.5}$$

Surface Renewal Model

In 1951, Danckwerts expanded on Higbie's work by introducing a new model for interface mass transfer. Danckwerts explains that the two-film model, which was the standard model at the time, is unrealistic and misleading.[35] Danckwerts does accept that in many cases the two-film model is convenient and harmless but in cases of unknown nature, may cause erroneous results.

The surface renewal model denies the assumption of a laminar film, stating that in turbulent systems it is more likely that turbulence will reach the interface between phases. As such, the interfacial region, combined with the well mixed bulk region of the continuous phase, can be seen as one thick film. As in the penetration model, the surface renewal model assumes that continuous phase elements are in an unsteady-state, and often renewed. However, unlike the penetration model, the elements are assumed to spend a random amount of time in contact with the interface, since eddies will constantly replace the surface. As such, the surface renewal frequency, f_{SR}, is used to capture the constant changing of the interface due to turbulences in stead of t_{con}. The new equation for the mass transfer coefficient is shown in Equation 2.6.[36]

$$k_{A,aq} = \sqrt{D_{AB} f_{SR}} \tag{2.6}$$

Due to complexity of the surface renewal and penetration models, as well as the lack of knowledge about the diffusivity in the system, the two-film model has been used throughout this thesis.

2.4.2 Mass Transfer with a Chemical Reaction

In order to account for a chemical reaction, an enhancement factor, $\mathrm{E_q}$, is introduced. $\mathrm{E_q}$ is defined in Equation 2.7 and will be a value equal to or greater than 1.[30]

$$E_q = \frac{\text{Mass transfer with chemical reaction}}{\text{Mass transfer without chemical reaction}} \tag{2.7}$$

$\mathrm{E_q}$ will equal 1 when then the chemical reaction has little to no effect on the molecular transfer, and when diffusion is the only relevant process. If a reaction at the interface will improve the mass transfer rate however, the value of $\mathrm{E_q}$ will be greater than 1.

2.4.3 The Rate Equation & Mass Transfer Resistance

The equation for the rate of mass transfer of a component, A, between an aqueous liquid phase and an organic liquid phase is given by Levenspiel and can be seen in Equation 2.8.[30]

$$q_A = \frac{1}{\frac{1}{k_{A,aq}a_v} + \frac{S}{k_{A,org}a_v E_q}}(c_{A,aq} - Sc_{A,org}) \tag{2.8}$$

The two terms in the denominator describe resistance to mass transfer in the different phases. The first term containing $k_{A,aq} \cdot a_v$ represents the resistance of component A to diffusion within the aqueous phase while the second term, containing $k_{A,org}a_v E_q$, denotes the resistance to reaction and diffusion within the organic phase.[30]

In the case of a fast chemical reaction at the interface, $\mathrm{E_q}$ will be much greater than 1 and the term including $k_{A,org}a_v E_q$ will tend towards zero with increasing reaction rate.

Stamatiaou and Muller define an overall mass transfer resistance, Ω_T, which is shown in Equation 2.9 to combine the two separate resistances.[37]

$$\Omega_T = \frac{1}{k_{A,aq} a_v} + \frac{S}{k_{A,org} a_v E_q} = \Omega_{aq} + \Omega_{org} \tag{2.9}$$

2.5 Extraction of Metals

Solvent extraction of metals is achieved by chemical complexation between a metal ion and an extractant molecule dissolved into the organic phase. The rate of extraction is dictated by diffusion of the metal ion through the aqueous phase or the rate of chemical reaction between the metal ion and the ligand. Diffusion rate, calculable through Fick's law of diffusion,[38] can be mitigated by increasing the dispersed phase surface area with increased agitation.[39]

In the 1970s, an interfacial mechanism for metal extraction was proposed.[19,40] Extractant ligands often possess amphiphilic qualities, with a hydrophobic alkyl group and an active hydrophilic group capable of complexing with the metal ion. The hydrophobicity of a ligand is increased with the alkyl chain length. Metal extracting ligands are less surface active than most surfactants, however they still adsorb to the phase interface, where they are able to react with metal ions near the surface of the aqueous phase. The rate of interfacial reactions is dependent on the interfacial concentration of ligand, which will increase with ligand concentration until the interface is saturated.[41] As such, a larger molecule would be expected to have a reduced extraction rate as it occupies a larger area. This is evidenced by the increased reaction rate associated with aliphatic extractants when compared against aromatic extractants.[42,43] A step by step extraction of a metal ion by chelation is shown in Equation 2.10, where M and L denote the metal ion and ligand respectively. Species present in the organic phase, adsorption layer and aqueous phase are given the subscripts org, ad and aq respectively.

$$\begin{aligned}
(L\cdot H)_{org} &\rightleftharpoons (L\cdot H)_{ad} && \Big\}\, S_{LH}=\frac{[LH]_{org}}{[LH]_{ad}}\\
(L\cdot H)_{ad} &\rightleftharpoons L^-_{ad}+H^+_{aq} && \Big\}\, K_{LH}=\frac{[L^-]_{ad}[H^+]_{aq}}{[LH]_{ad}}\\
\left.\begin{array}{r}
M(II)_{aq}+L^-_{ad}\rightleftharpoons (M(II)\cdot L^+)_{ad}\\
*(M(II)\cdot L^+)_{ad}+L^-_{ad}\rightleftharpoons (M(II)\cdot 2L)_{ad}\\
*(M(II)\cdot L^+)_{ad}+L^-_{aq}\rightleftharpoons (M(II)\cdot 2L)_{ad}
\end{array}\right\} && && K_f=\frac{[M(II)\cdot 2L]_{ad}}{[M(II)]_{ad}[L^-]_{ad}}\\
(M(II)\cdot 2L)_{ad} &\rightleftharpoons (M(II)\cdot 2L)_{org} && \Big\}\, S_{Cu2L}=\frac{[M(II)\cdot 2L]_{org}}{[M(II)\cdot 2L]_{ad}}
\end{aligned} \tag{2.10}$$

The steps marked with an asterisk (*) have been identified as the slowest reactions, and are therefore rate determining. The two marked stages differ only in the location of the L$^-$ ion. L$^-_{ad}$ and L$^-_{aq}$ refer to the ligand ion adsorbed to the interface and the small quantity of ligand ion that has transferred into the aqueous phase respectively. The overall complexation equilibrium is given in Equation 2.11.

$$M(II)_{aq}+2LH_{org}\rightleftharpoons M(II)\cdot 2L_{org}+2H^+_{aq} \tag{2.11}$$

Diluents are often used when an extractant material is too viscous to pump. By mixing the extractant with a lower viscosity material, transport and mixing are made easier. Choice of diluent is shown to have an effect on the extent of extraction.[44,45] Diluents which interact more heavily with the extractant molecule, for example dipole moments or solubility, induce a reduction in the extractants capability for mass transfer.[45] A solvent with increased dipole moment can cause a reduction in the extraction rate of a metal ion as there will be greater interaction between the diluent and extractant molecules.

2.5.1 Back-extraction of Metals

Back-extraction, or stripping, is the process by which a metal ion is removed from its organic complex and extracted into an aqueous phase. The rate of extraction is heavily dependent on the pH and H$^+$ concentration of the aqueous phase.

The rate of back-extraction is inversely proportional to the pH, i.e. an increased acidity will more rapidly strip a metal ion from its complex.[46]

Metal back-extraction is achieved by acidic decomposition of metal complexes. Decomposition only occurs when the metal complex transfers into the aqueous phase, coming into contact with acidic solution.[47] As such, complexes with lower partition coefficients (Equation 2.1) are more quickly back extracted.

2.5.2 Uranium & Plutonium Extraction

Solvent extraction of metals is of particular importance in nuclear reprocessing as uranium and plutonium are extracted from spent fuel to form MOx fuels.[2] This is achieved via the PUREX process, the only industrial method for spent fuel reprocessing currently in use.

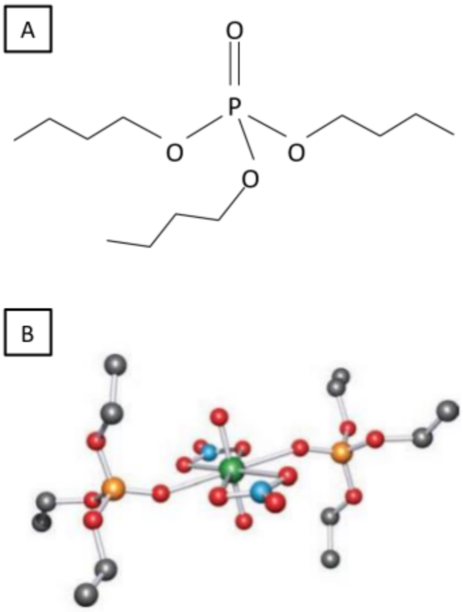

Figure 2.11: **(A)** *The TBP molecule. Image reconstructed from Housecroft and Sharpe (2012).*[48] **(B)** *A depiction of the* $U(VI)O_2(NO_3)_2{\cdot}2TEP$ *chelate complex. TEP (Triethyl phosphate) is a similar molecule to TBP, with shorter alkyl chains. Image taken from Housecroft and Sharpe (2012) and is based on data from Kanellakopulos et al. (1993).*[48,49]

Spent fuel is dissolved into a 3M HNO_3 aqueous phase and brought into contact with an organic phase constituting 30% tributyl phosphate (TBP) extractant in a 70% odourless kerosene diluent. The diluent is used to reduce the viscosity of the TBP. Uranium and plutonium are not extracted from spent fuel as metals, but instead form bidentate complexes with TBP as uranyl nitrate, $U(VI)O_2(NO_3)_2$, and plutonium nitrate, $Pu(IV)(NO_3)_4$.[50] The complexation is a bidentate chelation and is shown to be an interfacial reaction.[51,52] Chemical equations for both nitrate extractions can be seen in Equations 2.12 and 2.13.[53,54]

$$U(VI)O_2^{2+} + 2NO_3^- + 2TBP \rightleftharpoons U(VI)O_2(NO_3)_2 \cdot 2TBP \tag{2.12}$$

$$Pu(IV) + 4NO_3^- + 2TBP \rightleftharpoons Pu(IV)(NO_3)_4 \cdot 2TBP \tag{2.13}$$

To further separate U and Pu, Pu is extracted into a new aqueous phase. The aqueous phase consists of a low pH (< 0.5) nitric acid solution.[10] Pu(IV) first needs to be reduced to Pu(III) since the III oxidation state is not soluble in the organic solvent.[12] This results in transfer of plutonium nitrate back into an aqueous phase. Uranous nitrate, $U(IV)(NO_3)_4$, stabilized with hydrazine, is used as a reduction agent as shown in Equation 2.14.[10,55]

$$\begin{aligned}2Pu(IV)(NO_3)_4 + U(IV)(NO_3)_4 + 2H_2O \rightleftharpoons 2Pu(III)(NO_3)_3 \\ +U(VI)O_2(NO_3)_2 + 4HNO_3\end{aligned} \tag{2.14}$$

Other reprocessing techniques are being developed, though none of them are currently being used in any industrial processes. Newer processes are designed to replace PUREX and dilute the purity of the Pu stream with minor actinides such as neptunium. Doing this reduces the proliferation risk pure plutonium presents. Some examples of modern techniques are advanced PUREX,[25,26] UREX[23] and GANEX.[24]

2.5.3 Copper Extraction

Extraction of copper can be achieved with a range of organic extractants, for example oximes[19,40,56] and carboxylic acids.[57–59] This work uses the oxime 2-

hydroxy-5-nonylacetophenone oxime, a commonly used extractant in the mining industry. An oxime, the defining structure of which is seen in Figure 2.12, is defined by an NOH group double bonded to an organic side chain, R, and a secondary group, R'. R' can either be hydrogen or a second organic side chain, making the oxime an aldoxime or a ketoxime respectively. In a hydroxyoxime, the R group consists of a phenolic group with an attached hydroxyl group, as seen in Figure 2.13. When used as an extractant, a hydroxyoxime forms a 2:1 ligand:metal chelate complex[19] with several metals including copper, nickel and zinc.

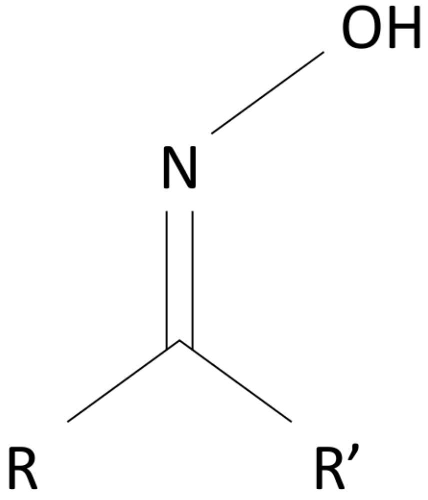

Figure 2.12: *The basic structure of an oxime. An NOH group is double bonded to an organic chain, R, and a secondary group R'. R' defines the oxime as a ketoxime or an aldoxime, depending on whether it consists of a second organic chain or a single hydrogen respectively.*

Hydroxyoxime solutions exhibit a decrease in the interfacial tension between an organic and aqueous phase. This is evidence for interfacial adsorption of the ligand, with the oxime adsorbing onto the organic/aqueous interface.[60,61] Adsorption occurs through hydrogen bonding between the water molecules and the lone pair of the oxygen present in the phenolic hydroxyl. Inclusion of additional groups near the phenolic hydroxyl shows a reduction in the extraction rate as adsorption is made more difficult by the physical structure of the molecule.[42]

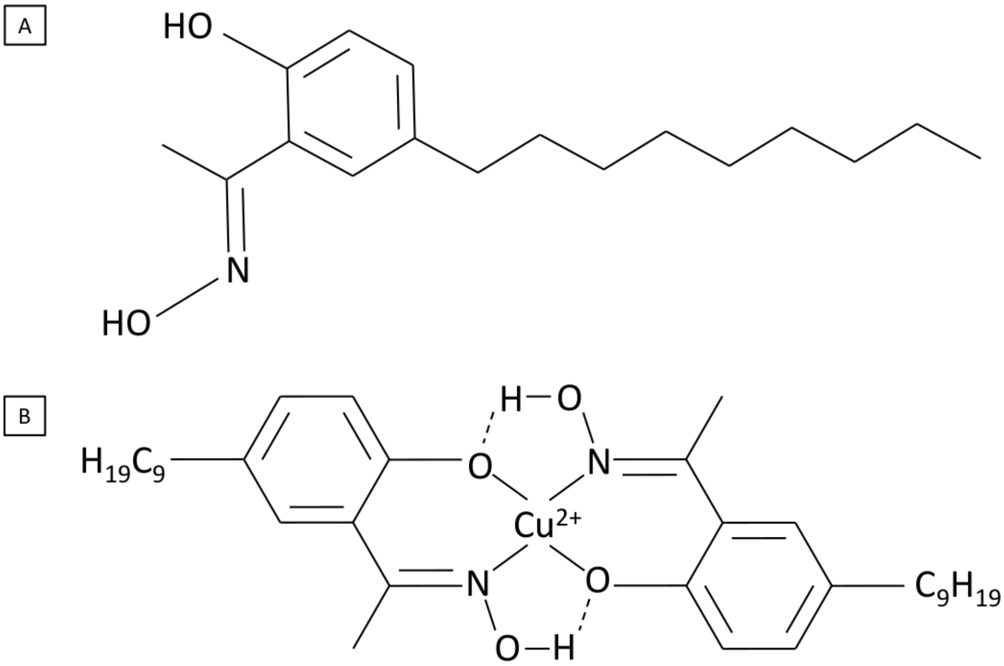

Figure 2.13: **(A)** *The 2-hydroxy-5-nonylacetophenone oxime ligand, commonly used for copper extraction.* **(B)** *The Cu(II)·2L chelate complex formed by a Cu(II) ion and two oxime ligands.*

Cu(II) extraction by hydroxyoximes is found to be first order with respect to Cu(II) concentration, hydroxyoxime concentration and time.[19,62] Extraction rate is also seen to be proportional and first order with respect to pH. This is only true between pH values of approximately 0.5-2 however, outside of which the reaction stops. At higher pH, this is simply explained as an extraction nearing 100% stage efficiency, whilst at low pH the reaction is stopped due to the high protonation of the aqueous phase.[63] The high concentration of H^+ ions deters the dissociation of the hydrogen from the ligand, thus not allowing for complexation with Cu(II).[63]

$$\ln\frac{c_t}{c_0} = k'_{aq} \qquad ; \qquad (k'_{aq} + k'_{org})t = \ln\left(\frac{c_{eq} - c_t}{c_t - c_{eq}}\right) \tag{2.15}$$

Equation 2.15 shows the pseudo first order mass transfer equation for continuous Cu(II) extraction by hydroxyoxime, where $\mathrm{k}'_{\mathrm{aq}}$ and $\mathrm{k}'_{\mathrm{org}}$ are the pseudo first order mass transfer coefficients for the aqueous and organic phases. $\mathrm{c_t}$, $\mathrm{c_0}$

and c_{eq} are the aqeuous concentrations at time t, t=0 and at equilibrium respectively.[64] The left equation applies to reactions which tend to completion, whilst the right hand equation is used for equilibrium constants below 10.

Table 2.1 shows a number of values for the mass transfer coefficient, k, with different extractants. Values are consistently in the order 10^{-5} m·s^{-1}, with the exception of the results presented by Dimitrov et al.[65] who report values a factor of 10 lower. Miyake et al.[66] use the extractant 2-hydroxy-5-nonylacetophenone oxime, which will be the focus system used in this thesis.

Table 2.1: *Literature values for the mass transfer coefficient. Values for the mass transfer coefficient are given as well as the physical and chemical systems used.*

Author	Extractant	System	Mass Transfer Coefficient (m·s^{-1})
Miyake et al. (1983)[66]	2-hydroxy-5-nonylacetophenone oxime	Liquid membrane	$k_{aq} = 2.01 \times 10^{-5}$
Dimitrov et al. (1997)[65]	2-hydroxy-5-nonylbenzophenone oxime (LIX-65N)	Liquid membrane	$k_{aq} = 0.5 \times 10^{-6}$ $k_{org} = 0.5 \times 10^{-6}$
Alguacil et al. (2002)[67]	5-dodecylsalicylaldoxime (MOC-55 TD)	Liquid membrane	$k_{aq} = 2.8 \times 10^{-5}$
Alguacil et al. (2012)[68]	2-hydroxy-5-nonyl benzaldehyde oxime	Pseudo-emulsion membrane	$K_{aq/org} = 5.5 \times 10^{-5}$

Mass transfer coefficients in Table 2.1 are given in a range of forms. This includes the aqueous phase mass transfer coefficient, k_{aq}, the organic phase mass transfer coefficient, k_{org}, and the overall mass transfer coefficient (inclusive of the mass transfer resistances for both phases), $K_{aq/org}$.

2.6 Current Reprocessing Equipment

2.6.1 Mixer-Settler

The mixer-settler is the most simple design of extraction equipment. The heavy and light phases both enter a mixing compartment in which they are agitated by an overhead, motor-driven mixer. The mixed phases overflow a weir, labelled A in Figure 2.14, into a separation compartment where they are allowed to separate under gravity.[69] Separation is often aided by coalescence plates in non-nuclear industries,[70] however within the nuclear industry these are not used as they provide an area for radioactive material to build. The two phases are separated by two weirs, labelled C in Figure 2.14, used to separate the two phases before they are moved on to the next stage of extraction. Mixer-settler arrays are generally counter-current, though flow within a single mixer-settler is co-current.

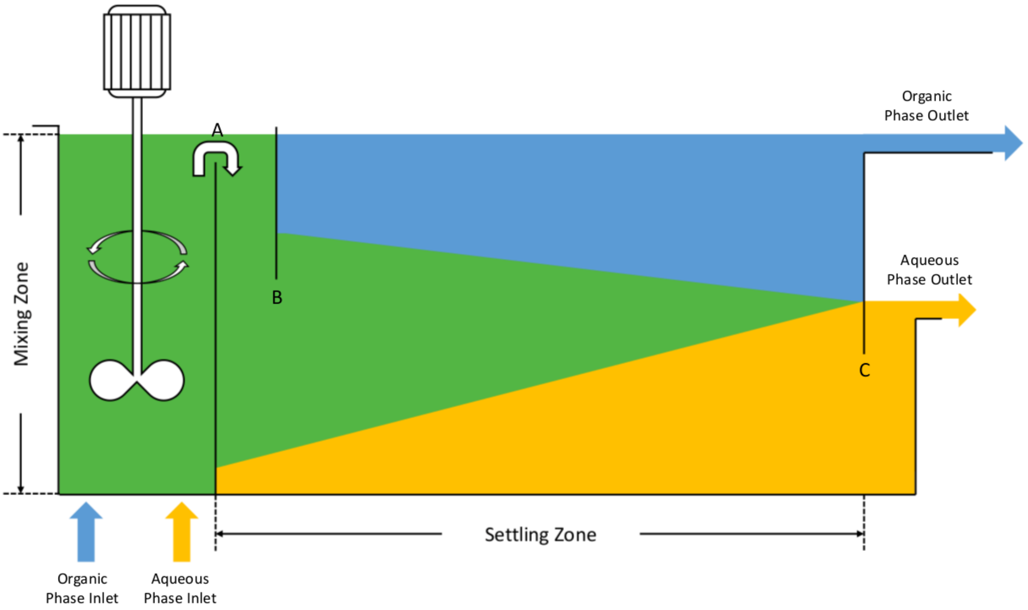

Figure 2.14: *A diagram of a single stage mixer-settler solvent extraction unit. The two immiscible phases enter a mixing chamber and are agitated by an overhead, motor-driven agitator. The two liquids pass into a settling chamber where they are allowed to separate. Weirs at C separate the two liquids as they continue to the next extraction stage.*

There are a number of disadvantages present when using mixer-settlers within the nuclear industry. Firstly, mixer-settlers require a large footprint and a large number of stages to reach the required separation. Long residence times mean solvent is in contact with concentrated nitric acid for long periods of time and may cause solvent degradation. As well as this, moving mechanical parts in a radioactive area, such as the mixing impeller, are a significant downside that may cause expensive repairs. The shape of a mixer-settler is not suitable for separation of highly radioactive materials and criticality (the point at which nuclear material is able to sustain nuclear fission) is a concern when not keeping to lower activity separation. This is due to the large volume to surface area ratio, reducing the number of neutrons able to escape the mixer-settler, increasing the probability of interaction with fissionable atoms.

Though outdated, mixer-settlers do have some advantages. Use in a range of industries means they are well understood with a considerable log of literature. A simple design means they are easily fixed (when not in a radioactive region) and modified if necessary.

Studies into mixer-settler hydrodynamics have found that droplet size is dependent on agitation rate and organic phase hold up.[71] Mean droplet size is shown to decrease with an increase in each of these parameters.[72] Droplet size distributions are shown to follow a log-normal distribution, with the peak of the curve being consistent with the average droplet size. At higher agitation rates, the distribution is shown to narrow.[72] Inclusion of a surfactant has also been shown to have an effect on droplet sizes in a mixer-settler. Introduction of a surfactant, such as SLS (sodium lauryl sulphate)[73] or aniline,[74] reduces the interfacial tension of a droplet, reducing the strength of shear forces required to break the droplet.

Stage efficiencies, as well as mass transfer coefficients, in mixer-settlers vary between systems, with some studies reporting efficiencies in the order of 90%[75] or 100%,[76] while others state their maximum efficiency to be around 50% for aqueous to organic mass transfer.[77] This variation is likely due to the differences in design or chemical system. A linear increase in stage efficiency with increasing agitation rate is however consistently observed.[78]

2.6.2 Pulsed Column

The pulsed column, designed specifically for the nuclear industry,[79] is an alternative contactor for solvent extraction. A schematic can be seen in Figure 2.15.

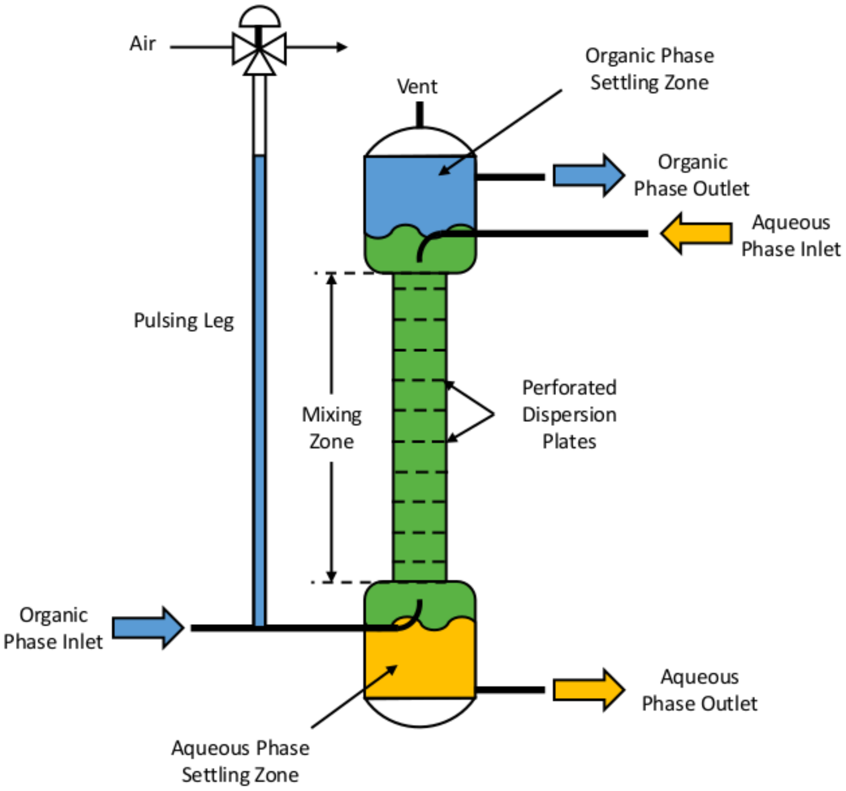

Figure 2.15: *Diagram of a single stage pulsed column extraction unit. The light and heavy phases enter at the bottom and top of the column respectively. They are then allowed to separate under gravity. Flow of the light phase is pulsed through perforated plates to increase the interface surface area via dispersion of the liquid. The two phases are separated in vessels at each end of the column before continuing to further stages of extraction.*

The aqueous and organic phase inlets are situated at the top and bottom of the column respectively, providing counter-current flow as the two phases separate via gravity separation.[80] A pulsation of the organic phase within the column, caused by a pulsing leg, forces the organic phase through a series of perforated plates.[81] By admitting compressed air into the pulsing leg, the liquid in the pulsed column is forced upwards. When the compressed air is released from the pulsing leg liquid is instead drawn downwards. This motion causes turbulence and drives the organic phase through the perforated plates, causing dispersion and increasing contact between the two liquids. Extent of dispersion is determined by the height of the column, the frequency and amplitude of the pulse and the size of the holes in the perforated discs.[82] The organic and the aqueous phases are removed from the column at the top and bottom settling zones respectively.

Pulsed columns require a far smaller footprint than a mixer-settler, however they are considerably taller and need a much higher ceiling. The shape of the column, due to the low volume to surface area ratio, is conducive to the extraction of highly active materials and criticality is not an issue. The external nature of the pulsing leg (shown in Figure 2.15) allows for no moving parts to be situated in the radioactive region. This makes any repairs considerably easier and cheaper to achieve.

Even though pulsed columns are commonly used, the hydrodynamics are poorly understood and further research is necessary to predict mass transfer and dispersion within the column. There have been several computational studies in recent years to rectify this and model pulsed columns. Yadav et al. present k-ε models, demonstrating a prediction of ± 10% when compared with dispersed phase hold-up[83] in experimental data provided by Laddha et al. (1976).[84] Theobald et al. (2018) conduct single and multiphase LES (large eddy simulation) studies, finding the single phase model to show good agreement with experimental data. The multiphase model on the other hand varied significantly.[85] LES simulations have also been used to show good prediction of turbulences in a pulsed column.[86]

Yadav et al. provide an extensive review of pulsed columns, including mass transfer coefficient correlations, some of which are listed in Table 2.2. Definitions of each term in the equations are listed in the Nomenclature section of this thesis. Correlations are written in literature in terms of the height per transfer unit

(HTU), which can be rewritten in terms of the mass transfer coefficient for a particular phase, $\frac{1}{\Omega}$, using Equation 2.16.

$$(HTU)_{aq} = u_{aq}\Omega_{aq} \qquad ; \qquad (HTU)_{org} = u_{org}\Omega_{org} \tag{2.16}$$

Where u_{aq} and u_{org} are the superficial velocities of the aqueous and organic phases respectively.

Table 2.2: *Mass transfer coefficient correlations for three pulsed column systems.*

Author	Correlations and Comments
Thornton (1957)[87]	$\frac{1}{\Omega_T}=u_{aq}\left[b\left(\frac{\mu_{aq}^2}{g\rho_{aq}^2}\right)\left(\frac{\mu_{aq}g}{u_d^3(1-\phi)^3\rho_c}\right)^{\frac{2m}{3}}\left(\frac{\Delta\rho}{\rho_{aq}}\right)^{\frac{2(m-1)}{3}}\left(\frac{u_{org}}{u_{aq}}\right)^{0.5}\left(\frac{V_{aq}^3\rho_{aq}}{g\mu_{aq}\phi^3}\right)^{0.33}\right]$ m = 0.5 for aqueous to organic transfer m = 0.25 for organic to aqueous transfer b is found experimentally
Smoot et al. (1959)[88]	$\frac{1}{\Omega_T} = 0.20\left(\frac{u_{org}D_h\rho_{org}}{\mu_{org}}\right)^{0.434}\left(\frac{\Delta\rho}{\rho_{org}}\right)^{-1.04}\left(\frac{\mu_{org}}{\rho_{org}D_h}\right)^{-0.865}\left(\frac{\sigma}{\mu_{org}u_{aq}}\right)^{-0.096}\left(\frac{u_{org}}{u_{aq}}\right)^{0.636}\left(\frac{D_c}{h_p}\right)^{-0.317}\left(\frac{\mu_{aq}}{\mu_{org}}\right)^{-4.57}\left(\frac{u_{aq}}{h_p}\right)$ Applicable for aqueous to organic transfer
Luo et al. (1998)[1]	$\frac{1}{\Omega_T} = \left(\gamma\frac{1}{\phi(1-\phi)^n}\right)^{-1}$ $\gamma = \frac{3\mu_{org}+2\mu_{aq}}{0.52(3\mu_{aq}+3\mu_{org})}\left(\frac{4\Delta\rho^2g^2}{225\rho_{aq}\mu_{aq}}\right)^{-1/3}\left(\frac{S+\kappa}{0.0225}\right)$ $n = 0.67 + 0.028\left(\frac{\mu_{aq}}{\mu_{org}}\right)^{0.26}\left(\frac{\rho_{aq}^2\sigma^3}{\mu_{aq}^4\Delta\rho g}\right)^{0.17}$ $\kappa = \frac{\mu_{org}}{\mu_{aq}}$

Yadav et al. (2008) show that the correlations listed in Table 2.2 fail to predict mass transfer rates not associated with the systems they were designed for.[80] As such, no general mass transfer coefficient correlation currently exists.

2.7 Alternative Solvent Extraction Equipment

2.7.1 Taylor-Couette Contactors

Taylor-Couette flow is a phenomenon exhibited when a fluid is contained between two concentric cylinders with relative rotational velocities. In 1923, Taylor showed, through a series of experiments, that Couette flow (purely rotational flow) between two concentric cylinders can become unstable above a critical rotational velocity.[89] The effect is to produce a series of toroidal vortices such as those photographed[90] and depicted[89] in Figures 2.16 and 2.17 respectively. Vortices rotate in opposing directions to their neighbours, balancing angular momentum.

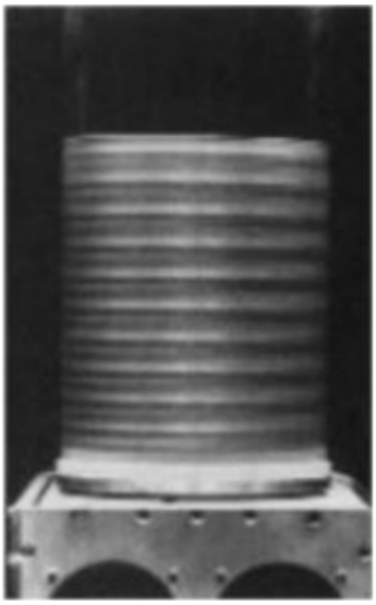

Figure 2.16: *A photograph of Taylor-Couette flow in two concentric cylinders. Photograph taken from Stewart and Golubitsky (2011)*[90]

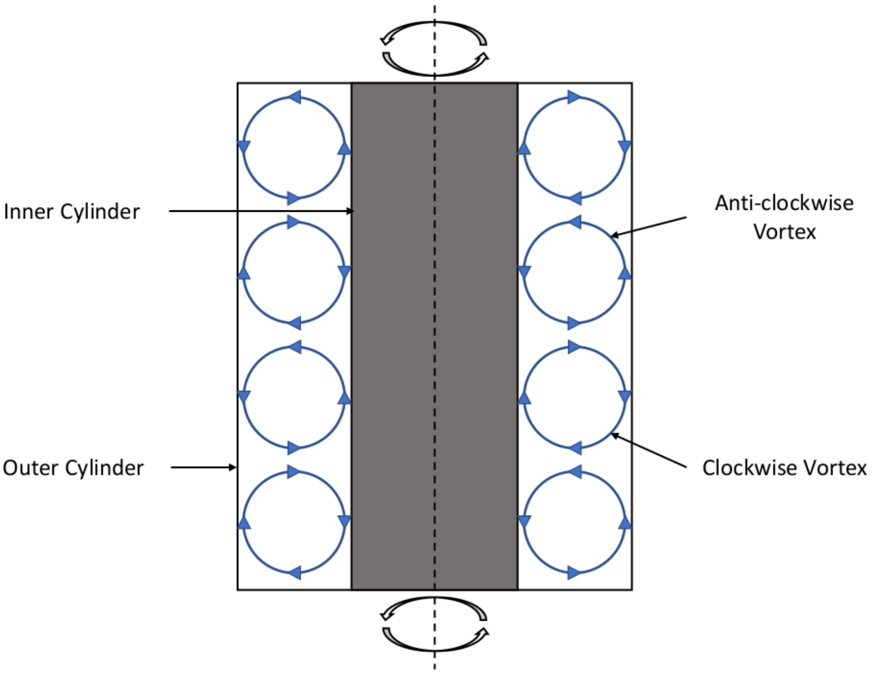

Figure 2.17: *A schematic showing the cross-section of a Taylor-Couette contactor. Toroidal vortices form upwards along the annulus, forming in pairs. Pairs rotate in opposite directions to balance momentum. Reconstructed from Taylor (1923).*[89]

Taylor introduces a quantity called the Taylor number, defined as the ratio of centrifugal to viscous forces. Above a critical value of the Taylor number a transition occurs between steady Couette flow and unstable Taylor-Couette flow.[89] The definition of the Taylor number is dependent on the systems physical parameters; the size of the annular gap and the relative velocities between the two cylinders can affect how the system operates. The Taylor number is given in Equation 2.17 in terms of the ratio of rotational velocities, $\theta = \frac{\omega_{out}}{\omega_{in}}$, and the cylinder radius ratio, $\eta = \frac{R_{in}}{R_{out}}$.[89]

$$N_{Ta} = \frac{4(\theta - \eta^2)}{\eta^2 - 1} \frac{\omega_{in}^2 D_{an}^4}{\nu^2} \tag{2.17}$$

For a system in which the inner cylinders rotational velocity, ω_{out}, is greater than the outer cylinders rotational velocity, ω_{in}, and both cylinders rotate in the same direction, no instability occurs. When the cylinders rotate in opposing directions two sets of vortices appear, each occupying half of the annular gap.[89] Annular gap distance also has an effect on the observed instabilities.[91–93] For the case in which the inner cylinder rotates and the outer cylinder is stationary, toroidal vortices form, filling the whole annular width. The Taylor number equation for this case is shown in Equation 2.18.[94]

$$N_{Ta} = \frac{2\eta^2}{\eta^2 - 1} \frac{\omega_{in}^2 D_{an}^4}{\nu^2} \tag{2.18}$$

For a system in which only the inner cylinder rotates, the critical Taylor number is approximately 1708.[95] In other configurations, an additional factor is included, to offset this constant. This will be based on the relative rotational velocities and gap width of the system.[89, 92, 93, 96, 97]

With further increase in the Taylor number, new instabilities are witnessed, displaying a wavy form such as those seen in Figure 2.18. Further increasing the rotational velocity increases the waviness until they become near indistinguishable.[98, 99]

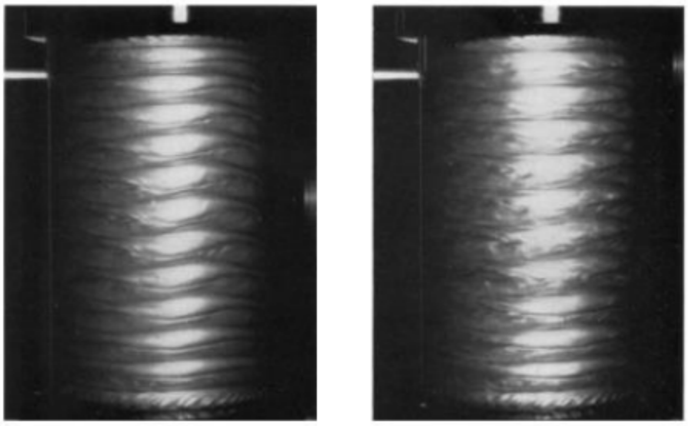

Figure 2.18: *Two photographs showing the wavy instabilities formed at high rotational velocities. The images on the left and right show wavy instabilities at two rotational velocities. The right hand image shows highly turbulent vortices induced at high rotational velocities. Images are taken from Coles (1965)*[98]

While Taylor-Couette flow is heavily discussed in literature, Taylor-Couette reactors are not often considered for practical applications.[100] However, some exceptions do exist, with some uses benefiting from the uniformity of physical conditions within the reactor. Taylor-Couette flow can be of benefit to crystallization[101] and polymer synthesis,[102] as the uniform process conditions allow narrow particle size distributions. Easily controlled shear stresses facilitate the fine-tuning of particle aggregation and flocculation[103] as well as being useful when considering fragile biological materials.[104,105] Adaptations to the traditional Taylor-Couette reactor, such as the Taylor-Couette disc contactor, have also been considered for solvent extraction processes.[106,107]

The Taylor-Couette Disc Contactor

The Taylor-Couette disc contactor (TCDC), originally designed by Aksamija et al.[106] and further developed by Grafschafter et al.,[107–110] is a novel combination of a Taylor-Couette contactor (TCC) and a rotating disc contactor (RDC). Diagrams of the RDC and TCDC can be seen in Figure 2.19.

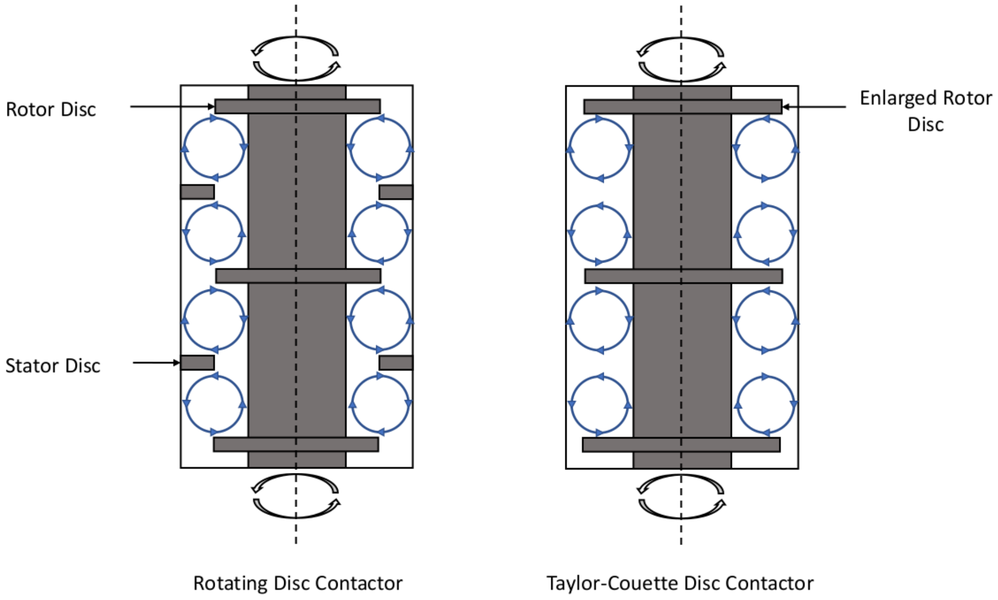

Figure 2.19: *A diagram comparing the RDC with the TCDC. An RDC (left) consists of two concentric cylinders with rotor and stator rings attached to the inner and outer cylinders respectively. The TCDC (right) is similar to the RDC, though the stator rings have been removed and accounted for with larger rotor discs. Image reconstructed from Grafschafter et al. (2017)*[108]

A TCC (refer to Figure 2.17) is constructed from two concentric cylinders with relative rotational velocities. An RDC uses the same principles as a TCC but includes the addition of rotor discs and stator rings connected to the inner and outer cylinders respectively. The aim of the discs and rings is to control vortices, making them more stable and predictable by limiting undesired flow regimes such as wavy motion. The TCDC removes the stator rings and compensates by increasing the rotor disc diameter. This has the effect of removing dead zones created by stator discs and minimizing axial dispersion.[106]

A design template for a TCDC is put forward by Grafschafter et al.,[108] a reconstruction of which can be seen in Figure 2.20. This design allows for two toroidal vortices to form between each pair of discs, each occupying half of the cavity.

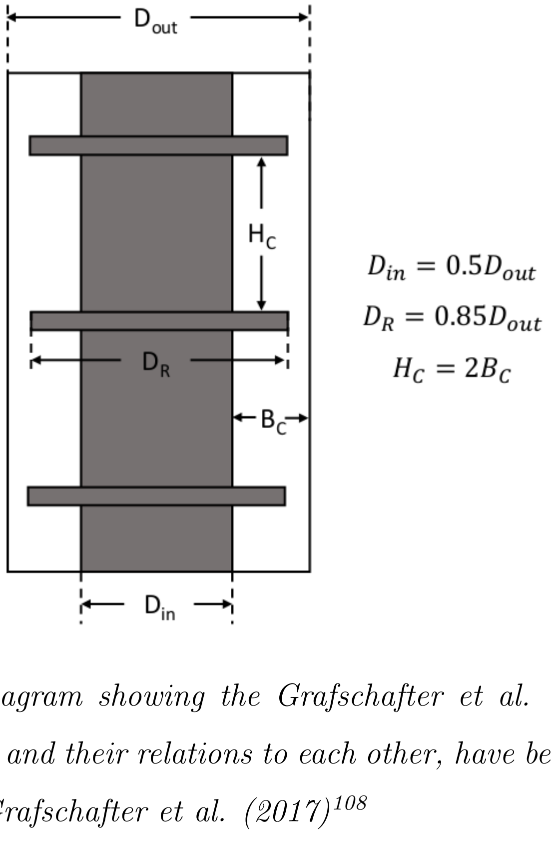

Figure 2.20: *A diagram showing the Grafschafter et al. design rules for a TCDC. Dimensions, and their relations to each other, have been included. Image reconstructed from Grafschafter et al. (2017)*[108]

2.7.2 Agitated Tube Reactor

For a new solvent extraction technology to be viable for the nuclear industry it would need to meet a few criteria in order to improve on current equipment:

- Extraction efficiency greater than or equal to current equipment
- Greater or equivalent cost efficiency than current technology
- Smaller or equivalent volumetric footprint
- No moving seals within radioactive regions to lower risk of active liquid leakage and reduce expensive repairs
- Ideal shape to remove criticality risk for extraction of highly active materials

The Coflore®-ATR (Agitated Tube Reactor) is a candidate that has the potential to meet these criteria and will be the subject of this research.

Originally designed as a flow chemistry reactor, the ATR, shown on the left-hand side of Figure 2.21, consists of an array of connected tubes each containing a free moving agitator. Subjecting the array to lateral motion causes the agitator to move, inducing mixing within the tube. The placement of the agitator bar within a single tube is shown on the right-hand side of Figure 2.21.

The design of the ATR makes it very versatile. The modular ability to connect only the necessary number of tubes gives the ATR the ability to be customisable and able to suit any individual process. Tubes can also be connected in such a way that a particular phase can come into contact with as many different extractants as required, allowing for multiple extractions to be performed in a single unit. This could be useful in the nuclear industry as two extraction stages are performed: the extraction of uranium and plutonium followed by the back extraction of uranium.

Figure 2.21: **(Left)** *A diagram of a ten tube agitated tube reactor.[111] Fluid passes through up to ten tubes via an inlet at the top of the array and flow through the tubes sequentially until leaving the reactor via an outlet at the bottom. Tubes are modular and can be added or removed as necessary.* **(Right)** *A diagram of the interior of a tube.[111] Each tube contains a free-moving agitator bar. As the ATR is subject to lateral shaking, the bars are forced to move, agitating the liquid flowing through the tube.*

The bulk of literature available for the ATR focusses on flow chemistry, for example biocatalysis[112–114] or chemical synthesis.[115] Some preliminary single phase direct or large eddy simulations (LES) between Reynolds numbers of 1200-1500 have been performed by Derksen in order to test their numerical simulation methods.[116] Beyond this, few studies on the flow characteristics of the ATR have been published and to the author's knowledge, no studies have been executed regarding solvent extraction in an ATR.

The ATR has been demonstrated to be analogous to a plug flow reactor.[117] Feeding water through the ATR and introducing a pulse of strong brine solution, Parrington measured the dissipation of that pulse through 4 and 6 ATR tubes. The outward pulses for a 6 tube array are shown in Figure 2.22 and have been measured after 2, 4 and 8 minute residence times. The time range between the initial and final time brine is detected is seen to be consistent regardless of the residence time. This indicates plug flow and allows the residence time of the tube contents to be extremely predictable.[117]

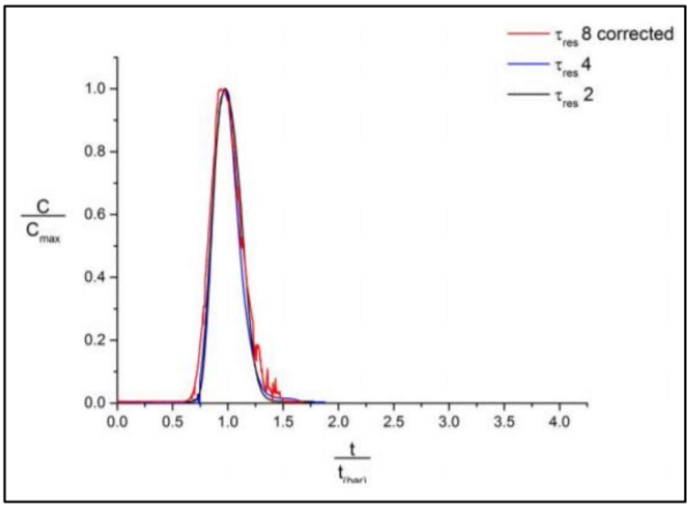

Figure 2.22: *Residence time distributions in an agitated tube reactor by Parrington.*[117] *Residence time distributions were recorded for a 6 tube array using a salt brine tracer. Residence times of 2, 4 and 8 minutes were applied. The relatively narrow distribution is indicative of plug flow as little axial dispersion is present.*

2.8 Droplet Dispersion

2.8.1 The Weber Number

The Weber number, N_{We}, is a dimensionless number defined as the ratio of inertial eddy forces to droplet surface tension.[118] The definition can be seen in Equation 2.19, where P is the dynamic pressure on the droplet, D_d is the droplet diameter and σ is the surface tension of a dispersed droplet.

$$N_{We} = \frac{Pd}{\sigma} = \frac{\rho_c \overline{u^2} D_d}{\sigma} \tag{2.19}$$

A critical Weber number, at which a droplet breaks, can be defined by introducing a maximum stable droplet size, D_{max}.

$$N_{We,crit} = \frac{\rho_c \overline{u^2} D_{max}}{\sigma} \tag{2.20}$$

A correlation between D_{max}, agitator diameter, D_I, and impeller speed, ω has been given in Equation 2.21, where $\omega D_I = u$.[119,120]

$$D_{max} \propto \left(\frac{\sigma}{\rho_c}\right)^{\frac{3}{5}} D_I^{-\frac{4}{5}} \omega^{-\frac{6}{5}} \tag{2.21}$$

Dividing through by D_I gives a ratio of droplet to impeller diameter, shown in Equation 2.22. This can subsequently be compared to the agitator Weber number, $N_{We,I}$, shown in Equation 2.23.

$$\frac{D_{max}}{D_I} \propto \left(\frac{\sigma}{\rho_c \omega^2 D_I^3}\right)^{\frac{3}{5}} \tag{2.22}$$

$$N_{We,I} = \frac{\omega^2 D_I^3 \rho_c}{\sigma} \tag{2.23}$$

Combining Equations 2.22 and 2.23 gives the correlation shown in Equation 2.24. Therefore the larger the Weber number, the smaller the maximum stable droplet size. This is to be expected as the larger inertial forces will be able to overcome the surface tension more readily.

$$\frac{D_{max}}{D_I} \propto N_{We,I}^{-\frac{3}{5}} \tag{2.24}$$

$$D_{max} = k_1 D_I N_{We,I}^{-\frac{3}{5}} \tag{2.25}$$

2.8.2 Droplet Dispersions and Diameters - TCDC

Asksamija et al. measure Sauter mean droplet diameter, d_{32}, in a TCDC with D_{out} = 100 mm at four rotational speeds.[106] The Sauter mean droplet diameter, d_{32}, represents an average droplet diameter, defined as the ratio of volume to surface area.[120]

$$d_{32} = \frac{\sum_{j=1}^{N} N_j D_j^3}{\sum_{j=1}^{N} N_j D_j^2} \tag{2.26}$$

Where N_j represent the number of droplets with diameter D_j. Several models, originally put forward by Weiß et al.,[121,122] Marr,[123] Kagan,[124] Fischer[125] and Kumar and Hartland[126] are then implemented by Grafschafter et al.[107] in an attempt to predict the experimental results. Experimental mean droplet diameters can be seen in Table 2.3 for a range of rotational speeds. It is found that modified versions of the Marr and Fischer models fit the experimental data most accurately. Equations for the Marr and Fischer models can be seen in Table 2.4. D_R represents the rotor disc diamter, ρ_c is the continuous phase density and N_C is the number of compartments. A compartment is defined as the spacing between two discs.

Table 2.3: *Sauter mean droplet diameters measured by Aksamija et al. (2015) in a 100 mm TCDC.[106] Droplet diameters were measured at four rotational velocities.*

Rotational Speed (rpm)	Grafschafter et al. (2016)[107] d_{32} (mm)
250	3.608
350	2.709
450	1.261
500	1.012

Table 2.4: *A table displaying the modified Marr[123] and Fischer[125] models for calculating droplet diameter. These two models were determined by Grafschafter et al (2016) to most closely match their experimental data in the TCDC.[107]*

Analytical Method	Droplet Diameter, d_{32}
Modified Marr Model	$d_{32} = \left(\frac{0.374^{0.667}}{\omega D_R^{0.778} \rho_c^{0.332}}\right)^{1.799}$
Modified Fischer Model	$d_{32} = 0.62 \frac{D_R}{N_{We}^{0.52}} \left(1 + \frac{35}{N_C^{1.22} N_{We}^{0.5}}\right)(1 + 2\phi)$

In subsequent literature by Grafschafter et al.,[108] the same experimental results were used to calculate droplet size distributions in the TCDC, correlated with log-normal, Gaussian and Weibull droplet size distribution functions. Each correlation was validated against a mean diameter, calculated using the volume-based area of the droplets (interfacial area per volume), a_v, derived in Equation 2.29.

$$a_v = \frac{\text{Interfacial Area}}{\text{Volume}} = \frac{A_{int}}{V} = \pi D_d^2 \cdot \frac{3}{4\pi} \cdot \left(\frac{2}{D_d}\right)^3 = \frac{6}{D_d} \tag{2.27}$$

This can be rearranged to calculate the mean diameter, d_{32}.

$$d_{32} = \frac{6}{a_v}\psi \tag{2.28}$$

Where ψ is the sphericity of the droplet. Since the droplet is assumed spherical, $\psi = 1$.

Distributions were plotted by integrating Equation 2.29 over the full range of droplet sizes and using a probability distribution function, q_3, which is a function of D_d and varies depending on the distribution function being used.[108]

$$a_v = 6\psi \int_{D_{d,min}}^{D_{d,max}} \frac{q_3}{D_d} dD_d \tag{2.29}$$

2.9 Gravity Separation

Gravity separation is the process in which two immiscible fluids separate under buoyancy. Stokes' law describes the force on a separating droplet and can be used to calculate the separation velocity of a spherical droplet or particle in a continuous fluid phase.[70] Equation 2.30 shows the velocity equation derived from Stokes' law.

$$u_{sf} = \frac{g(\rho_{aq} - \rho_{org})D_d^2}{18\mu_c} \tag{2.30}$$

Where u_{sf} is the superficial velocity, g is acceleration due to gravity, ρ_{aq} and ρ_{org} are the densities of the aqueous and organic phases respectively, D_d is the droplet diameter and μ_c is the dynamic viscosity of the continuous phase. Separation velocity increases with density difference between the two fluids and droplet size. Figure 2.23 shows the forces acting upon an organic droplet rising through a continuous aqueous phase. The droplet travels at a terminal velocity equivalent to u_{sf}.

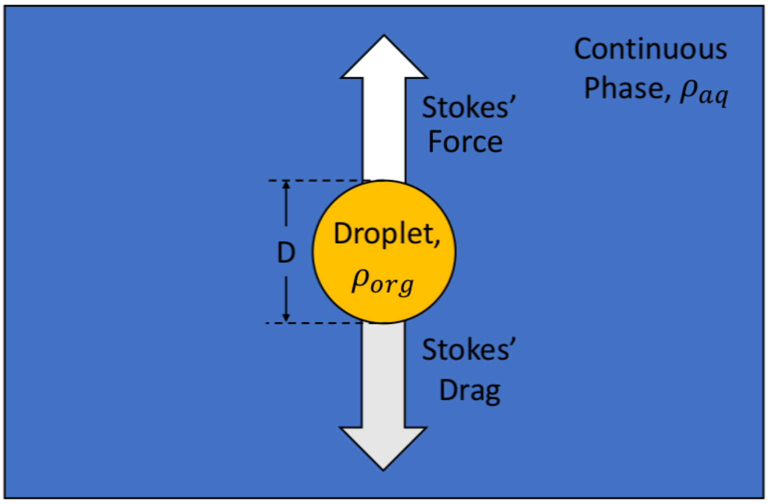

Figure 2.23: *Force diagram depicting the forces on a droplet of diameter* D_d. *The droplet has a density* ρ_{org} *and is travelling through a continuous aqueous phase of density* ρ_{aq}.

Stokes' law makes two main assumptions that limit its use.[70] Firstly, any droplets are assumed to be spherical and secondly, droplets are travelling through a stagnant continuous phase. Non-ideal conditions result in gravity separators being smaller than necessary when designed with Stokes' law alone. A 'correction factor' is needed to account for turbulence and droplet deformation in a system.[70] Turbulence can impart external forces, increasing the distance travelled and therefore the separation time of a droplet. Non-spherical droplets will be subject to increased drag, reducing separation velocity. Droplets that are too small are influenced by Brownian motion, which alters their path length from the vertical ascent assumed by Stokes' law. This results in a longer separation time.

Figure 2.24 shows a typical design for a liquid-liquid gravity separator. The two mixed phases enter the separator at the inlet and are subsequently allowed to separate in a settling zone. Once separated, the organic phase rises until it flows over a weir, after which it can be isolated and removed from the separator. The aqueous phase is able to be directly extracted from the bottom of the settling zone.

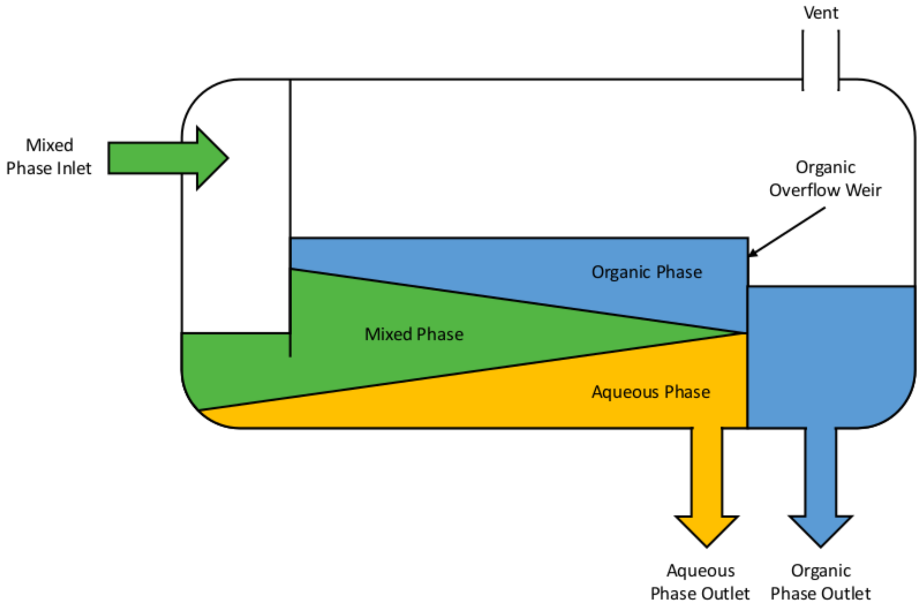

Figure 2.24: *A typical design for a gravity separator. Liquid enters the separator as a dispersed mixture of aqueous and organic phases. Once in the separator, the two phases separate under gravity at a rate determined by Stokes' law.*

2.10 Conclusions

The literature explored in this chapter will be used to inform and drive the research detailed in the rest of this thesis.

Solvent extraction is heavily used in the nuclear industry as a means to reprocess spent fuel, achieved using the PUREX process. In the name of process intensification and to improve efficiency, this thesis focusses on novel solvent extraction equipment, attempting to upgrade the out-dated technology currently in use. To understand the capability of the new equipment, mass transfer rates and models must first be understood for a given system. The mathematics and models of mass transfer rates, primarily the two-film model discussed in Section 2.4, will be used in conjunction with the chemical kinetics for copper extraction to derive equations for mass transfer resistance in co-current and counter-current systems. The mass transfer resistance values will be used to determine how well each contactor performs. Copper extraction kinetics will be used in place of uranium as it is not possible to place the ATR in a radiation safe environment. Copper has been deemed an acceptable replacement to facilitate a proof of concept since both metals form a 2:1 ligand:metal complex.

The design criteria used for a TCDC, as presented by Grafschafter et al.,[108] will be used to design a lab-scale TCDC as well as a novel contactor unique to this work, herein called a D-cell contactor. The critical Taylor number will be used to ensure Taylor vortices are present for each rotational velocity.

The size of droplets within a solvent extraction device is extremely important. As such, Stokes' law and the Weber number will be implemented to make estimates of the average droplet sizes in the TCDC and ATR. In the case of the TCDC, the modified models presented by Grafschafter et al.[107] will be used to compare with existing literature.

It is important to compare any new technology against existing industry techniques. The correlations detailed in Table 2.2 will be used to compare the ATR to a pulsed column, a commonly solvent extraction device used in the nuclear industry. As well as this, the plug flow characteristics reported by Parrington[117] will be used to calculate residence times in the ATR.

The literature on Stokes' law and gravity separation, described in Section 2.9, will be used to design liquid-liquid separators for the ATR. The separators will have two aims: Firstly, to separate the organic and aqueous phase after mixing, allowing for multiple extraction stages; secondly, to allow variation of liquid level within the ATR tube.

CHAPTER 3

Chemistry

When trying to characterise novel solvent extraction equipment, understanding the chemistry and chemical system being used is imperative. Many factors, including the extractant and diluent choice, have an effect on the extraction efficiency of a chemical system and it is therefore important to determine the equilibrium conditions before implementation.

This chapter aims to outline the chemicals and background chemistry used in subsequent chapters by exploring equilibrium concentrations and pH for the extraction of Cu(II) from aqueous copper nitrate solution, $Cu(II)(NO_3)_2$, by the industrial mining extractant Mextral® 84H. Uranium extraction via TBP has not been used due to the unavailability of a radiation safe laboratory. As such, Cu(II) extraction by Mextral® 84H has been used as a proof of concept, due to the chemical systems rich history of literature.

The recycling of the ligand and the conditions under which this is best achieved are also discussed. Mass transfer in a non-agitated system is calculated and will be used as a comparative device in later chapters.

3.1 Materials & Preparation

Preparation of Copper(II) Nitrate Solution

Copper(II) nitrate solution was prepared by dissolving copper(II) nitrate hemipentahydrate, $Cu(II)(NO_2)_3{\cdot}2.5H_2O$, in deionised water. Quantities of deionised water and $Cu(II)(NO_3)_2{\cdot}2.5H_2O$ were obtained via mass and were weighed using a milligram balance. The molecular weight of solid $Cu(II)(NO_3)_2{\cdot}2.5H_2O$ is 232.59 $g{\cdot}mol^{-1}$, and the density of water was taken as 997 $kg{\cdot}m^{-3}$.[127] The solution was stirred using a Camlab MS-H280-Pro magnetic stirrer at 400 rpm for 5 minutes, until all solid $Cu(II)(NO_3)_2{\cdot}2.5H_2O$ was dissolved. This method was used to prepare solutions between 10 and 200 mM concentration. These concentrations were chosen as they exceed the upper and lower limits expected in the contactors discussed in later chapters, as well as providing a range of data either side of the expected ligand saturation at approximately 80 mM.

Preparation of Mextral® 84H

5 L of the industrial copper extractant Mextral® 84H was provided by Kopper Chemical Industry Corp. Ltd. The organic liquid is a mixture of the ligand 2-hydroxy-5-nonylacetophenone oxime, $C_{17}H_{27}NO_2$, and a kerosene like diluent. Molecular diagrams of 2-hydroxy-5-nonylacetophenone oxime and the $Cu(II){\cdot}2L$ complex are depicted in Figure 3.1(A) and 3.1(B) respectively.

The density of Mextral® 84H, as received, was determined. Three 50 mL volumes were prepared in a 50 mL volumetric flask and weighed using a milligram balance. The average mass of the three samples was determined to be 46.07 ± 0.06 g and the average density 921.35 ± 1.23 $kg{\cdot}m^{-3}$.

Quantities of the ligand within the Metral® 84H were ambiguously listed, stating the oxime content to be <50%. The remainder of the solution was listed as "petroleum distillate hydrotreated light". Specific knowledge of the sample was necessary and performed using thermogravimetric analysis (TGA). TGA is a technique used to measure the fraction of a component in a mixture by monitoring the change in mass with gradually increasing temperature. Three 9.83 mg samples were analysed and the mass fraction of oxime measured. This fraction was converted into a concentration using the ligands molar mass, 262.4 g·mol^{-1}, and the sample volume.

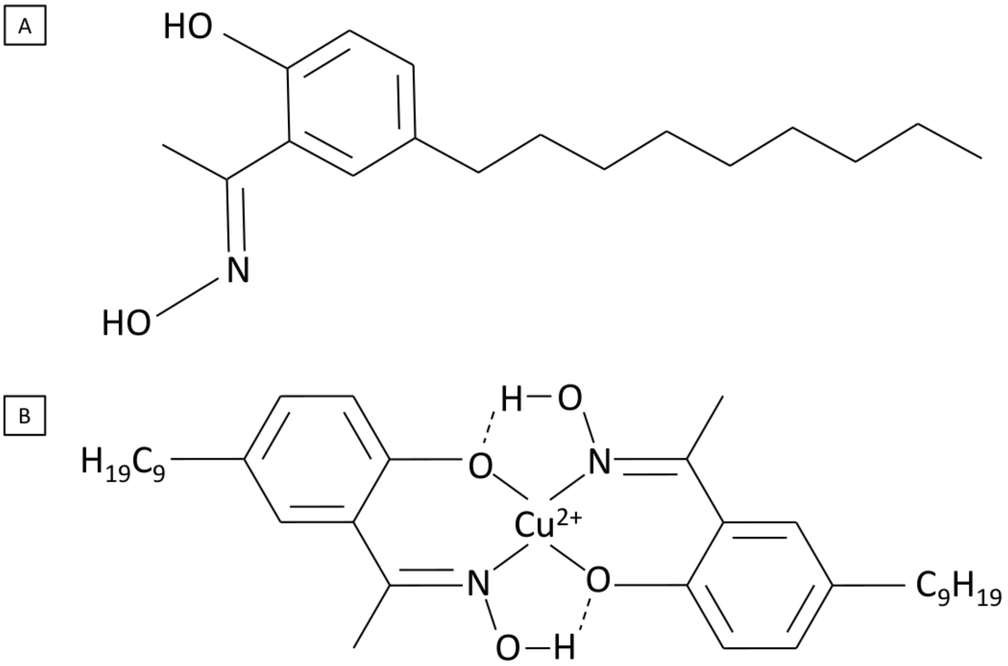

Figure 3.1: **(A)** *A molecular diagram of 2-hydroxy-5-nonylacetophenone oxime, the ligand component of Mextral® 84H.* **(B)** *The Cu(II)·2L complex formed between the Cu(II) ion and the 2-hydroxy-5-nonylacetophenone oxime ligand, where L denotes the ligand. The complex forms a chelate between two ligands and a single Cu(II) ion, losing two* H^+ *in the process.*

Gas chromatography mass spectrometry was considered as an option, however the inability to source pure 2-hydroxy-5-nonylacetophenone oxime as a comparison rendered this impossible.

In order to reduce the viscosity and increase the volume of available material, the Mextral® 84H was diluted with Exxsol™ D80 in a 1:9 ratio of Mextral® 84H to Exxsol™ D80. Exxsol™ D80 is a kerosene like diluent, similar to that present in the Mextral® 84H.

Salicylaldoxime was initially considered as an extractant prior to the use of Mextral® 84H. A depiction of the salicylaldoxime molecule can be seen in 3.2(A). The salicylaldoxime and 2-hydroxy-5-nonylacetophenone oxime molecule shown in Figure 3.1 can be seen to be similar, the difference being the addition of a nine-carbon chain on the phenol group in the 2-hydroxy-5-nonylacetophenone oxime. When complexed with Cu(II), salicyclaldoxime forms a precipitate at the interface of the two phases. The inclusion of the chain reduces the polarity of the complex, enabling the 2-hydroxy-5-nonylacetophenone oxime/Cu(II) complex to be soluble in the organic Exxsol™ D80.

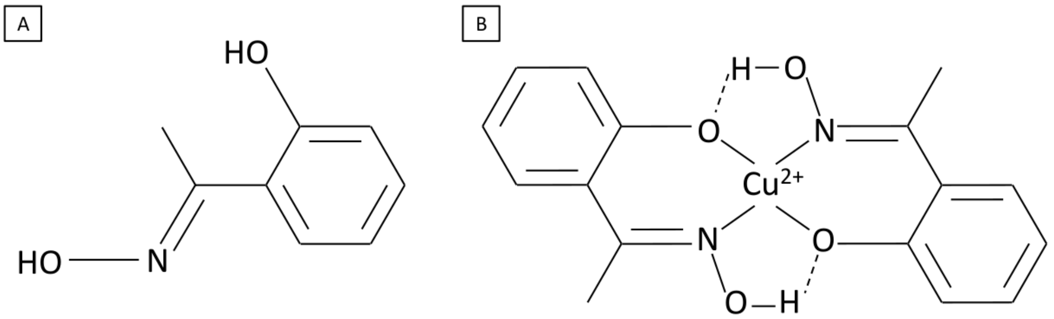

Figure 3.2: **(A)** *A molecular diagram of the salicylaldoxime molecule. Salicylaldoxime can be seen to differ from the 2-hydroxy-5-nonylacetophenone oxime molecule, shown in figure 3.1(A), by a nine-carbon chain on the phenol group. This chain allows the Cu(II)·2L complex to be soluble in the kerosene like diluent and Exxsol™ D80.* **(B)** *The Cu(II)·2L complex with ligand Salicylaldoxime. The Cu(II) ion forms a chelate complex with two salicylaldoxime molecules, losing two* H^+ *ions in the process.*[19]

Preparation of Nitric Acid

Two concentrations of nitric acid were prepared, 1 and 3 M solutions. 5 L batches of 3 M nitric acid were prepared in a fume hood. Mixing a concentrated acid and water is exothermic, therefore adding the acid to water avoids safety issues associated with localised sudden heat release and reduces the risk of spitting. 1.03 L of 65 wt% nitric acid was added to 1.25 L of water. This solution was allowed to cool and made up to 5 L with more water.

100 mL of 1 M nitric acid was prepared by adding 7 mL of 65 wt% concen-

trated nitric acid to 25 mL water. This was allowed to cool and then made up to 100 mL with more water.

3.2 Methodologies

3.2.1 Ultraviolet-Visible Spectroscopy

Ultraviolet-visible (UV-Vis) spectroscopy is a technique used in chemical analysis to determine chemical composition. Electromagnetic radiation in the ultraviolet (UV) (~190-400 nm) and visible spectra (~400-800 nm) are applied to a sample and the intensity of light transmitted through the sample measured. Different components of the sample will absorb radiation at specific wavelengths, thus reducing the transmittance at those wavelengths. This decrease in intensity can be used to measure the concentration of a component.

An advantage of UV-Vis is its ability to be used as both an inline and offline measurement technique. When used as an offline technique, a discreet sample can be positioned in the path of the radiation whereas, in inline continuous measurements, the sample can be measured as it flows through the radiation path.

In the context of this work, UV-Vis has been used to evaluate the remaining concentration of $Cu(II)(NO_3)_2$ in the aqueous raffinate after extraction.

Transmittance and Absorbance

Transmittance, T, is defined as the ratio of light intensity (after passing through a sample), I, to the incident light intensity (or the intensity based on a reference sample), I_0.[128] Transmittance is expressed as a percentage and the definition can be seen in Equation 3.1.

$$T = \frac{I}{I_0} \cdot 100\% \tag{3.1}$$

Transmittance can also be seen as a the ratio of the photoelectric current and the reference photoelectric current measured by the detector.[129] An example of a transmittance spectra for copper nitrate can be seen in Figure 3.3.

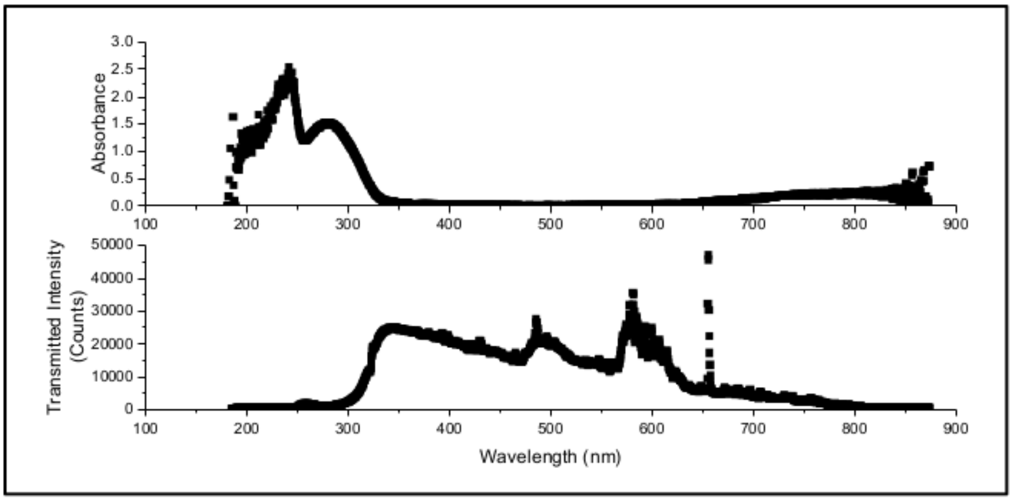

Figure 3.3: (Top) *An absorbance spectrum for aqueous 100 mM copper nitrate solution. Absorbance is defined as -*$log_{10}T$*.* **(Bottom)** *A transmittance spectrum for 100 mM aqueous copper nitrate solution. Peaks in Transmittance are seen when less light is absorbed by the sample.*

Absorbance, A, defined in Equation 3.2 as the negative logarithm of the transmittance, is a dimensionless quantity and another useful measurement option for UV-Vis spectroscopy.[128] An example absorbance spectrum can be seen in Figure 3.3.

$$A = -\log_{10}\left(\frac{I}{I_0}\right) = -\log_{10} T \tag{3.2}$$

Both transmittance and absorbance are typically a function of the wavelength of light passing through the sample. Components within a sample may absorb at different wavelengths. Peaks in the transmittance can be used to determine the composition of a sample. Since a decrease in transmittance, and therefore an increase in absorbance, denotes an increase in the concentration of a particular absorber, the concentration of each component can be gleaned.[130]

Beer-Lambert Law

In 1853, Beer proposed a correlation between the concentration of a sample and the absorbance of light passing through it.[130] The Beer-Lambert law, sometimes referred to as the Lambert-Beer law for gasses and solutions, is shown in Equation 3.3, where c is the sample concentration (mol·L^{-1}), d_s is the sample thickness (cm) and ε is the molar extinction coefficient (L·mol^{-1}·cm^{-1}), a quantity specific to the material being examined.

$$A = \epsilon c d_s \tag{3.3}$$

Equation 3.3 shows that for a given extinction coefficient and sample thickness, the absorbance of light is directly proportional to the concentration of component in the sample. If ε and the sample width are both known, the concentration can be calculated by measuring the transmittance or absorbance and rearranging Equation 3.3 to get Equation 3.4.

$$c = \frac{A}{\epsilon d_s} \tag{3.4}$$

Plotting concentration against absorbance yields a linear trend in which the y-intercept is equivalent to zero and the gradient is equal to $\frac{1}{\epsilon d_s}$. Using samples of known concentration, εd_s can be calculated and used to determine unknown concentrations.

The Beer-Lambert law is not without its limitations. At high solute concentrations, absorbance is no longer proportional to concentration. This results in a deviation from the linear trend, and an eventual plateau. One such cause of deviation is the interaction between absorbing molecules at high concentration. As the concentration increases, molecules in the system can no longer be assumed independent and interactions between the molecules may change a samples absorbing properties at particular wavelengths.[131]

Set-up & Hardware/Software

A schematic of the setup described in this section can be seen in Figure 3.4. The UV-Vis spectrometer comprised of a series of portable components. Light was produced by an Ocean Optics DH-mini lamp containing two bulbs. The combination of a UV producing deuterium bulb[132] and a visible light tungsten-halogen bulb[133] supplies frequencies between 200 and 2000 nm, covering the UV, visible and near infra-red (NIR) spectra. Each of the bulbs can be switched on or off independently, though both were used here. Light leaving the lamp travels through a fibre optic cable to a Z-flow cell. Light was transmitted into the flow cell through a fused silica window, designed to transmit all visible and UV frequencies. It was important that fibre-optic cables were kept in the same position, as a change in the shape of the cable could result in a difference in the light reaching the flow cell, and therefore a difference in the measured transmitted light.

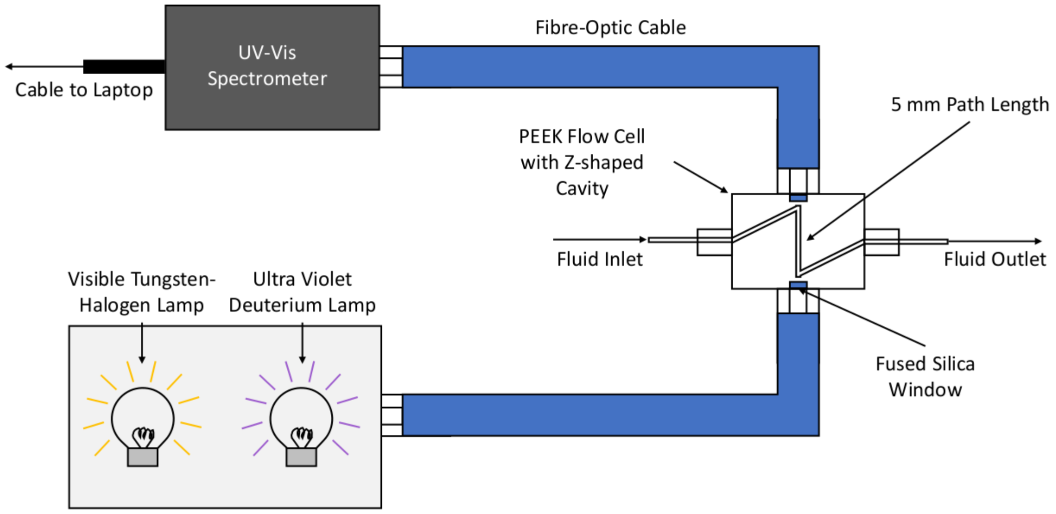

Figure 3.4: *Schematic of the UV-Vis spectrometer setup. Light in the range 200-2000 nm is radiated from a light-source containing two bulbs, a deuterium and a tungsten-halogen bulb. This light is then directed via a fibre-optic cable to a PEEK Z-flow cell through which it passes, being absorbed by the contained material. This is then directed through a second fibre-optic cable to a UV-Vis spectrometer, detecting frequencies in the 200-850 nm range.*

The Z-flow cell comprised of a block of PEEK (polyether ether ketone) with a Z-shaped, tubing-like cavity. The internal volume of the cavity was 13 µL. PEEK was chosen due to its high chemical resistance to nitric acid and the long chain alkanes present in Exxsol™ D80. The central length of the Z-shaped cavity (labelled in Figure 3.4) lies in the path of the incident radiation leaving the fibre-optic cable. This provides a known sample thickness, d_s, (also called the path length) for light to be absorbed by liquid flowing through the Z-flow cell. A long path length is required for materials that show little absorbance, whilst a shorter path length is better suited to materials with high absorbance. The path length in these experiments was 5 mm. The flow cell was wrapped in aluminium foil to reduce noise. This works by blocking external radiation, caused by lighting, windows or other laboratory equipment, from entering the fibre-optics cables.

Light transmitted through the flow cell is directed into another fibre-optic cable and passed to an Ocean Optics FLAME-S UV-Vis spectrophotometer. The FLAME-S was chosen based on its range and thermal stability. The sensor is capable of detecting frequencies in the 200-850 nm range, which encompasses the UV and visible spectra. Light entering the spectrophotometer passes through a 25 µm slit, diffracting the light into its constituent wavelengths. Light then encounters a 2048 linear-pixel silicon CCD (charge-coupled device) that generates an electric charge proportional to the incident light intensity. From this a spectrum can be produced. The spectrophotometer outputs to a laptop and is connected via a USB cable. Data can then be recorded using the OceanView software.

Calibration - Reference and Background Spectra

To ensure accurate data from the UV-Vis sensor, calibration is required to reduce noise from exterior sources. The background spectrum (also known as the dark spectrum) is used to remove electrical noise from within the sensor and determine the baseline offset for the data. A background level is built up by charge accumulation on the sensor and needs to be subtracted from the data and reference spectra to produce an accurate measurement.[128] An example of a background spectrum can be seen in Figure 3.5(B). In order to measure the background spectrum, no incident light from the lamp is permitted to enter the sensor, and the sensor is covered with reflective aluminium foil to reduce light from outside sources.

A reference spectrum, such as the one shown in Figure 3.5(A), is obtained by injecting a reference sample into the Z-type flow cell and recording the intensity of light transmitted. Deionised water has been used here as a reference material. Deionised water serves as the solvent in the aqueous $Cu(II)(NO_3)_2$ solution and therefore acts as a zero Cu(II) concentration sample.

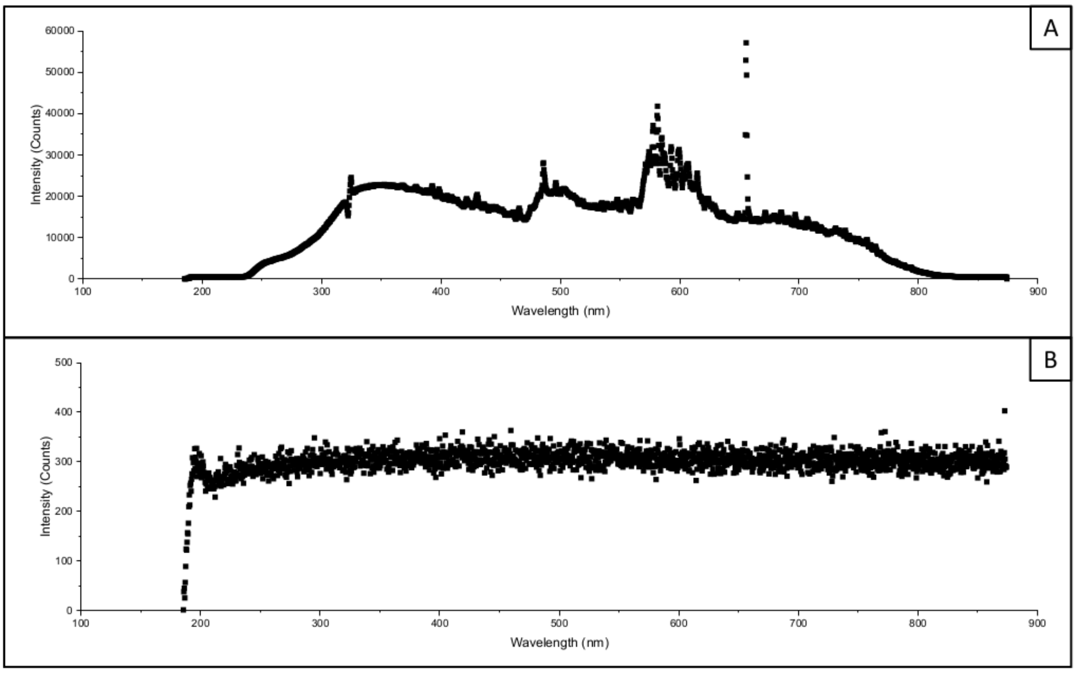

Figure 3.5: (A) *A reference spectrum for deionised water at ultraviolet and visible wavelengths ranging from 200 to 850 nm. Measured data is divided by the reference spectrum to reduce exterior noise.* **(B)** *A background spectrum for the FLAME-S UV-Vis spectrometer. The background spectrum is subtracted from measured data to remove the baseline offset caused by charge accumulation in the detector.*

Transmittance of light through a sample at a given wavelength is calculated relative to the reference sample, as seen in Equation 3.5. Where T_λ, G_λ, B_λ and

R_λ are the calibrated light intensity transmitted through the sample, the total measured intensity (before accounting for reference and background spectra), the background intensity and the reference intensity at a wavelength, λ, respectively.

$$T_\lambda = \frac{I}{I_0} \cdot 100\% = \left(\frac{G_\lambda - B_\lambda}{R_\lambda - B_\lambda} \right) \cdot 100\% \tag{3.5}$$

Absorbance at a given wavelength, A_λ, is calculated using the definition in Equations 3.2 and 3.5 to get Equation 3.6.

$$A_\lambda = -log_{10} T_\lambda = -\log_{10} \left(\frac{G_\lambda - B_\lambda}{R_\lambda - B_\lambda} \right) \tag{3.6}$$

Calibration - Concentration

For the OceanView software to provide a measurement, the quantity εd_s, present in the Beer-Lambert law, must be calculated. This can be achieved by measuring the absorbance and transmittance of samples with known concentration.

Aqueous $Cu(II)(NO_3)_2$ samples with concentrations ranging between 0 and 200 mM in deionised water were injected into the Z-flow cell using a syringe. This range of concentrations encompasses any concentrations expected from the Taylor-Couette disc contactor (TCDC), D-cell or agitated tube reactor (ATR) experimental data.

Calibration was performed at 715.16 nm, a wavelength within the Cu(II) absorbance region that was not too close to the noisy effects experienced towards the ends of the detector. Two examples of calibration plots can be seen in Figure 3.6. Plots are shown for 18°C (shown in blue) and 21°C (shown in red), the outer bounds of laboratory temperature during measurements. Both trends show a proportional relationship between absorbance and concentration, in agreement with the Beer-Lambert law shown in Section 3.2.1. The continuous linearity implies that all concentrations used fall below the deviation limits of the system, also discussed in Section 3.2.1.

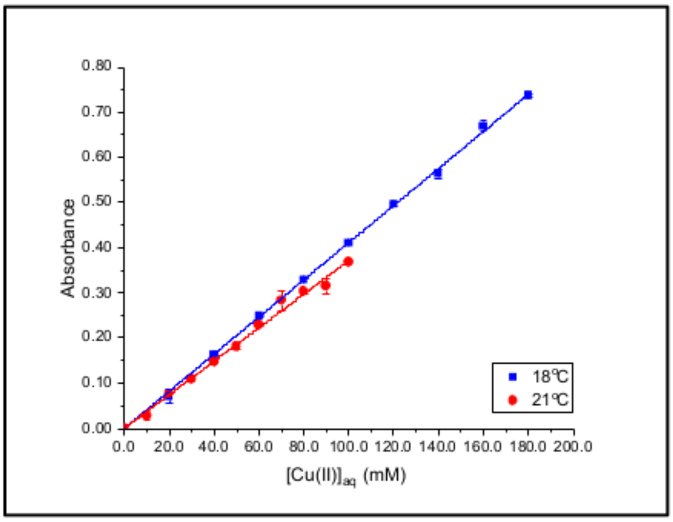

Figure 3.6: *Two calibration line examples, each used to calibrate aqueous Cu(II) concentrations for the UV-Vis spectrometer at different temperatures. Both calibrations were measured at 715.16 nm. The blue and red lines show calibrations at ambient temperatures of 18° C and 21° C respectively. Little difference is seen with temperature.*

The Beer-Lambert equations showing the variation in absorbance with concentration for the 18°C, A_{18}, and 21°C, A_{21}, calibration fits can be seen in Equation 3.7. Linear interpolation can then be used to calculate the concentration at any measured absorbance.

$$\begin{aligned} A_{18} &= 0.00411 c_{aq} \\ A_{21} &= 0.00372 c_{aq} \end{aligned} \tag{3.7}$$

Where A is the absorbance at 715.16 nm and c_{aq} is the Cu(II) concentration of the sample. Two temperatures have been shown as ambient temperature was expected to have an effect on absorbance measurements. Electrons in the CCD are released from the silicon crystal when an incident photon provides sufficient energy to overcome the binding energy. At an increased ambient temperature, electrons will have more thermal energy, reducing the photon energy needed to release it from the silicon atom. As such, absorbance measurements at higher temperatures would indicate a lower concentration than is present. This can be counteracted with a new calibration. The two lines in Figure 3.6 show that this is largely unnecessary within the temperature boundaries of this project, as such the 18° calibration was used as this was the most common temperature of the lab.

Analysis

Figure 3.7 shows an absorbance spectra for aqueous $Cu(II)(NO_3)_2$ solution, in which deionised water has been used as a reference. The absorbance seen in the wavelength ranges ~250-350 nm and ~600-850 nm can be attributed to Cu(II)[134] and $Cu(II)(NO_3)_2$ respectively, whilst the absorbance in the range ~200-350 nm is representative of the concentration of nitrate ion, NO_3^-.[135,136] At greater $Cu(II)(NO_3)_2$ concentrations, noise at the spectrophotometer limits increases, as seen in Figure 3.7. As such, a wavelength of 715.16 nm was chosen as this is comfortably within the isolated $Cu(II)(NO_3)_2$ absorbance range (not overlapping with any NO_3^- absorbance) but clear of any encroaching noise.

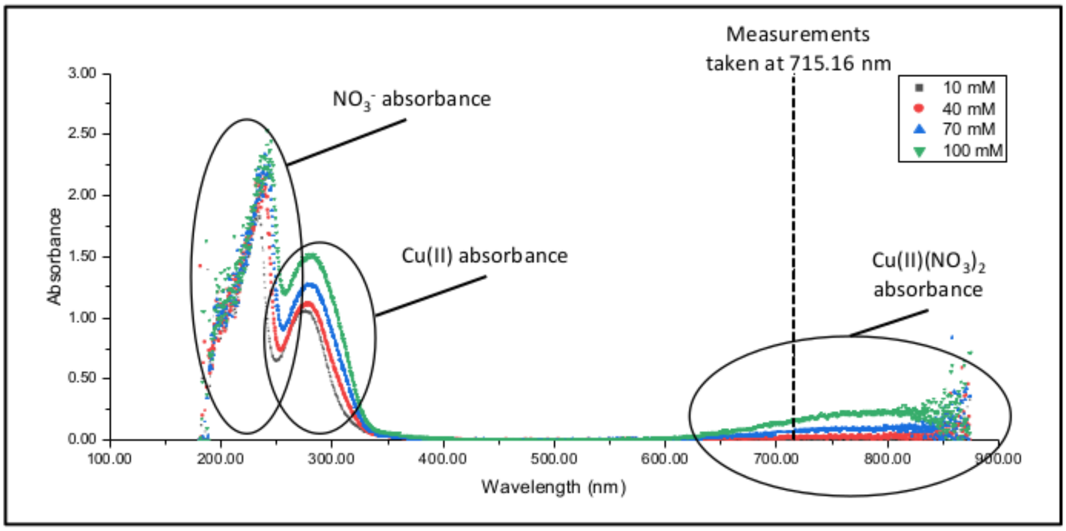

Figure 3.7: *Absorbance across the wavelength range of the FLAME-S UV-Vis spectrophotometer, shown for four initial Cu(II) concentrations. Plots show equilibrium spectra for the initial concentrations given, after extraction with Mextral® 84H. Absorbance bands caused by Cu(II),* $Cu(II)(NO_3)_2$ *and the* NO_3^- *are circled and a dotted black line depicts the wavelength at which absorbance was measured.*

Whilst the absorbance change with concentration in the $Cu(II)(NO_3)_2$ band is smaller than in the Cu(II) band, the wavelength was chosen based on its isolation from the NO_3^- absorbance band. Aqueous NO_3^- concentration varies between samples, therefore the 715.16 nm wavelength was chosen to minimise the NO_3^- concentration impact. This can be justified by comparing the calibrations in Figure 3.6 with the copper nitrate dissociation and the dissociation constant, K_{cn}, shown in Equations 3.8 and 3.9 respectively.

$$Cu(II)(NO_3)_2 \rightleftharpoons Cu(II) + 2NO_3^- \tag{3.8}$$

$$K_{cn} = \frac{[Cu(II)][NO_3^-]^2}{[Cu(II)(NO_3)_2]} \tag{3.9}$$

If the NO_3^- concentration had any impact on the absorbance, Figure 3.6 would exhibit 2nd order properties, due to the $[NO_3^-]^2$ term in Equation 3.9. The first order nature implies that either the Cu(II) or the $Cu(II)(NO_3)_2$ impacts the absorbance. $Cu(II)(NO_3)_2$ has a high dissociation in water, and therefore is assumed to be completely dissociated. Absorbance at 715.16 nm can therefore be used to measure [Cu(II)] in the aqueous phase.

The spectrometer is capable of taking multiple absorbance measurements for a single sample. The integration time is analogous to a camera shutter speed and is the amount of time over which sample data is collected and averaged.[128] The integration time is determined such that the total signal reaches 85% of the maximum capacity of the spectrophotometer. The required integration time was set to ~200 ms. The integration time is subject to small variations based on any external noise. Absorbance measurements in this chapter were taken over 10 scans.

Once an absorbance has been measured, this needs to be converted into a concentration. This can be achieved by dividing the absorbance by εd, i.e. the gradient determined through the concentration calibration seen in Equation 3.7. For each sample, an average of all concentrations was taken, and a standard deviation used to provide an error.

3.2.2 Determination of the Extraction Isotherm for Cu(II) by Diluted Mextral® 84H

Aqueous $Cu(II)(NO_3)_2$ solution was prepared at ten concentrations ranging from 10 mM to 200 mM in 10 mM intervals. All samples were prepared from a single 200 mM stock solution and diluted with deionised water until the desired concentration was reached. Three 5 mL samples of each concentration were syringed into a 14 mL sample vial, as well as three samples containing only deionised water. 5 mL of the undiluted Mextral® 84H was then added to the sample. The thirty-three samples were agitated using an IKA HS 260 basic reciprocal shaker at 4.5 Hz for a nominal 3 hours to ensure equilibrium had been reached. Once equilibrium had been reached, the aqueous phase was removed from the sample vial using a syringe and placed into a centrifuge tube. Samples were placed into a VWR CompactStar CS4 centrifuge for 10 minutes at 6500 rpm to ensure no entrained organic phase remained in the aqueous phase. The separated $Cu(II)(NO_3)_2$ solution was then injected into the Z-flow cell using a syringe and measured using the UV-Vis setup described in Section 3.2.1.

3.2.3 pH Measurements

pH of the samples described in Section 3.2.2 were measured before and after being mixed with the Mextral® 84H/Exxsol™ D80 mixture. This was performed using a HANNA Instruments HI 208 portable pH meter.

The pH probe was calibrated using aqueous calibration solutions. Since the samples were expected to be acidic after extraction, the probe was calibrated using solutions of 7.01 pH and 4.01 pH. The probe was inserted into a centrifuge tube containing the sample and left until the readout remained constant. The probe was cleaned with deionised water between measurements.

3.2.4 Back-extraction of Cu(II) from Cu(II)·2L

Back-extraction, also known as stripping, is the process of recycling a ligand by removing the metal ion from the complex and extracting that ion into another phase. Due to the lack of available material, it was important to determine if Cu(II) could be removed from the Cu(II)·2L complex and back-extracted into an aqueous phase, such that the Mextral® 84H/Exxsol™ D80 mixture could be reused.

In the case of Cu(II) back-extraction from the Cu(II)·2L complex, a strong acid is required as described in Section 2.5.1. A low pH and a high aqueous $[H^+]$ encourages the reverse reaction of Equation 2.11 to occur.

Acid Concentration

Six 5 mL samples of fresh Mextral® 84H/Exxsol™ D80 mixture were added to 5 mL 87.4 mM $Cu(II)(NO_3)_2$ in 14 mL sample vials. These were then agitated for a nominal 3 hours on an IKA HS 260 basic reciprocal shaker at 4.5 Hz until equilibrium had been reached. The two phases were separated and the organic phase placed into a VWR CompactStar CS4 centrifuge for 10 minutes at 6500 rpm to separate any entrained aqueous phase. The remaining [Cu(II)] of the separated aqueous phase samples was measured, such that the quantity of extracted Cu(II) could be calculated. The separated organic phase samples were then syringed into six 14 mL sample vials. 5 mL of 1 M nitric acid, HNO_3, was added to three of the vials and 5 mL of 3 M HNO_3 was added to the other three samples. Samples were agitated at 4.5 Hz on the reciprocal shaker for 1 hour, until an equilibrium had been reached. The Cu(II) concentration of the aqueous phases were measured using the UV-Vis set-up described in Section 3.2.1.

Redetermination of the Extraction Isotherm after Back-extraction

An equilibrium isotherm has been plotted in the same method described in Section 3.2.2. In this case, pre-used Mextral® 84H/Exxsol™ D80 mixture, back-extracted a single time, has been used instead of fresh extractant mixture. A reduced range of initial $Cu(II)(NO_3)_2$ concentrations were used, ranging from 10 to 130 mM in 30 mM intervals. These were then compared with the isotherm described in Section 3.3.2.

Large Scale Back-extraction

5 L of pre-used diluted Mextral® 84H, containing the Cu(II)·2L complex (seen in Figure 3.8(A)) was poured into a 10 L bottle containing 5 L of 3 M HNO_3. Equivalent volumes of the two phases were used to ensure the two phases were properly dispersed. Having a higher volume of organic than aqueous phase could result in an inhomogeneous dispersion in which the ligand has been insufficiently stripped. The two phases were completely dispersed at 1600 rpm using an IKA EUROSTAR20 overhead stirrer with a digital agitator speed readout (seen in Figure 3.8(B)). A 50 mm diameter impeller attachment, shown in Figure 3.9, was placed near the liquid-liquid interface and used to disperse the two phases.

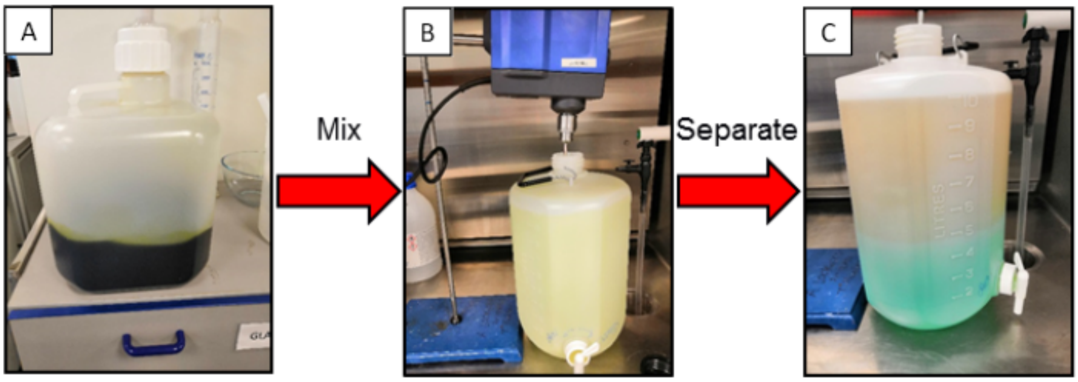

Figure 3.8: **(A)** *Mextral® 84H/Exxsol™ D80 mixture containing the Cu(II)·2L complex.* **(B)** *The Mextral® 84H/Exxsol™ D80 mixture is mixed with 3 M nitric acid to back-extract Cu(II) from the Cu(II)·2L complex in order to recycle the Mextral® 84H/Exxsol™ D80 mixture.* **(C)** *The two phases are allowed to separate. Now the Cu(II) has been back-extracted, the aqueous phase is drained and sent to waste while the organic phase is recycled and reused in future experiments. Batch experiments show the purity of the recycled material to be approximately 96%*

Figure 3.9: *The impeller attachment used during back-extraction of Cu(II) from the Cu(II)·2L complex in the pre-used Mextral® 84H.*

The two phases were allowed to re-separate after 5 minutes of agitation and the aqueous phase drained using the tap seen in Figure 3.8(C). The now processed organic Mextral® 84H/Exxsol™ D80 mixture has had the Cu(II) back-extracted from the Cu(II)·2L complex and can now be recycled and used again in future experiments. The aqueous phase, now containing the Cu(II) (as can be seen by the blue colour shown in Figure 3.8(C)) is disposed of as waste.

3.2.5 Batch Confirmation of Cu(II) Extraction by Mextral® 84H

In order to determine the rate of mass transfer across a non-agitated interface, 10 mL Mextral® 84H/Exxsol™ D80 mixture and 10 mL 0.10 M $Cu(II)(NO_3)_2$ solution were placed into a 40 mm diameter beaker. Beakers were then left undisturbed for the time period specified in Table 3.1.

After being left for the designated time, the aqueous $Cu(II)(NO_3)_2$ layer was removed using a syringe and injected into the UV-Vis Z-flow cell. The remaining $Cu(II)(NO_3)_2$ concentration was then measured. Each sample was performed in triplicate to ensure repeatability and an average final concentration calculated for each sample set. A number of beakers containing the non-agitated phases can be seen in Figure 3.10.

Table 3.1: *A set of three 10 mL samples of Mextral® 84H/Exxsol™ D80 mixture were positioned in a 40 mm diameter beaker with 10 mL aqueous Cu(II)(NO$_3$)$_2$ solution. The table lists the amount of time the two phases in each sample set were in contact.*

Sample Set	Time in Contact (s)
1	300
2	900
3	1200
4	1800
5	3600
6	5400
7	7200

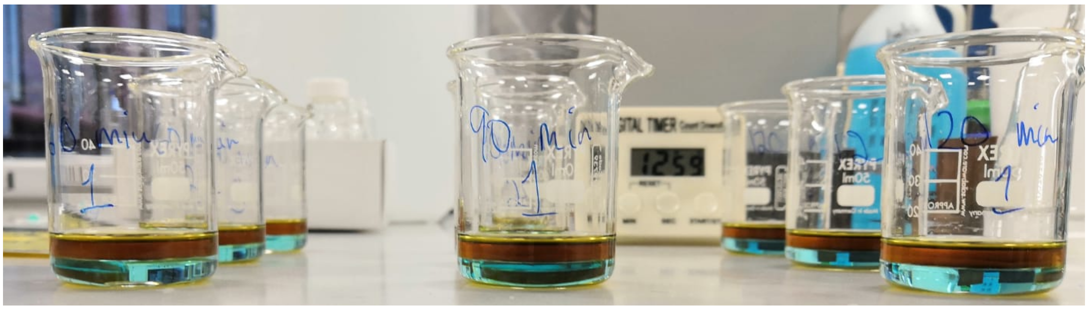

Figure 3.10: *Beakers containing 10 mL Cu(II)(NO$_3$)$_2$ aqueous phase and 10 mL Mextral® 84H/Exxsol™ D80 mixture organic phase. The beakers are left, un-agitated for a designated amount of time before being separated. The Cu(II) concentration of the aqueous phase is measured such that a value for the mass transfer coefficient, $\frac{1}{\Omega_T}$, could be calculated.*

Calculation of the Mass Transfer Coefficient

Equation 3.10 describes the decrease in aqueous concentration for a solute transferring into the organic phase. The equation is derived later in Section 6.1.4. ζ is introduced to shorten the left hand term of Equation 3.10. ζ is normalised such that an output value of 1 will occur at the initial concentration, $c = c_0$, and 0 when $c = c_{eq}$.

$$\frac{c - c_{eq}}{c_0 - c_{eq}} = \zeta = e^{-\frac{(1+S)}{\Omega_T}t} \tag{3.10}$$

Taking the natural logarithm yields Equation 3.11, which bares resemblance to Equation 2.15 shown in Section 2.5.3.

$$-\frac{1}{(1+S)}\ln\zeta = \frac{1}{\Omega_T}t \tag{3.11}$$

Comparing against the equation for a line shown in Equation 3.12, it can be seen that plotting residence time, t, on the x-axis and $-\frac{1}{1+S}\ln\zeta$ on the y-axis, yields a straight line with a gradient of $\frac{1}{\Omega_T}$ and a y-intercept of 0.

$$y = mx + c \tag{3.12}$$

3.3 Results & Discussions

3.3.1 Mextral® 84H Components

Figure 3.11 shows a TGA analysis of the pure, undiluted Mextral® 84H. The first peak (coloured black) reaches a maximum at 218.56°C. This corresponds with the observed boiling point of dodecane, $C_{12}H_{26}$, at 216.15°C.[137] The broadness of the peak implies the presence of shorter and longer chain alkanes. Taking the full-width half-maximum (FWHM) at a mass loss of approximately -0.275 mg, the majority of mass is lost in a temperature range between 160°C and 250°C. These temperatures indicate the presence of straight chain alkanes ranging from decane, $C_{10}H_{22}$, to tetradecane, $C_{14}H_{30}$, with boiling points of 173.95°C and 250.85°C respectively. The extended tails suggest small quantities of shorter and longer chain alkanes beyond this range. The mass loss suggests aliphatic hydrocarbons make up 50.9 wt% of the Mextral® 84H in a mixture similar to that of kerosene or Exxsol™ D80.

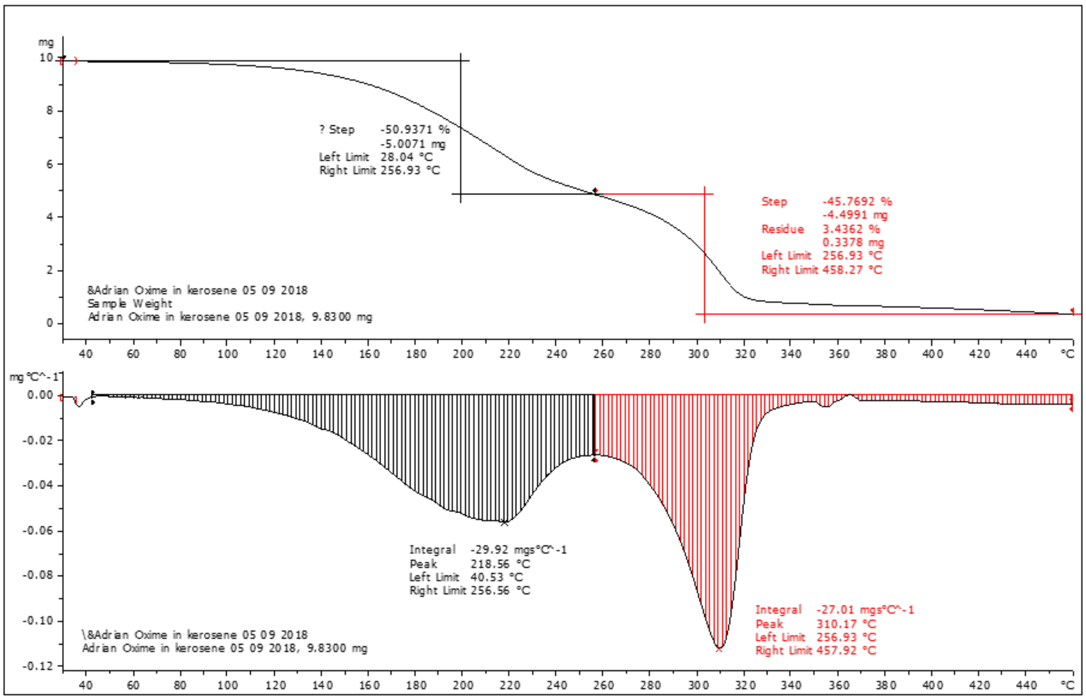

Figure 3.11: *Thermogravimetric analysis of undiluted Mextral® 84H. The broad black peak centred around 218.56° C suggests that a kerosene like diluent focused around dodecane, $C_{12}H_{26}$, makes up 50.9 wt% of the sample. The red peak reaches a maximum at 310.17° C falls within the range of boiling points for 2-hydroxy-5-nonylacetophenone oxime and indicates that 45.8 wt% of the sample consists of the oxime ligand.*

The second peak (coloured red) reaches a maximum at 310.17°C. This falls within the range of boiling temperatures for 2-hydroxy-5-nonylacetophenone oxime, at 298.5 ± 23°C. The relatively narrow peak about the maximum indicates small variation. The mass loss suggests a composition of 45.8 wt% 2-hydroxy-5-nonylacetophenone oxime, though the presence of long chain aliphatic hydrocarbons will provide an error in this value.

The remaining 3.3% mass was left as a residue in the sample vial. This could be made up of either impurities in the Mextral® 84H or long chain organic molecules.

Using this information it is possible to calculate a concentration of hydroxyoxime in the sample. Oxime mass in the sample is 45.8% of the sample mass, which is 9.83×10^{-3} g. Therefore the mass of hydroxyoxime in the sample is 4.5×10^{-3} g. The molar mass of 2-hydroxy-5-nonylacetophenone oxime is 262.4 $g \cdot mol^{-1}$, indicating that 1.72×10^{-5} mol of hydroxyoxime exists within the sample. The density of Mextral® 84H has been measured to be 9.21×10^{5} $g \cdot m^{-3}$, allowing the sample volume to be calculated as 1.07×10^{-5} L. By dividing the number of moles of hydroxyoxime by the sample volume, the hydroxyoxime concentration in the sample can be calculated to be 1.61 M.

3.3.2 Determination of the Extraction Isotherm for Cu(II) by Diluted Mextral® 84H

Kinetics of Copper Extraction and Isotherm Plotting

This section explores the chemistry and kinetics of Cu(II) extraction from an aqueous $Cu(II)(NO_3)_2$ solution into an organic kerosene-like phase by a 2-hyroxy-5-nonylacetophenone oxime ligand. The aim is to derive an equation for the overall partition coefficient, S, based on all chemical processes. This is derived from first principles.

So that it may form a chelate with Cu(II), ligand must adsorb to the interface or transfer into the aqueous phase.[19] Equation 3.13 shows the concentration distribution of the ligand, L, between the aqueous and organic phases, determined by the ligand partition coefficient, S_L. The aqueous and organic phases are denoted by the "aq" and "org" subscripts respectively. The phase volumes, V, have been included throughout this derivation to account for systems without a 1:1 organic:aqueous ratio.

$$V_{aq}[L]_{aq} = \frac{1}{S_L} V_{org}[L]_{org} \tag{3.13}$$

Once it has transferred into the aqueous phase, the ligand can then dissociate, producing a ligand ion, L^-, and a proton, H^+, thus protonating the aqueous phase. The dissociation constant of the oxime ligand, K_L, is shown in Equation 3.14. $[L^-]_{aq}$ and $[H^+]_{aq}$ are the aqueous concentrations of the ligand ion and dissociated proton respectively. By substituting $V_{aq}[L]_{aq}$ in Equation 3.14 for Equation 3.13, Equation 3.15 can be reached, removing the unknown quantity $[L]_{aq}$.

$$K_L V_{aq}[L]_{aq} = V_{aq}^2 [L^-]_{aq}[H^+]_{aq} \tag{3.14}$$

$$\frac{K_L}{S_L} V_{org}[L]_{org} = V_{aq}^2 [L^-]_{aq}[H^+]_{aq} \tag{3.15}$$

The chemical equilibrium for Cu(II)/ligand extraction is shown in 3.16. This is described based on the corresponding equilibrium constant, k_{Cu2L}, in Equation 3.17.

$$Cu_{aq}^{2+} + 2L_{aq}^{-} \rightleftharpoons Cu \cdot 2L_{aq} \tag{3.16}$$

$$k_{Cu2L} V_{aq}^3 [Cu^{2+}]_{aq}[L^-]_{aq}^2 = V_{aq}[Cu \cdot 2L]_{aq} \tag{3.17}$$

The ligand ion concentration, $[L^-]_{aq}$, is an unknown quantity and can be removed by rearranging Equation 3.15 for $[L^-]_{aq}$. Substituting this into Equation 3.17 yields Equation 3.18.

$$\frac{K_L^2 k_{Cu2L}}{S_L^2} V_{aq}[Cu^{2+}]_{aq} \frac{V_{org}^2 [L]_{org}^2}{V_{aq}^2 [H^+]_{aq}^2} = V_{aq}[Cu \cdot 2L]_{aq} \tag{3.18}$$

Once complexation has occurred, the complex transfers back into the organic phase.[19] This sets up another equilibrium, described by the partition equation of the Cu(II)·2L complex shown in Equation 3.19. S_{Cu2L} is the partition coefficient, describing the concentration of complex in the two phases.

$$V_{aq}[Cu(II) \cdot 2L]_{aq} = \frac{1}{S_{Cu2L}} V_{org}[Cu(II) \cdot 2L]_{org} \tag{3.19}$$

Equation 3.19 can be used to remove another unknown, the concentration of aqueous complex, $[Cu{\cdot}2L]_{aq}$. By substituting into Equation 3.18, $[Cu{\cdot}2L]_{aq}$ can be exchanged for a calculable quantity $[Cu{\cdot}2L]_{org}$. This substitution has been performed in Equation 3.20

$$\frac{k_{Cu2L}K_L^2 S_{Cu2L}}{S_L^2} \frac{V_{org}}{V_{aq}} \frac{[L]_{org}^2}{[H^+]_{aq}^2} = \frac{[Cu \cdot 2L]_{org}}{[Cu^{2+}]_{aq}} \tag{3.20}$$

Equation 3.20 can be simplified by combining all coefficients into an overall kinetic constant, H_T, as shown in Equation 3.21.

$$H_T = \frac{k_{Cu2L}K_L^2 S_{Cu2L}}{S_L^2} \tag{3.21}$$

Ligand concentration at any time is difficult to measure. As such, it is necessary to try and form an equation using the total/initial ligand concentration, $[L]_T$. The ligand mass balance in Equation 3.22 shows how the initial ligand is dispersed between phases at any given time.

$$\begin{aligned} V_T[L]_T = V_{aq}([L]_{aq} + [L^-]_{aq} + 2[Cu(II) \cdot 2L]_{aq}) \\ +V_{org}([L]_{org} \; + [L^-]_{org} + 2[Cu(II) \cdot 2L]_{org}) \end{aligned} \tag{3.22}$$

$[H^+]_{aq}$ is another quantity in Equation 3.20 that is unknown. Another mass balance, Equation 3.23, based on the proton concentration is therefore required to eventually remove this from our final equation. Each time a complex is formed, two protons are given off as two ligands dissociate and form a complex with the Cu(II) ion. $[H^+]_{aq}$ can therefore be seen as the sum of the dissociated ligand concentrations in both phases, $[L^-]_{aq}$ and $[L^-]_{org}$, as well as twice the complex concentrations in both phases, $2[Cu{\cdot}2L]_{aq}$ and $2[Cu{\cdot}2L]_{org}$ (since two ligand dissociations are required per complex).

$$\begin{aligned} V_{aq}[H^+]_{aq} &= V_{aq}([L^-]_{aq} + 2[Cu(II) \cdot 2L]_{aq}) \\ &+V_{org}([L^-]_{org} + 2[Cu(II) \cdot 2L]_{org}) \end{aligned} \tag{3.23}$$

Substituting 3.23 into 3.22 removes a number of unknowns, namely $[L^-]_{aq}$, $[L^-]_{org}$, $[Cu{\cdot}2L]_{aq}$ and $[Cu{\cdot}2L]_{org}$. This is shown in Equation 3.24. $[L]_{aq}$ can then be eliminated by substituting the partition relation in Equation 3.13 to reach Equation 3.25.

$$V_T[L]_T = V_{aq}[L]_{aq} + V_{org}[L]_{org} + V_{aq}[H^+]_{aq} \tag{3.24}$$

$$V_T[L]_T = V_{org}[L]_{org}\left(\frac{1}{S_L} + 1\right) + V_{aq}[H^+]_{aq} \tag{3.25}$$

In order to eliminate the proton concentration from the kinetics equation, 3.25 can be rearranged for $[H^+]_{aq}$ and substituted into 3.18, yielding Equation 3.26.

$$H_T V_{aq} V_{org} \frac{[L]^2_{org}}{\left(V_T[L]_T - V_{org}[L]_{org}\left(\frac{1}{S_L} + 1\right)\right)^2} = \frac{[Cu(II) \cdot 2L]_{org}}{[Cu^{2+}]_{aq}} \tag{3.26}$$

The final unknown, $[L]_{org}$, now needs to be eliminated. To do so, a correlation between the Cu(II) and ligand concentrations has been used. Equation 3.27 is the mass balance of the Cu(II) ion, distributed across both phases.

$$\begin{aligned} V_T[Cu^{2+}]_T &= V_{aq}([Cu^{2+}]_{aq} + [Cu(II) \cdot 2L]_{aq}) \\ &+V_{org}([Cu^{2+}]_{org} + [Cu(II) \cdot 2L]_{org}) \end{aligned} \tag{3.27}$$

$[Cu^{2+}]_{org}$ can be assumed to be approximately zero, as Cu(II) entering the organic phase will be part of the Cu(II)·2L complex.

Using Equations 3.27 and 3.23, a new relation between $[Cu^{2+}]_T$ and $[H^+]_{aq}$ can be found. Rearranging the Cu(II) mass balance equation, shown in Equation 3.28, for $V_{aq}[H^+]_{aq}$, and equating this with the ligand mass balance in Equation 3.25, gives a relationship for $[L]_{org}$ based on the initial ligand and Cu(II) concentrations. This relation can be seen in Equation 3.29.

$$2V_T[Cu^{2+}]_T = 2V_{aq}[Cu^{2+}]_{aq} + V_{aq}[H^+]_{aq} - V_{aq}[L^-]_{aq} - V_{org}[L^-]_{org} \tag{3.28}$$

$$\begin{aligned} &2V_T[Cu^{2+}]_T - 2V_{aq}[Cu^{2+}]_{aq} + V_{aq}[L^-]_{aq} + V_{org}[L^-]_{org} \\ &\quad = V_T[L]_T - V_{org}[L]_{org}\left(\frac{1}{S_L} + 1\right) \end{aligned} \tag{3.29}$$

If $S_L >> 1$, i.e. the concentration of ligand in the aqueous phase is negligible in comparison to the organic ligand concentration, it can be assumed that $\frac{1}{S_L}$ approximates 0. Since the aqueous ligand concentration is deemed exceptionally small, it is also reasonable to assume that $[L^-]_{aq}$ approximates 0. $[L^-]_{org}$ can also be assumed negligible as ligand crossing back into the organic phase is assumed to be part of the Cu(II)·2L complex. Based on these assumptions, Equation 3.29 can be simplified to Equation 3.30.

$$2V_T[Cu^{2+}]_T - 2V_{aq}[Cu^{2+}]_{aq} = V_T[L]_T - V_{org}[L]_{org} \tag{3.30}$$

The final unknown quantity, $[L]_{org}$, can now be removed by rearranging Equation 3.30 for $[L]_{org}$ and substituting back into Equation 3.26 to obtain Equation 3.31.

$$\begin{aligned} &H_T\frac{V_{aq}V_{org}}{V_{org}^2}\left(\frac{V_T[L]_T - (2V_T[Cu^{2+}]_T - 2V_{aq}[Cu^{2+}]_{aq})}{2V_T[Cu^{2+}]_T - 2V_{aq}[Cu^{2+}]_{aq}}\right)^2 \\ &\quad = \frac{[Cu(II)\cdot 2L]_{org}}{[Cu^{2+}]_{aq}} \end{aligned} \tag{3.31}$$

Equation 3.31 can be further simplified using the Cu(II) mass balance made in Equation 3.32. This simplification can be seen in Equation 3.33. The assumption made here is that Cu(II) is only ever present as either aqueous Cu(II) or as part of the Cu(II)·2L complex in the organic phase, i.e. $\frac{1}{S_{Cu2L}}$ approximates 0. The initial Cu(II) concentration, $[Cu^{2+}]_T$, and the aqueous Cu(II) concentration, $[Cu^{2+}]_{aq}$, can both be measured with UV-Vis spectroscopy and therefore allows the organic complex concentration, $[Cu(II)\cdot 2L]_{org}$, to be calculated.

$$V_T[Cu^{2+}]_T - V_{aq}[Cu^{2+}]_{aq} = V_{org}[Cu(II)\cdot 2L]_{org} \tag{3.32}$$

$$H_T \frac{V_{aq}}{V_{org}} \left(\frac{V_T[L]_T - 2V_{org}[Cu(II) \cdot 2L]_{org}}{2V_{org}[Cu(II) \cdot 2L]_{org}} \right)^2 = \frac{[Cu(II) \cdot 2L]_{org}}{[Cu^{2+}]_{aq}} \tag{3.33}$$

The numerator and denominator of the squared term on the left hand side of Equation 3.33, both contain $2V_{org}[Cu{\cdot}2L]_{org}$. Dividing out gives Equation 3.34.

$$H_T \frac{V_{aq}}{V_{org}} \left(\frac{V_T[L]_T}{2V_{org}[Cu(II) \cdot 2L]_{org}} - 1 \right)^2 = \frac{[Cu(II) \cdot 2L]_{org}}{[Cu^{2+}]_{aq}} \tag{3.34}$$

For the systems discussed within this work, a 1:1 organic:aqueous ratio has been used. Therefore the statement made in Equation 3.35 is true. Equation 3.34 can now be reduced to Equation 3.36, which is the final kinetic equation for the Cu(II)/oxime complexation.

$$V_{aq} = V_{org} = \frac{V_T}{2} \tag{3.35}$$

$$H_T \left(\frac{[L]_T}{[Cu(II) \cdot 2L]_{org}} - 1 \right)^2 = \frac{[Cu(II) \cdot 2L]_{org}}{[Cu^{2+}]_{aq}} \tag{3.36}$$

Equation 3.36 is an equation containing the total kinetic coefficient for the kinetics of the Cu(II)/oxime extraction. Plotting $\left(\frac{[L]_T}{[Cu(II) \cdot 2L]_{org}} - 1 \right)^2$ on the x-axis against $\frac{[Cu(II) \cdot 2L]_{org}}{[Cu^{2+}]_{aq}}$ on the y-axis yields a linear isotherm of gradient H_T. H_T can then be used to calculate the total partition coefficient, S, across the phases at any aqueous Cu(II) concentration. The definition of S can be seen in Equation 3.37.

$$S = \frac{[Cu(II) \cdot 2L]_{org}}{[Cu^{2+}]_{aq}} = H_T \left(\frac{[L]_T}{[Cu(II) \cdot 2L]_{org}} - 1 \right)^2 \tag{3.37}$$

Figure 3.12 describes the mechanism of Cu(II) extraction from a continuous aqueous phase into a dispersed organic droplet by an oxime ligand. All relevant processes and constituent constants of H_T are shown.

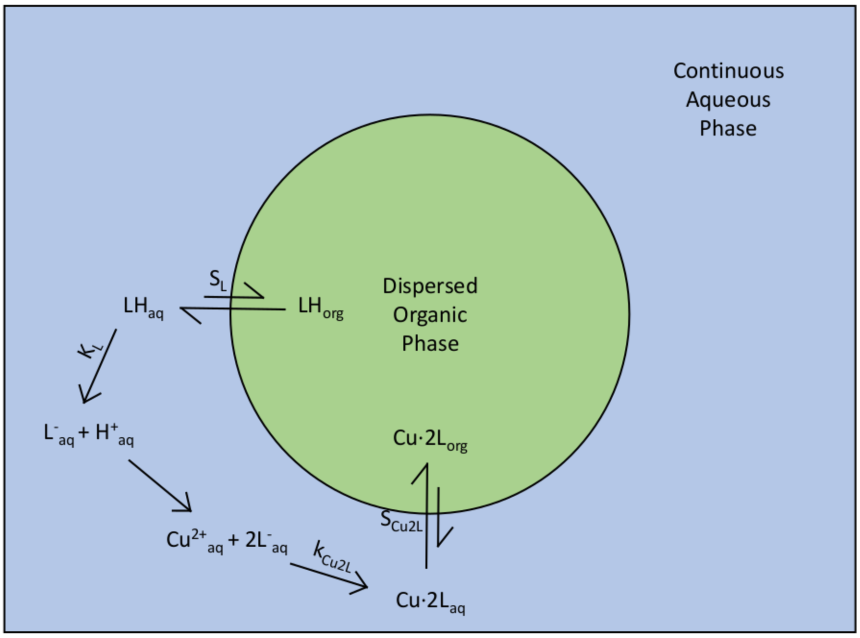

Figure 3.12: *A depiction of the chemical processes outlined. The diagram shows the mechanism of Cu(II) extraction from a continuous aqueous* $Cu(II)(NO_3)_2$ *phase into an organic droplet containing the 2-hydroxy-5-nonylacetophenone oxime ligand.*

Extraction Isotherm

Figure 3.13 is an isotherm for the initial Cu(II) extraction from aqueous $Cu(II)(NO_3)_2$ by fresh, un-stripped Mextral® 84H/Exxsol™ D80 mixture. The gradient is equal to the total kinetic coefficient, H_T. A linear plot is seen as expected from Section 3.3.2, which details the equation for H_T displayed in Equation 3.36.

The gradient suggests a value for H_T of 0.65±0.03. Error in the gradient is calculated by the plotting software as the difference between the plotted gradient and the maximum and minimum possible gradients. The y-intercept is set to the expected value of zero. The linearity of the plot supports the assumptions made in Section 3.3.2 that quantities such as the concentrations of $[L^-]_{aq}$, $[L^-]_{org}$, $[Cu\cdot 2L]_{aq}$ and $[Cu^{2+}]_{org}$ are negligible. If any of these quantities had a significant effect on the kinetics, the plot shown in Figure 3.13 would diverge from a linear trend.

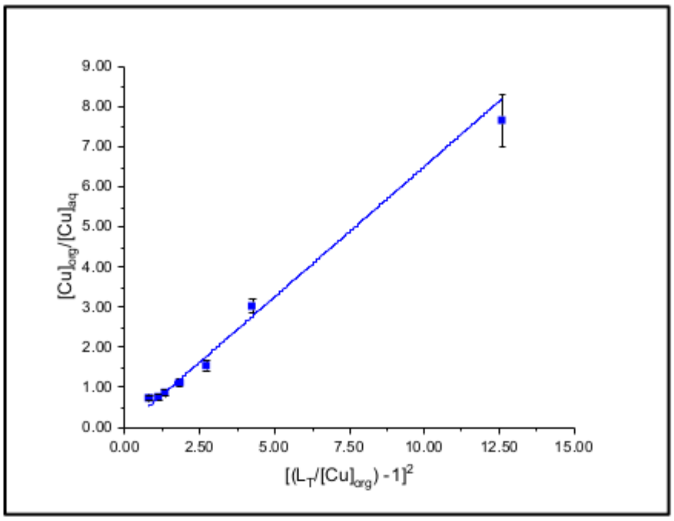

Figure 3.13: *An isotherm displaying the chemical kinetics of Cu(II) extraction by a hydroxyoxime ligand. The gradient of the plot is equal to the total kinetic coefficient, H_T, a constant made up from the individual coefficients of each reaction step.*

Figure 3.14 plots the initial aqueous Cu(II) concentration, c_0, against the equilibrium aqueous Cu(II) concentration, c_{eq}. This plot has been used to calculate c_{eq} for a given c_0. This will become useful in experiments discussed later in this text. Beyond this chapter all experiments have been conducted with $c_0 =$ 0.10 M, therefore for simplicity only the linear section of the plot has been fitted as, even with some variation, c_0 should remain in this region. When mixing large quantities, some variation in batch concentration is possible. As such, the fit equation written in Equation 3.38, has been used to predict c_{eq} in future calculations. The errors in the gradient and y-intercept moving forward have been taken as ±0.007 and ±0.0008 respectively. These have been calculated based on the error in the fitted linear trend. The black line is plotted such that $c_{eq} = c_0$. The difference between the black line and the plotted data is equivalent to the mass transfer driving force of the system.

$$c_{eq} = 0.7626c_0 - 0.0361 \tag{3.38}$$

When discussing the extent of mass transfer in the contactors used in future chapters, the knowledge of the expected equilibrium concentration will give a benchmark value.

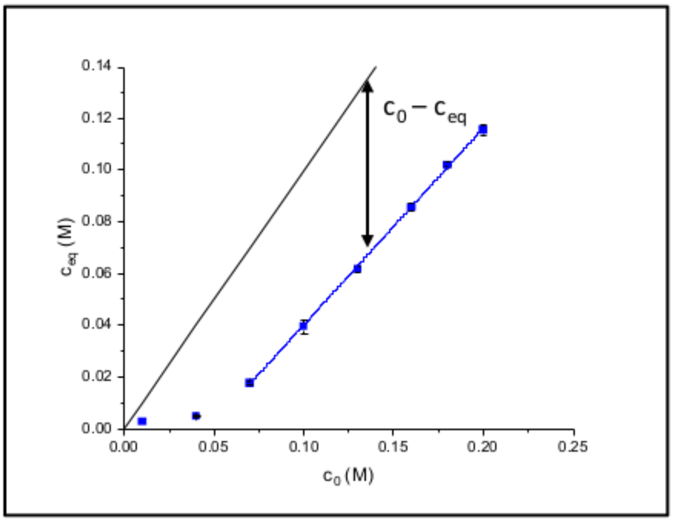

Figure 3.14: *A graph showing the expected aqueous equilibrium concentration,* c_{eq}*, for a given initial aqueous concentration,* c_0*. The initial concentrations range from 0.01 to 0.20 M. A linear fit has been plotted for data points greater than or equal to 0.07 M as future experiments use 0.10 M initial aqueous Cu(II) concentrations. As such, a linear fit is sufficient to calculate the necessary* c_{eq}*. The black line is representative of* $c_{eq} = c_0$*. The difference between the black line and the plotted points is equivalent to the mass transfer driving force.*

3.3.3 pH Measurements

During the dissociation of the ligand, $2H^{+}{}_{aq}$ are released, acidifying the aqueous phase. pH was measured in the method explained in Section 3.2.3.

Figure 3.15 shows the pH of aqueous samples at both their initial and equilibrium pH after extraction. The initial pH of the system is seen to be acidic, due to $Cu(II)(NO_3)_2$ being a Lewis acid.[138] The initial pH of approximately 4.25 supplies ideal conditions for copper extraction.[139] pH rapidly decreases towards a pH of 1, at which point the extraction stops.[139]

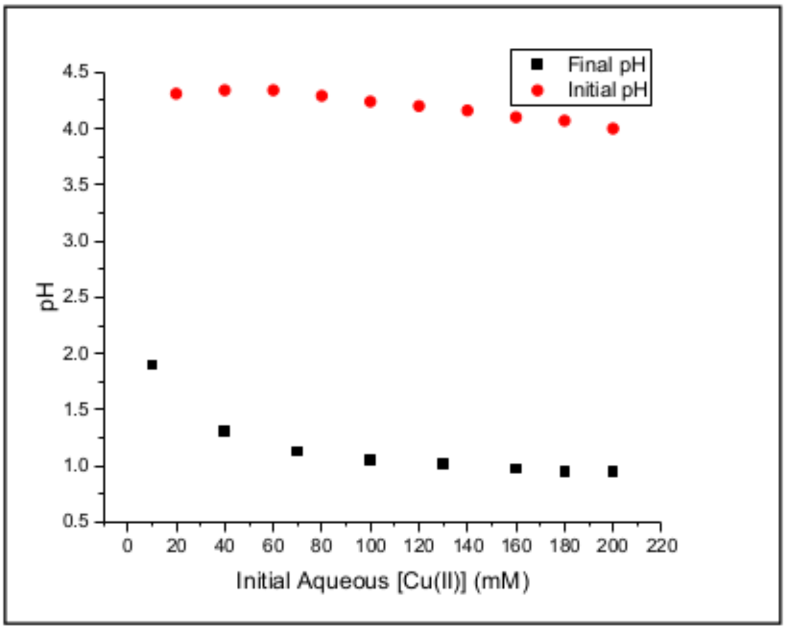

Figure 3.15: *A graph showing the change in sample pH with change in initial* $[Cu(II)]_{aq}$*. Initial pH (red) is shown to be stable with increasing* $[Cu(II)]_{aq}$ *at approximately pH 4.25. The samples are shown to become more acidic after extraction (black), and pH is shown to rapidly decrease to a pH of approximately 1.*

In future experiments, an initial concentration of 0.10 M will be used to ensure pH does not reach its minimum possible value at equilibrium.

3.3.4 Back-Extraction of Cu(II) from Cu(II)·2L

Acid Concentration

The aqueous Cu(II) concentration of the nitric acid phase was measured and compared with the original unprocessed aqueous material. The initial and final $[\mathrm{Cu(II)}]_{\mathrm{aq}}$ after processing, as well as the concentration of material not back-extracted, can be seen in Table 3.2.

Figure 3.16(B) shows two vials of post-processed organic material, one processed with 1 M (left) and one with 3 M (right) HNO_3. Small quantities of the Cu(II)·2L complex produces an easily visible colour change. Fresh Mextral®

84H is an amber colour while the inclusion of Cu(II)·2L turns the solution a dark green, almost black. This dark colour can be seen in the pre-back-extracted organic phase in Figure 3.16(A).

Table 3.2: *Table listing the initial aqueous [Cu(II)] before extraction with the Mextral® 84H/Exxsol™ D80 mixture, the aqueous [Cu(II)] after back-extraction of Cu(II) from the Cu(II)·2L complex and the concentration of non-back-extracted Cu(II) left in the organic phase. This data is shown for a 1 M and 3 M nitric acid back-extractant.*

Initial $[HNO_3]_{aq}$ (M)	$[Cu(II)]_{aq}$ before extraction (mM)	Back-extracted $[Cu(II)]_{aq}$ (mM)	$[Cu(II)]_{aq}$ not back-extracted (mM)
1.0	87.4	53.9	33.5
3.0	87.4	83.9	3.5

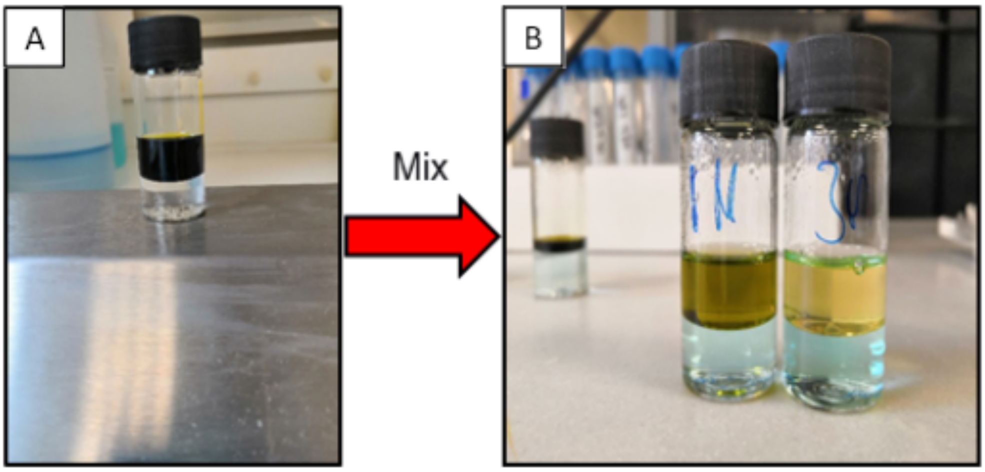

Figure 3.16: **(A)** *A sample vial containing 5 mL used Mextral® 84H/Exxsol™ D80 mixture, which contains the Cu(II)·2L complex. Cu(II) is about to be back-extracted from the complex by the 5 mL nitric acid layer in the bottom of the vial.* **(B)** *Two sample vials containing processed Mextral® 84H/Exxsol™ D80 mixture. Left: The Cu(II)·2L complex has been back-extracted by 1 M nitric acid. Right: The Cu(II)·2L has been processed with 3 M nitric acid.*

It is clear, based on the clear amber colour of the organic phase, that the 3 M vial in Figure 3.16(B) better back-extracts the Cu(II) from the Mextral®

84H relative to the much darker 1 M case. This is further evidenced by Table 3.2 which shows that the 1 M vial back-extracts 30.0 mM less Cu(II) than the 3 M vial. The presence of Cu(II) in the aqueous phase is also easily noted by the change in colour from colourless to a pale blue.

Extraction Isotherm

Once it was confirmed that stripping the complex of Cu(II) was possible, it was necessary to see how the chemical kinetics were affected. Figure 3.17 compares the plot shown in Figure 3.13 with a similar plot for the stripped material. Once again the gradient represents the total kinetic coefficient, H_T, and produces a value of 0.236±0.005. A y-intercept of -0.504±0.036 is also seen. The reduction in gradient is indicative of some damage to the ligand produced by the low pH during back-extraction.[140]

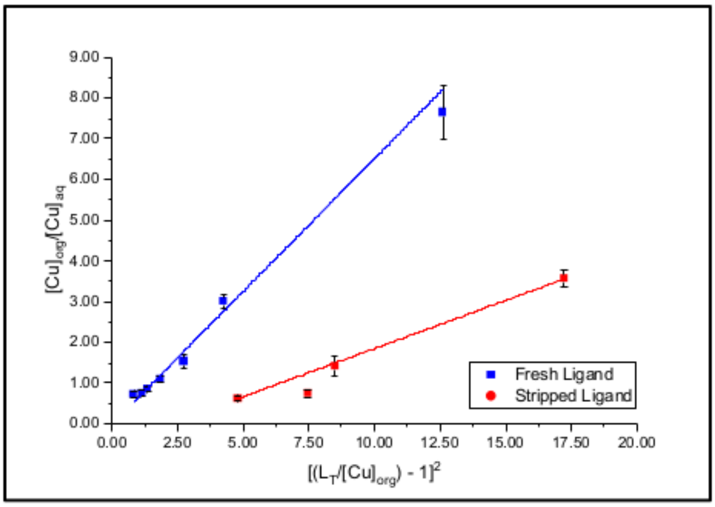

Figure 3.17: *A comparison of the total kinetic coefficients for Cu(II) extractions using fresh (shown in blue) and stripped (shown in red) material. The stripped material is shown to extract less Cu(II) from the aqueous phase and have a lower* H_T*, (equal to the gradient) than the fresh material.*

Figure 3.18 shows the change in c_{eq} against c_0 for the stripped ligand system. A comparison with the data plotted in Figure 3.14 is also shown (blue). More Cu(II) is extracted into the organic phase by fresh material when compared with stripped material. The black line represents $c_{eq} = c_0$. The difference between the black line and the plotted data is equal to the mass transfer driving force in the system.

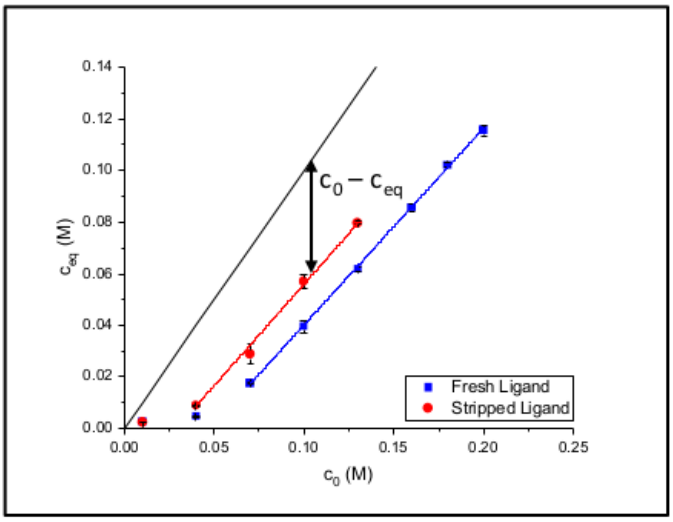

Figure 3.18: *A graph showing the aqueous equilibrium Cu(II) concentration, c_{eq}, at varying initial Cu(II) concentrations, c_0. A comparison between equilibrium values for stripped (shown in red) and fresh (shown in blue) Mextral® 84H/Exxsol™ D80 mixture are shown. More Cu(II) is present after extraction with stripped material. Linear plots are shown for simplicity at c_0 greater than or equal to 0.04 M or 0.07 M for the stripped and fresh material respectively. The black line represents $c_{eq} = c_0$. The difference between the black line and the plotted data is equal to c_0-c_{eq}, the initial mass transfer driving force.*

Figure 3.18 shows the linear fit used to calculate the equilibrium Cu(II) concentration for a given initial concentration. The equation for the linear fit can be seen in Equation 3.39. The errors in the gradient and y-intercept have been taken forward as ±0.0049 and ±0.003 respectively. These were taken as the error in the fitted linear trend, calculated as the difference between the plotted gradient and the maximum and minimum possible gradients.

$$c_{eq} = 0.7870c_0 - 0.0227 \tag{3.39}$$

Stripping of the material is possible and will be used in future experiments, though it is important to note that the kinetics are different.

3.3.5 Batch Confirmation of Cu(II) Extraction by Mextral® 84H

When looking at the contactors in later chapters, it will be important to know the rate of mass transfer when no agitation is present. This allows an easy comparison when trying to determine if the system is well mixed or not. Since no agitation is present in the phase separation systems discussed later, it is important to understand if the mass transfer across a steady interface is relevant or negligible.

Figure 3.19 shows the reduction in ζ over time. It is shown to fit an exponential, exhibiting an R^2 value of 0.95, tending to zero at c_{eq}. It is estimated that the contact time necessary to reach equilibrium is in the order 10^6 s.

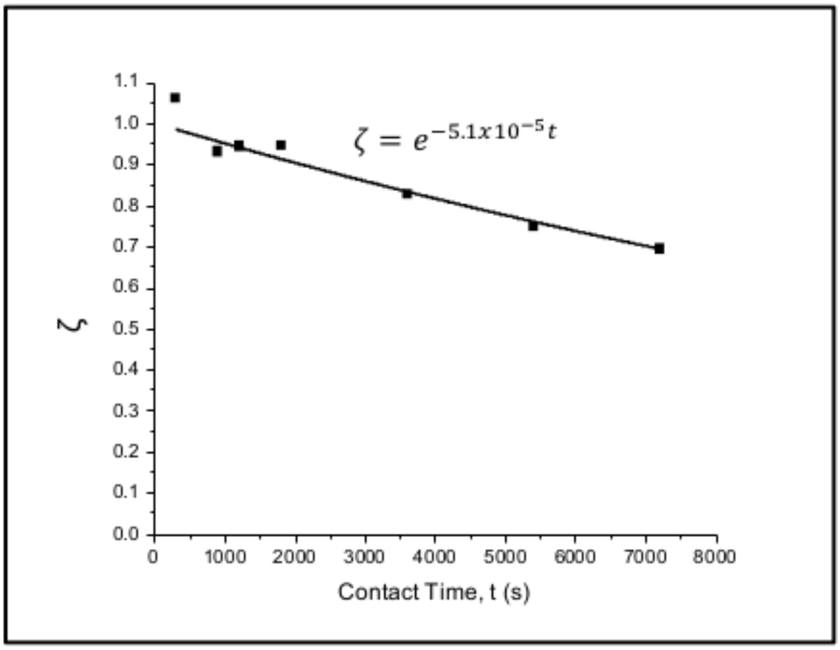

Figure 3.19: *A plot showing the exponential decay of normalised Cu(II) concentration,* ζ*, against contact time,* t*. The decay is seen (via the fit equation shown above the line) to tend towards zero at equilibrium. For equilibrium to occur, the two phases would need to be in contact for approximately* 10^6 *s.*

The plot in Figure 3.20 shows $-\frac{1}{1+S}\ln\zeta$ against the time in contact, t. The gradient represented will be approximately equal to the mass transfer coefficient, $\frac{1}{\Omega_T}$. The y-intercept of the fit has been set to zero, as at $c = c_0$, $\ln\zeta$ will equal zero.

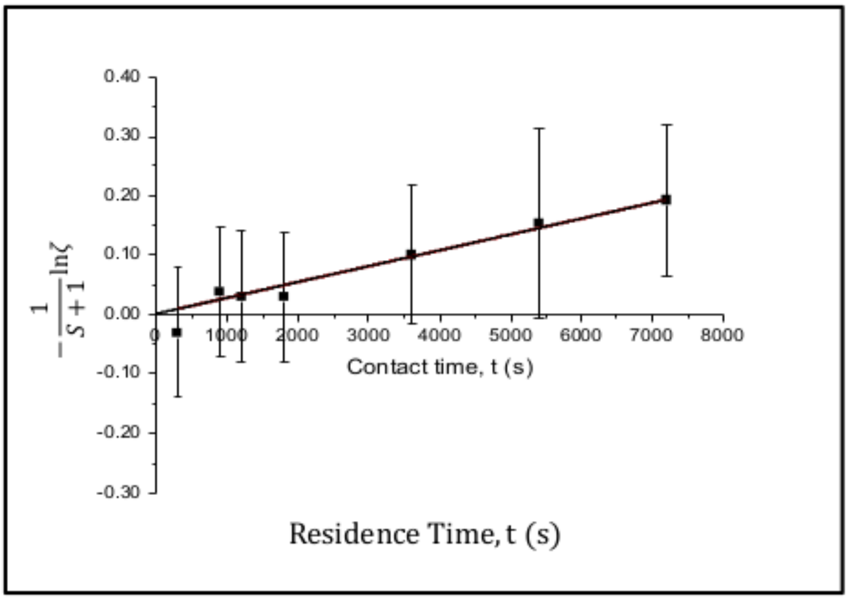

Figure 3.20: *A plot describing mass transfer in a system with no agitation. The system consists of two phases: organic Mextral® 84H/Exxsol™ D80 mixture and aqueous Cu(II)(NO$_3$)$_2$ solution. The gradient of the fitted line represents a mass transfer coefficient,* $\frac{1}{\Omega_T}$, *of (2.67±0.23)×10^{-5} s^{-1}.*

The gradient of the linear trend shown in Figure 3.20 gives a $\frac{1}{\Omega_T}$ value of (2.67±0.23)x10^{-5} s^{-1}. This can be compared with the literature values stated in Table 2.1 by estimating k$_\mathrm{T}$, using equation 3.40.

$$k_T = \frac{1}{\Omega_T a_v} = \frac{1}{\Omega_T}\frac{V_{aq}}{A_{int}} \tag{3.40}$$

Where surface area, A$_\mathrm{int}$, is equal to $\pi\left(\frac{D_b}{2}\right)^2$ and V$_\mathrm{aq}$ is the aqueous volume. This gives an estimate of approximately 10^{-7} m·s^{-1}, showing a slow mass transfer across the interface when compared with results reported by Miyake et al.,[66] who used the same chemical system.

Large errors in the data points are likely introduced when the two phases are brought into contact. Small perturbations will generate a temporary, though potentially significant, increase in the surface area. Mass transfer between the two phases will vary across samples with the degree of perturbation.

Based on the calculated mass transfer rate, mass transfer across any stable interfaces in future experiments can be assumed negligible.

3.4 Conclusions

The aim of this chapter was to outline the chemical kinetics and systems that are going to be used in future mass transfer experiments. The first necessary quantity was the initial ligand concentration in the Mextral® 84H, $[\mathrm{L}]_\mathrm{T}$. $[\mathrm{L}]_\mathrm{T}$ was determined to be 1.61 M for the undiluted material, and therefore 0.16 M for the Mextral® 84H/Exxsol™ D80 mixture. $[\mathrm{L}]_\mathrm{T}$ was used to calculate the total kinetic coefficient, first shown in Equation 3.36, and reiterated in Equation 3.41.

$$H_T \left(\frac{[L]_T}{[Cu(II) \cdot 2L]_{org}} - 1 \right)^2 = \frac{[Cu(II) \cdot 2L]_{org}}{[Cu^{2+}]_{aq}} \tag{3.41}$$

Equation 3.41 has been used to plot a graph of $\left(\frac{[L]_\mathrm{T}}{[Cu(II) \cdot 2L]_\mathrm{org}} - 1 \right)^2$ against $\frac{[Cu(II) \cdot 2L]_\mathrm{org}}{[Cu^{2+}]_\mathrm{aq}}$ to calculate a value for the total kinetic coefficient of the system, $\mathrm{H_T}$, determined by the gradient of the linear trend. $\mathrm{H_T}$ was calculated to be 0.65±0.03 for fresh ligand and is a value that will be used in conjunction with the initial, measured and equilibrium concentrations to calculate the mass transfer coefficient of the contactors discussed in future chapters. $\mathrm{H_T}$ for stripped ligand, which has had Cu(II) removed from the complex and back-extracted into an aqueous phase, has also been calculated. $\mathrm{H_T}$ for stripped ligand was found to be 0.236±0.005, which is a significant reduction compared with the fresh material. There is the chance that some ligand degradation has occurred due to the strong $\mathrm{HNO_3}$. It was determined that stripping of the Cu(II)·2L complex is possible, though careful attention needs to be paid to the reduction in $\mathrm{H_T}$. $\mathrm{H_T}$ will be used in later chapters to determine the partition coefficient, S, at a measured aqueous Cu(II) concentration.

To determine the equilibrium Cu(II) concentration, an equation based on the initial Cu(II)$(NO_3)_2$ concentration has been found. This has been completed for both fresh and stripped material.

The pH change in a series of samples was monitored. The solutions are shown to become rapidly more acidic, with pH decreasing from ∼4.25 to ∼ 1.0. Cu(II) extraction is shown to drastically reduce at pH of 1. As such an initial $[\mathrm{Cu(II)}]_{\mathrm{aq}}$ of 0.10 M has been used in all mass transfer experiments so that the reaction does not completely stop based on the pH.

The mass transfer coefficient, $\frac{1}{\Omega_T}$, has been determined first for a system in which no agitation occurs. This has two purposes: firstly, the value for $\frac{1}{\Omega_T}$ acts as an easy comparison, to ensure that good mixing is present during operation of the contactors. In addition to this, both contactor separation systems contain a stagnant interface between the organic and aqueous phases. The agitation free $\frac{1}{\Omega_T}$ value of $(2.67 \pm 0.23)\mathrm{x}10^{-5}$ s^{-1} shows that the mass transfer across this interface is negligible when compared with the mass transfer in the active regions of the contactors.

CHAPTER 4

Design, Hydrodynamics and Mass Transfer in a Taylor-Couette Disc Contactor and a D-cell Contactor

4.1 Introduction

The aim of this chapter is to design a lab-scale contactor that can provide a simple comparison, by which mass transfer capabilities of the more complicated ATR can be easily assessed. Based on the designs presented by Aksamija et al.[106] and Grafschafter et al.,[107–110] a Taylor-Couette disc contactor (TCDC) has been designed and subsequently used to design a novel D-cell contactor. A D-cell contactor is a design, unique to this work, expected to improve upon prototype TCDC designs.[141] The design focusses on removing dispersed organic material which has been trapped beneath rotor discs. This is achieved by curving the inner wall of the disc spacing to trace the circumference of the vortices.

Effects of flow rate, rotational velocity and droplet rise time on mass transfer for both contactors are discussed, as well as the effect of flow rate and rotational velocity on the rise time. Mass transfer coefficients, $\frac{1}{\Omega_T}$, of an aqueous

$Cu(II)(NO_3)_2$ phase and an organic Mextral® 84H/Exxsol™ D80 mixture extractant phase have been calculated by measuring the remaining Cu(II) concentration present in the aqueous raffinate after it has passed through the contactor.

4.2 Methodologies

4.2.1 Design of a Taylor-Couette Disc Contactor and a D-cell Contactor

Figure 4.1 shows the designs for the TCDC (4.1(A)) and D-cell contactor (4.1(B)). One PERSPEX outer cylinder and overflow zone were built with interchangeable stainless steel inner cylinder attachments. The dimensions for the two inner cylinders are the same, with the exception of the curved compartment between discs in the D-cell. The dimensions listed are the outer cylinder diameter, $\mathrm{D_{out}}$; the inner cylinder diameter, $\mathrm{D_{in}}$; the disc diameter, $\mathrm{D_R}$; the disc separation, $\mathrm{H_C}$; the annular distance between cylinders, $\mathrm{B_C}$; the heavy phase (aqueous) inlet height, $\mathrm{H_{aq,in}}$; the light phase (organic) inlet height, $\mathrm{H_{org,in}}$; the light phase inlet height, $\mathrm{H_{aq,out}}$ and the radius of the D-cell curvature, $\mathrm{R_D}$. The value for each of these quantities is listed below.

$$D_{out} = 50.0\ mm \quad ; \quad D_{in} = 25.0\ mm \quad ; \quad D_R = 42.5\ mm$$

$$H_C = 25.0\ mm \quad ; \quad B_C = 12.5\ mm \quad ; \quad R_D = 6.3\ mm$$

$$H_{aq,out} = 2.0\ mm \quad ; \quad H_{aq,in} = 79.0\ mm \quad ; \quad H_{org,in} = 27.0\ mm$$

The inlet and outlet positions are shown in Figure 4.1(A). Inlets are positioned in the centre of two discs, pumping fluid directly between the two vortices. This ensured liquid entering the contactor would be immediately dispersed. The aqueous phase outlet is positioned at the very bottom of the contactor within an aqueous phase separation zone beneath the bottom disc. A similar separation zone, this time designed to separate the organic phase, is situated above the top disc. Organic liquid, after passing through the contactor, will collect in a reservoir above the top disc, gradually building up and overflowing into the surrounding organic phase overflow. From here it will be removed via the light phase outlet. The floor of the overflow zone is sloped to direct the organic liquid towards the outlet.

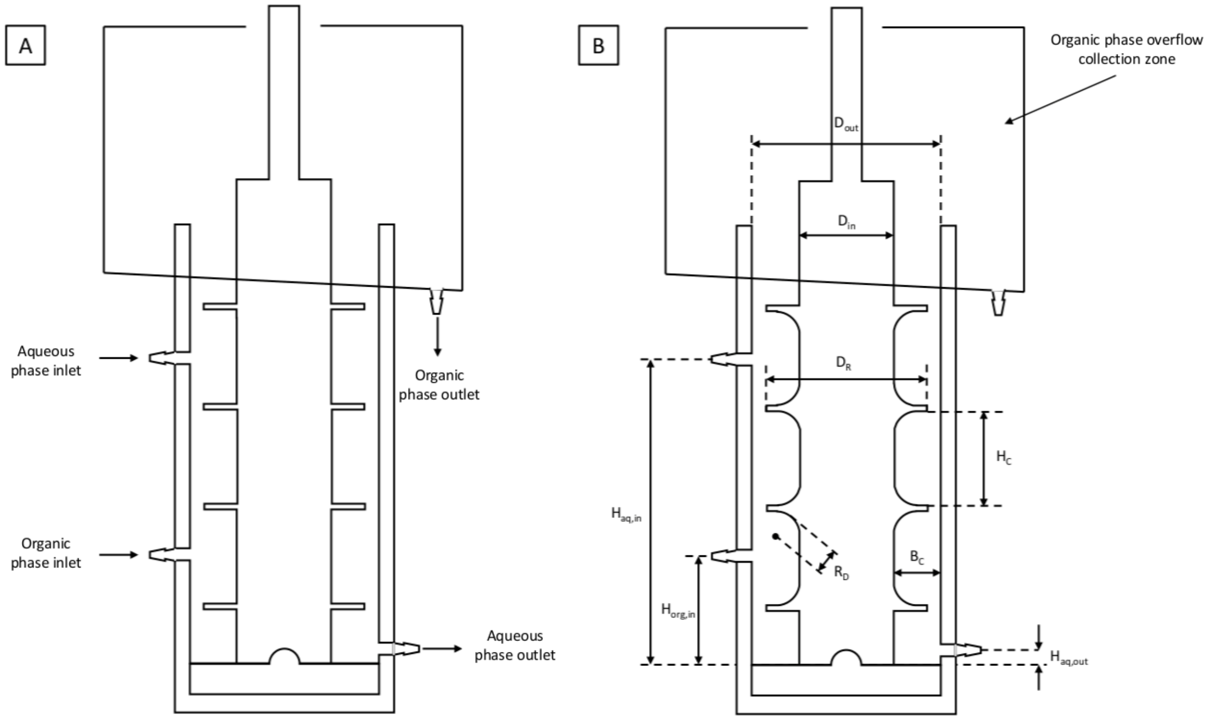

Figure 4.1: **(A)** *The design for the TCDC used in this chapter. Positions of the inlets and outlets are labelled. The dimensions are equal to those shown in (B)* **(B)** *The design for the D-cell used in this chapter. Dimensions shown are relevant for both TCDC and D-cell, with the exception of the spacing curve radius,* R_D.

Figure 4.2(A) shows the constructed inner cylinders for the TCDC (left) and D-cell (right) contactors. Figure 4.2(B) shows the organic collection zone in use. Organic liquid overflows into the collection zone and is drained via an outlet in the corner.

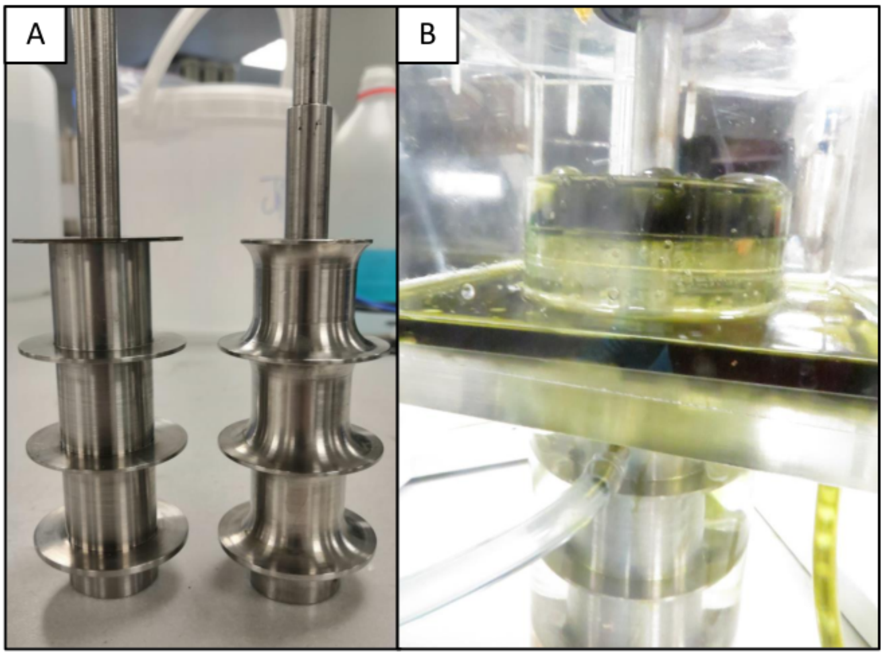

Figure 4.2: **(A)** *A photograph of the two agitator attachments being compared in this chapter. Either attachment could be inserted into the PERSPEX outer cylinder. Left: The TCDC attachment. Right: The D-cell attachment.* **(B)** *A photograph of the organic phase overflow collection zone. Liquid enters the collection zone after overflowing from the contactor. The floor is sloped to direct fluid towards the outlet.*

Initial Computational Design

Some initial design work, continuing from previous work carried out by the author,[141] was executed using computational fluid dynamics (CFD). The CFD package ANSYS Fluent was used to create the geometry and mesh, as well as run a single phase model. The model looked at water entering through the organic phase inlet, travelling through the contactor and exiting through a plane at the top of the contactor, analogous to the organic overflow described in the previous section. The model used a Reynolds stress turbulence model to model vortex motion in a prototype TCDC,[141] a TCDC designed using Grafschafter's design rules[108] and a D-cell contactor. Rotational velocities of 300, 500, 700, 900 and 1100 rpm were simulated for each of the designs.

CFD work has not been presented in this thesis due to technical issues surrounding COVID-19.

4.2.2 Physical Setup

TCDC

Figure 4.3 shows a piping & instrumentation diagram (P&ID), detailing the experimental setup for the Taylor-Couette disc contactor.

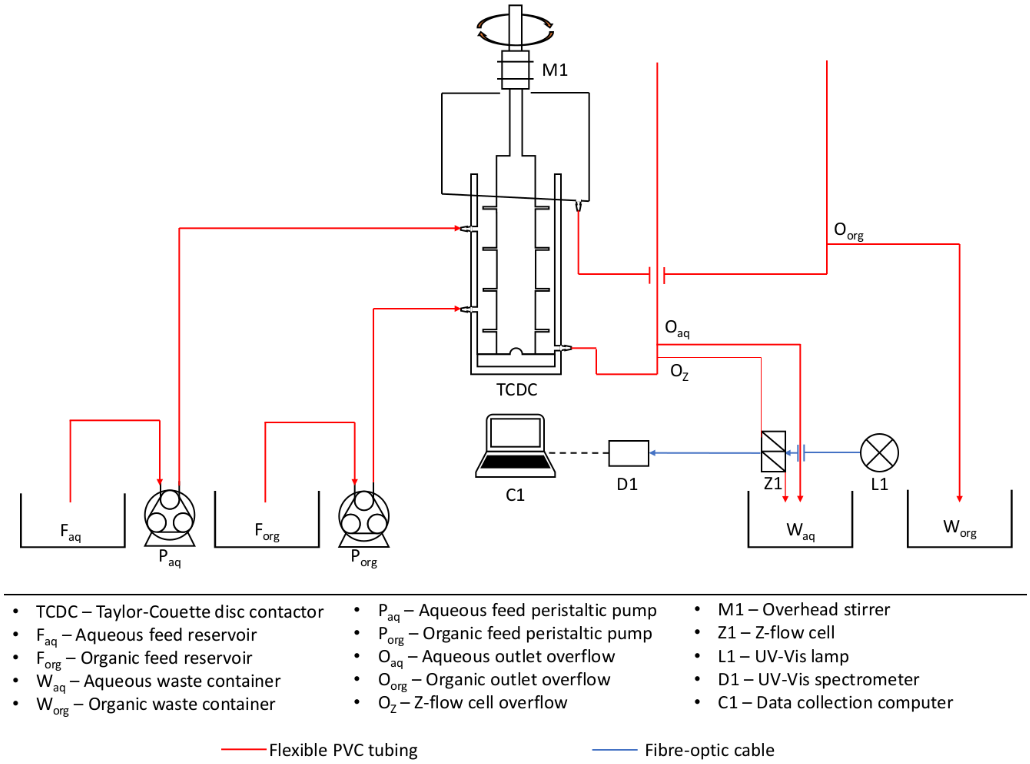

Figure 4.3: *A piping and instrumentation diagram of a Taylor-Couette disc contactor. Red lines depict PVC tubing whilst the blue lines represent fibre-optic cables. The overhead stirrer rotates in a clockwise direction at a speed set using a digital readout.*

The TCDC consisted of a PERSPEX outer cylinder and an inner stainless steel cylinder with four flat disc attachments. The discs were 1.5 mm thick and the spacing between them was twice the length of the distance between the two cylinders. This allows for two vortices with circular cross-sections to form between each pair of discs.

505S and 520S peristaltic pumps, purchased from Watson-Marlow, were used to pump aqueous $Cu(II)(NO_3)_2$ and stripped organic Mextral® 84H/Exxsol™ D80 respectively. The phases were drawn from two 5 L reservoirs and pumped through flexible PVC tubing (1/8 inch internal diameter (ID), 1/4 inch outer diameter (OD)) into their respective inlets. Inlets were constructed from an 1/8 inch hose barb attached to the edge of the PERSPEX outer cylinder. The inlets were positioned at opposing ends of the contactor, with the heavy aqueous phase entering the vessel below the upper disc and the light organic phase entering between the lowest two discs. The organic phase is forced to settle through the aqueous phase, coming into contact with the stainless steel TCDC agitator, becoming dispersed and broken down into droplets. The agitator is rotated by an IKA EUROSTAR20 digital overhead stirrer, positioned directly above the agitator. The overhead stirrer has an adjustable rotational speed, which can be accurately set using the digital readout.

Settling zones at the top and bottom of the TCDC vessel allow for two distinct phases to be removed. The aqueous phase is drawn from the base of the vessel using an overflow lute. Since the overflows and the TCDC are open to atmospheric pressure, the height of the overflow determines the height of the liquid-liquid interface between the pure aqueous phase and the mixed aqueous/organic dispersion. This is in accordance with Equation 4.1.

$$P = \rho g \Delta h \tag{4.1}$$

As the pressures at the liquid-liquid interface and the lute are equivalent, and the density in the two regions are also the same, the liquid depth, Δh, must also be equal. Two overflows are present on the aqueous outlet, one carries the majority of the fluid to a waste reservoir, whilst the other passes through a UV-Vis Z-flow cell, such that the concentration of the aqueous $Cu(II)(NO_3)_2$ raffinate, c_{aq}, can be measured.

The organic phase is drawn from a settling zone at the top of the vessel. Four baffles were positioned at 90° angles around the rim of the PERSPEX outer cylinder. These were 5 mm x 5 mm x 40 mm and were implemented to reduce the vortex effects pulling settled fluid back into the agitation zone. Organic fluid is allowed to settle and gradually fill until it reaches the rim of the vessel. At this point, it overflows into a box-like container surrounding the rim. A single overflow, similar to that described for the aqueous outlet, was positioned in the corner of the container and carried the organic phase to a waste bottle. The container was sloped to direct fluid towards the outlet. The need for a container to capture organic fluid (as opposed to a copy of the aqueous phase outlet) was based on the initial design of the agitator, in which a centrifugal separator was attached to the top of the central cylinder. This separator was designed to reduce the contact time between the two phases and stop mass transfer as soon as the organic phase leaves the agitation zone. The separator was unsuccessful and was subsequently removed. The mass transfer rate across the interface is shown to be extremely small in Section 3.3.5 and was therefore deemed negligible.

D-cell

The experimental setup for the D-cell contactor is identical to that for the TCDC but with one exception. The discs in the D-cell follow the curved shape described in Section 4.2.1, as opposed to the flat disc shape of the TCDC. This shape has been designed to follow the curve of the vortices, limiting trapped organic material beneath the discs. The setup can be seen in the P&ID shown in Figure 4.4, which is identical to Figure 4.3, with the exception of the agitator shape.

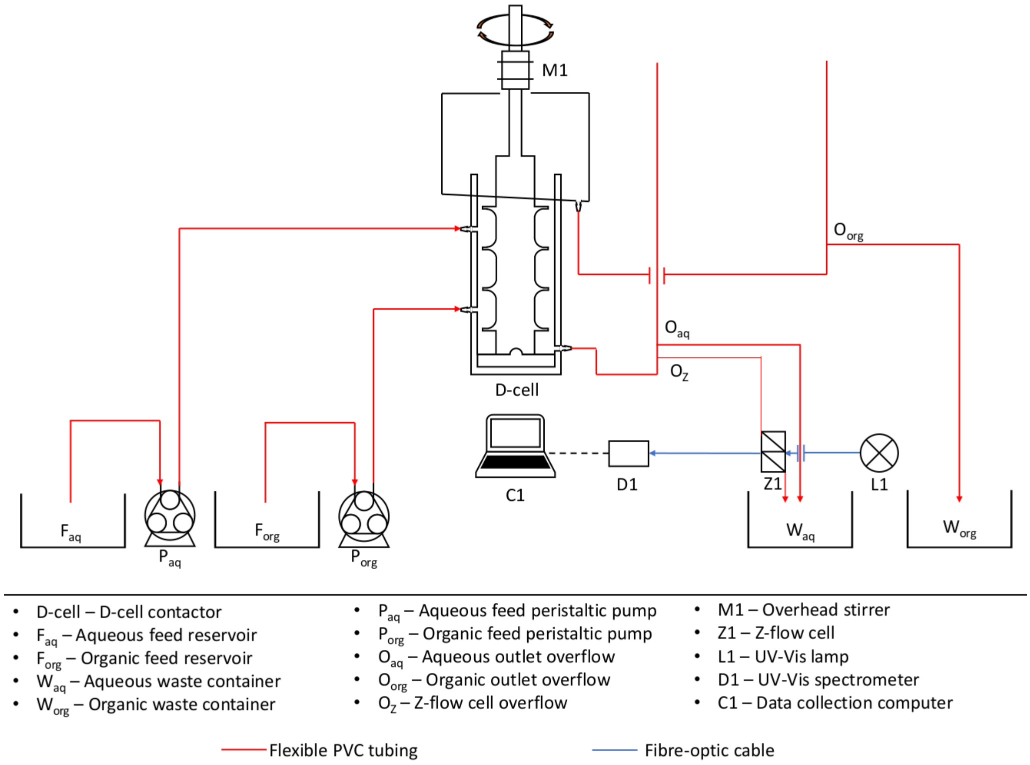

Figure 4.4: *A piping and instrumentation diagram of a D-cell contactor. Red lines depict PVC tubing whilst the blue lines represent fibre-optic cables. The agitator differs from the TCDC in disc shape only. The discs are curved as opposed to flat, to remove droplet holdup in the contactor. The overhead motor rotates in a clockwise direction at a speed set using a digital output.*

4.2.3 Pump Calibration

505S and 520S peristaltic pumps from Watson-Marlow were used to pump Cu(II)-$(NO_3)_2$ solution and the Mextral® 84H/Exxsol™ D80 mixture respectively. The two pumps were set-up as described in Section 4.2.2 and the end of the flexible PVC tubing was positioned at the required height and distance from the pump. The pumps were set at their minimum setting and turned on. The end of the tubing was placed in a measuring cylinder and the volume measured after 60 s of flow to measure the rate of flow per minute. The settings were altered until they corresponded with the flow rates necessary for the experiment. All measurements were taken in triplicate and pumps were recalibrated every two weeks or between experiments.

4.2.4 Droplet Rise Times Measurements

The time droplets spend in the contactors, the droplet rise time, was estimated using video footage recorded using a Canon Powershot SX280 HS digital camera. The relevant contactor was positioned within the frame of the video alongside a stopwatch timer, used to indicated the entry and exit times of a tracer material.

The TCDC and D-cell contactors were set up as shown in Figures 4.3 and 4.4, and set rotating at rotational velocities of 300, 500, 700, 900 and 1100 rpm for the TCDC and 300, 500, 700 and 900 rpm for the D-cell. At rotational speeds greater than 1100 rpm and 900 rpm for the TCDC and D-cell respectively, flooding occurred and liquid in the organic separation zone was drawn back into the active region of the contactor. Flooding occurs when droplets are too small to rise against the flow of the aqueous phase, causing the organic phase volume to gradually increase over time. The rise time at these rotational velocities was therefore not measurable.

Rotational speeds were not used when studying the effect of rotation speed, but were instead converted into the square of the agitator tip speed, u_R^2, such that $u_R^2 = \left(\frac{D_R}{2}\right)^2 \omega^2$. u_R^2 has been used as it provides an estimate of the local energy dissipation, ρu_R^2. u_R^2 values corresponding to each rotational velocity are listed in Table 4.1. Taylor numbers, $\mathrm{N_{Ta}}$, have also been calculated for each rotational velocity such that may be compared with the critical Taylor number, approximately equal to 1708.[95] Table 4.1 shows that 300 and 500 rpm exhibit $\mathrm{N_{Ta}}$ values below the critical Taylor number, therefore not exhibiting strong vortex motion.

Initially Exxsol™ D80, a colourless organic fluid, was pumped into the TCDC or D-cell at 40 mL·min^{-1}. At this point a stopwatch timer was initiated. After the Exxsol™ D80 had been pumped into the contactor for approximately 30 s, a tracer material was added. This was achieved using a three-way valve, the setup of which can be seen in Figure 4.5. A 4 s pulse of pre-used Mextral®

84H/Exxsol™ D80 mixture was injected into the contactor from a separate reservoir. Pre-used Mextral® 84H/Exxsol™ D80 mixture was used as a tracer material due to its contrasting dark black-green colour, and similar physical properties to Exxsol™ D80. A sample frame from footage of the tracer material can be seen in Figure 4.6.

Table 4.1: *Table presenting the corresponding square of the agitator tip speed, u_R^2, as well as the calculated Taylor number, N_{Ta}, for each rotational speed.*

Rotational Velocity (rpm)	u_R^2 ($\mathrm{m^2 \cdot s^{-2}}$)	$\mathrm{N_{Ta}}$
300	0.45	576.0
500	1.24	1600.0
700	2.43	3136.0
900	4.01	5183.9
1100	5.99	7743.9

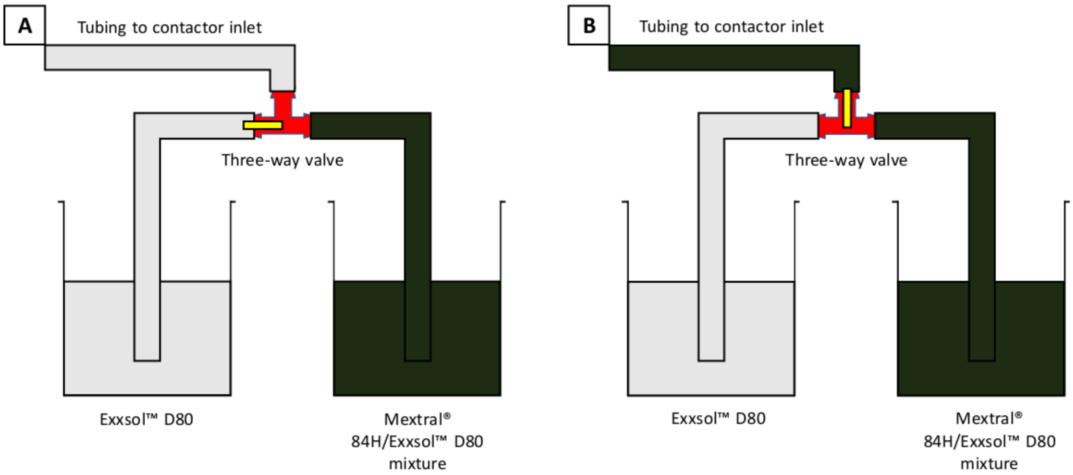

Figure 4.5: *Schematic of the three-way valve setup. During rise time measurements, a three-way valve was used to introduce tracer material into the contactors.* **(A)** *Colourless Exxsol™ D80 was initially pumped into the reactor.* **(B)** *Using a three-way valve, 4 s pulses of pre-used Mextral® 84H/Exxsol™ D80 mixture were pumped into the contactor. This material was chosen based on its contrasting colour and similar physical properties to Exxsol™ D80*

Figure 4.6: *Frames from rise time measurement videos.* **(A)** *A digital timer sits in the foreground of the TCDC to measure the amount of time coloured tracer material remains in the TCDC.* **(B)** *A digital timer is used to measure rise time in the D-cell contactor.*

Footage was then reviewed and, using the stopwatch timer, two times were measured, resulting in times corresponding to the shortest and longest droplet rise times. The difference in time between the coloured droplets entering the contactor and the first coloured droplets leaving the contactor provides an estimate for the shortest rise time. The time difference between droplets entering the contactor and the final coloured droplets leaving the contactor provides an estimate for the longest rise time. A sample calculation is given in the Appendix. For each set of parameters, 3 recordings were taken. The mean of the six estimates was calculated and plotted against the square of the agitator tip speed, u_R^2. Ranges in the rise time (The difference between the longest and shortest times) are used to estimate the distribution of droplet rise times.

Initially, droplet rise time was hoped to be measured using the UV-Vis. This provided a much wider rise time distribution of approximately half an hour. This was due to the liquid not being able to flow quickly through the extremely narrow cavity within the Z-flow cell.

4.2.5 Mass Transfer in Counter-current Systems

The aim of this section is to provide a relation between the measured aqueous concentration, c_{aq}, and contact time, t. As the two phases flow in opposite directions, an equilibrium between bulk aqueous liquid and an organic droplet is never achieved and mass transfer only ceases if the organic phase becomes saturated.

In this instance, mass transfer rate will be written in terms of the number of moles per second being transferred, F. The definition of F, and how it relates to the mass transfer rate, q, is shown in Equation 4.2.

$$F = \frac{N}{t} \qquad ; \qquad q = \frac{1}{V}\frac{dN}{dt} = \frac{dF}{dV} \tag{4.2}$$

F can be converted into a concentration by stating that $F = Qc$, where Q is the molar flow rate of a particular phase. Equations 4.3 and 4.4 restate the definitions of the mass transfer rate, q, in terms of the concentration change, dc, in the organic and aqueous phases.

$$SdF_{org} = SQ_{org}dc_{org} = S\frac{1}{\Omega_T}(c_{i,org} - c_{org})dV \tag{4.3}$$

$$-\,dF_{aq} = -Q_{aq}dc_{aq} = \frac{1}{\Omega_T}(c_{aq} - c_{i,aq})dV \tag{4.4}$$

The relation shown in Equation 4.5 is taken from the partition coefficient definition given in Equation 2.1. This is true for concentrations at the liquid-liquid interface, which will be in equilibrium.

$$Sc_{i,org} = c_{i,aq} \tag{4.5}$$

Substituting Equation 4.5 into Equation 4.3 and subsequently adding Equations 4.3 and 4.4 together yields Equation 4.6, which can be easily integrated.

$$dc_{aq} - Sdc_{org} = -\frac{1}{\Omega_T}\left(\frac{1}{Q_{aq}} + \frac{S}{Q_{org}}\right)(c_{aq} - Sc_{org})dV \tag{4.6}$$

Integration occurs from one end of the contactor to the other. In the case of a counter-current device, each end of the contactor contains an inlet and an outlet. The labels here, top and bottom, refer to the top and bottom of the contactor respectively. This is based on a TCDC, in which one phase travels downwards, and the other upwards.

$$\int_{(c_{aq}-Sc_{org})_{bottom}}^{(c_{aq}-Sc_{org})_{top}} \frac{d(c_{aq}-Sc_{org})}{c_{aq}-Sc_{org}} = -\frac{1}{\Omega_T}\left(\frac{1}{Q_{aq}}+\frac{S}{Q_{org}}\right)\int_0^{V_T} dV \tag{4.7}$$

$$\ln\left[\frac{(c_{aq}-Sc_{org})_{top}}{(c_{aq}-Sc_{org})_{bottom}}\right] = -\frac{1}{\Omega_T}\left(\frac{1}{Q_{aq}}+\frac{S}{Q_{org}}\right)V_T \tag{4.8}$$

Situated at the top of the contactor are the aqueous inlet and the organic outlet. As such, the relations shown in Equation 4.9 hold true. The aqueous concentration will be that of the initial concentration at the inlet. Furthermore the organic concentration will be equivalent to the loss in aqueous concentration over the contactor, as all solute lost from the aqueous will be transferred into the organic phase.

$$c_{aq} = c_0 \qquad ; \qquad c_{org} = c_0 - c_{aq} \tag{4.9}$$

The organic inlet can be found at the bottom of the contactor with an initial solute concentration of 0. The aqueous outlet is also situated at the bottom of the contactor, and will have a concentration c_{aq}.

$$c_{org} = 0 \tag{4.10}$$

Substituting the relationships in Equation 4.9 and 4.10 into Equation 4.8 yields Equation 4.11.

$$\ln\left[\frac{c_0 - S(c_0-c_{aq})}{c_{aq}}\right] = -\frac{1}{\Omega_T}\left(\frac{1}{Q_{aq}}+\frac{S}{Q_{org}}\right)V_T \tag{4.11}$$

$$\ln\left[S + (1-S)\frac{c_0}{c_{aq}}\right] = -\frac{1}{\Omega_T}\left(\frac{1}{Q_{aq}}+\frac{S}{Q_{org}}\right)V_T \tag{4.12}$$

The total volume, V_T, is the sum of the aqueous and organic volumes, which are also equal to the product of the phase flow rate and residence time.

$$V_T = (V_{aq} + V_{org}) = Q_{aq}t_{aq} + Q_{org}t_{org} \tag{4.13}$$

This results in Equation 4.14, which relates the aqueous solute concentration to the either the organic or aqueous residence time in the system.

$$\ln\left[S + (1 - S)\frac{c_0}{c_{aq}}\right] = -\frac{1}{\Omega_T}\left(\frac{1}{Q_{aq}} + \frac{S}{Q_{org}}\right)(Q_{aq}t_{aq} + Q_{org}t_{org}) \tag{4.14}$$

For the special case in which the aqueous and organic phase flow rates, Q_{org} and Q_{aq} are equal, Equation 4.14 collapses to Equation 4.15.

$$\frac{1}{(1 + S)}\ln\left[S + (1 - S)\frac{c_0}{c_{aq}}\right] = -\frac{1}{\Omega_T}(t_{aq} + t_{org}) \tag{4.15}$$

4.2.6 Mass Transfer Measurements

Concentration Measurements

Concentration measurements were performed using UV-Vis spectroscopy. The background and analysis of the data use the same methods described in Section 3.2.1. Here however, inline measurements using a continuous flow of sample, are recorded instead of offline measurements, in which discreet samples are used. A small volume of aqueous $Cu(II)(NO_3)_2$ raffinate leaving the contactor is diverted from the main overflow lute forcing it to pass through the UV-Vis Z-flow cell. As with the offline data collected in chapter 3, absorbance is measured over an integration time of ∼200 ms (85% of the spectrometers maximum capacity) and averaged across the scan to form a single measurement. Unlike with offline measurement, multiple measurements are recorded over a designated period of time instead of a specified number of scans. In this case measurements were recorded over 60 s to ensure that at least two rise times had passed, ensuring a steady-state was reached and minimising any variation in the data.

Between runs, the Z-flow cell was flushed out with deionised water. This had two functions: firstly, to remove any of the previous sample and not contaminate future runs; secondly, putting deionised water into the flow cell ensured the calibration of the spectrometer was still correct, since deionised water was used as a reference material. Figure 4.7 shows the change in the aqueous $Cu(II)(NO_3)_2$ concentration within the Z-flow cell over the course of 400 s. The flow cell was initially filled with deionised water and the $Cu(II)(NO_3)_2$ entered the Z-flow cell after passing through the contactor. The increase in concentration between 25 and 75 s shows the flushing out of the deionised water. After 100 s the concentration can be seen to plateau, showing a stable concentration is reached free from dilution by deionised water. As a result, the system was left for a minimum of 100 s to ensure a steady state was reached before conducting any measurements.

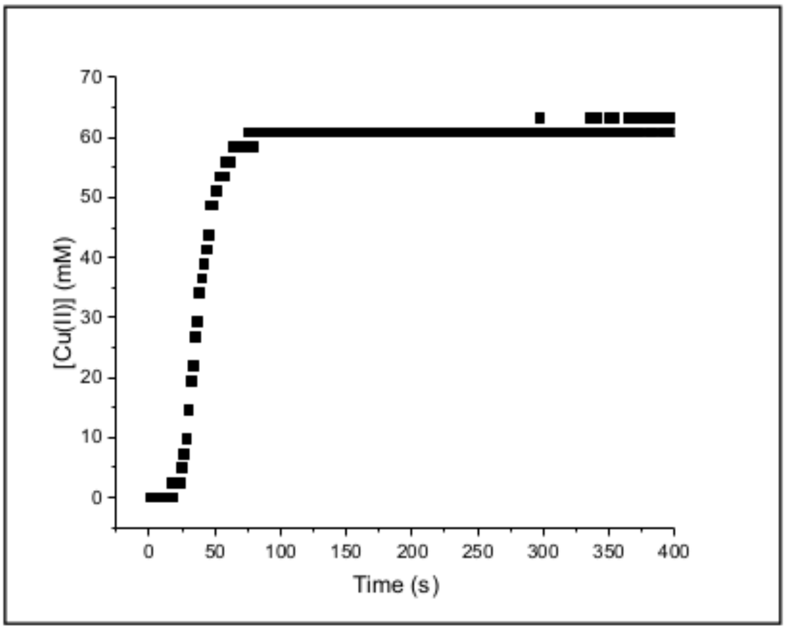

Figure 4.7: *A plot showing the change in Cu(II) concentration within the Z-flow cell. The initial 0 mM concentration is based on the deionised water reference sample. As aqueous Cu(II) enters the Z-flow cell, the concentration gradually increases as the deionised water is flushed out. Beyond ≈ 100 s the concentration reaches a steady state.*

Effect of Flow Rate on Cu(II) Concentration

505S and a 520S peristaltic pumps from Watson Marlow were used to pump 0.10 M aqueous Cu(II)$(NO_3)_2$ and stripped Mextral® 84H/Exxsol™ D80 mixture into the TCDC at varying flow rates. The peristaltic pumps were calibrated in the same method described in Section 4.2.3. Cu(II) content of the aqueous raffinate was measured for four flow rates using UV-Vis spectroscopy, as described in Section 4.2.6. Each measurement was taken in triplicate and a mean value of the results taken. Aqueous and organic flow rates, Q_{aq} and Q_{org} respectively, were adjusted between experiments and pump settings were chosen such that the flow rates were equal, or as near as possible. The flow rates used for each experiment are shown in Table 4.2. Each flow rate experiment was performed at two disc speeds, 0.45 and 2.43 $m^2 \cdot s^{-2}$, as an initial investigation into the effect of rotational speed. All parameters were altered individually.

Table 4.2: *Phase flow rates for each experiment. Pumps were calibrated, as near as possible, to a 1:1 solvent:aqueous ratio.*

Experiment number	Q_{aq} ($\pm$0.5 mL·min^{-1})	Q_{org} ($\pm$0.5 mL·min^{-1})
1	12.0	10.0
2	21.0	20.0
3	41.0	40.0
4	62.0	60.0

The quantity plotted on the y-axis in Figure 4.14, $\frac{c_{aq}}{c_0}$, is a normalised form of the measured concentration, in which the quantity is equal to 1 at $c_{aq} = c_0$. Only Mextral® 84H/Exxsol™ D80 mixture that had been stripped a single time was used in this experiment.

Effect of Disc Tip Speed on Mass Transfer

The effect of u_R^2 on mass transfer in the TCDC and D-cell contactors has been measured. 0.10 M aqueous $Cu(II)(NO_3)_2$ and stripped organic Mextral® 84H/ Exxsol™ D80 mixture were initially pumped into the TCDC at 40 and 41 mL·min^{-1} respectively, in accordance with the results seen in Section 4.3.3. u_R^2 was changed by adjusting the rotational velocities in increments of 200 rpm, starting at 300 rpm and working up to 1100 rpm. An IKA EUROSTAR20 digital overhead stirrer, positioned directly above the agitator, was used to vary the rotational velocity. A digital readout on the stirrer allowed accurate setting of the rotational velocity to within 1 rpm. Cu(II) concentration was measured using the UV-Vis setup described in Section 4.2.6. This process was then repeated for the D-cell agitator cylinder.

A graph comparing the change in the normalised aqueous Cu(II) concentration, $\frac{c_{aq}}{c_0}$, with u_R^2 for the two contactors was then plotted.

Only Mextral® 84H/Exxsol™ D80 mixture that had been stripped a single time was used in this experiment.

Effect of Droplet Rise Time on Cu(II) Concentration

The effect of TCDC and D-cell contactor rise time on the Cu(II) concentration present in the aqueous raffinate has been measured using UV-Vis spectroscopy. 0.10 M aqueous $Cu(II)(NO_3)_2$ and the organic phase, Mextral® 84H/Exxsol™ D80 mixture, were pumped into their respective inlets at 40 and 41 mL·min^{-1} respectively. The square of the mean rise time, t^2, has been plotted against the normalised concentration, $\frac{c_{aq}}{c_0}$. t^2 was chosen empirically, as it was shown to follow a linear trend.

The mass transfer coefficient, $\frac{1}{\Omega_T}$, has been calculated by rearranging the derived equation for mass transfer in a counter-current contactor, Equation 4.15, shown in Section 4.2.5. 4.16 shows the equation rearranged for $\frac{1}{\Omega_T}$. t_{org} and t_{aq} can be taken as the droplet rise time, t, and the aqueous residence time, $\frac{V_{aq}}{Q_{aq}}$

respectively.

$$\frac{1}{\Omega_T} = -\frac{1}{(t_{aq} + t_{org})(1+S)} \ln \left[S + (1-S)\frac{c_{aq}}{c_0} \right] \tag{4.16}$$

Mextral® 84H/Exxsol™ D80 mixture that has been stripped a single time has been used as an organic phase, therefore the stripped value of the total kinetic coefficient, $\mathrm{H_T}$, has been used to calculate the partition coefficient, S. S has been calculated to be 0.89±0.01 for an initial Cu(II) concentration of 0.10 M.

4.2.7 Error Propagation

This section outlines the propagation of errors used in this chapter.

The error in the average initial concentration was calculated via standard error of the initial concentrations of all batches. Standard error was also used to calculate the error in the average of the three measured concentrations. Error in S has been calculated using the standard error of all calculated values. Some variation in S exists based on the variation in the initial concentration of each aqueous phase batch. The equation for the standard error is given in the Appendix.

Error in the droplet rise time was calculated as the error in the average rise time, t, using Equation 9.2 shown in the Appendix. Further propagation of these errors, in order to calculate the uncertainty in the $\frac{c_{aq}}{c_0}$, is also shown in the Appendix.

The error in the quantity $\frac{1}{\Omega_T}$ was calculated using the standard error.

4.3 Results & Discussions

4.3.1 Design of a Taylor-Couette Disc Contactor and a D-cell Contactor

Following work presented by Aksamija et al.,[106] an initial attempt was made to design a lab-scale TCDC.[141] This predated Grafschafter's design rules,[108] and some design mistakes were made. An image of the initial prototype design can be seen in Figure 4.8.

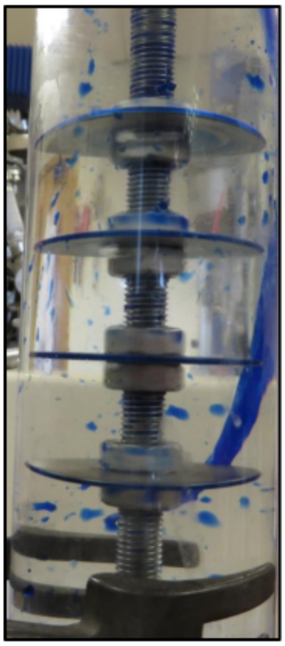

Figure 4.8: *The initial TCDC design. Four discs were placed 25 mm apart on an 8 mm inner cylinder. The inner cylinder was threaded, such that the discs could be held in place by two screw nuts.*[141]

The initial design featured four 40 mm diameter discs, spaced at 25 mm intervals, situated on an 8 mm threaded inner cylinder. Discs were held in place by two nuts. These were housed within a 50 mm PERSPEX outer cylinder.

Through computational fluid dynamics (CFD) it was determined that a dead zone was present around the central shaft of the prototype TCDC, causing organic material to accumulate between a pair of discs.[141] The accumulated organic liquid is shown in Figure 4.9. Vortices exhibit a circular cross-section, with diameter equal to half the disc separation, and as such they were unable to fill the full spacing, thus creating the dead zones labelled in Figure 4.10. Based on this information, two new designs were implemented; a TCDC, designed using Grafschafter's criteria,[108] and a D-cell contactor, a novel design intending to completely remove dead zones. Both designs, and their vortices are also shown in Figure 4.10.

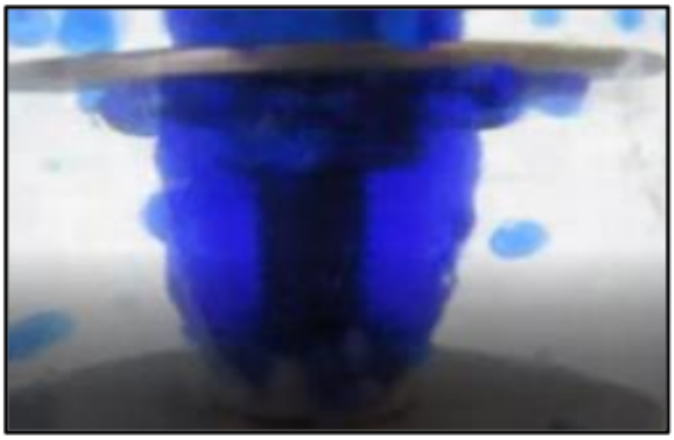

Figure 4.9: *Accumulation of organic phase between two discs rotating at 700 rpm. This has been attributed to the dead zone that is present around the inner cylinder. The presence of the dead zones influenced further designs.*[141]

A D-cell is extremely similar to a TCDC with one distinct difference. Instead of rectangular spacing between the discs, the D-cell features curved, D-shaped spacings designed to follow the curvature of the vortices, encouraging gravity separation of droplets. This should remove any dead zones in the corners of the rectangular TCDC and remove any coalescence and accumulation beneath the discs. The three compartment shapes (prototype TCDC, TCDC and D-cell) can be seen in Figure 4.10. To determine the shape and size of the vortices, the CFD package ANSYS Fluent was used to trace their outline.

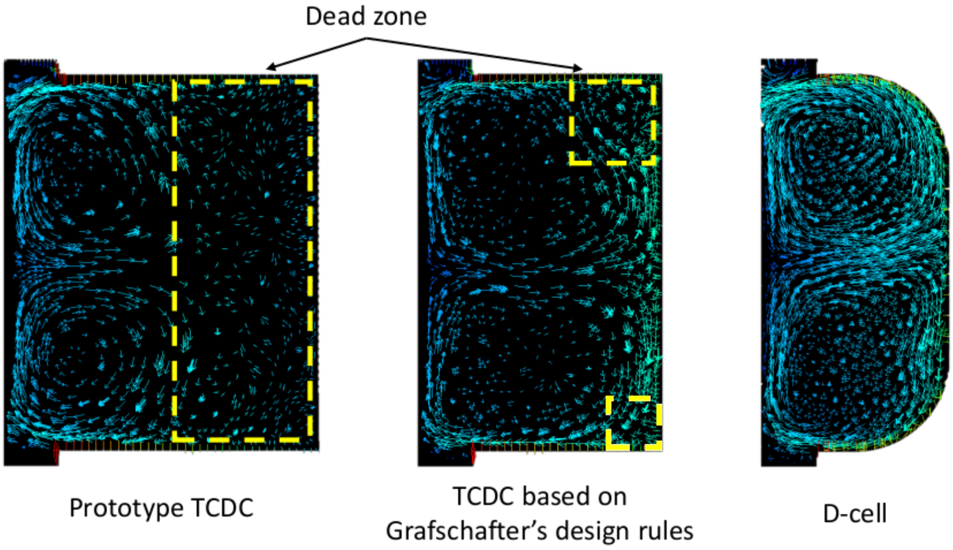

Figure 4.10: *CFD velocity vector plots of the three contactor designs, the prototype TCDC (left),*[141] *the TCDC based on Grafschafter's design rules (centre),*[108] *and the D-cell contactor (right). Images represent a cross-section of the compartment between two discs. All images were generated using the CFD package ANSYS Fluent and are to scale. The yellow dotted line represents the dead zones, in which organic material can accumulate.*

Further CFD work was completed, with the intent of including quantitative data to support findings in this chapter. However technical difficulties, not fixable due to COVID-19 restrictions, rendered this impossible.

4.3.2 Rise Time Measurements

The time a droplet spends in a contactor is an important piece of information as, alongside the data collected in chapter 3, it enables the calculation of the mass transfer coefficient, $\frac{1}{\Omega_T}$. The value of $\frac{1}{\Omega_T}$ will then be used to compare the different contactors discussed in this work. A comparison of droplet rise times in the TCDC and D-cell contactors, at varying disc tip speeds, are depicted in Figure 4.11 and listed in Table 4.3. The droplet rise time is defined as the average time it takes a droplet to pass through the contactor.

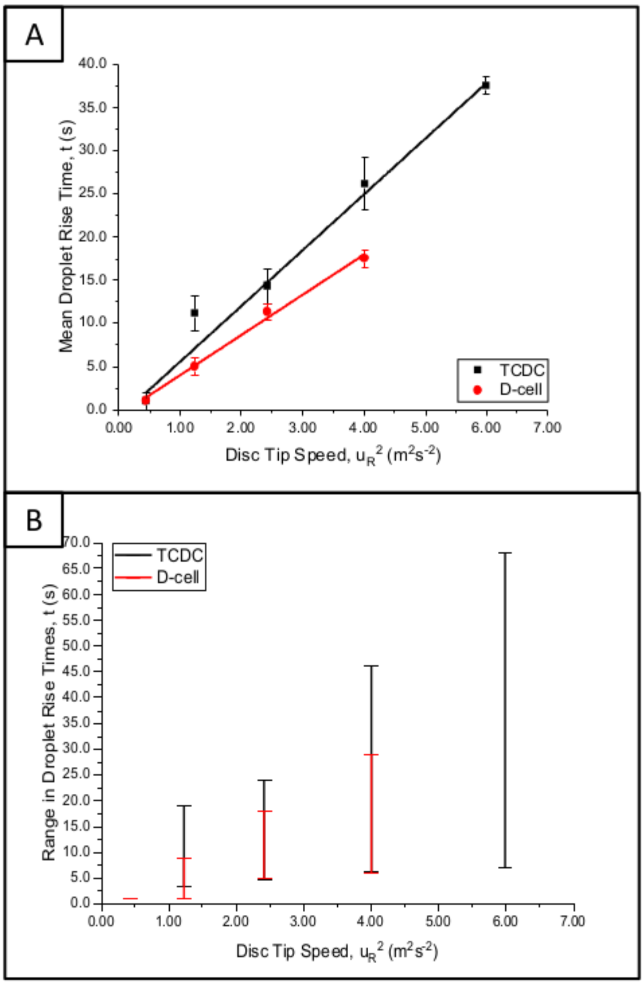

Figure 4.11: *Two graphs showing the change in droplet rise time with increasing tip speed for the Taylor-Couette disc contactor and the D-cell contactor.* **(A)** *Time taken for a droplet to leave the active region vs the square of the agitator tip speed, $u_R{}^2$. Plotted data points are calculated as the mean rise time. A comparison is made between the TCDC (shown in black) and the D-cell (shown in red)* **(B)** *A plot showing the range in droplet rise times against the square of the tip speed. A larger time distribution can be seen at greater tip speeds, as droplets will be broken down further. Smaller droplets will exhibit longer rise times due to smaller buoyancy forces and more susceptibility to Taylor vortices. However, some droplets will escape being broken down and pass through the contactor undisturbed, resulting in a consistent shortest rise time.*

Table 4.3: *A table listing the mean rise times for five rotational velocities. Data is listed for two contactors, a TCDC and a D-cell. A time is not given for the D-cell at 5.99* $m^2{\cdot}s^{-2}$ *as organic material is drawn back into the contactor at this velocity.*

u_R^2 ($m^2{\cdot}s^{-2}$)	Mean Rise Time, t TCDC (s)	Mean Rise Time, t D-cell (s)
0.45	1	1
1.24	11	5
2.43	14	11
4.01	26	18
5.99	38	-

Figure 4.11(A) shows a plot of the square of the agitator tip speed, $u_R{}^2$, against the mean value of a range of droplet rise times for a TCDC (shown in black) and a D-cell contactor (shown in red) respectively. The range in measured rise times is plotted in Figure 4.11(B).

As disc speed increases, the power per volume, expressed in Equation 4.17, as well as the turbulent energies in the system will also increase.

$$\frac{P_w}{V_L} = \frac{N_P \rho_c \omega_R^3 D_R^5}{V_L} \tag{4.17}$$

Where N_P is the power number, a dimensionless quantity defined as the ratio of resistance forces to inertial forces. Power per volume is seen to vary by the cube of the rotation speed, ω_R^3. Figure 4.12 shows the calculated power per volume against u_R^2 for the five u_R^2 values used. The power number varies with impeller shape and as such N_P for a saw tooth impeller, N_P=0.10,[142] has been used as this is extremely close to a disc, which is not a commonly used shape.

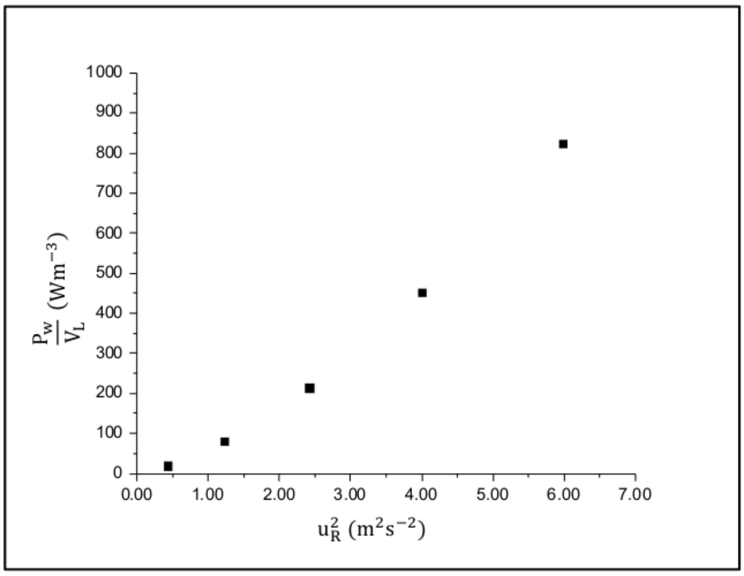

Figure 4.12: *A plot depicting the change in power per volume vs* u_R^2 *for a TCDC or D-cell. The power number for a sawtooth impeller,* N_P*=0.10, has been used.*[142]

Droplets entering the vessel will be broken down further by the increased power and torque present at the tip of a disc. The rise velocity is proportional to the droplet diameter squared, therefore any increase in the disc tip speed will cause an increase in the droplet rise time. This is evidenced by the power per volume plot shown in Figure 4.12. While power per volume and rise time do not follow the exact trend (power per volume is proportional to u_R^3, whilst t is proportional to u_R^2), there is a clear correlation between the two.

Stronger vortices between the discs, induced by higher disc tip speeds, may also cause droplets to be trapped within the contactor, further increasing the rise time. Both of these effects cause the droplets to remain in the contactor for a longer period of time. This can be seen by the rise time ranges shown in Figure 4.11(B). The shortest time, in which droplets quickly exit the contactor, is relatively consistent as some droplets will pass straight through without much interference. The longest droplet rise times are seen to increase with disc speed, resulting in an increase in the mean value. A linear relationship is shown between mean rise time and u_R^2.

Figure 4.11(A) shows a comparison between the mean rise time values for the TCDC and D-cell. While the two contactors show the same trend it is clear that, for a given disc speed, droplets spend longer in the TCDC than the D-cell. This trend is seen across all tip speeds greater than 0.45 $m^2 \cdot s^{-2}$. The flat TCDC discs may be trapping droplets beneath them, creating a settling zone.[107,108] On the other hand, the rounded surface of the D-cell agitator directs the droplets upward, allowing them to rise through the reactor via their own buoyancy.

The rise times presented in Table 4.3 can be used to estimate droplet sizes within the TCDC and D-cell. Stokes' law, shown in Section 2.9, can be rearranged for the droplet diameter, D_d, as in Equation 4.18. The Stokes' velocity can be estimated as $u_s = \frac{h_{con}}{t}$ where h_{con} is the height of the contactor.

$$R_d^2 = \left(\frac{D_d}{2}\right)^2 = \frac{9}{2}\frac{\mu u_s}{g\Delta\rho} = \frac{9}{2}\frac{\mu h_{con}}{g\Delta\rho t} \tag{4.18}$$

A plot of droplet diameters calculated in this method is shown in Figure 4.13. The modified Marr model,[123] used by Aksamija et al.[106] and discussed in Section 2.7.1, has been included for comparison.

Diameters calculated using Stokes' law show good agreement with data collected by Aksamija et al.[106] and the modified Marr model (both detailed in Section 2.8.2), all showing a decrease in droplet diameter with increasing rotational speed. Droplet diameter is also calculated to be in the same order of magnitude as those described by Aksamija et al.,[106] supporting the method and calculation of the mean droplet rise times. It is important to note that these droplet size estimates may appear smaller than in actuality. This is due to the assumption that all droplets are only affected by buoyancy, which ignores the effects of Taylor vortices on the droplet path. While droplet sizes are not accurate, the decrease in droplet size diameter with u_R^2 is still a relevant trend.

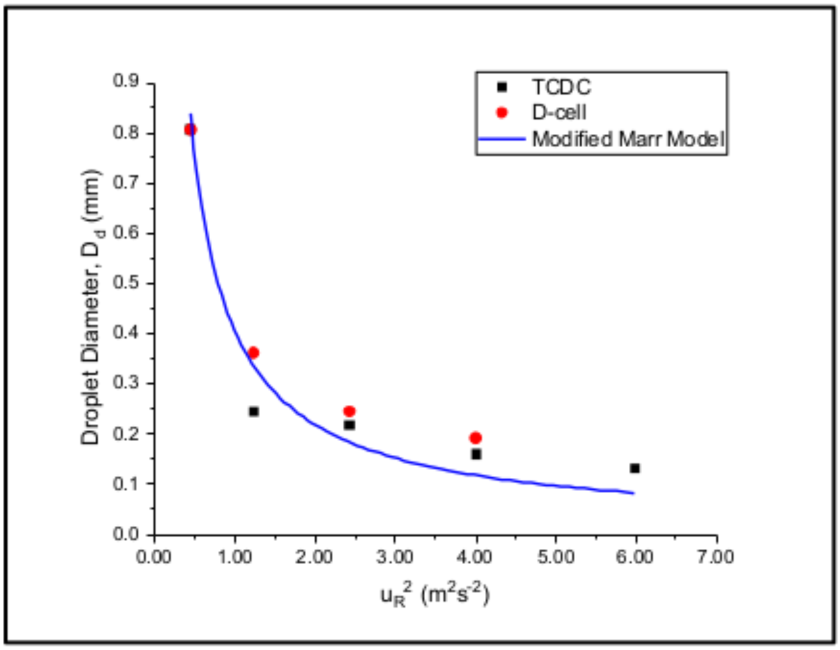

Figure 4.13: *A plot of droplet diameter against tip speed for both the TCDC and D-cell. A plot of the modified Marr model,*[123] *used by Aksamija et al.,*[106] *has been included in blue for comparison. The droplet diameters for the TCDC and D-cell were calculated using the Stokes' velocity.*

4.3.3 Mass Transfer Experiments

Effect of Flow Rate on Mass Transfer

When trying to characterise a solvent extraction contactor, it is first necessary to determine which parameters effect mass transfer in the system. As such, a small experiment was implemented to determine whether the inlet flow rate and disc tip speed have any impact on mass transfer rates in the TCDC and D-cell contactors.

Figure 4.14 shows how aqueous raffinate concentration, after passing through a TCDC, changes with increasing flow rate for two u_R^2 values, 0.45 and 2.43 $m^2 \cdot s^{-2}$. These two values of u_R^2 have been chosen as the corresponding Taylor numbers fall either side of the critical Taylor number.

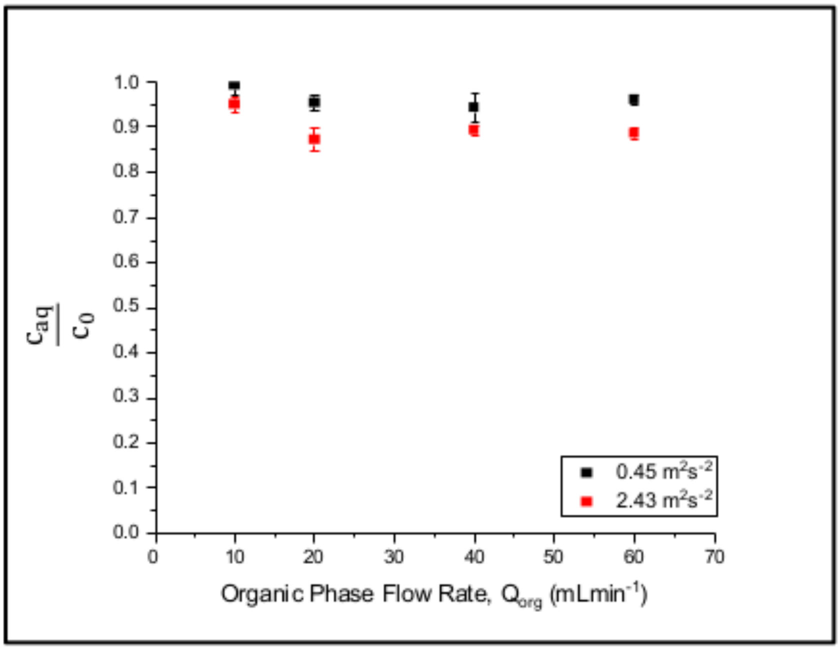

Figure 4.14: *Effect of flow rate on Cu(II) mass transfer in a Taylor-Couette disc contactor. Two tip speeds, 0.45 and 2.43 m*^{2}*·s*$^{-2}$*, are shown. Flow rate is shown to have little effect on the mass transfer in the system beyond 20 mL·min*$^{-1}$*. This is consistent for both tip speeds.*

Within the measured range, flow rate is shown to have little effect on concentration, and therefore mass transfer, beyond 20 mL·min^{-1}. This trend is consistent for both rotational velocities, though the greater tip speed at 2.43 m^2·s^{-2} provides a greater reduction in concentration than the 0.45 m^2·s^{-2} case, which shows little to no mass transfer at all. This is perhaps to be expected as the mean rise time at 0.45 m^2·s^{-2} is only 1 s, not providing enough time for significant measurable mass transfer to occur.

The measured concentration, c_{aq}, at 10 mL·min^{-1} is not consistent with the other data points, though this trend is seen in both cases. At a flow rate of 10 mL·min^{-1}, organic liquid does not enter the vessel as a jet, and instead clings to the PERSPEX wall of the outer cylinder. The fluid does not come into direct contact with the agitator, reducing rise time and limiting the dispersion and liquid-liquid contact necessary for significant mass transfer. Both rotational velocities show no concentration change at this speed.

One possible reason for consistent mass transfer when changing flow rate is a rise time that is unaffected by flow rate. This is possible if the droplet rise time is dominated by buoyant forces. It is shown that the disc tip speed of the system has a marked impact on the mass transfer in the TCDC. An increase in the rotational velocity would also bring an increase in the shear and turbulent forces experienced by a droplet. An increase in the shear force would reduce the average droplet diameter and increase the droplet surface area. The effect of increasing turbulent forces would form stronger vortices between the discs of the TCDC, therefore increasing the average rise time and the time spent in contact with the aqueous phase. Both effects would result in a higher overall mass transfer in the system. This suggests a system in which rise time and mass transfer are solely based on the disc tip speed of a given agitator shape. As such, more experiments are needed to determine the effect of disc tip speed. These will be discussed in the next section.

It is important to note that, while the inlet flow rates (determined by pump settings) for both phases are equivalent, the hold-up volume of each phase within the contactor is significantly different. Droplet buoyancy determines the rate at which the organic phase leaves the contactor, therefore organic volume will increase with disc tip speed. This has also been shown in the TCDC designed by Grafschafter et al., in which they show an exponential increase in hold-up with rotation speed.[107]

Based on the results discussed in this section, a constant flow rate of 40 mL·min^{-1} has been used in all further experiments laid out in this chapter.

Effect of Rotational Velocity on Cu(II) Concentration

Based on the conclusions gathered from Figures 4.11 and 4.14, it is expected that higher rotational velocity will provide greater mass transfer in the two contactors. This is due to the increased rise times discussed in Section 4.3.2, as well as the increased shear forces breaking droplets down further.

Figure 4.15 shows a plot of the square of the tip speed, $u_R{}^2$, against the normalised concentration of Cu(II) measured in the aqueous raffinate, $\frac{c_{aq}}{c_0}$. Plots are given for both the TCDC (shown in black) and the D-cell (shown in red) for comparison between the two contactors. For each contactor, $\frac{c_{aq}}{c_0}$ is shown to decrease linearly with increasing u_R^2 of the central cylinder discs. Therefore an increased net mass transfer into the organic Mextral® 84H/Exxsol™ D80 extractant is present at higher tip speeds.

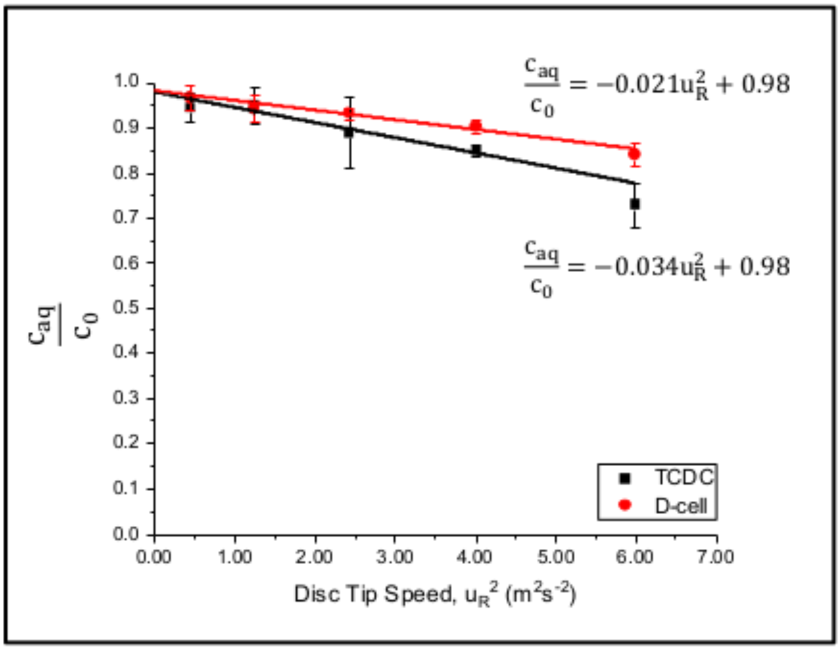

Figure 4.15: *A graph plotting the effect of* u_R^2 *on the normalised concentration of Cu(II),* $\frac{c_{aq}}{c_0}$*, in the aqueous raffinate after contact with Mextral® 84H/Exxsol™ D80 mixture in two contactors. The concentration in a TCDC and D-cell contactor are represented by the black and red data points respectively. For a given tip speed, more Cu(II) is seen to be extracted from the TCDC when compared with the D-cell.*

Mass transfer is greater in the TCDC than the D-cell for a given tip speed. This is in agreement with the effect of rotational velocity on rise time discussed in Section 4.3.2, and provides further evidence that rise time in the contactors is based on both agitator shape and speed.

Effect of Droplet Rise Time on Mass Transfer

The mass transfer coefficient, $\frac{1}{\Omega_T}$, can now be calculated using the rise times determined in Section 4.3.2, the concentrations shown in Figure 4.15 and the value for the partition coefficient, S, calculated as 0.89±0.01 for an initial aqueous Cu(II) concentration of 0.10 M.

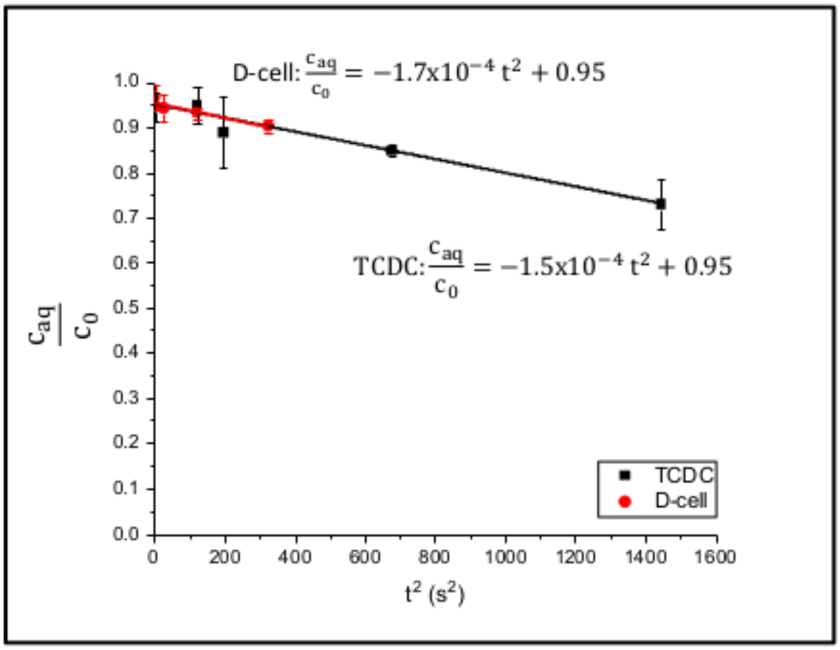

Figure 4.16: *A graph plotting* t^2 *against the normalised concentration for two contactors, the TCDC (shown in black) and the D-cell (shown in red). The concentration in the two contactors are shown to decay at the same rate, though the rise time in the D-cell is shorter for any given rotational velocity.*

Figure 4.16 shows the change in Cu(II) concentration in the aqueous raffinate as a function of the mean rise time. This is shown for both the TCDC (shown in black) and D-cell (shown in red) contactors. Rise time has been altered by changing the rotational velocity and applying the corresponding time from Table 4.3. Comparing the two contactors at a given rise time, both contactors exhibit equivalent copper extraction.

$\frac{1}{\Omega_T}$ values, calculated with Equation 4.16, for the TCDC and D-cell are given in Table 4.4.

Table 4.4: *Table displaying the mass transfer coefficient, $\frac{1}{\Omega_T}$ for both the TCDC and the D-cell contactor. The two contactors are shown to have similar mass transfer coefficients for a given rise time.*

	$\frac{1}{\Omega_T}$ $(10^{-4}s^{-1})$	
Droplet Rise Time (s)	TCDC	D-cell
1	0.16 ± 0.05	0.11 ± 0.05
5	-	0.18 ± 0.06
11	0.14 ± 0.06	0.26 ± 0.02
14	0.37 ± 0.01	-
18	-	0.36 ± 0.05
26	0.54 ± 0.04	-
38	1.31 ± 0.35	-

Mass transfer in the two contactors is extremely low when compared to literature values. An estimate for the total mass transfer coefficient, k_T, can be evaluated based on $\frac{1}{\Omega_T}$ values and the droplet diameters presented in Figure 4.13.

$$\frac{1}{\Omega_T} = \frac{1}{\frac{1}{k_{aq}a_v} + \frac{1}{k_{org}a_v E_q}} = k_T a_v \tag{4.19}$$

$$\frac{1}{k_T a_v} = \frac{1}{k_{aq}a_v} + \frac{1}{k_{org}a_v E_q} \tag{4.20}$$

Where k_T is a summation of the the aqueous and organic mass transfer coefficients and a_v is the interfacial area, A_{int}, per unit volume, V.

$$a_v = \frac{A_{int}}{V_{aq}} = \frac{\pi D_d^2}{\frac{\pi D_d^3}{6}} = \frac{6}{D_d} \tag{4.21}$$

Droplet diameter in the contactors, D_d, are of the order 10^{-4} m, and $\frac{1}{\Omega_T}$ is approximately 10^{-4} s^{-1}, k_T will be in the order of 10^{-8} m·s^{-1}. This value is extremely low when compared with Miyake's presented values of approximately 10^{-5} m·s^{-1}, given in Section 2.5.3.[66]

The low mass transfer in the system could be explained due to the short rise time of the droplets, as there may not be enough time to overcome the mass transfer resistance. Another possible explanation is the low organic phase hold-up volume present within the contactors. At such a low volume, the interfacial contact between the two phases is small, minimising mass transfer across the interface. Increasing the rotation speed would increase hold-up as droplets are broken down further and are more susceptible to Taylor vortices. Unfortunately this was not possible in the contactors discussed here, due to flooding at high rotation speeds.

4.4 Conclusions

The aim of this chapter was to determine which parameters affect mass transfer in a TCDC and D-cell contactor and to monitor the effects those parameters have on solvent extraction. A comparison between the TCDC and D-cell has also been presented.

A mean rise time, with ranges representing the slowest and fastest observed droplets have been calculated for both contactors, showing a linear increase with u_R^2. The rise time in the TCDC is shown to be greater than that for a D-cell at any given u_R^2 greater than 0.45 $\mathrm{m^2 \cdot s^{-2}}$. This is expected to be because of the curved disc shape in the D-cell allowing droplets to rise under their own buoyancy, compared to the flat disc shape in a TCDC which temporarily traps the droplets.[107, 108]

In order to conclude which parameters had an effect on mass transfer, the Cu(II) concentration in the aqueous raffinate leaving a TCDC after contact with Mextral® 84H/Exxsol™ D80 mixture was measured. It was concluded that flow rate had no significant effect on mass transfer and that tip speed dominates the length of time a droplet spends in the contactor. As such, higher rotational velocities have been confirmed to increase mass transfer in the TCDC and D-cell. The operational parameters for the TCDC and D-cell are limited to square tip speeds between 0.45 and 5.99 $\mathrm{m^2 \cdot s^{-2}}$. At 0.45 $\mathrm{m^2 \cdot s^{-2}}$ and below, very few droplets are produced resulting in a 1 s mean rise time and low mass transfer.

The mass transfer coefficient has been shown to be low for both contactors, with a mass transfer coefficient approximately 1000 times below that seen in literature. This is assumed due to the low organic phase hold-up in the contactor.

CHAPTER 5

Hydrodynamics of an Agitated Tube Reactor

5.1 Methodologies

5.1.1 Operation

The ATR motion is modelled as a sinusoid such as that in Figure 5.1. The equation for the modelled motion can be seen in Equation 5.1 where X(t) is the distance travelled at a time in seconds, t, a is the maximum amplitude in mm, f is the frequency of motion in Hz and β and γ are angular and linear offsets based on the angle and position of the ATR when measuring.[143]

$$X(t) = asin(2\pi ft + \beta) + \gamma \tag{5.1}$$

Motion is driven by air pressure; increasing the air pressure increases the amplitude of the sinusoid. At excessive amplitudes, the motion may cease to be sinusoidal and mechanical knocking may occur.[143] Mechanical knocking happens when the ATR is unable to complete a full sinusoidal path and encounters the restraints of the pistons driving the motion. Motion undergoing mechanical knocking moves in a clipped sinusoidal path, as seen in Figure 5.1.

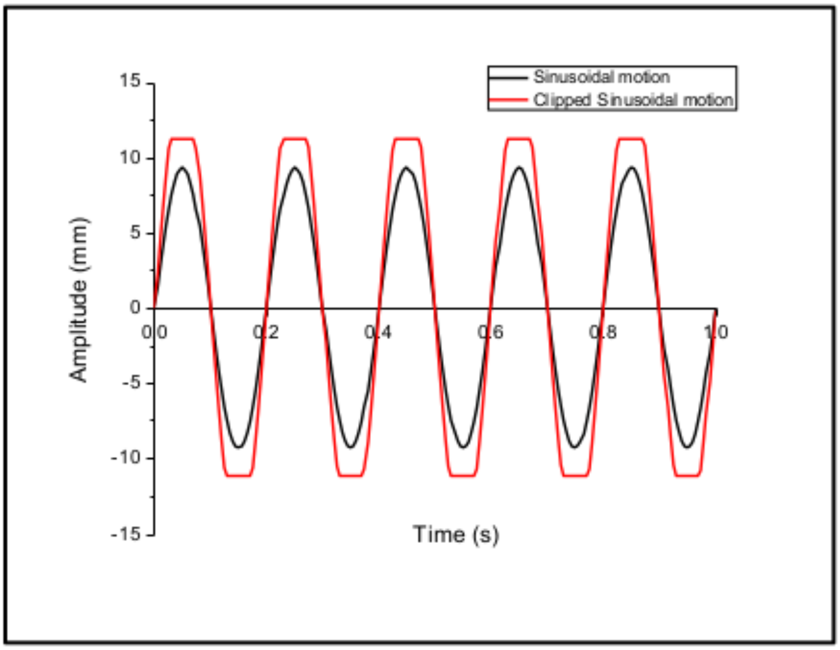

Figure 5.1: *A graph showing how a 5 Hz agitation frequency in the ATR moves under two different air pressures. For an air pressure of 3.5 bar (shown in black), a sinusoidal motion with an amplitude of 9.3 mm is visible. On the other hand, an air pressure of 4 bar (shown in red) exhibits mechanical knocking and therefore a sinusoidal motion clipped at 11.2 mm.*

A regime map by Rice, displaying the shape of motion at a variety of air pressures, is shown in Figure 5.2. It is important to note that different agitation frequencies operate optimally at different air pressures. The distance of travel is also shown by Rice and can be seen in Figure 5.3. Since power per volume is calculated with respect to oscillation amplitude[143] (later described in Section 5.1.6), the optimal air pressure has been chosen as the setting that produces the largest sinusoidal amplitude. A limitation on possible air pressure settings is shown at 4 Hz agitation frequency. This is expected to be a resonance frequency for the ATR, causing an increased amplitude of motion. As such, mechanical knocking is observed at lower air pressures than other frequencies.

Air Pressure (bar)	2	3	4	5	6
4	■ N			■ S	○ S
3.5	✓ N	■ S		✓ S	✓ S
3	✓ N	✓ S		✓ S	✓ S
2.5	✓ N	✓ S	■ S	✓ S	✓ S
2	✓ N	✓ S	✓ S	✓ S	•
1.5	•	•	•	•	•

Agitation Frequency (Hz)

•	No motion or peters out
✓	Normal motion
○	Mechanical lag
■	Mechanical limit (knocking)
S	Sinusoidal motion
N	Not sinusoidal motion

Figure 5.2: *A regime map by Rice describing the shape of motion of the agitated tube reactor.*[143] *For each setting it is determined whether motion is sinusoidal or not. Moreover, the ability for a setting to provide a clean sinusoidal path is shown. This map has been used to determine the settings for the ATR in all experiments in this work.*

Air Pressure (bar)	2	3	4	5	6
4	11.3			11.2	5.0
3.5	11.4	12.7		9.3	4.7
3	10.0	11.8		9.0	3.9
2.5	7.3	9.9	13.9	7.4	2.2
2	5.2	6.3	9.7	4.2	0.0
1.5	0.0	0.0	0.0	0.0	0.0

Agitation Frequency (Hz)

Figure 5.3: *A regime map by Rice describing the amplitude of the agitated tube reactor during its cycle.*[143] *When compared with Figure 5.2, the shape and amplitude of motion for each air pressure setting can be determined. This map has been used to determine the amplitude for the ATR at all frequencies.*

Figures 5.2 and 5.3 show a correlation between maximum amplitude and air pressure. Figure 5.2 has been used to determine the ideal air pressure settings for each agitation frequency. The highest possible air pressure setting at which no mechanical knocking or lag occurs has been chosen. In most cases this is sinusoidal, however this was not possible for a 2 Hz agitation frequency. Table 5.1 shows the ideal air pressure settings for each frequency. The corresponding amplitude taken from Figure 5.3 is also shown and has been used in all future calculations.

Table 5.1: *A table containing the used air pressure for each agitation frequency and the corresponding amplitude in mm. Values have been taken from work on the motion of the ATR by Rice, shown in more detail in Figures 5.2 and 5.3.*[143]

Frequency (Hz)	Air Pressure (bar)	Amplitude (mm)
2	3.5	11.4
3	3.0	11.8
4	2.0	9.7
5	3.5	9.3
6	3.5	4.7

5.1.2 Physical Set-up

Figure 5.4 shows a piping & instrumentation diagram (P&ID) for the set-up described within this section.

5 L of 0.10 M aqueous $Cu(II)(NO_3)_2$ solution and 5 L of the Mextral® 84H/ Exxsol™ D80 mixture were drawn from two reservoirs by a 505S peristaltic pump and a 520S peristaltic pump respectively, both purchased from Watson-Marlow. The two pumps were calibrated at the tubing length and height they were required to pump. Calibration of the peristaltic pumps is explained in Section 4.2.3. JCS mini centrifugal pumps were initially trialled based on their

ability to provide continuous flow. Their difficulty with pumping air proved difficult to overcome and made calibration impossible, so peristaltic pumps were used for flow rate consistency. Though peristaltic pumps provide pulsed flow, the consistency they provide over the centrifugal pumps was deemed more important.

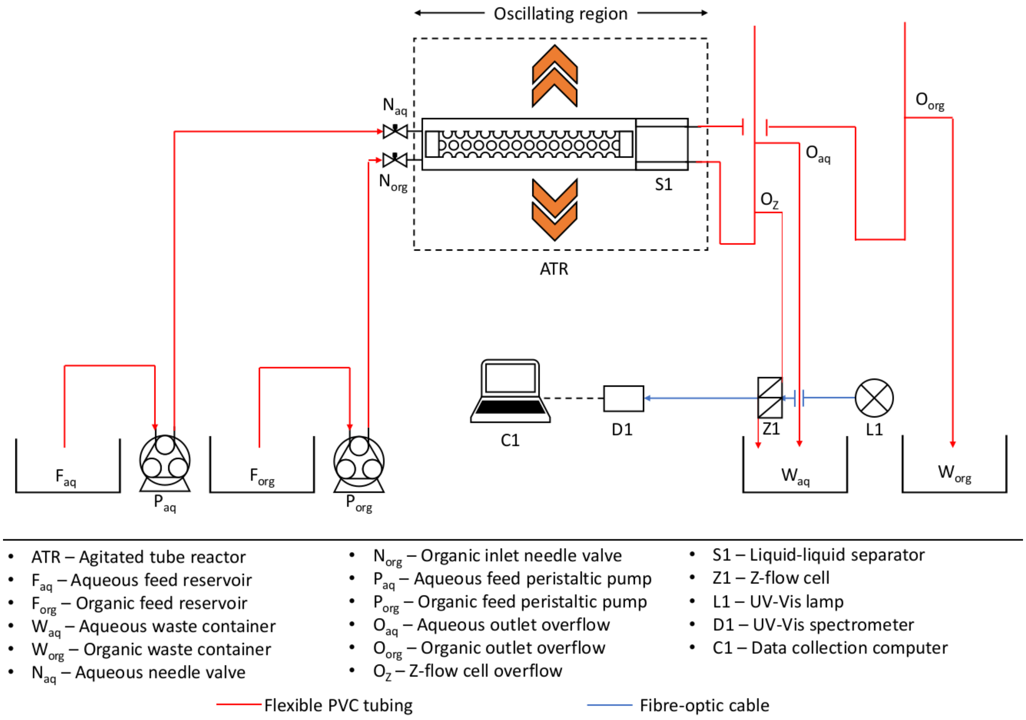

Figure 5.4: *A Piping & Instrumentation Diagram showing the ATR set-up. Red lines depict flexible PVC tubing whilst the blue lines represent fibre-optic cables. Orange arrows show the direction of motion of the ATR with respect to the ATR tube.*

Both phases were pumped through 1/8 inch interior diameter (ID) flexible PVC tubing with 1/4 inch outer diameter (OD) into a PERPSEX ATR tube. Flow within a single ATR tube is co-current, though future work with the ATR would see a partial counter-current flow across multiple tubes. Using a PERSPEX tube, attached to the top of the ATR, instead of the existing stainless steel tubes allowed for better visibility during experiments. Attaching the PERSPEX tube to the top of the ATR ensured the shaking motion was consistent with that experienced by Rice.[143] The PERSPEX ATR tube consisted of a hollow PERSPEX rod with a length of 30.0 cm and inner and outer diameters of 2.2 cm and 3.0 cm respectively.

A stainless steel inlet plate was designed to attach to the start of the PERSPEX tube using the same tri-clamp and sanitary gasket setup as the pre-existing tubes. The plate, shown in Figure 5.5, consists of two 2.5 cm lengths of stainless steel tubing with the same dimensions as the flexible PVC. The ends of the stainless and PVC tubing were connected with 1/4 inch to 1/4 inch stainless steel Swagelok® needle valves. Needle valves were used to ensure no leakage occurred if flexible PVC tubing needed to be removed for pump calibration but were left open during experiments. The two inlets were positioned such that the organic phase entered the PERSPEX tube at the lowest point of the tube and the aqueous phase at the highest. Positioning the inlets in such a way forces the two phases to pass through each other and aids dispersion.

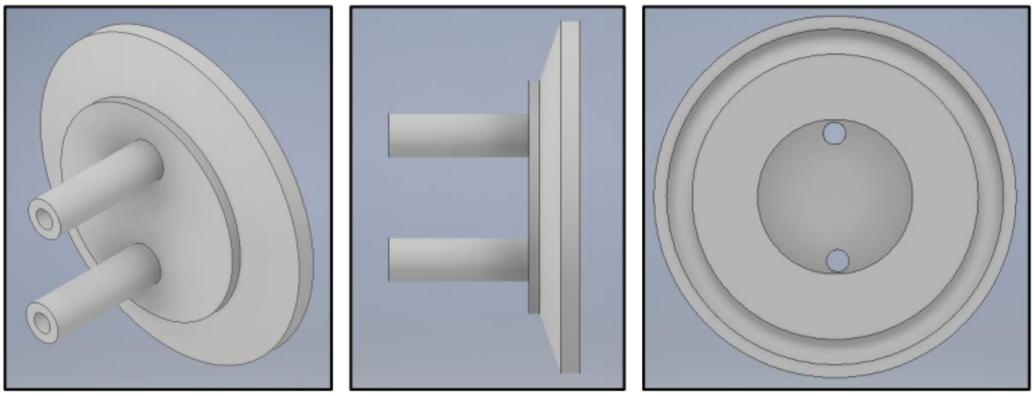

Figure 5.5: *Computer Aided Design (CAD) images of the ATR tube inlet. The inlet consists of two lengths of 1/8 inch ID stainless steel tubing, one for each phase. The inlet connects to a PERSPEX ATR tube with the use of a rubber sanitary gasket.*

The PERSPEX ATR tube contains the free moving agitator bar seen in Figure 5.6. The bar is constructed from a folded stainless steel sheet with an array of holes along the shaft to improve mixing. The length of the bar is 30 cm and the diameter is 1.5 cm. Feet on each end of the bar raise the bar from the base of the tube and protect the tube wall. Since the bar is longer than the

PERSPEX tube, extensions had to be added to each end. This is consistent with the existing ATR tubes, which are the same length as the PERSPEX tube.

Figure 5.6: *The agitator bar in the ATR tube. Motion of the bar influenced by the shaking of the ATR causes the two liquids to disperse. This is facilitated by the holes along the length of the bar. The feet on the each end of the bar raise it from the base of the tube to prevent damage.*

An air vent, constructed from a probe inlet designed to fit the ATR, was included after the tube to open the ATR to atmospheric pressure and allow the flow of air. The probe inlet also acted as the end extension to the tube. The liquid-liquid separator described in Section 5.1.4 was attached to the end of the PERSPEX tube via a tri-clamp and sealed with a sanitary gasket. The separator consists of two 1/8 inch ID outlets, each consisting of a 2.5 cm length of stainless steel connected to 1/8 inch ID flexible PERSPEX tubing via a 1/4 inch to 1/4 inch Swagelok® union. The two phases, now separated, enter an overflow lute such as the one shown in Figure 5.7. The lutes were open to atmospheric pressure to equalise the pressure with that in the ATR tube. The height of the overflow was set in accordance with Equation 5.2. In principle, the height of the aqueous overflow should be in line with the height of the liquid-liquid interface within the ATR tube and the organic phase slightly above the height of the organic phase (as the aqueous layer is more dense than the organic layer, the average density over Δh in the ATR tube is higher than that in the overflow tubing). In practice, as there are some pressure losses through the overflow lute, the overflows are below the calculated height and were adjusted based on the outflow rate of the overflow into two waste reservoirs.

$$\Delta P = \rho g \Delta h \tag{5.2}$$

The aqueous outlet consisted of two overflows: one draining directly into a waste container, the other passing through a Z flow-cell. The Z flow-cell was intercepting the path of fibre optic cables carrying UV-visible light as described in Section 3.2.1. This allowed for measurement of the aqueous phase concentration as described in Section 3.2.1.

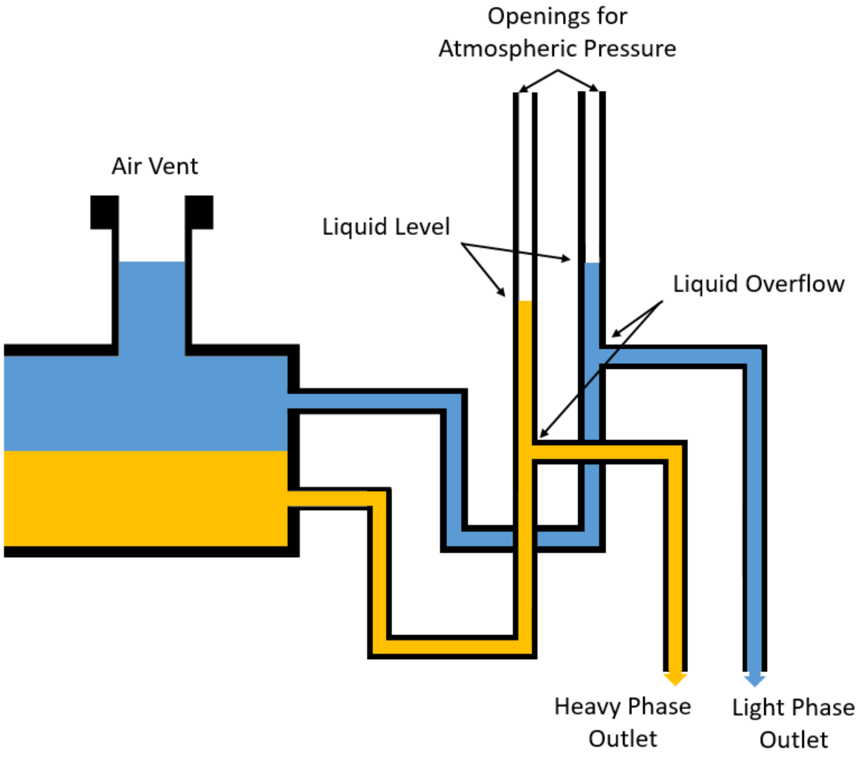

Figure 5.7: *A schematic of the overflow system used. Two overflow lutes, positioned after the separator, have been used to isolate the two phases.*

5.1.3 Air Vent

The necessity for an air vent in the tube was determined by monitoring liquid height within a PERSPEX ATR tube. A PERSPEX tube with no vent, a single inlet and a single outlet was attached to the top of the ATR. Water was pumped into the ATR tube through the single inlet with a Watson-Marlow 505S peristaltic pump. The single outlet consisted of an adjustable overflow lute.

Measurements were taken at three flow rates, 40 mL·min^{-1}, 25 mL·min^{-1} and 10 mL·min^{-1} with four overflow heights for each. The four heights were set relative to the base of the ATR tube OD and were 0.0 cm (the bottom of the ATR tube), 1.1 cm (the centre of the tube) and 2.2 cm (the top of the tube OD) and -2.0 cm below the ATR tube. Outflow rates were also recorded to ensure a steady state had been reached. This was achieved by measuring the volume of water exiting the outlet with a measuring cylinder over 60 s. Each measurement was recorded three times to ensure repeatability.

A Canon Powershot SX280 HS digital camera, shown in Figure 5.8, was attached to the ATR to allow it to remain at a constant distance from the ATR tube. A length of 1/4 inch OD PVC flexible tubing was attached to the camera button with masking tape so that images could be taken whilst the camera moved. Pulling on the flexible tubing triggered the camera, thus taking a photograph.

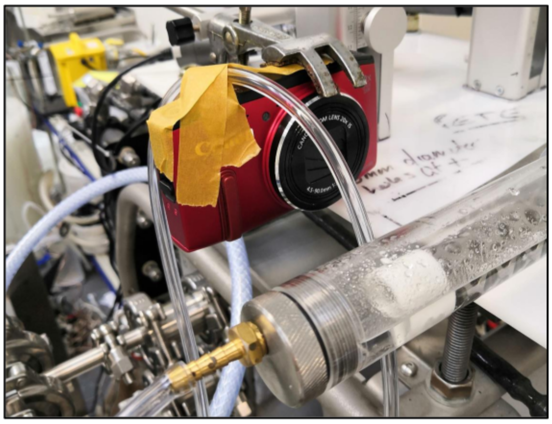

Figure 5.8: *A setup for remotely activating the camera. A Canon Powershot SX280 HS digital camera was held in place with a clamp stand screwed to the base plate beneath the PERSPEX tube. The camera was positioned such that the centre of the camera lens lined up with the centre of the PERSPEX tube. In order to trigger the camera while the ATR was in motion, a length of flexible 1/4 inch OD tubing was taped to the button. The tubing could easily be accessed and pulled while the ATR was in motion, triggering the camera. The camera was set to take rapid images such that photos were taken at a range of positions on the ATR's cycle.*

Images were analysed using ImageJ image processing software. The height of the liquid surface from the base of the ATR was measured relative to the known width of the PERSPEX ATR tube to calibrate each image. The surface height was measured at 40 points along the length of the image. This was repeated for 3 images per set of parameters and an average height value calculated from those 120 points. Figure 5.9 shows example measurements of the calibration width and surface height. A binary image has been used to measure surface height as it improves clarity of the interface.

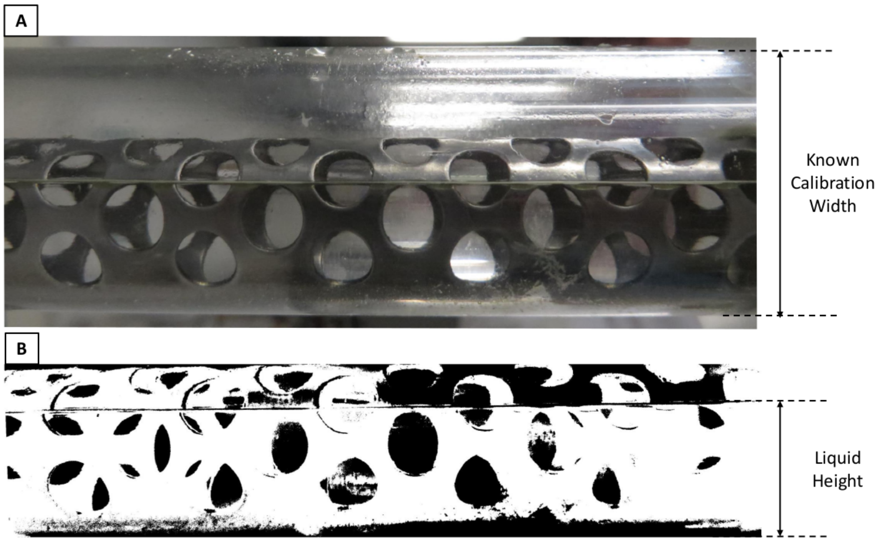

Figure 5.9: **(A)** *A close up image of the PERSPEX ATR tube containing the agitator bar. This image was used to calibrate the length scale.* **(B)** *A cropped, binary image of the ATR tube. Converting the image to binary allowed for easier viewing of the liquid-air interface. This image was used to measure the height of the liquid in the tube.*

An 1/8th inch hole was drilled into the top of the PERSPEX tube to act as a vent. The same process as the non-vented tube was conducted on the newly vented tube.

5.1.4 Separator Designs

The initial design of the separator was purposefully simple and was designed to allow the two phases to separate under gravity via Stokes' law, as shown in Equation 2.30. The length of the separator is long enough such that a droplet of size 150 µm[69] can be separated from the bottom wall to the interface at 200 mL·min^{-1}. The droplet sizes and flow rates chosen are extreme values, far from the ranges expected from the experiments listed in this work. Starting with Stokes' law[70] shown in Equation 5.3, the separation velocity can be calculated.

$$u_s = \frac{g\Delta\rho D_d^2}{18\mu_c} \tag{5.3}$$

Using the equation for linear distance in Equation 5.4 and rearranging to achieve Equation 5.5, the time for vertical separation can be obtained.

$$h = \frac{(u_0 + u_s)}{2} t_s \tag{5.4}$$

Where h is the distance from the bottom wall of the ATR tube to the liquid-liquid interface, u_0 is the initial velocity (equal to zero) and t_s is the separation time.

$$t_s = \frac{2h}{u_s} = \frac{36h\mu_c}{g\Delta\rho D_d^2} \tag{5.5}$$

The product of separation time and flow velocity, u_f, gives an indication of the maximum separation length and therefore the minimum separator length, L_s.

$$L_s = u_f t_s = \frac{36h\mu_c}{g\Delta\rho D_d^2} u_f \tag{5.6}$$

Using the values h = 1.1x10^{-2} m, μ_c = 8.90x10^{-4}, Pa·s,[127] g = 9.81 m·s^{-2}, ρ_{aq} = 997 kg·m^{-3},[127] ρ_{org} = 750 kg·m^{-3}, D = 150 µm and u_f = 8.8x10^{-3} m·s^{-1} gives a value of $L_s \approx 3$ cm.

The separator is required to work under moving conditions and therefore sloshing of the liquid-liquid interface needs to be reduced. Positioning four baffles along the inner wall of the separator at 90° increments can help reduce the sloshing. Baffles should be approximately 1/12th the diameter of the tube and therefore have a width of 1.8 mm. The constructed separator, displaying the interior baffles and the outlet tubing, can be seen in Figure 5.10.

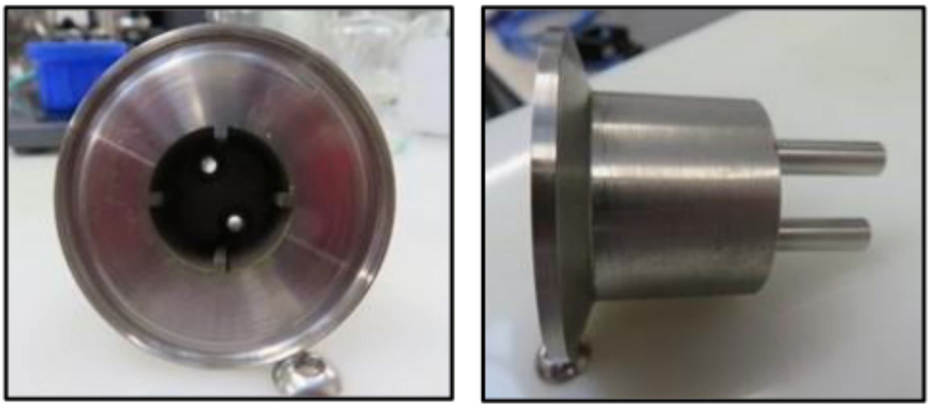

Figure 5.10: (Left) *Front view of the stainless steel liquid-liquid separator. The four baffles are positioned at 90° increments to reduce sloshing in the separator.* **(Right)** *Side view of the separator. Two 1/4 inch OD, 1/8 inch ID tubing outlets are shown to the right of the main separating unit.*

5.1.5 Imaging

Droplet Imaging for Varying Fill Volumes

A Photron Fastcam SA5 high-speed camera was positioned at the end of a PERSPEX ATR tube designed with transparent caps in place of an inlet and outlet. No liquid flow-through was permitted. A diagram of this setup can be seen in Figure 5.11.

The ATR tube was initially completely filled with 50% water and 50% Exxsol™ D80, giving a fill volume of 100%. This was subject to 5 integer agitation frequencies from 2-6 Hz and recorded at 6000 fps and a resolution of 1024x896. The two phases were agitated for 2 minutes before recording began to ensure the best possible mixing, after which a 4 s recording was taken. This process was then repeated for 1:1 organic:aqueous ratios corresponding to total liquid volumes of 25%, 50% and 75% the volume of the tube.

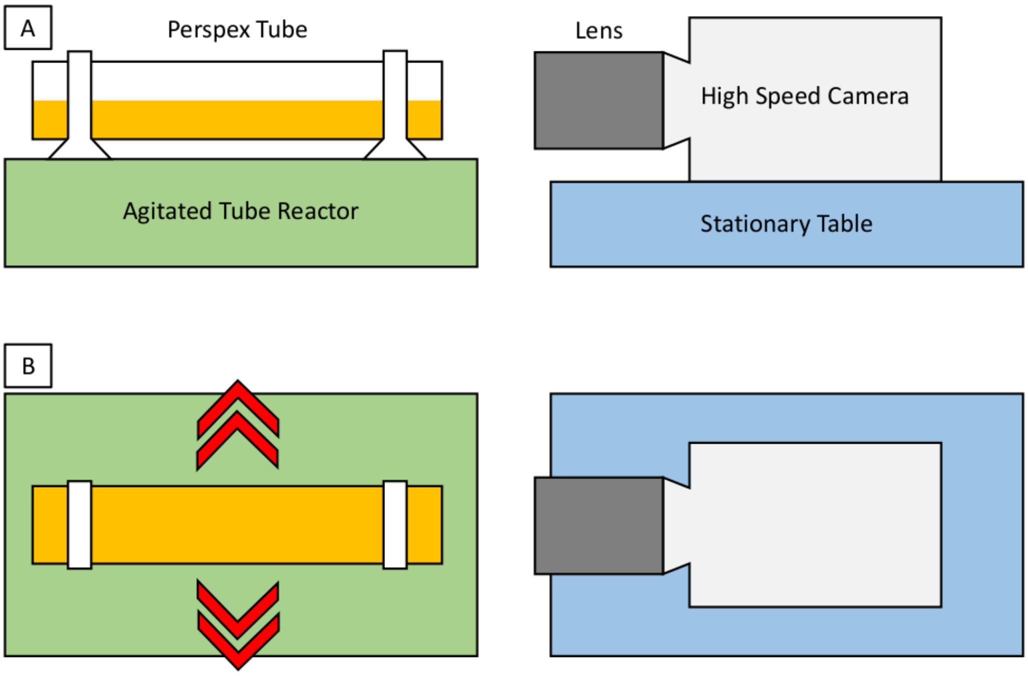

Figure 5.11: **(A)** *Side view of the high speed camera setup. The high speed camera, on a stationary table, is pointed at the end of the PERSPEX ATR tube which is attached to the top of the ATR.* **(B)** *Top view of the high speed camera setup. The red arrows show the direction of motion of the ATR.*

Obtaining quantitative data was exceptionally difficult for multiple reasons and as such, images have only been used qualitatively. Due to the transparency of both phases, a significant contrast was impossible to set up during image processing. Another issue is caused by the agitator bar itself. When lights are placed behind the camera, the stainless steel construction of the bar creates glare, whereas the bar provides a silhouette when the lighting is positioned behind the ATR tube and facing the camera.

Focus beam reflectance measurement (FBRM) and particle video microscopy (PVM) were considered as methods for sizing droplets within the ATR. Though FBRM produces a smaller than accurate size distribution for liquid droplets,[144] it can be used to provide a relative distribution compared with other settings and parameters. However, the fragile FBRM probe could be damaged when subject to the motion of the ATR tube and was therefore deemed unsuitable.

5.1.6 Power per Volume

The power per unit volume of an agitator is a useful unit when considering scale-up. It can also be used as a comparison between agitation systems. A greater power per volume should provide higher dispersion and therefore improved mass transfer. In practice, the power consumption of the fluid will be dampened by the viscous and turbulent forces.

An estimate for the power per volume can be gauged from the power, P_w, and kinetic energy, E_k, relation shown in Equation 5.7, where E_k is the kinetic energy of the agitator bar and T_{osc} and f are the period and frequency of oscillation respectively.

$$P_w = \frac{E_k}{T_{\mathrm{osc}}} = E_k f \tag{5.7}$$

The use of u_{max} in the definition of E_k shown in 5.8 gives a maximum kinetic energy and therefore a maximum power per volume. This definition has been substituted into 5.7 to give Equation 5.9. It is assumed here that all kinetic energy in the system is transferred into the liquid. While this is not the case, it is a necessary assumption as it is extremely difficult to calculate energy loss due to friction or the agitator's collision with the walls.

$$E_k = \frac{1}{2} m_A u_{max}^2 \tag{5.8}$$

$$P_w \propto m_A u_{max}^2 f \tag{5.9}$$

The mass of the agitator bar, m_A, is given by Equation 5.10 as the product of the density and volume of the agitator bar, ρ_A and V_A respectively. Since the bar is constructed from stainless steel, a density of 7800 kg·m^{-3} has been used.

$$m_A = \rho_A V_A \tag{5.10}$$

V_A has been calculated using the volume equation for a hollow cylinder shown in Equation 5.11, where $\mathrm{L_A}$ is the length of the bar and $\mathrm{R_{A,ID}}$ and $\mathrm{R_{A,OD}}$ are the inner and outer radii of the bar respectively.

$$V_A \propto L_A \left(R^2_{A,OD} - R^2_{A,ID}\right) \tag{5.11}$$

Substituting Equations 5.10 and 5.11 into Equation 5.9 yields Equation 5.12.

$$P_w \propto \rho_A L_A u^2_{max} f(R^2_{A,OR} - R^2_{A,IR}) \tag{5.12}$$

The maximum velocity of the ATR during its period of motion, $\mathrm{u_{max}}$, is shown by Rice[143] to be at the centre point of its amplitude, a. Equation 5.13 is a basic form of the distance/velocity relation.

$$s = \left(\frac{u_0 + u_{max}}{2}\right) t \tag{5.13}$$

Since the ATR begins its period from a stationary position and reaches its maximum velocity at the midpoint of its amplitude, $\mathrm{v_0}$ is 0 $\mathrm{m{\cdot}s^{-1}}$ and s is $\frac{a}{2}$ m. The time at which the ATR reaches $\mathrm{u_{max}}$, t, is assumed to be $\frac{1}{4}$ of its total period, T.

$$\frac{a}{2} = \left(\frac{u_{max}}{2}\right)\frac{T}{4} = \frac{u_{max}}{8f} \tag{5.14}$$

Rearranging Equation 5.14 gives an expression for the maximum velocity as a function of amplitude and agitation frequency. This is shown in Equation 5.15. This has then been substituted into 5.12 to reach Equation 5.16.

$$u_{max} \propto af \tag{5.15}$$

$$P_w \propto \rho_A a^2 f^3 L_A (R^2_{A,OD} - R^2_{A,ID}) \tag{5.16}$$

Power Number, N_P, is a dimensionless quantity defined as the ratio of resistance and inertial forces. For Reynolds numbers greater than 1000, power number is shown to be constant and can be calculated using Equation 5.17.[143, 145]

$$N_P = \frac{P_w}{\rho_A a^2 f^3 L_A D_A^2} \tag{5.17}$$

Power per volume can therefore be calculated by rearranging Equation 5.17 and dividing by the liquid volume, V_L.

$$\frac{P_w}{V_L} = \frac{N_P \rho_A a^2 f^3 L_A}{V_L}(R_{A,OD}^2 - R_{A,ID}^2) \tag{5.18}$$

A value for N_P has been determined via CFD by Rice et al. (2017) such that N_P=0.125.[143]

5.1.7 Droplet Size Estimates

Droplet size estimates have been calculated using the Weber number, N_{We}, described in Section 2.8.1. Equation 2.19 has been used to calculate a maximum stable droplet size.

$$D_{max} \propto D_A \left(\frac{\sigma}{\rho_c \omega^2 D_A^3}\right)^{\frac{3}{5}} \propto D_A \left(\frac{\sigma}{\rho_c a^2 f^2 D_A^3}\right)^{\frac{3}{5}} \tag{5.19}$$

Where ω is the agitator speed, estimated to be equal to the agitation frequency, f, multiplied by the amplitude of oscillation, a. σ is the interfacial tension of the system. This has been estimated as the interfacial tension for a water/dodecane system since Exxsol™ D80 is a mixture of long chain alkanes, predominantly dodecane. D^I is the bar diameter, 0.015 m.

Due to the proportionality, the droplet sizes will be out by a factor of the proportionality constant. They will however show a general trend which can be used to determine which operating conditions are optimal. The volume fill fraction is also not able to be accounted for by the Weber number estimate.

5.1.8 Sloshing

Wave Amplitude

Amplitude of the sloshing motion was measured using the images obtained from Section 5.1.5 and the high speed camera setup depicted in Figure 5.11.

The wave amplitude was defined as the maximum displacement of the liquid-air surface up the side of the tube during sloshing. This is measured as the difference between the highest and lowest point of the surface. Images were recorded over the multiple periods of the ATR's cycle and measurements were recorded from photographs in which the ATR had reached its own amplitude, as this is the position at which the sloshing height is greatest. Photographs were analysed using the image analysis software ImageJ. An example of a measurement can be seen in Figure 5.12.

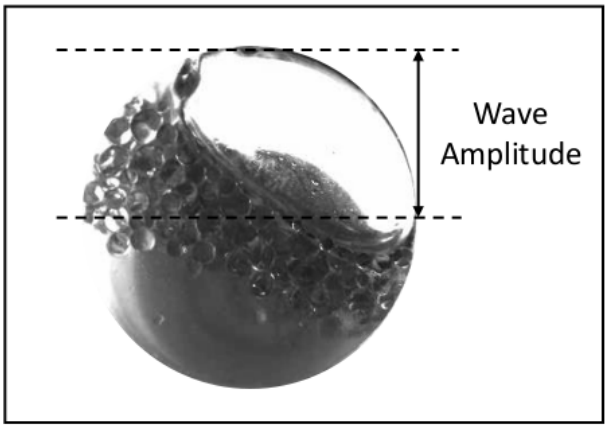

Figure 5.12: *Example measurement of the wave amplitude taken at 50% fill volume and a 2 Hz agitation frequency. The wave amplitude is measured as the difference in height between the liquid at the two walls.*

5.2 Results & Discussions

5.2.1 Air Vent

Figure 5.13 shows the necessity for an air vent in the ATR tube. Figure 5.13(A) describes a system with no air vent. It shows the variation in liquid height in the ATR tube with changing overflow height. This is shown for three flow rates. The liquid height shows no significant change across all lute heights and flow rates. Since air is not allowed to enter or escape the ATR tube, there is no room for the liquid surface to rise as this would increase the pressure in the system. As a result, liquid leaves the outlet at the same rate as it enters the inlet, regardless of overflow height.

A system with a vented ATR tube is shown in Figure 5.13(B). The inclusion of a vent sets the pressure in the ATR tube to atmospheric pressure and causes it to be equal to that in the overflow lute. Air is able to enter and escape the tube through the vent allowing a variation in the surface height. Increasing the height of the overflow therefore forces the liquid surface to rise until pressure at the outlet is great enough to reach the overflow. This change in height can be seen in 5.13(B). Beyond a height of 0 cm, the ATR tube began to overflow. Friction in the outlet tubing causes a decrease in lute pressure, forcing the surface to be lower than that in the ATR tube. As a result, values for 15 and 30 mm were not recorded as fluid leaked from the vent. A value at -10 mm was included to ensure another data point.

Figures 5.14(A) and 5.14(B) compare liquid height in a vented and unvented tube respectively. The liquid in the vented tube can be seen to be deeper that that in the unvented tube.

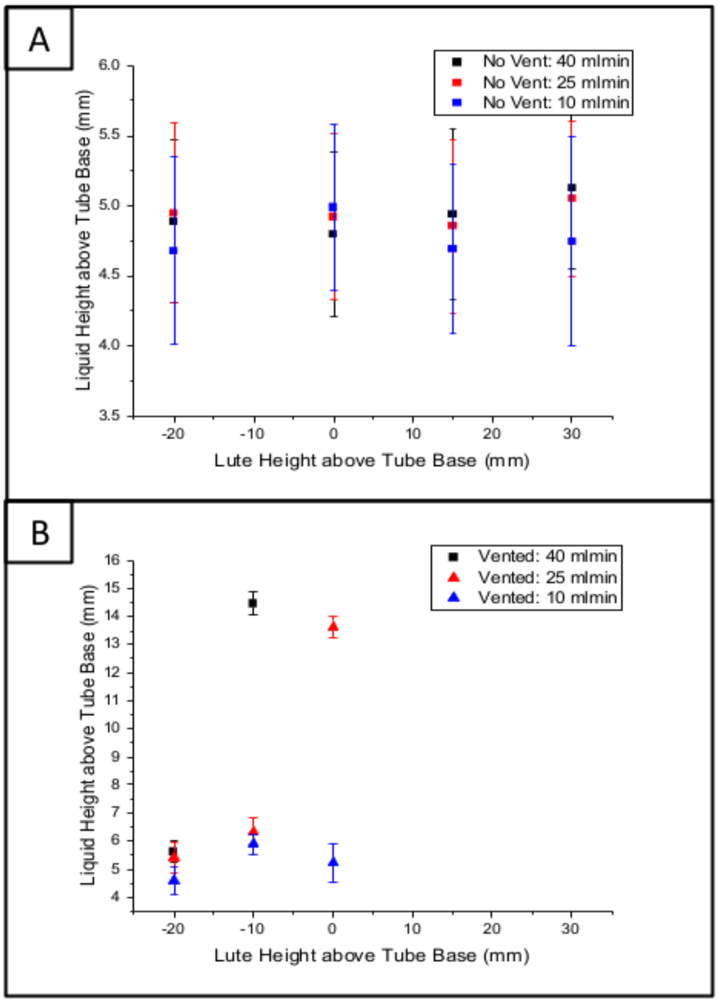

Figure 5.13: **(A)** *Plot showing the variation in height of the liquid surface with a change in overflow height for a non-vented system. Without a vent, air is unable to leave the tube liquid is forced to leave the tube at the same rate as it enters. As such, no height variation is present.* **(B)** *Plot showing the variation in height of the liquid surface with a change in overflow height for a vented system. Venting the system allows air to pass in and out of the tube, allowing the liquid surface to rise to the height of the overflow. No data is shown beyond the 0 mm lute height as liquid begins to overflow through the vent.*

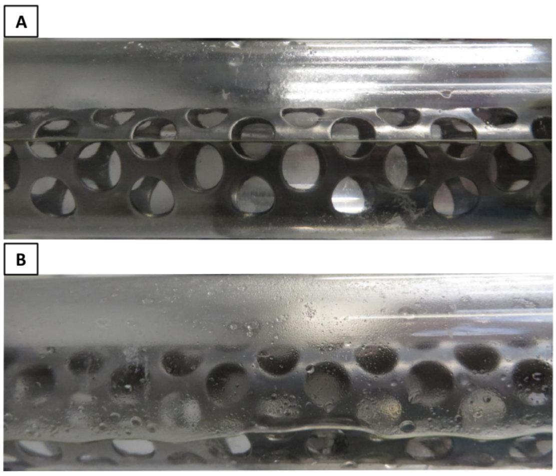

Figure 5.14: **(A)** *Liquid height in an ATR tube with an air vent. The liquid height is allowed to change as air is able to enter and leave the tube.* **(B)** *Liquid height in an ATR tube without an air vent. The liquid height is unable to change as the air in the tube is not able to escape. Liquid therefore enters and leaves the tube at the same rate, regardless of outlet lute height.*

5.2.2 Variable Fill Fraction

Based on underwhelming mass transfer results using a full ATR tube, the decision was made to vary the volume of liquid within the ATR tube. The inclusion of an air phase may improve the ability of the liquid phases to move and disperse. Figure 5.15 shows a scale image depicting the heights of the liquids at different fill volume, $\mathrm{V_L}$. Regions depicted in white, blue and yellow represent the air, organic and aqueous phases respectively. Percentages represent the fill fraction $\frac{V_L}{V_T}$

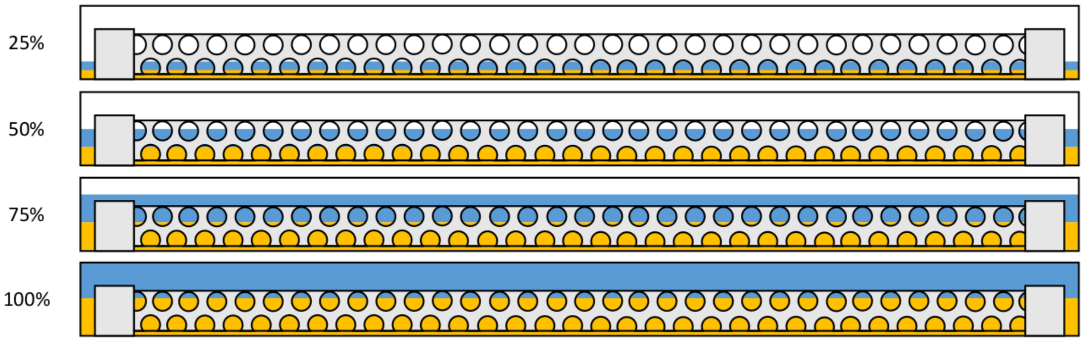

Figure 5.15: *A scale image showing the liquid height relative to the agitator bar at 25%, 50%, 75% and 100% liquid fill volume. Regions depicted in white, blue and yellow represent the air, organic and aqueous phases respectively.*

Droplet Imaging

The plot shown in Figure 5.16 qualitatively looks at the dispersion of droplets within the ATR tube. The high-speed camera was positioned at the end of the ATR tube as shown in Figure 5.11. An attempt was made to position the camera pointing towards the side of the tube, however due to the motion of the ATR, the camera had to be positioned too far away from the tube and droplet resolution was impossible.

At a fill volume of 100% the tube contains no air and is completely filled. At this fill volume no droplets are visible. Any mass transfer must therefore occur over a large liquid-liquid interface with small relative surface area. The case in which 75% of the tube is filled with liquid and 25% air, more droplets are visible around the interface, though little dispersion is seen in the bulk liquid phases.

When looking at the 25% and 50% fill volumes, a distinct number of droplets are visible in frequencies greater than or equal to 4 Hz. The 4 and 5 Hz cases show the greatest number of droplets and would therefore be expected to provide the best mass transfer.

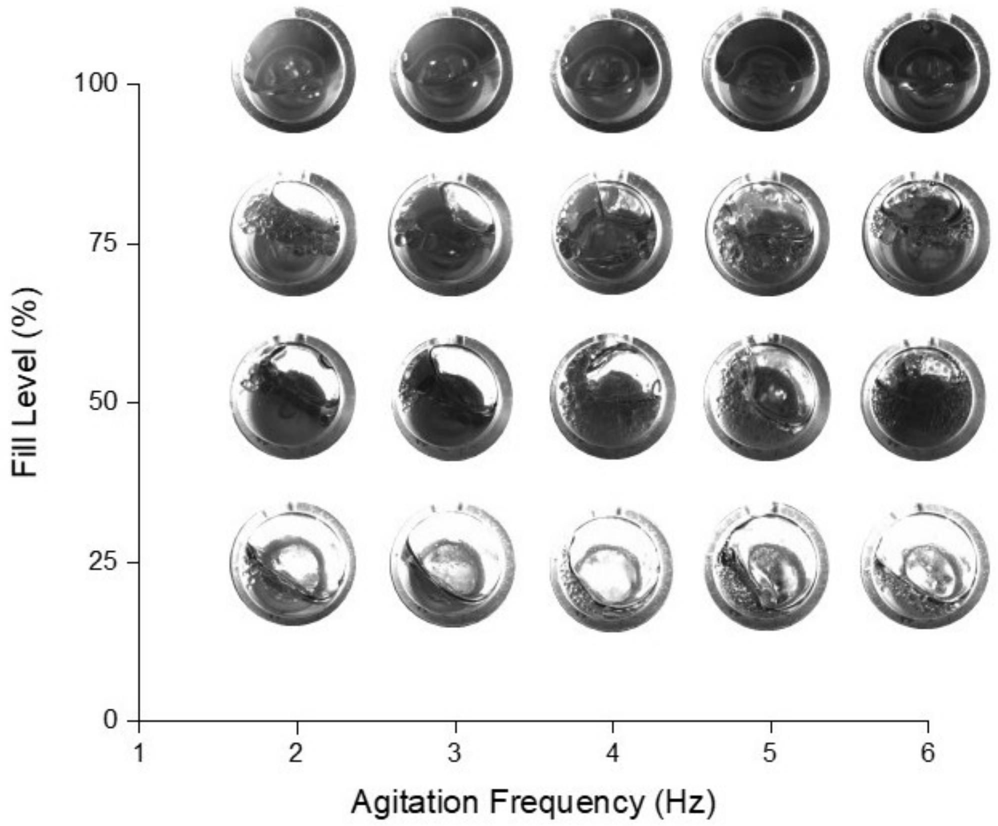

Figure 5.16: *A chart containing high-speed camera images of the ATR tube at a variety of fill volumes and agitation frequencies. The plot charts agitation frequency against percentage fill level to qualitatively review the level of dispersion within the ATR tube. Each photograph was selected at the amplitude of the ATR. No droplets are seen in a tube with no air and 100% liquid and most droplets are seen in the 25% and 50% cases. The increased ability for the liquid to slosh at lower liquid fill may be the cause.*

The images shown in Figure 5.17, taken with the setup described in 5.8, show snapshots of droplets at different ATR parameters. Two phases are present in the tube, a colourless aqueous water phase and an organic kerosene phase dyed with the organic dye Sudan blue.

Figure 5.17(A) shows the effect of agitation frequency on the formation of droplets in the tube. Each image is taken with a liquid fill volume of 50% and the image taken so that the liquid was sloshing up the side of the tube nearest the camera. Figure 5.17(A) appears to indicate the highest number of droplets are present at 5 Hz and the fewest at 3 Hz, with 4 Hz exhibiting a droplet count between the two. Figure 5.17(B) shows the effect of liquid fill volume at a constant agitation frequency. 5 Hz was chosen as the agitation frequency as it has been shown to be the best frequency for dispersing the organic phase and forming droplets. Liquid fill volumes of 25% and 50% show similar quantities of droplets and will require further experimentation with mass transfer to determine which is best. The 75% case shows a distinct reduction in droplet number. Both Figures 5.17(A) and (B) are consistent with the corresponding images shown in Figure 5.16.

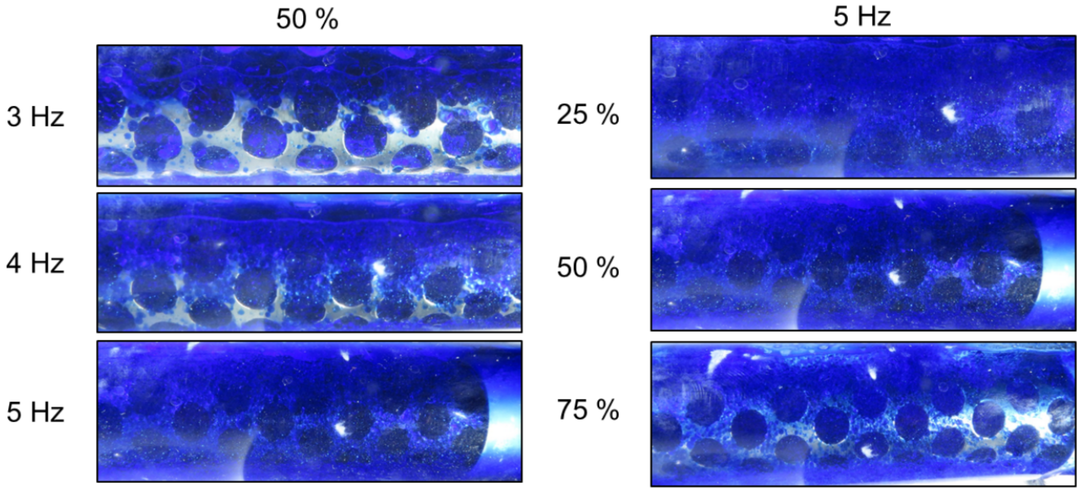

Figure 5.17: *Droplet dispersion images taken with a Canon Powershot SX280 HS digital camera.* **(Left)** *Three agitation frequencies, all at a constant 50% fill volume are compared. Most droplets are seen at 5 Hz, while 3 Hz appears to provide least.* **(Right)** *Three fill volumes, all at a constant 5 Hz agitation frequency are compared. While 75% volume shows a distinct reduction in droplet numbers compared with the other two cases, the 25% and 50% liquid fill volumes are difficult to differentiate and show no significant qualitative difference.*

No real conclusion can be drawn from this qualitative data and further research into the mass transfer capabilities of each setting is needed. This will be seen in the subsequent chapter.

Power per Volume Calculations

It is expected that the power per unit volume for the agitator bar would increase with a reduction in liquid volume. This can be seen in Figure 5.18, in which the power per volume has been plotted against agitation frequency for a number of liquid fill volumes. As expected, for a given agitation frequency, power per volume is inversely proportional to volume such that: 25% > 50% > 75% > 100%. The power per volume has been calculated with Equation 5.18. A value for the power number, N_P, for the agitator bar has been taken from an unpublished paper by Rice et al., in which a computational fluid dynamics model of the ATR is used to obtain a value of ≈ 0.125. This value is calculated for a system with a Reynolds number greater than 1000.

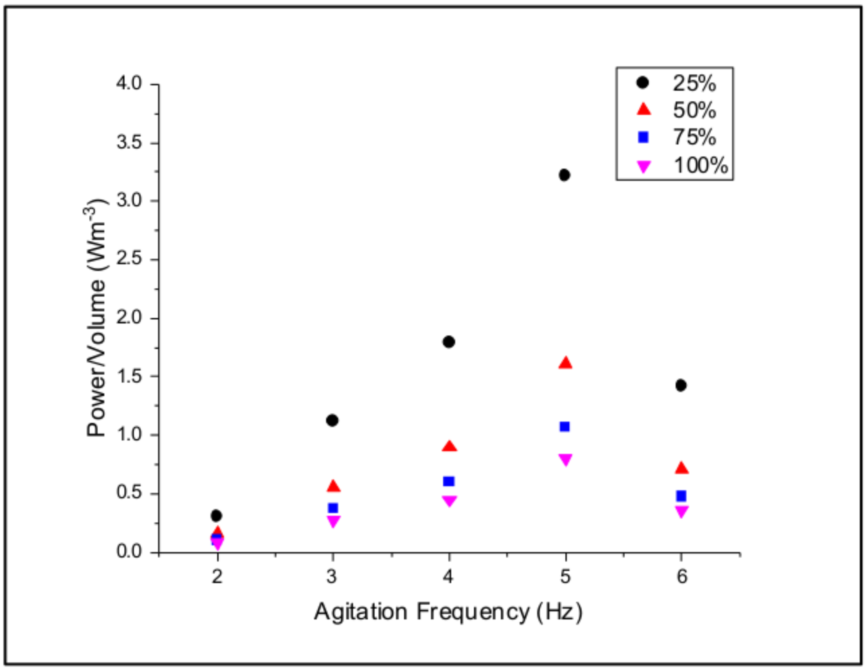

Figure 5.18: *Plot of power per unit volume against agitation frequency for four liquid fill volumes. A maximum can be found at 5 Hz. The drop in power per volume at 6 Hz can be attributed to the drop in amplitude found at this setting. All other frequencies have will have a dominant frequency term,* f^3.

At a given frequency, the amplitude, and therefore maximum velocity, is constant. Power per volume is therefore inversely proportional to liquid volume such as seen in Equation 5.20.

$$\left.\frac{P_w}{V_L}\right|_f \propto \frac{1}{V_L} \tag{5.20}$$

For a given volume, power per volume reaches a maximum at 5 Hz. The drop in power per volume at 6 Hz is due to the significant drop in amplitude at this frequency compared with the other cases. The square of the amplitude present in Equation 5.18 amplifies this difference. In other cases, the variation in amplitude is less pronounced and the dependency on the frequency term, f^3, becomes dominant.

In reality, the power consumption described by Equation 5.18 will not all contribute to the dispersion of the fluids. Agitator power will also be consumed by the turbulences and viscosities associated with the liquids. The trend does however appear to follow that of the droplets images shown in Figures 5.16 and 5.17.

Wave Characteristics

The wave amplitude of the liquid in the ATR was measured using images taken by a high speed camera. The maximum height difference of the liquid was measured and plotted against agitation frequency in Figure 5.19(A) for three liquid fill volumes. 100% fill volume has not been included here due to the lack of liquid-air interface.

For a given fill volume, the wave amplitude follows the same trend as the power per volume plot in Figure 5.18 and the inverse of the maximum droplet size trend in Figure 5.20.

Though the 75% fill volume shows the expected reduction in wave amplitude, the 25% and 50% cases are extremely similar across the range of frequencies. This is in close agreement with the photographs shown in Figure 5.17(B), in which the 25% and 50% liquid fill volumes show similar dispersion. This indicates that the shear forces created when the liquid sloshes through the agitator bar are an important part of droplet dispersion in the ATR.

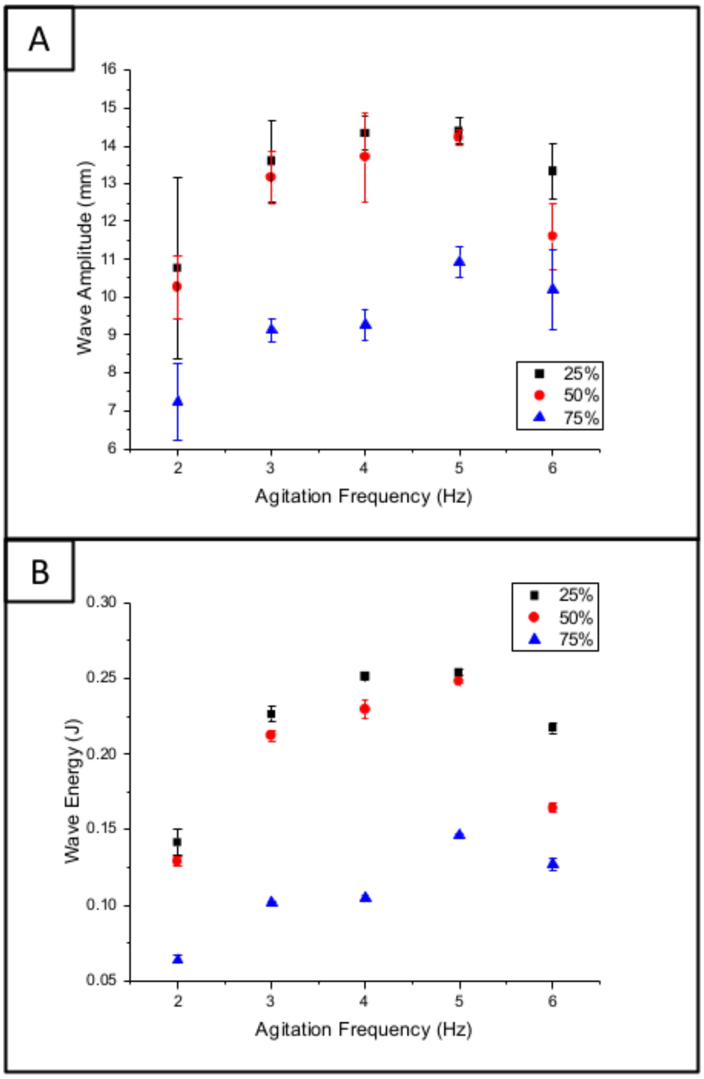

Figure 5.19: **(A)** *Plot of wave amplitude during sloshing and agitation frequency for three liquid fill volumes. The 25% and 50% cases show extremely similar sloshing amplitudes and the 75% case has far less motion. For a given volume, the trend follows that of the power per volume plot in Figure 5.18.* **(B)** *A plot demonstrating the energy associated with the sloshing liquid-liquid interface at five agitation frequencies and three liquid fill volumes. The interface has been treated as a wave. 25% and 50% show extremely similar trends, whilst 75% shows little motion. A maximum is seen at 5 Hz for all liquid fill volumes*

The energy in the sloshing system can be described by Equation 5.21. At the maximum displacement from the liquid's resting position, the kinetic energy,

E_k can be assumed equal to zero, and all energy stored as potential energy, E_p.

$$E_T = E_k + E_p \tag{5.21}$$

Fluid pressure, P_f, defined in Equation 5.22, can be expressed as an energy per unit volume. Using these two equations together gives the energy expression in Equation 5.23, in which the energy in the system is described based on the liquid fill volume, V_L, and the displacement of the liquid-air surface, Δh.

$$\Delta P_f = \rho g \Delta h \tag{5.22}$$

$$E_T = E_p = V_{\mathrm{L}} \Delta P_f = \rho g V_{\mathrm{L}} \Delta h \tag{5.23}$$

The measurement of the wave amplitude, Δh, is described in Section 5.1.8, and the results are presented in Section 5.2.2.

The energy associated with the sloshing waves is shown in Figure 5.19(B). The plot follows the same trend as the sloshing waves, showing a maximum at 5 Hz for all fill volumes. 25% and 50% show an extremely similar trend.

Droplet Size Estimates

Figure 5.20 presents estimates of the maximum stable droplet diameter in the ATR, calculated using the Weber number as described in Section 5.1.7. Droplet size is seen to follow the inverse of the power per volume and wave amplitude trends. As expected, a higher power per volume will induce further break up of droplets in the tube, potentially improving mass transfer. The similarities with wave amplitude measurements implies that sloshing is an important factor in the droplet breakup.

As with the power per volume calculations, the droplet size is a function of agitation frequency and oscillation amplitude. The reduction in amplitude at 6 Hz is large enough to dominate the increase in frequency and increase the maximum droplet size.

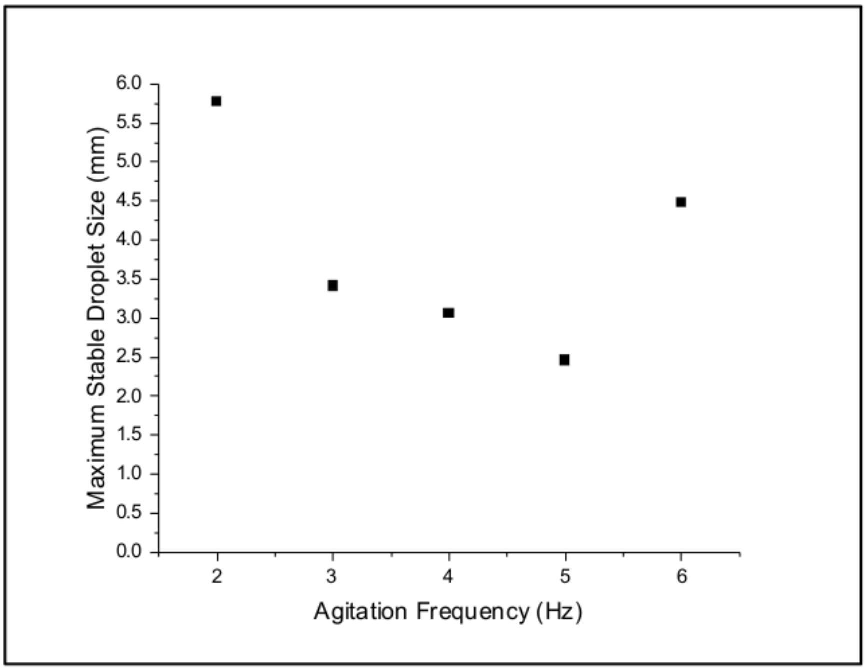

Figure 5.20: *Estimate of maximum droplet diameter in the ATR. Estimates are based on the Weber number. The plot follows an inverse relationship with the calculated power per volume. Smaller droplets are generated at higher power per volumes.*

5.3 Conclusions

The aim of this chapter was to outline the design and relevant parameters associated with mass transfer in an ATR tube. Based on previous underwhelming data, it was hypothesised that the inclusion of a third air phase would improve the ability for liquid to slosh, mix and disperse within the tube. This was observed with high-speed footage of the liquid-liquid interface and droplets present within the tube at three liquid fill volumes. It was concluded that a reduction in liquid volume provides higher sloshing and more droplets, plausibly resulting in a higher mass transfer capability within the system. Experiments to test this hypothesis will be discussed in the next chapter.

The power per volume and maximum stable droplet size have been estimated for each liquid fill volume and agitation frequency. The trends in these quantities have shown a remarkable similarity to the sloshing amplitudes and wave energy, the implication of which is that sloshing is the dominant mechanism for dispersion and droplet breakup. Higher power per volume and smallest maximum stable droplet size are seen at 5 Hz.

CHAPTER 6

Mass Transfer in an Agitated Tube Reactor

This chapter discusses the effects of process conditions on mass transfer in an agitated tube reactor. The mass transfer coefficient, $\frac{1}{\Omega_T}$, has been determined by extraction of Cu(II) from aqueous Cu(II)$(NO_3)_2$ with Mextral® 84H, as described in chapter 3. $\frac{1}{\Omega_T}$ has been evaluated against residence time, agitation frequency and liquid fill fraction. The chapter aims to find the optimal set-up and conditions for solvent extraction in an ATR tube.

6.1 Methodologies

6.1.1 Physical Setup

The set-up of the ATR (shown in the P&ID in Figure 6.1) before the separator stage is equivalent to that in Section 5.1.2. When the separator was attached to the moving ATR tube, phases were seen to not separate fully, resulting in phase carry-over. A stationary separator was held in place by a clamp stand and achieved phase separation. To accommodate the motion of the ATR tube, 22 mm diameter flexible tubing (the same diameter as the ATR tube) was used to connect the two. The tubing material was unknown and samples were therefore submerged in 3 M nitric acid and the Mextral® 84H/Exxsol™ D80 mixture for 24 hours to ensure compatibility with the chemical system and no chemical degradation of the material.

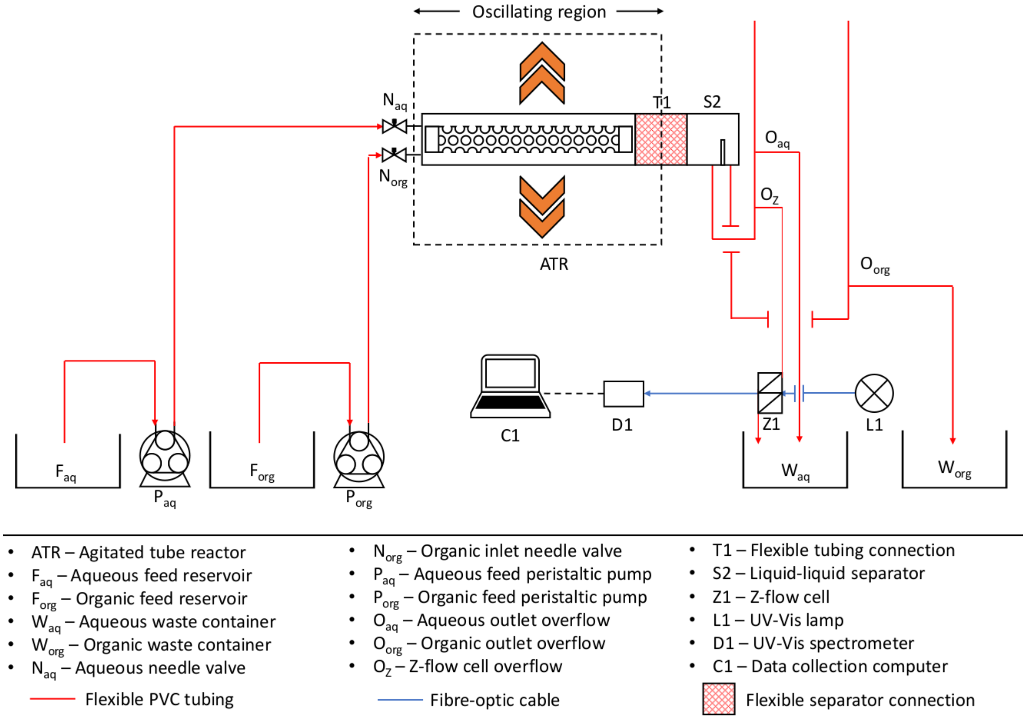

Figure 6.1: *A Piping & Instrumentation Diagram showing the ATR set-up. Red lines depict PVC tubing whilst the blue lines represent fibre-optic cables. Orange arrows show the direction of motion of the ATR with respect to the ATR tube.*

Overflow lutes were used as in Section 5.1.2. The organic outlet overflow was positioned as far below the separator as possible: draining fluid that had overflowed the weir and making sure no flooding occurred. The aqueous phase outlet was positioned at a height that allowed for a 1:1 organic:aqueous ratio within the tube, typically around 1 cm above the interface. The interface height was calculated and marked along the side of the tube.

Measurement of the aqueous phase and waste disposal methods are equivalent to those described in Section 5.1.2.

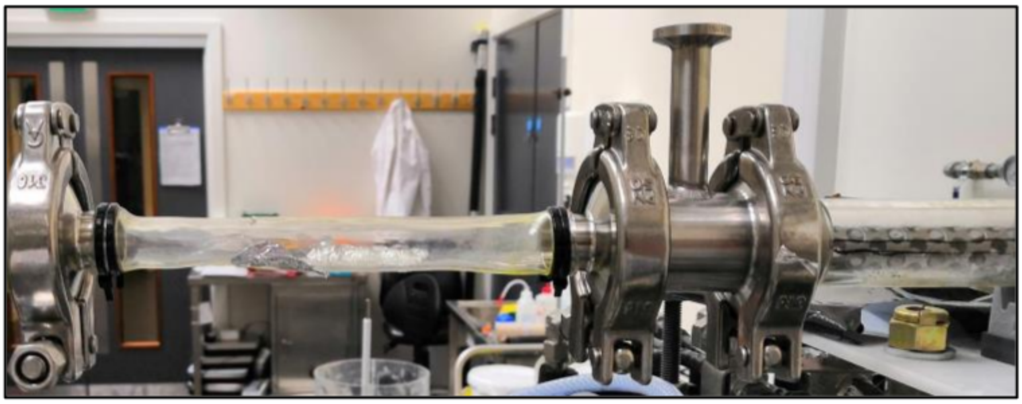

Figure 6.2: *Photograph of the flexible ATR tube extension. The extension was intended to keep the separator stationary whilst the ATR was in motion.*

6.1.2 Separator Design

The separator described in Section 5.1.4 required a redesign that allowed for variable fill heights. The calculations used in Section 5.1.4 are still valid, though the separator length, L_s, was doubled to 6 cm to ensure complete separation.

Volume fill fraction was required to be 25%, 50% and 75%. To achieve this, outlets were moved from the end wall of the separator to the base and a weir placed between them. This can be seen in Figure 6.3. Once separated, the aqueous layer exits the separator through the outlet before the weir whilst the organic layer overflows the weir into the cavity behind and through the outlet.

Three types of separator were constructed, each with a differing weir height. Weir height was determined by positioning a cord through the cross-section which produced an area of 25%, 50% or 75% covered by the weir wall. Annotated CAD (Computer Aided Design) images can be seen in Figure 6.3.

Each separator requires baffles at different positions for effective separation due to the variation in liquid height. As a result, 8 baffles have been included instead of the 4 in the previous design. The inclusion of all 8 baffles in each separator was to simplify the design process and reduce the differences between the 25%, 50% and 75% cases. As a result, only the weir height varies between them. All separators were 3D printed from VeroWhite, an acrylic based plastic.

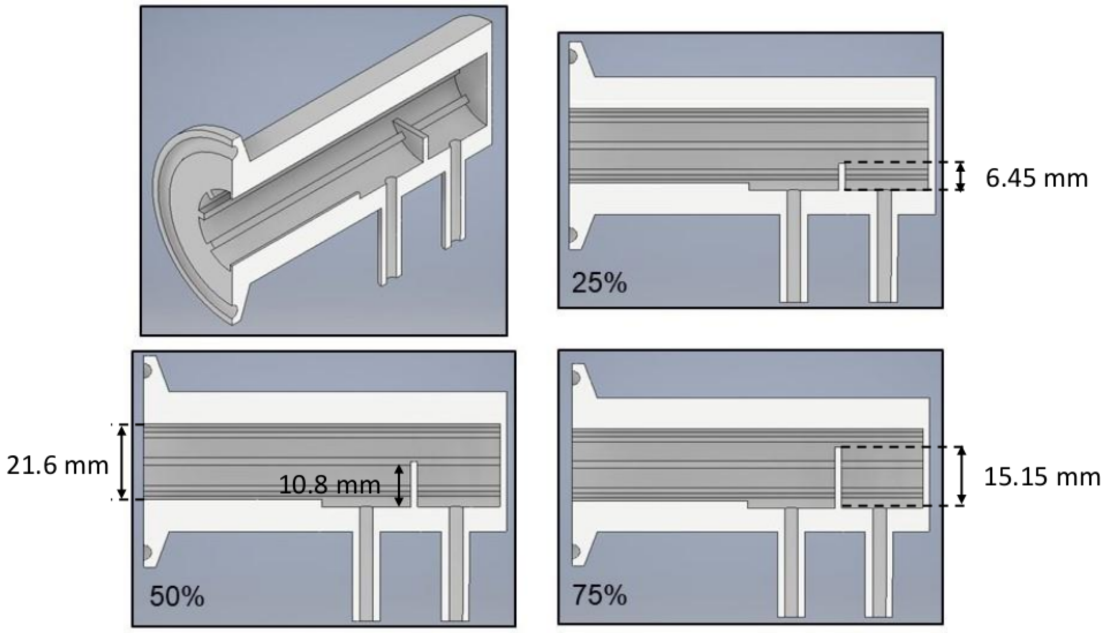

Figure 6.3: *CAD images of a redesigned liquid-liquid separator. The percentages stated in the bottom left corners of each quadrant represent to the total phase fill volume achieved by the corresponding weir.*

6.1.3 Residence Time Calculation

The plug flow characteristics of the ATR were shown by Parrington.[117] The average residence time, t, has been calculated for given flow rate, Q_T, and liquid volume, V_L. Both Q_T and V_L can be treated as the sum of the individual phase flow rates and volumes. For a given fill fraction, residence time is proportional to flow rate.

$$t = \frac{V_L}{Q_T} = \frac{V_{aq} + V_{org}}{Q_{aq} + Q_{org}} \tag{6.1}$$

Residence times were initially selected for a 50% fill volume. These were chosen as the times corresponding to the flow rates shown in Table 6.1. Total flow rate, Q_T, was treated as the sum of the flow rates for the two peristaltic pumps, Q_{aq} and Q_{org}. Pumps were calibrated as described in Section 4.2.3 and Q_{aq} and Q_{org} were kept as equal as possible, given the discreet nature of the pump settings. This ensured a 1:1 aqueous:organic ratio. Times in Table 6.1

have been rounded to the nearest second.

Table 6.1: *Phase flow rates and corresponding residence times for each liquid fill fraction. Residence times are calculated based on the ratio of total liquid volume and the sum of the aqueous and organic flow rates.*

Q_{aq} (mL·min)$^{-1}$	Q_{org} (mL·min)$^{-1}$	t for 25% Fill Fraction (s^{-1})	t for 50% Fill Fraction (s^{-1})	t for 75% Fill Fraction (s^{-1})
10	11	169	337	-
15	16	114	228	343
25	23	-	-	221
25	26	69	139	-
30	30	59	118	-
35	34	51	103	-
40	40	44	88	133
44	46	-	-	118
50	49	-	-	107
60	62	-	-	87

The lowest possible flow rate for each peristaltic pump was 10 mL·min^{-1}. The maximum possible flow rate was not based on pump capacity but instead on flooding within the ATR tube. This occurred at $Q_T > 120$ mL·min^{-1}.

The same flow rates were used for the 25% fill fraction experiments, effectively halving the residence times calculated for the 50% fill fraction case.

$$t_{25\%} = \frac{1}{2} t_{50\%} \tag{6.2}$$

Flow rates for the 75% fill fraction experiments were adjusted such that the residence times matched those for the 50% fill volume case.

$$t_{75\%} = \frac{3}{2} t_{50\%} \tag{6.3}$$

6.1.4 Mass Transfer in Co-current Systems

The aim of this section is to derive an expression for the mass transfer resistance, Ω_{T}, in a continuous co-current system. Equations describing the mass transfer rate, q, from an aqueous phase into an organic phase are shown in Equations 6.4 and 6.5.[30] Equation 6.4 represents mass transfer driven by the concentration difference between the aqueous liquid bulk, $\mathrm{c_{aq}}$, and the interface, $\mathrm{c_{i,aq}}$. Since material is transferred into the organic phase, transfer occurs away from the interface and is driven by the concentration difference between the interfacial concentration, $\mathrm{c_{i,org}}$ and the bulk concentration, $\mathrm{c_{org}}$. q will be equivalent for both phases, however it will occur in opposing directions.

$$q = k_{aq} a_v (c_{aq} - c_{i,aq}) \tag{6.4}$$

$$q = k_{org} a_v E_q (c_{i,org} - c_{org}) \tag{6.5}$$

Multiplying Equation 6.5 by the partition coefficient, S, allows the equivalence in Equation 6.6 to be applied to Equation 6.5, yielding Equation 6.7. This relation is true at the interface as the two liquids will be in equilibrium.

$$S c_{i,org} = c_{i,aq} \tag{6.6}$$

$$qS = S k_{org} a_v E_q (c_{i,org} - c_{org}) = k_{org} a_v E_q (c_{i,aq} - S c_{org}) \tag{6.7}$$

Rearranging Equations 6.4 and 6.7 yield Equations 6.8 and 6.9.

$$q \frac{1}{k_{aq} a_v} = (c_{aq} - c_{i,aq}) \tag{6.8}$$

$$q \frac{S}{k_{org} a_v E_q} = (c_{i,aq} - S c_{aq}) \tag{6.9}$$

Equations 6.8 and 6.9 can be combined to reach a mass transfer rate based on the mass transfer through both phases. This is achieved by adding Equation 6.8 to 6.9.

$$q \left[\frac{1}{k_{aq} a_v} + \frac{S}{k_{org} a_v E_q} \right] = (c_{aq} - c_{i,aq}) + (c_{i,aq} - S c_{org}) = c_{aq} - S c_{org} \tag{6.10}$$

As a result of the addition, the unknown interfacial concentrations are eliminated. The terms in the square brackets, on the left-hand side of Equation 6.10, are equivalent to the mass transfer resistances shown in Equation 2.9.[37]

$$\frac{S}{k_{org}a_vE_q} = \Omega_{org} \qquad ; \qquad \frac{1}{k_{aq}a_v} = \Omega_{aq} \tag{6.11}$$

$$\Omega_{org} + \Omega_{aq} = \Omega_T \tag{6.12}$$

Equation 6.10 simplifies to Equation 6.13.

$$q = \frac{1}{\Omega_T}(c_{aq} - Sc_{org}) \tag{6.13}$$

Equation 6.14 shows another relationship for the mass transfer rate, this time in terms of the number of moles per second transferring between the two phases, N. This can be described in relation to both phases. The negative aqueous rate describes the solute leaving the aqueous phase. Using the the relation $c = \frac{N}{V}$, a relation can be found with respect to the concentration of solute, c in each phase.

$$q = \frac{1}{V}\frac{dN_{org}}{dt} = \frac{V_{org}}{V}\frac{dc_{org}}{dt} \quad ; \quad q = -\frac{1}{V}\frac{dN_{aq}}{dt} = -\frac{V_{aq}}{V}\frac{dc_{aq}}{dt} \tag{6.14}$$

The volume term, V, is a general volume term which can be chosen as either the aqueous volume, $\mathrm{V_{aq}}$ or the organic volume, $\mathrm{V_{org}}$. The value of the interfacial area per unit volume, a (shown most recently in Equation 6.10), and the phase it represents will depend on which volume is chosen.

Applying Equation 6.14 to the derived mass transfer rate equation in Equation 6.13 yields two differential equations describing the change in phase concentration with time. These are shown in Equation 6.15. The organic rate has been multiplied by a factor of S on both sides of the equation as this will be useful in later stages of the derivation.

$$S\frac{dc_{org}}{dt} = S\frac{V}{V_{org}}\frac{1}{\Omega_T}(c_{aq} - Sc_{org}) \; ; \; \frac{dc_{aq}}{dt} = -\frac{V}{V_{aq}}\frac{1}{\Omega_T}(c_{aq} - Sc_{org}) \tag{6.15}$$

Subtracting the aqueous rate equation from the organic rate equation gives Equation 6.16.

$$\frac{dc_{aq}}{dt} - S\frac{dc_{org}}{dt} = \frac{d}{dt}(c_{aq} - Sc_{org}) = -\frac{1}{\Omega_T}\left(\frac{V}{V_{aq}} + S\frac{V}{V_{org}}\right)(c_{aq} - Sc_{org}) \quad (6.16)$$

It is now apparent why Equation 6.15 was multiplied by a factor of S, since now the term $(c_{aq} - Sc_{org})$ can be easily integrated with respect to itself. The time integral is performed in the limits t=0 to time, t, which represents contact time between the two phases. Integration on the left-hand side will be conducted between the inlet concentration at t=0, and the concentration at time t.

$$\int_{(c_{aq}-Sc_{org})_{inlet}}^{(c_{aq}-Sc_{org})_t} \frac{d(c_{aq} - Sc_{org})}{c_{aq} - Sc_{org}} = -\frac{1}{\Omega_T}\left(\frac{V}{V_{aq}} + S\frac{V}{V_{org}}\right)\int_0^t dt \quad (6.17)$$

$$ln\left[\frac{(c_{aq} - Sc_{org})_t}{(c_{aq} - Sc_{org})_{inlet}}\right] = -\frac{1}{\Omega_T}\left(\frac{V}{V_{aq}} + S\frac{V}{V_{org}}\right)t \quad (6.18)$$

It can be assumed that the concentration in the aqueous and organic phases are equivalent to their initial values at the inlet, since no extraction has yet occurred. The initial organic concentration of solute will be zero, whilst the aqueous concentration will be the initial concentration at t=0, c_0.

$$c_{org} = 0 \qquad ; \qquad c_{aq} = c_0 \quad (6.19)$$

$$ln\left[\frac{(c_{aq} - Sc_{org})_t}{c_0}\right] = -\frac{1}{\Omega_T}\left(\frac{V}{V_{aq}} + S\frac{V}{V_{org}}\right)t \quad (6.20)$$

While this is a simple equation, for use in later chapters, it is advantageous to eliminate c_{org} from the equation.

Equation 6.21 shows the relation between the organic and aqueous concentrations at any point, simply defined as the difference between the initial and current aqueous concentration. The volume fraction is included to account for systems without a 1:1 aqueous:organic ratio. A factor S has been included to be consistent with the term present in Equation 6.20.

$$Sc_{org} = S\frac{V_{aq}}{V_{org}}(c_0 - c_{aq}) \tag{6.21}$$

At equilibrium, the equilibrium concentration of solute in the aqueous phase, c_{eq}, can be related to the concentration in the organic phase by Equation 6.22.

$$c_{aq} = c_{eq} = Sc_{org,eq} \tag{6.22}$$

Equation 6.21 can now be rewritten for the case in which the phases are in equilibrium.

$$Sc_{org} = c_{eq} = S\frac{V_{aq}}{V_{org}}(c_0 - c_{eq}) \tag{6.23}$$

Grouping the c_{eq} terms in Equation 6.23 to generate Equation 6.24, and subsequently rearranging for the equilibrium concentration yields a relation between c_{eq} and the initial concentration, shown in Equation 6.25.

$$\left(1 + S\frac{V_{aq}}{V_{org}}\right)c_{eq} = S\frac{V_{aq}}{V_{org}}c_0 \tag{6.24}$$

$$c_{eq} = \frac{S\frac{V_{aq}}{V_{org}}c_0}{1 + S\frac{V_{aq}}{V_{org}}} \tag{6.25}$$

$$ln\left[\frac{\left(c_{aq} - S\frac{V_{aq}}{V_{org}}(c_0 - c_{aq})\right)_t}{c_0}\right] = -\frac{1}{\Omega_T}\left(\frac{V}{V_{aq}} + S\frac{V}{V_{org}}\right)t \tag{6.26}$$

The numerator within the natural logarithm can be expanded as shown in Equation 6.27.

$$c_{aq} - S\frac{V_{aq}}{V_{org}}(c_0 - c_{aq}) = \left(1 + S\frac{V_{aq}}{V_{org}}\right)c_{aq} - S\frac{V_{aq}}{V_{org}}c_0 \tag{6.27}$$

Taking the term within the natural logarithm in Equation 6.26 and dividing by a factor of $\frac{1}{1+S\frac{V_{aq}}{V_{org}}}$, as shown in Equation 6.28, allows this fraction to be significantly simplified.

$$\frac{\frac{1+S\frac{V_{aq}}{V_{org}}}{1+S\frac{V_{aq}}{V_{org}}}c_{aq} - \frac{S\frac{V_{aq}}{V_{org}}}{1+S\frac{V_{aq}}{V_{org}}}c_0}{\frac{c_0}{1+S\frac{V_{aq}}{V_{org}}}} \tag{6.28}$$

The first simplification is shown in Equation 6.29 using the numerator in Equation 6.28. The proof for this has been demonstrated in Equation 6.25.

$$\frac{1+S\frac{V_{aq}}{V_{org}}}{1+S\frac{V_{aq}}{V_{org}}}c_{aq} - \frac{S\frac{V_{aq}}{V_{org}}}{1+S\frac{V_{aq}}{V_{org}}}c_0 = c_{aq} - c_{eq} \tag{6.29}$$

In order to simplify the denominator in Equation 6.28, it is best to start with Equation 6.30, again using Equation 6.25 as a substitute for c_{eq}. Multiplying and dividing the c_0 term by $\left(1+S\frac{V_{aq}}{V_{org}}\right)$, effectively multiplying by a factor of 1, equates (c_0 - c_{eq}) to the right-hand part of Equation 6.30.

$$c_0 - c_{eq} = \frac{1+S\frac{V_{aq}}{V_{org}}}{1+S\frac{V_{aq}}{V_{org}}}c_0 - \frac{S\frac{V_{aq}}{V_{aq}}}{1+S\frac{V_{aq}}{V_{org}}}c_0 \tag{6.30}$$

$$\frac{1+S\frac{V_{aq}}{V_{org}}}{1+S\frac{V_{aq}}{V_{org}}}c_0 - \frac{S\frac{V_{aq}}{V_{aq}}}{1+S\frac{V_{aq}}{V_{org}}}c_0 = \left(\frac{1+S\frac{V_{aq}}{V_{org}} - S\frac{V_{aq}}{V_{org}}}{1+S\frac{V_{aq}}{V_{org}}}\right)c_0 = \frac{c_0}{1+S\frac{V_{aq}}{V_{org}}} \tag{6.31}$$

The term in the right-hand part of Equation 6.31 is the same as the denominator in Equation 6.28. Therefore, Equation 6.28 can be simplified further by Equation 6.32.

$$\frac{c_0}{1+S\frac{V_{aq}}{V_{org}}} = c_0 - c_{eq} \tag{6.32}$$

Substituting Equations 6.29 and 6.32 into Equation 6.26 gives an equation only in terms of aqueous concentrations. This is shown in Equation 6.33

$$ln\left[\frac{(c_{aq} - c_{eq})_t}{c_0 - c_{eq}}\right] = -\frac{1}{\Omega_T}\left(\frac{V}{V_{aq}} + S\frac{V}{V_{org}}\right)t \tag{6.33}$$

A value for V can then be chosen based on the phase of interest. This can be V_T, V_{aq} or V_{org}. The choice of V determines which phase the mass transfer coefficient relates to. This is based on the definition of the interfacial area per unit volume, a_v, where the volume, V, is the volume of the phase of interest and is equivalent to V in Equation 6.33.

$$a_v = \frac{A_{int}}{V} \tag{6.34}$$

6.1.5 Concentration Measurements

Cu(II) concentration in the aqueous raffinate, c_{aq}, was measured following the same methodology and setup described in Sections 3.2.1 and 4.2.6. The Z-flow cell was positioned as described in Section 6.1.1.

The system was left to reach steady state for a period of two residence times or, if longer, a minimum of 100 s (in accordance with Figure 4.7). Measurements were taken over a single residence time after the system had reached its steady state. Measurements were taken approximately every 200 ms, though this varied depending on the necessary integration time. Each set of measurements was repeated in triplicate to show repeatability. Between each measurement, deionised water was injected into the Z-cell to check the calibration was still accurate. In cases where the detector was no longer calibrated, the deviation was recorded and subtracted from the measurement. Deviation from the calibrated zero was recorded at 10 points and an average taken.

6.1.6 Analysis

Plotting Concentration

Batches of $Cu(II)(NO_3)_2$ solution were made as described in Section 3.1. The initial concentration of each batch was measured using UV-Vis spectrometry. The standard error was calculated to provide an error in the initial concentrations. The equilibrium concentration was calculated as described in Section 3.2.4. The organic phase consisted of previously stripped Mextral® 84H/Exxsol™ D80 mixture (stripped a single time only), and as such the partition coefficient, S, for stripped material has been used. The value of S has been calculated for an initial concentration of 0.10 M to be 0.89±0.01, as described in 3.2.2.

When plotting concentration, the axes were chosen based on the derivation presented in 6.1.4. Equation 6.33, derived in Section 6.1.4, has been restated in Equation 6.35.

$$\ln\left[\frac{c_{aq}-c_{eq}}{c_0-c_{eq}}\right]=\ln\zeta=-\frac{1}{\Omega_T}\left(\frac{V}{V_{aq}}+S\frac{V}{V_{org}}\right)t \tag{6.35}$$

In this case, it is most appropriate to choose the aqueous volume for V. Since all experiments are performed in a 1:1 aqueous:organic ratio, this results in all volume terms cancelling out.

Removing the natural logarithm results in Equation 6.36, an Equation relating aqueous concentration to residence time, t.

$$\frac{c_{aq}-c_{eq}}{c_0-c_{eq}}=\zeta=e^{-\frac{(1+S)}{\Omega_T}t} \tag{6.36}$$

Plotting concentration in this method provides a normalised concentration ranging between 1 and 0 at the initial concentration, $c_{aq}=c_0$, and equilibrium, $c_{aq}=c_{eq}$, respectively.

Calculation of $\mathbf{\Omega_T}$

Rearranging Equation 6.35 yields an equation for a linear plot with gradient $\frac{1}{\Omega_T}$. This is shown in Equation 6.37.

$$-\frac{1}{1+S}\ln\zeta=\frac{1}{\Omega_T}t \tag{6.37}$$

Plotting residence time, t, on the x-axis and $-\frac{1}{1+S}\ln\zeta$ on the y-axis yields a straight line with gradient equal to $\frac{1}{\Omega_T}$ and a y-intercept equal to 0 when $c_{aq}=c_0$.

Error Propagation

Error calculations for ζ and $\frac{1}{\Omega_T}$ are given in the Appendix.

6.2 Results & Discussions

6.2.1 Effect of Residence Time on Mass Transfer

If in contact for a long enough period of time, the two phases will reach an equilibrium. Once reached, no net mass transfer will occur. Figure 6.4 shows the reduction in normalised aqueous Cu(II) concentration, ζ, with residence time/time spent in the reactor, t. Initial agitation frequency was chosen based on anecdotal evidence and was set to 4 Hz. The ATR tube was filled in a 1:1 solvent:aqueous ratio such that each phase occupied 25% of the ATR tubes volume (i.e. a 50% total fill fraction).

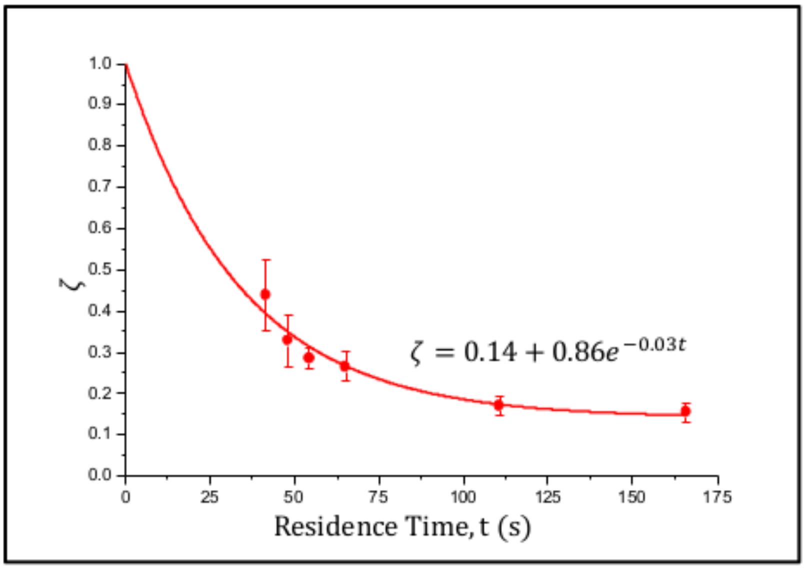

Figure 6.4: *A graph representing the normalised change in aqueous Cu(II) concentration, ζ, against reactor residence time, t. Measurements were taken at 4 Hz agitation frequency with a 1:1 aqueous:organic ratio and a total phase fill fraction of 50%. The exponential decay is seen to asymptotically approach 0.14, not zero as initially expected. This implies the system is not fully mixed.*

Aqueous concentration is seen to decrease exponentially with residence time. This is due to the increased contact time between the two phases. While the system appears to reach an equilibrium, the trend tends towards an asymptote at 0.14, not at 0 as would be expected for a system reaching equilibrium. The implication is that some liquid is left unmixed by the agitator. Any mixed liquid reaches equilibrium, but a portion bypasses agitation and is not dispersed. Figure 6.5 shows two schematics of an ATR tube, one exhibiting partial dispersion (Figure 6.5(A)) the other ideal total dispersion (Figure 6.5(B)). The blue, yellow and green phases represent the organic phase, aqueous phase and a dispersed mixture of both. The dispersed liquid is expected to reach equilibrium while the unmixed phases do not experience any mass transfer. This explains the ATR's inability to reach the anticipated equilibrium as a large portion of the material is not in contact with the other phase and bypasses dispersion altogether. For settings in which mass transfer is increased, the mixed phase will be more dominant with thinner unmixed phases. In an ideal scenario, both the aqueous and organic phases would be completely mixed. In such a case, the system would be expected to reach equilibrium.

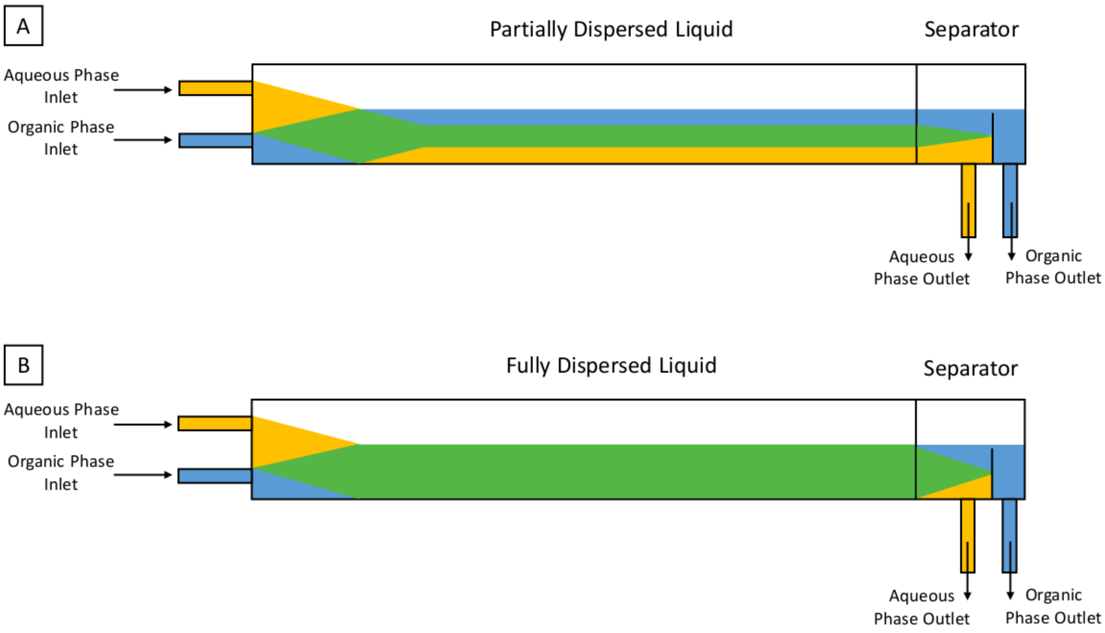

Figure 6.5: **(A)** *A diagram showing the unmixed liquid within the ATR tube at 50% fill fraction. The colours: yellow, blue and green represent the aqueous phase, organic phase and a mixed phase respectively. The mixed phase contains a continuous aqueous phase with a dispersed organic phase.* **(B)** *A diagram showing the ideal mixing conditions within an ATR tube with 50% fill fraction.*

To account for unmixed liquid, the data has been fitted with Equation 6.38, in which α and β represent the fraction of unmixed fluid and the quantity $\frac{1+S}{\Omega_T}$ respectively. The trend now tends towards α instead of 0, meaning that the fraction of unmixed liquid can be calculated.

$$\zeta = \alpha + (1-\alpha)e^{-\beta t} \tag{6.38}$$

Using the fit in Figure 6.4 and Equations 6.38 and 6.39, the percentage of mixed liquid can be calculated as 86%.

$$\text{Percentage of Mixed Liquid} = 100(1-\alpha) \tag{6.39}$$

To calculate $\frac{1}{\Omega_T}$, it is easiest to plot a logarithmic equation in the method described in Section 6.1.6. However, The proportion of unmixed fluid, α, must now be taken into consideration. Equation 6.40 shows the modified equation.

$$-\frac{1}{1+S}\ln\left[\frac{\zeta-\alpha}{1-\alpha}\right] = \frac{1}{\Omega_T}t \tag{6.40}$$

The mass transfer coefficient, $\frac{1}{\Omega_T}$, calculated in this method will be the mass transfer coefficient for the mixed liquid, ignoring any unmixed fluid. The assumption is made that the two phases are still mixed in a 1:1 aqueous:organic ratio.

Figure 6.6 shows a logarithmic plot using the exponential fit described in Figure 6.4. The inverse mass transfer resistance, $\frac{1}{\Omega_T}$, is shown to be 0.016 s^{-1}. This value is a factor of 10^3 greater than the non-agitated system described in Section 3.3.5. Using the same calculation used in Section 4.3.3 and approximating D_d as 10^{-3} m (based on results presented in Section 5.2.2), k_T can be estimated to be of the order 10^{-5} m·s^{-1}. This is the same order of magnitude as literature data, for the same chemical system, presented in Table 2.1.[66]

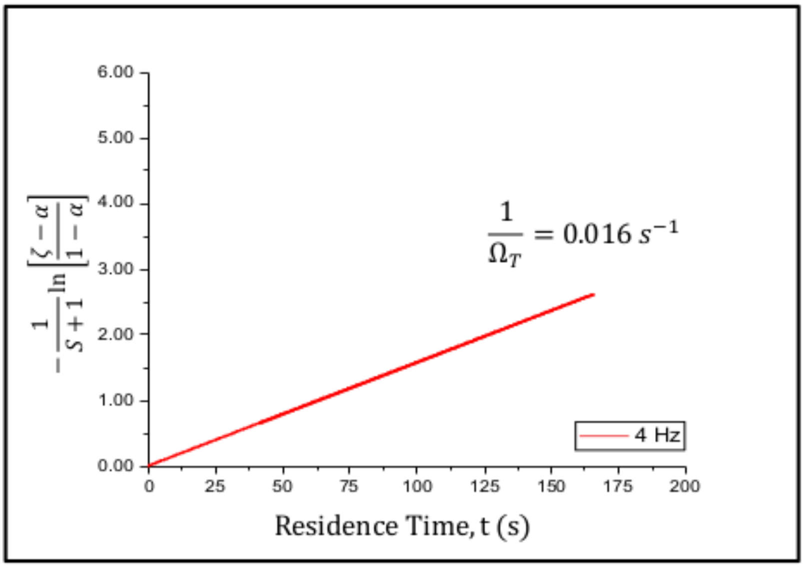

Figure 6.6: *A logarithmic plot of* $-\frac{1}{1+S}\ln\zeta$ *against reactor residence time, t.* $\frac{1}{\Omega_T}$ *is shown to be 0.16×10*$^{-5}$ *s*$^{-1}$

6.2.2 Effect of Agitation Frequency on Mass Transfer

Plots showing ζ versus residence time, t, for a range of agitation frequencies can be seen in Figures 6.7(A), (B) and (C). The corresponding log plots, as described in Section 6.2.1, can be seen in Figure 6.7(D). In each case, the ATR tube was filled with an aqueous:organic ratio of 1:1, with each phase filling 25% of the tube: equivalent to a fill fraction of 50%. The log plots represent the same information shown in Figure 6.6.

In all three cases, the concentration is shown to reach an early equilibrium, plateauing above the expected equilibrium at $\zeta = 0$. The 5 Hz case disperses the most liquid, with only 5% left unmixed. On the other hand, the 3 Hz case only disperses 53% of the liquid.

The trend is fitted to the data using the Equation in 6.38. The order of increasing dispersion displayed in Figure 6.7 is consistent with the maximum stable droplet size, power per volume and wave amplitudes described in Chapter 5. A higher power input from the agitator bar will provide a higher shear on the liquid phases, creating a better dispersion.

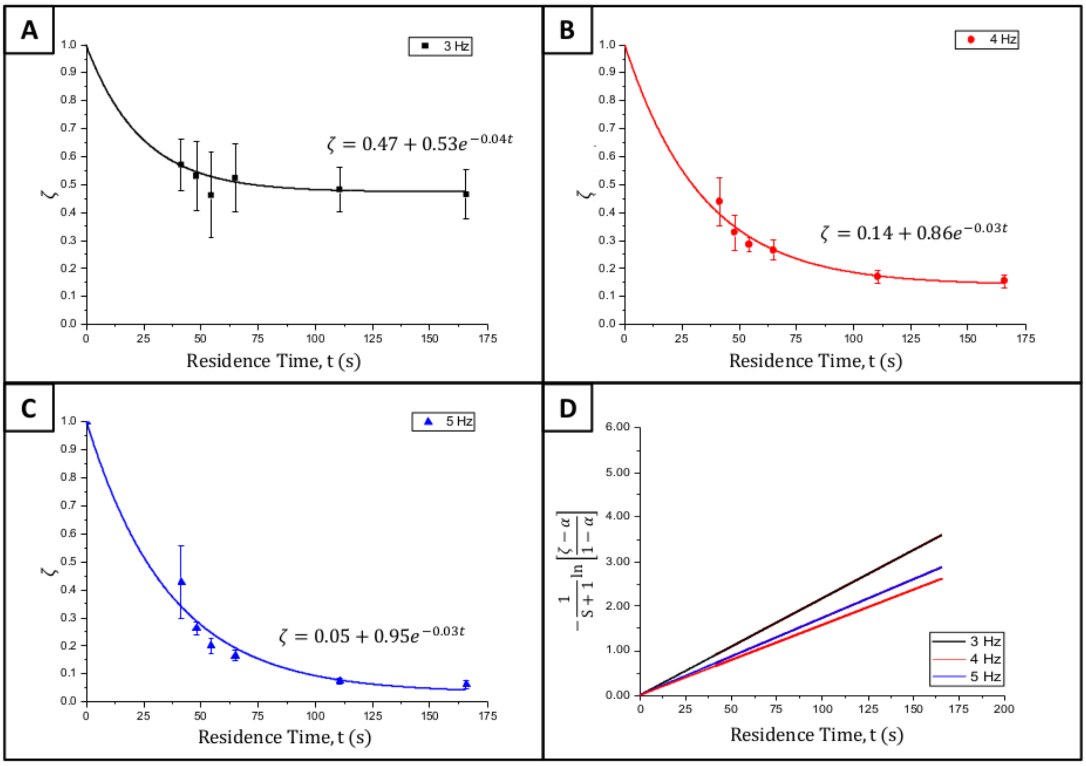

Figure 6.7: *Plots showing the change in normalised concentration, ζ, with reactor residence time, t, at a total fill fraction of 50%.* **(A)**, **(B)** *and* **(C)** *show plots for agitation frequencies of 3 Hz, 4 Hz and 5 Hz respectively.* **(D)** *shows the log plot described in Equation 6.40 for 3, 4 and 5 Hz agitation frequencies. The plots use the fitted exponential trends in* **(A)**, **(B)** *and* **(C)** *. These have been used to determine the mass transfer coefficient, $\frac{1}{\Omega_T}$.*

Table 6.2 shows the values for $\frac{1}{\Omega_T}$ and the mixed volume percentage $(1-\alpha)$ for all three agitation frequencies. Even though 3 Hz exhibits the least mixing, it has the highest mass transfer coefficient of the three. This is also apparent from the gradients in 6.7(D). This implies that, though there is little dispersed fluid, the mass transfer rate is higher in the 3 Hz case. This may be due to the reduction in the dispersed volume. Since a lower volume is being mixed, there will be more energy input into a smaller quantity of liquid. This could have the effect of reducing droplet diameter in the mixed liquid, increasing the mass transfer rate.

Table 6.2: *A table displaying the calculated values for* $\frac{1}{\Omega_T}$ *and the percentage of dispersed liquid for each of the three agitation frequencies. A 50% liquid fill fraction has been used such that each liquid phase constitutes 25% of the total tube volume.*

Agitation Frequency (Hz)	$\frac{1}{\Omega_T}$ for the Mixed Liquid (s^{-1})	Percentage of Dispersed Liquid, $(1-\alpha)$
3	0.022 ± 0.002	53%
4	0.016 ± 0.001	86%
5	0.017 ± 0.001	95%

6.2.3 Effect of Fill Volume on Mass Transfer

Concentration plots for 3, 4 and 5 Hz can be seen for fill fraction totals of 25% and 75% in Figures 6.8 and 6.9 respectively. Figures 6.8(D) and 6.9(D) show their corresponding log plots with gradient $\frac{1}{\Omega_T}$. Table 6.3 contains mass transfer coefficients, $\frac{1}{\Omega_T}$, and the percentage of dispersed liquid, 1-α, for 25%, 50% and 75% fill fractions.

Much like the 50% fill fractions shown in Figure 6.7, the concentration plots for both 25% and 75% can be seen to plateau before reaching the expected equilibrium. The 25% case exhibits a greater extent of mixing at 5 Hz, with the least mixing occurring at 3 Hz. This is consistent with the 50% case. The mass transfer coefficient, $\frac{1}{\Omega_T}$, also follows the same trend as the 50% case, providing the fastest mass transfer at 3 Hz, with 5 Hz providing the slowest. This is the inverse of the trend seen in α. This is counter-intuitive but can be explained with Figure 6.10. Only a fraction of the liquid is dispersed, and therefore the energy input per unit volume is intensified into a the mixed portion of the liquid. Equation 6.41 describes the modified energy per unit dispersed volume. Where V_d is the dispersed liquid volume.

$$\frac{E_k}{V_d} = \frac{E_k}{(1-\alpha)V_L} \tag{6.41}$$

Figures 6.10(C) and (D) show the energy per dispersed volume, which shows a very different trend to the wave energy shown in Figure 5.19(B). The 3 Hz case is now shown to introduce more energy into the dispersed liquid, closely following the trend shown in Figures 6.10(A) and (B).

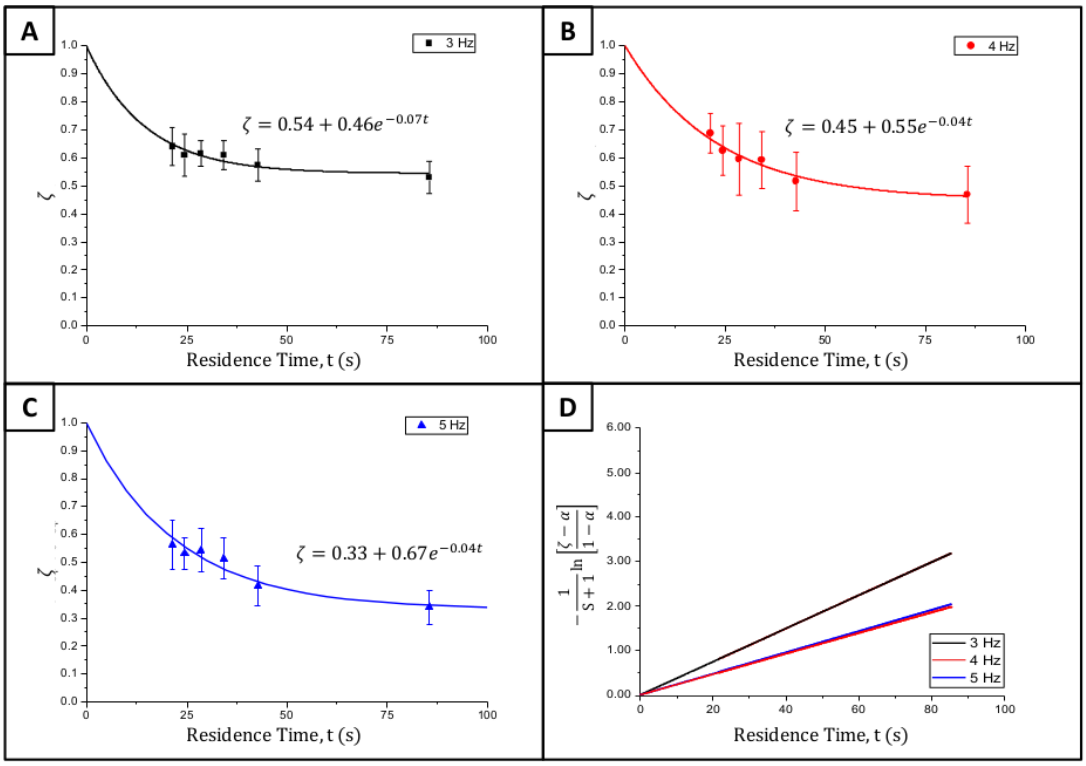

Figure 6.8: *Plots showing the change in normalised concentration, ζ, with reactor residence time, t, at a total fill fraction of 25%.* **(A)**, **(B)** *and* **(C)** *show plots for agitation frequencies of 3 Hz, 4 Hz and 5 Hz respectively.* **(D)** *shows the log plot described in Equation 6.40 for 3, 4 and 5 Hz agitation frequencies. The plots use the fitted exponential trends in* **(A)**, **(B)** *and* **(C)** *. These have been used to determine the mass transfer coefficient,* $\frac{1}{\Omega_T}$.

The 25% case exhibits the highest values of $\frac{1}{\Omega_T}$, while the 75% case exhibits the lowest. This is consistent for all three agitation frequencies and can be described with the power per volume plot in Section 5.18. The volume of dispersed fluid follows a different trend, with 50% dispersing up to 28% more liquid volume than corresponding agitation frequency for the 25% case. 75% is again shown to disperse the least liquid. Liquid motion, as shown in Figure 5.19(A), is lowest in the 75% case and reduced dispersion is expected. The 25% and 50%, however, show similar wave amplitudes, defined as the change in height of the liquid surface, from peak to trough. The increased initial depth of the liquid in the 50% case may provide the answer, as the liquid surface was nearer to the top of the tube. Though the two cases have similar amplitude, the proximity to the top of the tube in the 50% case causes the wave to crash, dispersing the liquid more than in the 25% case. The 25% case will not reach the top of the tube and will not crash.

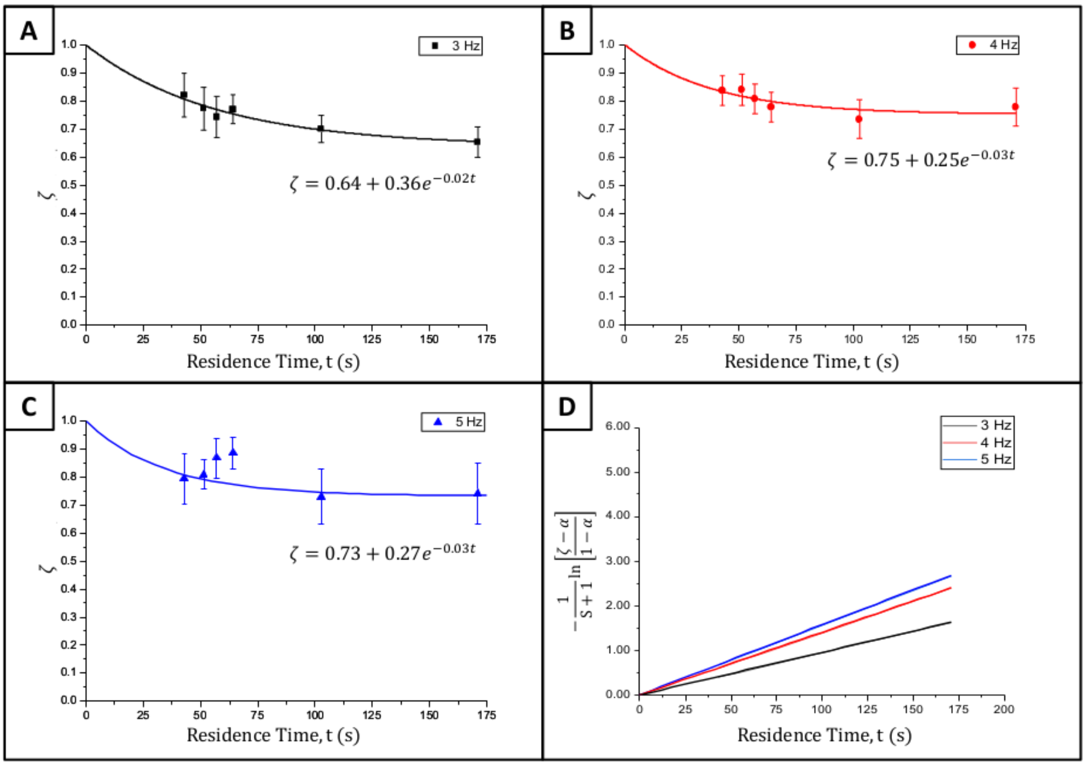

Figure 6.9: *Plots showing the change in normalised concentration, ζ, with reactor residence time, t, at a total fill fraction of 75%.* **(A)**, **(B)** *and* **(C)** *show plots for agitation frequencies of 3 Hz, 4 Hz and 5 Hz respectively.* **(D)** *shows the log plot described in Equation 6.40 for 3, 4 and 5 Hz agitation frequencies. The plots use the fitted exponential trends in* **(A)**, **(B)** *and* **(C)** *. These have been used to determine the mass transfer coefficient,* $\frac{1}{\Omega_T}$.

Table 6.3: *Table displaying the values for* $\frac{1}{\Omega_T}$ *as well as the percentage of dispersed liquid. These values are shown for all three fill fractions and all three agitation frequencies within each fill volume.*

Fill Fraction	Agitation Frequency (Hz)	$\frac{1}{\Omega_T}$ For the Mixed Liquid (s^{-1})	Percentage of Dispersed Liquid, ($1-\alpha$)
25%	3	0.037 ± 0.005	46%
	4	0.023 ± 0.002	55%
	5	0.024 ± 0.003	67%
50%	3	0.022 ± 0.002	53%
	4	0.016 ± 0.001	86%
	5	0.017 ± 0.001	95%
75%	3	0.010 ± 0.001	36%
	4	0.014 ± 0.002	25%
	5	0.016 ± 0.003	27%

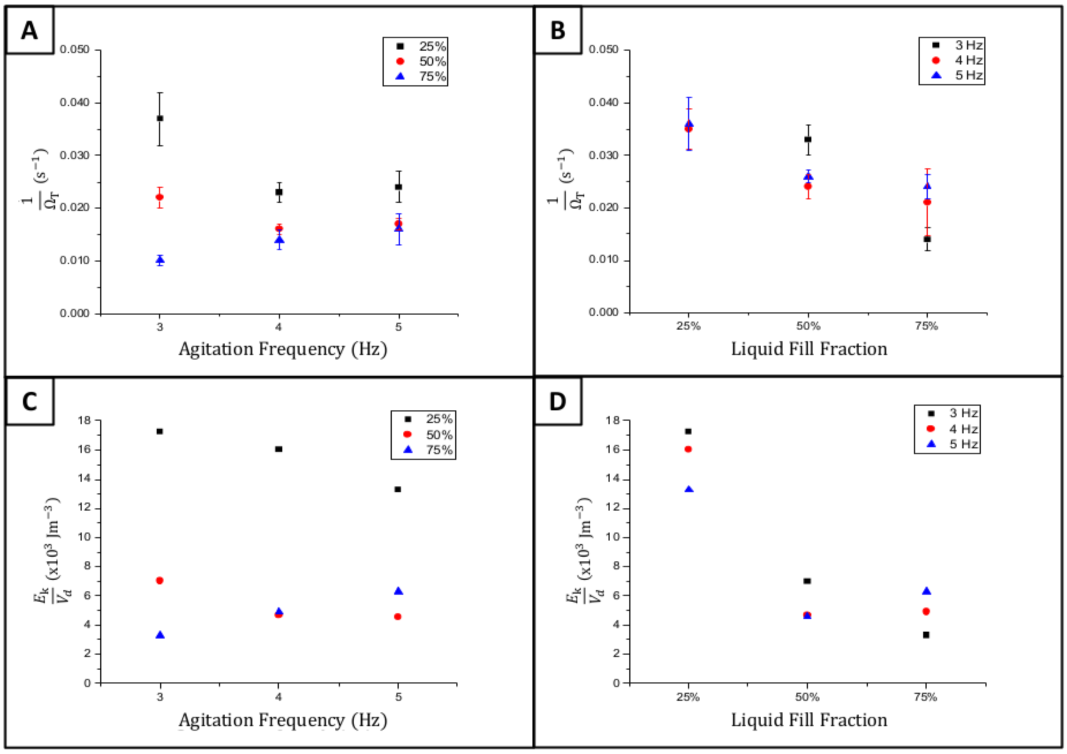

Figure 6.10: **(A)** $\frac{1}{\Omega_T}$ *for mixed fluid against agitation frequency at three liquid fill fractions.* **(B)** *Plot showing* $\frac{1}{\Omega_T}$ *for mixed fluid against liquid fill fractions at three agitation frequencies.* **(C)** *Plot showing the energy per dispersed volume against agitation frequency. The dispersed volume has been used instead of the fill fraction, as such the trend is now more similar in shape to (A).* **(D)** *Plot showing the energy per dispersed volume against fill fraction. The trend now shows remarkable similarity to (B).*

6.3 Conclusions

The extent of mass transfer in an Agitated Tube Reactor has been observed by measuring aqueous Cu(II) concentrations with UV-Visible spectroscopy.

Mass transfer is seen to initially increase with reactor residence time, however beyond a point it plateaus and no further net mass transfer occurs. Though this is expected to arise when the system reaches equilibrium, mass transfer within the ATR tube ceases earlier than expected. The extent to which the ATR reaches equilibrium is attributed to a volume of unmixed fluid bypassing agitation. The proportion of this unmixed fluid has been calculated and a mass transfer coefficient for the mixed phase only has been calculated. 5 Hz agitation frequency is shown to provide the most mixing, with 3 Hz providing the least. This is not true of the 75% case, though the low overall mass transfer means that all frequencies fall within margin of error. The extent to which mass transfer approaches equilibrium is dependent on the liquid fill fraction and agitation frequency.

The optimal conditions for a 1:1 aqueous:organic ratio in the ATR appear to be 50% fill fraction subject to 5 Hz agitation frequency. This provides the highest level of mixing, and as such is the closest to an ideal system. Though mass transfer coefficients may be higher in other fill fractions, they are likely skewed by the low extent of mixing, since energy input will be intensified over a smaller volume.

The ability of the ATR to achieve equilibrium in just one 30 cm long tube shows that the ATR is capable of solvent extraction. Further redesign is necessary to counteract the limited mixing in the system.

CHAPTER 7

Comparisons

7.1 TCDC and ATR comparison

In order to compare the TCDC and the ATR directly, it is easiest to look at the mass transfer coefficient in terms of the organic phase, such that the interfacial area per unit volume, $\mathrm{a_v}$, is expressed as the interfacial area per unit organic volume. The reason for this is the low organic hold-up present in the TCDC may reduce the value of the overall mass transfer coefficient when compared to a 1:1 ratio. For the ATR, the mass transfer coefficient relating to the organic phase, $\frac{1}{\Omega_d}$, can be derived using Equations 7.1 to 7.7. The equation for the total mass transfer coefficient, $\frac{1}{\Omega_T}$, in a co-current system is seen in Equation 7.1.

$$-\ln\left[\frac{\zeta-\alpha}{1-\alpha}\right]=\frac{1}{\Omega_T}\left(\frac{V_T}{V_{aq}}+S\frac{V_T}{V_{org}}\right)t \tag{7.1}$$

Ω_T can be written in terms of the total mass transfer coefficient $\mathrm{k_Ta}$.

$$\frac{1}{\Omega_T}=\frac{1}{\frac{1}{k_{aq}a_v}+\frac{1}{k_{org}a_v}}=k_Ta_v \tag{7.2}$$

Equation 7.3 shows the relation between the total residence time, t, and the total volume and flow rates. As well as this, the definition of the interfacial area per unit dispersed volume, a_d, is also shown.

$$t = \frac{V_T}{Q_T}\frac{V_{org}}{V_{org}} \qquad ; \qquad a_d = a_v\frac{V_T}{V_{org}} \tag{7.3}$$

Substituting these equations into Equation 7.1 yields Equations 7.4 and 7.5.

$$-\ln\left[\frac{\zeta-\alpha}{1-\alpha}\right] = k_T\left(\frac{V_T}{V_{aq}} + S\frac{V_T}{V_{org}}\right)a_v\frac{V_T}{Q_T}\frac{V_{org}}{V_{org}} \tag{7.4}$$

$$-\ln\left[\frac{\zeta-\alpha}{1-\alpha}\right] = k_T\left(\frac{V_T}{V_{aq}} + S\frac{V_T}{V_{org}}\right)a_d\frac{V_{org}}{Q_T} \tag{7.5}$$

Equation 7.6 contains three more relations. $V_{org} = V_{aq}$ is only valid in a 1:1 aqueous:organic ratio, as is the case in the ATR.

$$k_T a_d = \frac{1}{\Omega_d} \qquad ; \qquad V_{org} = V_{aq} \qquad ; \qquad \frac{V_T}{Q_T} = t \tag{7.6}$$

Substituting the relations in Equation 7.6 into Equation 7.5, yields a final equation for $\frac{1}{\Omega_d}$, shown in Equation 7.7.

$$-\frac{1}{t(S+1)}\ln\left[\frac{\zeta-\alpha}{1-\alpha}\right] = \frac{1}{\Omega_d} \tag{7.7}$$

Using a similar derivation starting with the counter-current flow equations shown in Section 4.2.5, Equation 7.8 can be reached.

$$-\frac{2}{t_{org}(1+S)}\ln\left[S + (1+S)\frac{c_0}{c_{aq}}\right] = \frac{1}{\Omega_d} \tag{7.8}$$

Comparing the $\frac{1}{\Omega_d}$ values for ATR parameters in which full mixing is not achieved would not be a fair comparison. These values represent a falsely high mass transfer rate as, given ideal mixing, energy would be dissipated over a larger volume and produce larger droplets. As such, only the optimum condition of 50% fill fraction subject to 5 Hz agitation will be compared, as this is the closest to ideal mixing achieved, with 95% of the fluid mixed. Figure 7.1 plots the values for $\frac{1}{\Omega_d}$ in the TCDC, D-cell and ATR against the dispersed phase hold-up in the system, ϕ_{org}, defined in Equation 7.9. Hold-up in the ATR is a constant at ϕ_{org}=0.5.

$$\phi_{org} = \frac{V_{org}}{V_T} \tag{7.9}$$

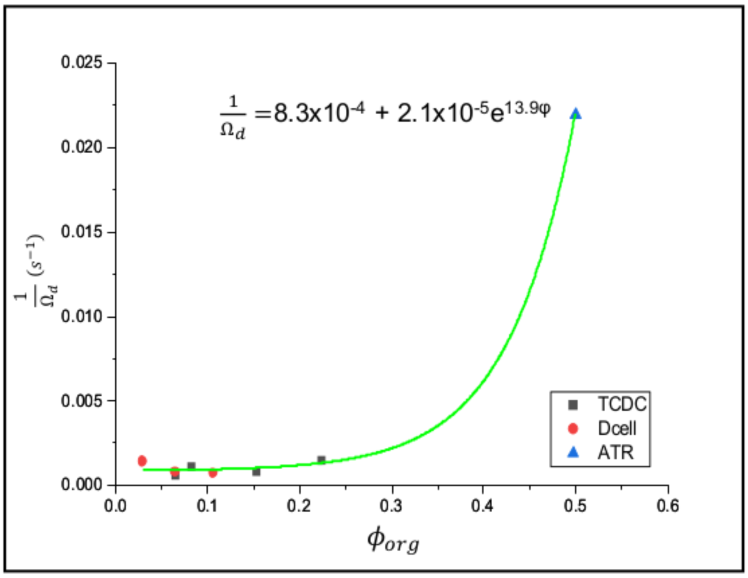

Figure 7.1: *A plot of the organic mass transfer coefficient against the dispersed hold-up in the contactor. For the ATR, this is constant at 0.5, however in the TCDC or D-cell, this varies with* u_R^2*. An exponential correlation has been fitted to show a potential correlation between the mass transfer coefficient and the volume fraction of organic fluid.*

While there are clearly significant gaps in the data, it is plausible that Figure 7.1 could show an exponential relationship between the dispersed phase hold-up and the mass transfer coefficient. This implies that improvements of the TCDC and D-cell, such that they run at a 1:1 aqueous:organic ratio, could give mass transfer comparable to the ATR. Mass transfer coefficients are proportional to $\frac{A_{int}}{V}$. An increase in $\mathrm{A_{int}}$ is achieved by reducing the droplet diameter, which have been calculated in the ATR and TCDC as being within an order of magnitude of each other. Therefore the increase in dispersed volume is likely to increase the mass transfer coefficient.

7.2 Viability for Nuclear Reprocessing

Comparison with Literature Pulsed Column

To test the ATR's viability in the nuclear industry, it needs to be compared with current technology, such as a pulsed column. A number of mass transfer coefficient correlations can be found in Table 2.2. Other than the correlation by Luo et al. (1998),[1] all correlations contain terms specific to pulsed columns, such as the plate hole diameter. As such, a comparison will be made against the correlation provided by Luo et al. (1998).[1]

The only non-constant parameter in the pulsed column correlation is the liquid hold-up, ϕ_{org}. The value $\phi_{\mathrm{org}} = 0.5$ will be used to calculate the organic mass transfer coefficient, $\frac{1}{\Omega_d}$, as this is a constant in the ATR. As with the TCDC comparison, only the 50% fill fraction, subject to 5 Hz agitation, will be compared as this is the only phase that completely mixed the two phases.

$\frac{1}{\Omega_d}$ (s^{-1})	
ATR	Pulsed Column Luo et al. Correlation[1]
0.022	0.021

The ATR is shown to have an almost equivalent mass transfer coefficient to the pulsed column at $\phi_{org} = 0.5$. This suggests the ATR is a viable option as a solvent extraction contactor. However, correlations on pulsed columns, as shown by Yadav et al. (2008),[80] don't predict data accurately for systems beyond the parameters it was designed for. So while it cannot be said for certain that the ATR provides a better mass transfer coefficient than the pulsed column, it is shown that it is a viable solvent extraction unit.

Throughput Volume

Another possible issue with the ATR is its low flow rate capability. In the 50% fill fraction and 5 Hz agitation frequency case, the system can be said to approach equilibrium at a residence time of approximately 110 s. This correlates to a total flow rate, Q_T, of 60 mL·min^{-1}. Extending this to a full day gives a volume throughput of approximately 86.4 L·day^{-1}.

This flow rate can be compared with that of the UK's now closed reprocessing plant, THORP, which had a daily throughput of approximately 4300 L·day^{-1}.[146] To match the throughput of THORP, 50 ATR arrays would be required. This is only a rough calculation as the differing mass transfer rates between PUREX and Cu(II) extraction makes it difficult to assess accurately. However, this does somewhat mitigate the small footprint of the ATR.

CHAPTER 8

Summary and Conclusions

8.1 TCDC and D-cell

A TCDC has been designed based on literature.[106,108] CFD of the TCDC and an earlier prototype design[141] showed dead-zones, accounting for high volumes of organic phase being collected beneath discs in the prototype. A novel contactor, called the D-cell, was designed with curved compartments between discs to eliminate any dead zones by closely following the circumference of the vortices. The TCDC and D-cell were then constructed and experimentally compared with the use of Cu(II) extraction.

For a given disc speed, droplet rise times in the TCDC are longer than those seen in the D-cell. This is attributed to the flat disc shape of the TCDC trapping droplets temporarily, causing them to remain in the contactor longer and possibly re-dispersing fluid into the vortex below. Contrarily, the curved shape of the D-cell encourages droplet motion upward via their own buoyancy. Measured rise times have been used to estimate droplet sizes within each contactor. This has been achieved using Stokes' law. Droplets are shown to be in close agreement with the modified Marr model described by Aksamija et al.[106]

Flow rate has no discernable effect on the extraction of Cu(II) from the aqueous phase unlike in the ATR, in which flow rate determines the residence time. Rise time is determined instead by the droplet diameter as buoyancy forces dominate. Disc speed is shown to effect copper extraction as higher disc speeds will impart greater shear force on droplets, causing further breakup and therefore reducing buoyant effects. The increase in vortex strength induced by higher disc speeds also causes droplets to be contained in the contactor for longer. This will also be a contributing factor to the increase in extracted Cu(II).

Mass transfer coefficients, $\frac{1}{\Omega_T}$, are calculated for the two contactors. Mass transfer coefficients are shown to increase with rotational velocity. This is attributed to the reduction in droplet diameter achieved with higher power per volume.

8.2 ATR Hydrodynamics

An ATR, originally designed as a flow chemistry reactor, has been converted into a solvent extraction contactor. This has been achieved with the addition of a liquid-liquid separator, positioned at one end of the ATR tube. The separator was designed as a miniature gravity separator, using Stokes' law to calculate the dimensions. An air vent has been determined as a necessary addition, to ensure pressure is equivalent to that in the overflow system. The vent also allows liquid volume to be adjustable.

Liquid volume in the ATR has a large effect on the liquid's ability to move. Liquid motion in the tube increases the shear forces caused by contact with the bar, thus increasing dispersion. It is seen that liquid volumes below 50% fill fraction have the greatest sloshing amplitude, while 75% and above shows very little motion. 50% and 25% fill fractions show similar amplitudes and are seen to create a higher density of droplets than the 75% case.

Estimates of the power per volume between 2 and 6 Hz show that the highest power input occurs at 5 Hz. Power per volume is related to agitation frequency and amplitude of oscillation by Equation 8.1. Between 2 and 5 Hz, the frequency is dominant. At 6 Hz however, the reduced amplitude causes a significant reduction in the power input.

$$\frac{P_w}{V_L} \propto a^2 f^3 \tag{8.1}$$

Wave amplitude measurements of sloshing liquid in the ATR tube very closely match the trend exhibited by the power per volume calculations and maximum stable droplet sizes. This implies that sloshing is the dominant mechanism for droplet breakup in the ATR.

8.3 Mass Transfer in an ATR

Measurements of the Cu(II) concentration in the aqueous raffinate suggest that large portions of liquid passing though the ATR are not extensively mixed and bypass dispersion. A fill fraction of 50% is shown to be the optimal volume for liquid-liquid dispersion at all frequencies, mixing 53%, 86% and 95% at 3, 4 and 5 Hz respectively. Though 25% was shown to have similar sloshing amplitudes to the 50% case, it displays significantly reduced dispersion with 46%, 55% and 67% at 3, 4 and 5 Hz respectively. This is attributed to the initial depth of the 50% case, as this allows the liquid wave to crash at the roof of the tube and mix further. 75% fill fraction is only able to mix between 27% and 36%, in keeping with the power per volume calculations and wave amplitude measurements.

Mass transfer coefficients, $\frac{1}{\Omega_T}$, were also calculated for each fill volume and agitation frequency. The value for $\frac{1}{\Omega_T}$ corresponds to the dispersed liquid, ignoring any unmixed fluid in the tube. As such, higher mass transfer coefficients, indicating faster mass transfer, are seen for the cases in which a lower proportion of liquid is dispersed. A higher mass transfer coefficient implies a higher interfacial area per liquid volume and a smaller droplet diameter. Greater droplet break-up is caused by a higher power per volume. Power input into the system for a given frequency is constant, however if some liquid is bypassing agitation, a greater power per volume will be applied to the dispersed liquid. When this is accounted for, the energy input per volume is shown to match closely with the calculated mass transfer coefficients.

The aim of this thesis was to ascertain whether an ATR, originally designed as a flow chemistry reactor, could be converted into a solvent extraction contactor. Data presented in this paper acts as a proof of concept, though it highlights many issues with the basic design.

8.4 Conclusions

An agitated tube reactor (ATR) has been converted from a commercially available flow chemistry reactor into a working solvent extraction contactor. It has been determined that the ATR has potential to be an industrial option for solvent extraction.

Mass transfer coefficients have been calculated for a wide range of agitation frequencies and residence times using Cu(II) extraction by extractant Mextral® 84H. Mass transfer has then been compared to a Taylor-Couette Disc Contactor, and a novel design, presented in this work, called a D-cell contactor.

Based on the current design, optimum parameters are found when a tube is half filled and subject to 5 Hz frequency of agitation. With these operational conditions, the ATR is shown to mix 95% of the fluid and reaches equilibrium within approximately 160 s.

The viability of the ATR as a solvent extractor has been compared against a Taylor-Couette Disc Contactor and a Pulsed Column. It is seen that at 5 Hz, with 50% fill fraction, the ATR produces a comparable mass transfer coefficient to a pulsed column correlation,[1] as well as other mass transfer coefficients in literature. This makes the ATR a potential new technology for solvent extraction in industry.

8.5 Future Work

8.5.1 TCDC and D-cell

The TCDC and D-cell showed disappointing results, with lower than anticipated mass transfer. This is expected to be due to low organic phase hold-up in the contactors. Further experimentation at higher phase hold-ups would help to conclude if this were the case, and provide a better comparison with the ATR.

A centrifugal separator was initially designed to separate the organic and aqueous phases at the top of the contactor. While the stagnant interface was deemed to contribute negligible mass transfer, it was difficult to control at high rotational speeds. Improvements to the design may allow access to higher rotational speeds without flooding. Due to the reduction in droplet size at higher rotational speeds, this could result in increased hold-up, phase contact and mass transfer within the TCDC and D-cell.

The TCDC and D-cell only contained 4 discs each. Increasing the number of discs, and therefore the overall height of the contactor, may improve mass transfer in the contactor due to the increased contact time between the two phases.

8.5.2 ATR

While the work presented in this thesis has shown that it is possible to convert an agitated tube reactor into a solvent extraction contactor, there are still many issues to overcome. The most significant issue is the inability to fully disperse the two phases and achieve equilibrium within the tube. Altering the physical parameters, such as the size or shape of the agitator bar is likely to have an effect on the mixing extent. Though this could be achieved experimentally, CFD would allow for a better understanding of the hydrodynamics and more freedom with shape design. Computational modelling of the ATR would be complex, and large eddy simulation (LES) would likely be necessary to accurately model the complex motion of the agitator bar and its effects on the fluids. Multiphase modelling would also be required to determine the extent of dispersion. Literature modelling the ATR computationally exists, so use of existing models in the context of dispersion optimisation would be ideal.[116,143]

Scale-up of the ATR, such that higher liquid throughput is possible, is also a necessity if the ATR is to be used in nuclear reprocessing. A throughput greater than 60 mL·min^{-1} is not possible with the current design as flooding of the separator occurs, increasing the volume within the tube.

A uranium/TBP system could not be used for the work presented in this thesis, due to restrictions on radioactive material. To fully gauge whether the ATR is a viable option for spent fuel reprocessing, and move beyond a proof of concept, uranium extraction via TBP needs to be conducted. This would allow for a direct comparison with current equipment, and make estimating quantities of processed material more simple.

The PUREX process is most commonly performed in counter-current. Though mass transfer in a single tube is co-current, partial counter-current flow can be achieved with the addition of more tubes, such that the two liquid phases travel in opposing directions. This would be very similar to a mixer-settler array, in which the two phases are mixed, allowed to settle and then separated, continuing to further extraction stages. A diagram depicting counter-current flow in an ATR is shown in Figure 8.1.

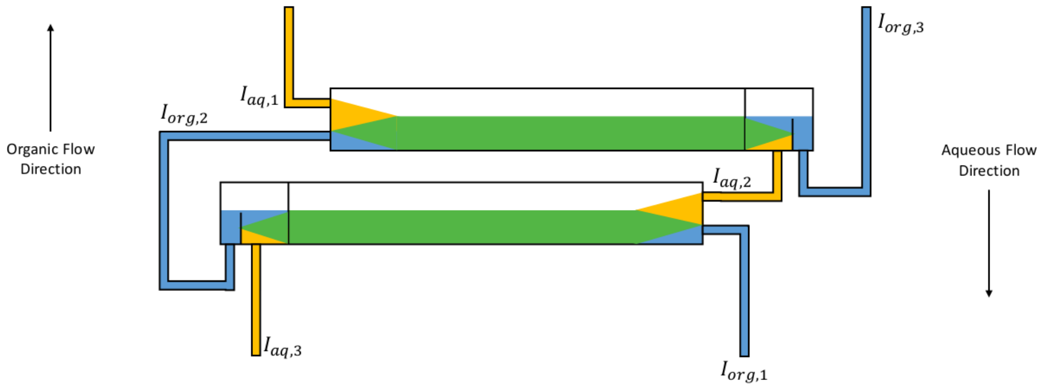

Figure 8.1: *A schematic showing counter-current flow in two ATR tubes. The aqueous phase begins by flowing through the top tube into the bottom tube. The organic phase begins by flowing through the bottom tube before travelling upwards to the top tube. Aqueous and organic inlets, denoted by the subscripts "aq" and "org" respectively, are labelled numerically to indicating the direction of flow.*

References

[1] G. Luo, H. Li, W. Fei, and J. Wang, "A simplified correlation of mass transfer in a pulsed sieve plate extraction column," *Chemical Engineering Technology*, vol. 21, no. 10, pp. 823–827, 1998.

[2] R. Taylor, *Reprocessing and Recycling of Spent Nuclear Fuel.* Woodhead Publishing, 2015.

[3] Sellafield Ltd., "Green light to restart Magnox reprocessing," 2020. Online; Available: `https://www.gov.uk/government/news/green-light-to-restart-magnox-reprocessing`.

[4] NDA, "The Magnox operating programme (MOP 9," 2012. Online; Available: `https://assets.publishing.service.gov.uk/government/uploads/system/uploads/attachment_data/file/457808/The_Magnox_Operating_Programme__MOP9_.pdf`.

[5] M. Leafe, "End in sight for reprocessing nuclear fuel at Sellafield," 2017. Online; Available: `https://nda.blog.gov.uk/2017/01/24/end-in-sight-for-reprocessing-nuclear-fuel-at-sellafield/`.

[6] NDA and Sellafield Ltd., "End of reprocessing at Thorp signals new era for Sellafield," 2018. Online; Available: `https://www.gov.uk/government/news/end-of-reprocessing-at-thorp-signals-new-era-for-sellafield`.

[7] E. Irish and W. Reas, "The PUREX process - a solvent extraction reprocessing method for irradiated uranium," 1957.

[8] Boxall, C., "Spent nuclear fuel reprocessing." University Lecture, 2015.

[9] IAEA, "The nuclear fuel cycle," 2011. Online; Available: `https://www.iaea.org/sites/default/files/nfc0811.pdf`.

[10] Hanson, B., "NGN - Introduction to the nuclear fuel cycle." University Lecture, 2015.

[11] IAEA, "Nuclear fuel cycle information system," 2009. Online; Available: `https://www.oecd-nea.org/science/docs/2012/nsc-wpfc-doc2012-15.pdf`.

[12] W. Lanham and T. Runion, "PUREX process for plutonium and uranium recovery," tech. rep., Oak Ridge National Lab, 1949.

[13] R. Herbst, P. Baron, and M. Nilsson, "Standard and advanced separation: PUREX processes for nuclear fuel reprocessing," in *Advanced Separation Techniques for Nuclear Fuel Reprocessing and Radioactive Waste Treatment* (K. Nash and G. Lumetta, eds.), ch. 6, Cornwall: Woodhead Publishing, 2011.

[14] OECD-NEA, "Spent nuclear fuel reprocessing flowsheet," 2012. Online; Available: `https://www.oecd-nea.org/science/docs/2012/nsc-wpfc-doc2012-15.pdf`.

[15] P. Schweitzer, *Handbook of Separation Techniques for Chemical Engineers.* London: McGraw-Hill, 2 ed., 1988.

[16] J. Humphrey and G. Keller, *Separation Process Technology.* London: McGraw-Hill, 1997.

[17] K. Crowell, "Pharmaceutical applications of liquid-liquid extraction," in *Handbook of Downstream Processing* (E. Goldberg, ed.), Dordrecht: Springer, 1997.

[18] P. Kiezyk and D. Mackay, "Waste water treatment by solvent extraction," *The Canadian Journal of Chemical Engineering*, vol. 49, no. 6, pp. 747–752, 1971.

[19] D. Flett, D. Okuhara, and D. Spink, "Solvent extraction of copper by hydroxyoximes," *Journal of Inorganic and Nuclear Chemistry*, vol. 35, no. 7, pp. 2471–2487, 1973.

[20] F. Muller, "How green is your engineering proposal? life cycle impact assessment in high value chemical manufacturing," *Chimica Oggi - Chemistry Today*, vol. 31, no. 4, pp. 34–38, 2013.

[21] M. Fellett, "Green chemistry and engineering: Towards a sustainable future," *ACS*, 2013. Online; Available: `https://www.acs.org/content/dam/acsorg/membership/acs/benefits/extra-insights/green-chemistry.pdf`.

[22] World Nuclear Association, "Processing of used nuclear fuel," 2020. Online; Available: `https://www.world-nuclear.org/information-library/nuclear-fuel-cycle/fuel-recycling/processing-of-used-nuclear-fuel.aspx`.

[23] I. Kumari, B. Kumar, and A. Khanna, "A review on UREX processes for nuclear spent fuel reprocessing," *Nuclear Engineering and Design*, vol. 358, 2020. Online; Available: https://reader.elsevier.com/reader/sd/pii/S0029549319304418?token=DDA38641392C73BC5B3BA2C3A5B4900577A32203F078D5750E916A955736081E960F896A4AC50E751F70133454D99F8D.

[24] K. Bell, C. Capentier, M. Carrott, A. Geist, C. Gregson, X. Hérès, D. Magnusson, R. Malmbeck, F. McLachlan, G. Modolo, U. Müllich, M. Sypula, R. Taylor, and A. Wilden, "Progress towards the development of a new GANEX process," *Procedia Chemistry*, vol. 7, pp. 392–397, 2012.

[25] R. Taylor, C. Gregson, M. C. Carrott, M.J., and M. Sarsfield, "Progress towards the full recovery of neptunium in an advanced PUREX process," *Solvent Extraction and Ion Exchange*, vol. 31, no. 4, pp. 442–462, 2013.

[26] H. Chen, R. Taylor, M. Jobson, D. Woodhead, C. Boxall, A. Masters, and S. Edwards, "Simulation of neptunium extraction in an advanced

PUREX process - model improvement," *Solvent Extraction and Ion Exchange*, vol. 35, no. 1, pp. 1–18, 2017.

[27] A. Pichugin and V. Tarasov, "Mass transfer with chemical reactions in two-phase liquid-liquid flow," in *Liquid-Liquid Systems* (N. Kulov, ed.), ch. 3, p. 248, USA: Nova Science Publishers Inc, 1996.

[28] W. Whitman, "The two-film theory of gas absorption," *Chemical and Metallurgical Engineering*, vol. 29, pp. 146–148, 1923.

[29] W. Lewis and W. Whitman, "Principles of gas absorption," *Industrial and Engineering Chemistry*, vol. 16, no. 12, pp. 1215–1220, 1924.

[30] O. Levenspiel, *Chemical Reaction Engineering.* USA: John Wiley and Sons Inc., 3 ed., 1992.

[31] R. Higbie, "The rate of absorption of a pure gas into a still liquid during short periods of exposure," *Transactions of the American Institute of Chemical Engineers*, vol. 31, pp. 365–389, 1935.

[32] H. Toor and J. Marchello, "Film-penetration model for mass and heat transfer," *American Institute of Chemical Engineers Journal*, vol. 4, no. 1, pp. 97–101, 1958.

[33] H. Hottel, J. Noble, A. Sarofim, G. Silcox, P. Wankat, and K. Knaebel, "Heat and mass transfer," in *Perry's Chemical Engineering Handbook* (D. Green and R. Perry, eds.), ch. 5, p. 45, London: McGraw-Hill, 8 ed., 2007.

[34] R. Bird, W. Stewart, and E. Lightfoot, *Transport Phenomena.* USA: John Wiley & sons Inc., 1976.

[35] P. Danckwerts, "Significance of liquid-film coefficients in gas absorbtion," *Engineering and Process Development*, vol. 43, no. 6, pp. 1460–1467, 1951.

[36] I. Horvath and C. S.G., "A surface renewal model for unsteady-state mass transfer using the generalized danckwerts age distribution function," *Royal Society Open Science*, vol. 5, 2018.

[37] I. Stamatiaou and F. Muller, "Determination of mass transfer resistances of fast reactions in three-phase mechanically agitated slurry reactors," *AIChe Journal*, vol. 63, pp. 273–282, 2016.

[38] A. Skelland, "Interphase mass transfer," in *Science and Practice of Liquid-Liquid Extraction* (J. Thornton, ed.), vol. 1, Oxford: Clarendon Press, 1992.

[39] J. Szymanowski, "Kinetics and interfacial phenomena," *Solvent Extraction and Ion Exchange*, vol. 18, no. 4, pp. 729–751, 2000.

[40] M. Cox and D. Flett, "The significance of surface activity in solvent extraction reagents," *Proceedings International Solvent Extraction Conference ISEC*, vol. 77, pp. 63–72, 1979.

[41] D. Flett, "Chemical kinetics and mechanisms in solvent extraction of copper chelates," *Accounts of Chemical Research*, vol. 10, no. 3, pp. 99–104, 1977.

[42] R. Price and J. Tumilty, "Hydrometallurgy," in *Institute of Chemical Engineering London Symposium Series* (G. Davies and J. Scuffham, eds.), vol. 18, 1975.

[43] R. Dalton, F. Hauxwell, and J. Tumilty, "Diluent effects on the hydrometallurgical extraction of metals by o-hydroxy-aryl-oximes," *Chemical & Industry*, vol. 5, pp. 181–184, 1976.

[44] I. Komasawa and T. Otake, "The effects of diluent in the liquid-liquid extraction of copper and nickel using 2-hydroxy-5-nonylbenzophenone oxime," *Journal of Chemical Engineering Japan*, vol. 16, no. 5, pp. 377–383, 1983.

[45] P. Kuipa and M. Hughes, "Diluent effect on the solvent extraction rate of copper," *Separation Science and Technology*, vol. 37, no. 5, pp. 1135–1152, 2002.

[46] T. Kojima and M. Terukatsu, "Extraction kinetics of copper-LIX65N system. 2. stripping rate of copper," *Industrial & Engineering Chemistry Fundamentals*, vol. 20, no. 1, pp. 20–25, 1981.

[47] B. Magnusson and S. Westerlund, "Solvent extraction procedures combined with back-extraction for trace metal determinations by atomic absorption spectroscopy," *Analytica Chema Acta*, vol. 131, pp. 63–72, 1981.

[48] C. Housecroft and A. Sharpe, *Inorganic Chemistry.* Essex: Pearson Education Limited, 4 ed., 2012.

[49] B. Kanellakopulos, E. Dernberger, R. Maier, B. Nuber, H. Stammler, and M. Ziegler, "Molekulstruktur und ladungsverteilung iv. elektrisches diplomoment von 1:2-addukten des uranylnitrats mit trialkylphosphaten. die kristallstruktur von $UO_2(TEP)_2(NO_3)_2$ und bis[(μ-diethylphosphato-O-O)nitrato(triethyl-phosphato)-dioxourant(VI],$(UO_2)[(EtO)_2PO_2](EtO)_3PO](NO_3)_2$, journal = Marz, volume = 619, number = 3, year = 1993, pages=593-600, type = Journal Article,"

[50] J. Rydberg, G. Choppin, C. Musikas, and T. Sekine, "Solvent extraction equilibria," in *Solvent Extraction Principles and Practice, Revised and Expanded* (J. Rydberg, M. Cox, C. Musikas, and G. Choppin, eds.), New York: Marcel Dekker, 2 ed., 1992.

[51] M. Brooker, C. Huang, and J. Sylwestrowicz, "Raman spectroscopic studies of aqueous uranyl nitrate and perchlorate systems," *Journal of Inorganic and Nuclear Chemistry*, vol. 42, no. 10, pp. 1431–1440, 1980.

[52] X. Ye, S. Cui, V. de Almeida, and B. Komami, "Interfacial complex formation in uranyl extraction by tributyl phosphate in dodecane diluent: A molecular dynamics study.," *Journal of Physical Chemistry*, vol. 113, pp. 9852–9862, 2009.

[53] K. Nukada, K. Naito, and U. Maeda, “On the mechaniusm of the extraction of uranyl nitrate by tributyl phosphate II. infrared study.,” *Bulletin of the Chemical Society of Japan*, vol. 33, no. 7, pp. 894–898, 1960.

[54] M. Alibrahim and H. Shlewitt, “Solvent extraction of uranium (VI by tributyl phosphate/dodecane from nitric acid medium,” *Perioda Polytechnica*, vol. 51, no. 2, pp. 57–60, 2007.

[55] J. Birkett, M. Carrott, O. Fox, C. Jones, C. Maher, C. Roube, R. Taylor, and D. Woodhead, “Recent developments in the PUREX process for nuclear fuel reprocessing: Complexant based stripping for uranium/plutonium separation,” *Chemistry and Materials in Nuclear Power Production*, vol. 59, no. 12, pp. 898–904, 2005.

[56] R. Whewell, M. Hughes, and C. Hanson, “The kinetics of the solvent extraction of copper(II) LIX reagents - I single drop experiments,” *Journal of Inorganic and Nuclear Chemistry*, vol. 37, no. 11, pp. 2303–2307, 1975.

[57] I. Kojima, M. Uchida, and M. Tanaka, “Extraction of copper(II) with carboxylic acids,” *Journal of Inorganic and Nuclear Chemistry*, vol. 32, no. 4, pp. 1333–1340, 1970.

[58] A. Ashbrook, “Extraction of metals from ammonium sulphate solution using a carboxylic acid - III copper,” *Journal of Inorganic and Nuclear Chemistry*, vol. 34, no. 11, pp. 3523–3530, 1972.

[59] Y. Baba and K. Inoue, “Solvent extraction equilibria of copper(II) by carboxylic acids with high acid dissociation constants,” *Hydromettalurgy*, vol. 21, no. 2, pp. 203–212, 1988.

[60] I. Komasawa, T. Otake, and A. Yamada, “Equilibrium studies of copper extraction from sulphaste media with hydroxyoxime extractant,” *Journal of Chemical Engineering Japen*, vol. 13, no. 2, p. 7, 1980.

[61] F. Vasilyev, S. Virolainen, and T. Sainio, “Modeling the phase equilibrium in liquid-liquid extraction of copper over a wide range of copper and

hydroxyoxime extractant concentrations," *Chemical Engineering Science*, vol. 171, pp. 88–99, 2017.

[62] D. Flett, M. Cox, and J. Heels, "Kinetics of nickel extraction by α hydroxy oxime/carbolic acid mixtures," *Journal of Inorganic and Nuclear Chemistry*, vol. 31, no. 12, pp. 2533–2537, 1975.

[63] F. Alguacil, A. Cobo, and M. Alonso, "Copper separation from nitrate/nitric acid media using Acorga M5640 extractant: Part I: solvent extraction study," *Chemical Engineering Journal*, vol. 85, no. 2-3, pp. 259–263, 2002.

[64] S. Carter and H. Freiser, "Kinetics and mechanism of the extraction of copper with 2-hydroxy-5-nonylbenzophenone oxime," *Analytical Chemistry*, vol. 52, no. 3, pp. 511–514, 1980.

[65] K. Dimitrov, S. Alexandrova, L. Boyadzheiv, S. Ruellan, and M. Burgard, "Recovery of copper from solutions by rotating film pertraction," *Separation and Purification Technology*, vol. 12, no. 2, pp. 165–173, 1997.

[66] Y. Miyake, Y. Takenoshita, and M. Teramoto, "Extraction of copper with SME 529," *Journal of Chemical Engineering of Japan*, vol. 16, no. 3, pp. 203–209, 1983.

[67] F. Alguacil, M. Alonso, and A. Sastre, "Modelling of mass transfer in facilitated support liquid membrane transport of copper(II) using MOC-55 TD in iberfluid," *Journal of Membrane Science*, vol. 15, no. 1, pp. 117–122, 2002.

[68] F. Alguacil, F. Lopez, and I. Garcia-Diaz, "Copper removal from acidic wastewaters using 2-hydroxy-5-nonylbenzaldehyde oxime as ionophore in pseudo-emulsion membrane with strip dispersion (PEMSD) technology," *Journal of Industrial and Engineering Chemistry*, vol. 18, no. 1, pp. 255–259, 2012.

[69] W. Genck, D. Dickey, F. Baczek, D. Bedell, K. Brown, W. Chen, D. Ellis, P. Harriot, T. Laros, W. Li, J. McGillicuddy, and T. McNulty, "Liquid-solid

operations and equipment," in *Perry's Chemical Engineering Handbook* (D. Green and R. Perry, eds.), ch. 18, pp. 115–147, London: McGraw-Hill, 8 ed., 2007.

[70] R. Cusack, "Rethink your liquid-liquid separations," *Hydrocarbon Processing*, vol. 88, no. 6, pp. 53–60, 2009.

[71] N. Eckert and L. Gormely, "Phase separation in an experimental mixer-settler," *Chemical Engineering and Research Design*, vol. 67, no. 2, pp. 175–184, 1989.

[72] Q. Tang, J. Zhang, Y. Wu, Y. Wang, and Z. Liu, "An experimental study of immiscible liquid-liquid dispersions in a pump-mixer of mixer-settler," *Chinese Journal of Chemical Engineering*, vol. 28, no. 1, pp. 33–45, 2020.

[73] J. Horng and J. Maa, "The effect of a surfactant on mixer-settler operation," *Journal of Chemical Technology and Biotechnology*, vol. 36, no. 1, pp. 15–26, 1986.

[74] A. Khakpay, H. Abolghasemi, and A. Salimi-Khorshidi, "The effects of a surfactant on mean drop size in a mixer-settler extractor," *Chemical Engineering and Processing: Process Intensification*, vol. 48, no. 6, pp. 1105–1111, 2009.

[75] N. Rao and M. Baird, "Davy McKee combined mixer settler: Some laboratory studies," *The Canadian Journal of Chemical Engineering*, vol. 62, pp. 497–506, 1984.

[76] M. Horvath and S. Hartland, "Mixer-settler-extraction column: Mass-transfer efficiency and entrainment," *Industrial and Engineering Chemistry.*

[77] M. Torab-Mostaedi, J. Safdari, A. Moosavian, and M. Maragheh, "Stage efficiency of hanson mixer-settler extraction column," *Chemical Engineering and Processing: Process Intensification*, vol. 48, no. 1, pp. 224–228, 2009.

[78] K. Takahashi, S. Nii, K. Nakanishi, and H. Takeuchi, “Stage efficiency of mixer-settler extraction column,” *Journal of Chemical Engineering of Japan*, vol. 26, no. 6, pp. 715–719, 1993.

[79] W. Dijck, “Process and apparatus for intimately contacting fluids.” US Patent, 1935.

[80] R. Yadav and A. Patwardhan, “Design aspects of pulsed sieve plate columns,” *Chemical Engineering Journal*, vol. 138, no. 1-3, pp. 389–415, 2008.

[81] G. Sege and F. Woodfield, “Pulse column variables. solvent extraction of uranyl nirtate with tributyl phosphate in a 3-in. -diam pulse column.,” *Chemical Engineering Progress*, vol. 50, 1953.

[82] W. Chantry, R. Von Berg, and H. Wiegandt, “Application of pulsation to liquid-liquid extraction,” *Industrial and Engineering Chemistry*, vol. 47, no. 6, pp. 1153–1159, 1955.

[83] R. Yadav and A. Parwardhan, “CFD modelling of sieve and pulsed-sieve plate extraction columns,” *Chemical Engineering Research and Design*, vol. 87, no. 1, pp. 25–35, 2009.

[84] G. Laddha and T. Degaleesan, *Transport Phenomena in Liquid Extraction.* McGraw-Hill, 1976.

[85] D. Theobald, B. Hanson, M. Fairweather, and P. Heggs, “Multiphase large eddy simulation of a pulsed sieve-plate extraction column,” in *Proceeding of the 44th Annual Waste Management Conference*, (Phoenix, Arizona), Waste Management Symposia, March 2018.

[86] D. Theobald, B. Hanson, M. Fairweather, and P. Heggs, “Implications of hydrodynamics on the design of pulsed sieve-plate extraction columns: A one-fluid multiphase CFD model using the volume of fluid method,” *Chemical Engineering Science*, vol. 221, 2020. Online; Available: https://www.sciencedirect.com/science/article/pii/S000925092030172X?ca

sa_token=TkDhgj7cTecAAAAA:1Lp0Xt1nPzU8jkdgGJRMW7Wxk99IaGLYl0Yzb-1IMjNfZR2nxOaCycXXCTzJ5xdarhcU871p.

[87] J. Thornton, "Liquid-liquid extraction. part XIII. the effect of pulse waveform and plate geometry on the performance and throughput of a pulsed column.," *Industrial and Engineering Chemistry*, vol. 51, no. 9, pp. 1005–1010, 1959.

[88] L. Smoot, B. Mar, and A. Babb, "Flooding characteristics and separation efficiencies of pulsed sieve-plate extraction columns," *Industrial and Engineering Chemistry*, vol. 51, no. 9, pp. 1005–1010, 1959.

[89] G. Taylor, "Stability of a viscous liquid contained between two rotating cylinders," *Philosophical Transactions of the Royal Society*, vol. 223, no. 605-615, pp. 289–343, 1923.

[90] I. Stewart and M. Golubitsky, *Fearful Symmetry: Is God a Geometer?* Mineola, New York: Dover Publications, dover edition ed., 2011.

[91] S. Chandrasekhar, "The stability of viscous flow between cylinders," *Proceedings of the Royal Society A*, vol. 246, no. 1246, pp. 301–311, 1958.

[92] S. Donnelly, "Experiments on the stability of viscous flow between rotating cylinders-i. torque measurements.," *Proceedings of the Royal Society A*, vol. 246, no. 1246, pp. 312–325, 1958.

[93] S. Chandrasekhar, "The hydrodynamic stability of viscid flow between coaxial cylinders," *Proceedings of the National Academy of Sciences of the United States of America*, vol. 46, no. 1, pp. 141–143, 1960.

[94] E. Koschmieder, "Turbulent taylor vortex flow," *Journal of Fluid Mechanics*, vol. 93, no. 3, pp. 515–527, 1979.

[95] S. Vedantam and J. Joshi, "Annular centrifugal reactors - a review," *Chemical Engineering Research and Design*, vol. 84, no. A7, pp. 522–542, 2006.

[96] S. Chandrasekhar, "The stability of spiral flow between rotating cylinders," *Proceedings of the Royal Society A*, vol. 265, no. 1321, pp. 188–197, 1962.

[97] J. Walowit, S. Tsao, and R. DiPrima, "Stability of flow between arbitrarily spaced concentric cylinder surfaces including the effect of a radial temperature gradient," *Journal of Applied Mechanics*, vol. 31, no. 4, pp. 585–593, 1964.

[98] D. Coles, "Transition in circular couette flow," *Journal of Fluid Mechanics*, vol. 21, no. 3, pp. 385–425, 1965.

[99] P. Fenstermacher, H. Swinney, and J. Gollub, "Dynamic instabilities and the transition to chaotic taylor vortex flow," *Journal of Fluid Mechanics*, vol. 94, no. 1, pp. 103–128, 1979.

[100] M. Schrimpf, J. Esteban, H. Warmeling, T. Färber, A. Behr, and A. Vorholt, "Taylor-Couette reactor: Principles, design and applications," *Reaction Engineering, Kinetics and Catalysis*, vol. 67, no. 5, pp. 1–24, 2021. Online; Available: `https://aiche.onlinelibrary.wiley.com/doi/10.1002/aic.17228?af=R`.

[101] S. Kang, S. Lee, W. Jung, M. Kim, W. Kim, C. Choi, and R. Feigelson, "Effect of Taylor vortices on calcium carbonate crystallization by gas-liquid reaction," *Journal of Crystal Growth*, vol. 254, no. 1-2, pp. 196–205, 2003.

[102] Z. Liu, T. Jin, and M. Kind, "Continuous polymerization of methyl methacrylate in a Taylor-Couette reactor. I. influence of fluid dynamics on monomer conversion," *Polymer Engineering and Science*, vol. 53, no. 1, pp. 96–104, 2013.

[103] L. Guérin, C. Coufort-Saudejaud, A. Liné, and C. Frances, "Dynamics of aggregate size and shape properties under sequences flocculation in a turbulent Taylor-Couette reactor," *Journal of Colloid and Interface Science*, vol. 491, pp. 167–178, 2017.

[104] R. Giordano, R. Giordano, D. Prazeres, and C. Cooney, "Analysis of a Taylor-Poiseuille vortex flow reactor - II: Reactor modeling and performance assessment using glucose-fructose isomerization as test reaction," *Chemical Engineering Science*, vol. 55, no. 18, pp. 3611–3626, 2000.

[105] M. Resende, P. Viera, R. Sousa, R. Giordano, and R. Giordano, "Estimation of mass transfer parameters in a Taylor-Poiseuille heterogeneous reactor," *Brazillian Journal of Chemical Engineering*, vol. 21, no. 2, pp. 175–184, 2004.

[106] E. Aksamija, C. Weinländer, R. Sarzio, and M. Siebenhofer, "The taylor-couette disc contactor: A novel apparatus for liquid/liquid extraction," *Separation Science and Technology*, vol. 20, no. 18, pp. 2844–2852, 2015.

[107] A. Grafschafter, E. Aksamija, and M. Siebenhofer, "The taylor-couette disc contactor," *Chemical Engineering and Technology*, vol. 39, no. 11, pp. 2087–2095, 2016.

[108] A. Grafschafter and M. Siebenhofer, "Design rules for the taylor-couette disc contactor," *Chemie Ingeniur Technilk*, vol. 89, no. 4, pp. 409–415, 2017.

[109] A. Grafschafter, G. Rudelstorfer, and M. Siebenhofer, "Hydraulics and operation performance of tcdc extractors," *Chemie Ingeniur Technilk*, vol. 90, no. 6, pp. 864–871, 2018.

[110] A. Grafschafter and M. Siebenhofer, "Effect of rotor disc diameter on holdup, axial dispersion and droplet size in a taylor-couette disc contactor," *Chemie Ingeniur Technilk*, vol. 91, no. 11, pp. 1589–1596, 2019.

[111] AMTechnology Online; Availabile: `http:www.amtechuk.com/pilot-and-plant-scale-atr/`.

[112] G. Gasparini, I. Archer, E. Jones, and R. Ashe, "Scaling up biocatalysis reactions in flow reactors," *Organic Processes and Research Development*, vol. 16, no. 5, pp. 1013–1016, 2012.

[113] E. Jones, K. McClean, S. Housden, G. Gasparini, and I. Archer, "Biocatalytic oxidase: Batch to continuous," *Chemical Engineering Research and Design*, vol. 90, no. 6, pp. 726–731, 2012.

[114] J. Britton, S. Majumdar, and G. Weiss, “Continuous flow catalysis,” *Chemical Society Reviews*, vol. 47, no. 15, pp. 5891–5918, 2018.

[115] P. Filipponi, A. Gioiello, and I. Baxendale, “Controlled flow precipitation as a valuable tool for synthesis,” *Organic Process Research and Development*, vol. 20, no. 2, pp. 371–375, 2015.

[116] J. Derksen, “Mixing in an agitated tubular reactor,” *The Canadian Journal of Chemical Engineering*, vol. 97, no. 2, pp. 523–527, 2018.

[117] C. Parrington and B. Hanson, “First principles design evaluation of a laterally agitated tube reactor,” Master’s thesis, School of Chemical and Process Engineering, University of Leeds, 2015.

[118] G. Davies, “Mixing and coalescence phenomena in liquid-liquid systems,” in *Science and Practice of Liquid-Liquid Extraction* (J. Thornton, ed.), vol. 1, Oxford: Clarendon Press, 1992.

[119] J. Hinze, “Fundamentals of the hydrodynamic mechanism of splitting in dispersion processes,” *American Institute of Chemical Engineers*, vol. 1, no. 3, pp. 289–295, 1955.

[120] M. Prudich, H. Chen, T. Gu, R. Gupta, K. Johnston, H. Lutz, G. Ma, and Z. Su, “Liquid-liquid extraction and other liquid-liquid operations and equipment,” in *Perry’s Chemical Engineering Handbook* (D. Green and R. Perry, eds.), ch. 15, p. 42, London: McGraw-Hill, 8 ed., 2007.

[121] S. Weiß, W. Berghoff, E. Grahn, G. Gruhn, M. Güsewell, W. Plötner, H. Robel, and M. Schubert, *Verfahrenstechnische Berechnungsmethoden 2. Thermisches Trennen – Ausrüstungen und ihre Berechnung.* Weinheim, Germany: Wiley VCH, 1986.

[122] S. Weiß, E. Militzer, and K. Gramlich, *Thermische Verfahrenstechnik.* Liepzig, Germany: Deutscher Verlag für Grundstoffindustrie, 1993.

[123] R. Marr, G. Husang, and F. Moser, “Die auslegung von drehscheibenextraktoren.,” *Verfahrenstechnik*, vol. 12, no. 3, pp. 139–144, 1978.

[124] S. Kagan, M. Aerov, T. Volkova, and V. Trukhanov, "Calculation of the drop diameter in rotary-disc contactors," *Journal of Applied Chemistry USSR*, vol. 37, pp. 67–73, 1964.

[125] E. Fischer, "Drop size in agitated liquid-liquid extraction columns. effect of physical properties, column geometry, agitator type and agitation speed," *Verfahrenstechnik*, vol. 5, pp. 360–365, 1971.

[126] A. Kumar and S. Hartland, "Prediction of drop size in rotating disc contactors," *The Canadian Journal of Chemical Engineering*, vol. 64, no. 6, pp. 915–924, 1986.

[127] J. C. Crittenden, R. Rhodes Trussell, D. W. Hand, K. J. Howe, and G. Tchobanoglous, *MWH's Water Treatment - Principles and Design.* New Jersey: John Wiley & Sons, 3 ed., 2012.

[128] Ocean Optics, *Ocean View Installation and Operation Manual.* Ocean Optics.

[129] H. H. Perkampus, *UV-Vis Spectroscopy and Its Applications.* Springer-Verlag, 1992.

[130] A. Beer, *Einleitung in die hohere Optik.* Friedrich Vieweg und Sohn, 1853.

[131] T. S. University, "Beer-Lambert law." University Lecture, 2003.

[132] R. Saunders, W. Ott, and J. Bridges, "Spectral irradiance standard for the ultraviolet: The deuterium lamp," *The Optical Society*, vol. 17, no. 4, pp. 593–600, 1978.

[133] L. Thoms and R. Girdwidz, "Experimenting from a distance: Optical spectrometry via the internet," in *MPTL18 - Book of Proceedings*, (Madrid), pp. 59–63, MPTL, September 2013.

[134] T. Wen, F. Qu, N. Li, and Q. Luo, "A facile, sensitive, and rapid spectrophotometric method for copper(II) ion detection in aqueous media using polyethyleneimine," *Arabian Journal of Chemistry*, vol. 10, no. 2, pp. S1680–S1685, 2017.

[135] R. Bastian, R. Weberling, and F. Palilla, "Ultraviolet spectrophotometric determination of nitrate. application to analysis of alkaline earth carbonates," *Analytical Chemistry*, vol. 29, no. 2, pp. 1795–1797, 1957.

[136] I. Kalinichenko and L. Demutskaya, "Determination of nitrates in drinking water by three-wavelength ultraviolet photometry," *Journal of Analytical Chemistry*, vol. 59, no. 3, pp. 211–214, 2004.

[137] G. Egloff, J. Sherman, and R. Dull, "Boiling point relationships among aliphatic hydrocarbons," *Journal of Physical Chemistry*, vol. 44, no. 6, pp. 730–745, 1940.

[138] M. Gao, R. Ye, W. Shen, and B. Xu, "Copper nitrate: A privileged reagent for organic sythesis," *Organic & Biomolecular Chemistry*, vol. 16, no. 15, pp. 2602–2618, 2018.

[139] J. Preston, "Solvent extraction of base metals by mixtures of organophosphoric acids and non-chelating oximes," *Hydromettalurgy*, vol. 10, pp. 187–204, 1983.

[140] R. Whewell, H. Foakes, and M. Hughes, "Degradation in hydroxyoxime solvent extraction systems," *Hydrometallurgy*, vol. 7, no. 1-2, pp. 7–26, 1981.

[141] J. Miller, F. Muller, and B. Hanson, "Continuous countercurrent extraction in a Coflore® agitated tube reactor for use in the reprocessing of spent nuclear fuel," Master's thesis, School of Chemical and Process Engineering, University of Leeds, 2017.

[142] R. Grenville and J. Glacomelli, "Mixing: Impeller performance in stirred tanks," *Chemical Engineering*, 2017.

[143] H. Rice, "Mechanical motion of an agitated tube reactor (ATR) - summary of travel distance and dynamics," 2017. Unpublished.

[144] H. Schümann, M. Khabiti, M. Tutkun, B. Pettersen, Z. Yang, and O. Nydal, "Droplet size measurements in oil-water dispersions: A comparison

study using FBRM and PVM," *Journal of Dispersion Science and Technology*, vol. 36, no. 10, pp. 1432–1443, 2015.

[145] M. Edwards, M. Baker, and J. Godfrey, "Mixing of liquids in stirred tanks," in *Mixing in the Process Industry* (N. Harnby, M. Edwards, and A. Nienow, eds.), ch. 8, pp. 137–158, Butterworth-Heinemann, 2 ed., 1997.

[146] Health and Safety Executive, "Report of the investigation into the leak of dissolver product liquour at the Thermal Oxide Reprocessing Plant THORP, Sellafield, notified to hse on 20 April 2005,"

CHAPTER 9

Appendix

9.1 Rise Time Measurements

An outline of the calculation used to estimate rise time in a TCDC and D-cell contactor is presented here.

$$t = \frac{t_{short} + t_{long}}{2} = \frac{(t_{out,1} - t_{in}) + (t_{out,2} - t_{in})}{2} \tag{9.1}$$

Where $\mathrm{t_{short}}$ and $\mathrm{t_{long}}$ are the shortest and longest measured rise times. $\mathrm{t_{in}}$ is the time (as displayed on a stop watch timer) at which coloured tracer droplets are injected into the contactor and $\mathrm{t_{out,1}}$ and $\mathrm{t_{out,2}}$ are the times at which the first and last coloured droplets exit the contactor respectively.

9.2 Error Calculations

9.2.1 Taylor-Couette

Error in the average droplet rise time has been calculated as shown in equation 9.2.

$$\Delta t = \Delta\left(\frac{t_{long} + t_{short}}{2}\right) = \frac{1}{\sqrt{2}}\sqrt{(\Delta t_{long})^2 + (\Delta t_{short})^2} \tag{9.2}$$

Equation 9.3 shows the error calculation in the quantity $\frac{c_{aq}}{c_0}$.

$$\Delta\left(\frac{c_{aq}}{c_0}\right) = \frac{c_{aq}}{c_0}\sqrt{\left(\frac{\Delta c_{aq}}{c_{aq}}\right)^2 + \left(\frac{\Delta c_0}{c_0}\right)^2} \tag{9.3}$$

9.2.2 ATR

The error in the average initial concentration was calculated via standard deviation of the initial concentrations of all batches. Standard deviation was also used to calculate the error in the average of the three measured concentrations. The uncertainty in $\mathrm{S_T}$ was calculated using the gradient errors presented in Section 3.2.4. This section outlines the propagation of errors used in this chapter.

Equations 9.4 and 9.5 show the error calculation in the quantities (c-$\mathrm{c_{eq}}$) and ($\mathrm{c_0}$-$\mathrm{c_{eq}}$) respectively.

$$\Delta(c - c_{eq}) = \sqrt{(\Delta c)^2 + (\Delta c_{eq})^2} \tag{9.4}$$

$$\Delta(c_0 - c_{eq}) = \sqrt{(\Delta c_0)^2 + (\Delta c_{eq})^2} \tag{9.5}$$

A similar equation, shown in Equation 9.6, was used to propagate the error in $\frac{c - c_{eq}}{c_0 - c_{eq}}$.

$$\Delta\left(\frac{\Delta(c - c_{eq})}{c_0 - c_{eq}}\right) = \left(\frac{c - c_{eq}}{c_0 - c_{eq}}\right)\sqrt{\left(\frac{\Delta(c - c_{eq})}{c - c_{eq}}\right)^2 + \left(\frac{\Delta c_0 - c_{eq}}{c_0 - c_{eq}}\right)^2} \tag{9.6}$$

The error in the mass transfer coefficient, $\frac{1}{\Omega_T}$, is also needed. Equation 6.36 shows the equation used to fit aqueous concentration against time in this chapter. This can be expressed more generally, as seen in Equation 9.7.

$$\zeta = e^{-\beta t} \tag{9.7}$$

Where $\beta = -\frac{1+S}{\Omega_T}$. The error in S is taken as the standard error in the calculated value for each batch. The error in β is taken as the error in the exponential constant, provided by the fitting software. The error in the mass transfer coefficient, $\frac{1}{\Omega}$, can then be calculated using Equation 9.8.

$$\Delta\left(\frac{1}{\Omega_T}\right) = \frac{1}{\Omega_T}\sqrt{\left(\frac{\Delta S}{S}\right)^2 + \left(\frac{\Delta\beta}{\beta}\right)^2} \tag{9.8}$$

9.2.3 Standard Error

The standard error has been used to calculate a number of errors in this thesis, for example the error in the measured aqueous concentration, c. The general equation for the standard error is shown in Equation 9.9.

$$\Delta x = \frac{\sigma}{\sqrt{N}} \tag{9.9}$$

Where Δx is the error in a desired variable, x, σ is the standard deviation in each measurement of x (expanded in Equation 9.10) and N is the number of measurements of x present in the dataset.

$$\sigma = \sqrt{\frac{\Sigma_{i=1}^{N}\left(x_i - \overline{x}\right)}{N-1}} \tag{9.10}$$

Where $\overline{x}$ is the mean value of x. For the example of measured concentration, $\mathrm{c_{aq}}$, the error for three measurements is calculated as shown in Equation 9.11.

$$\Delta c_{aq} = \frac{1}{\sqrt{3}}\sqrt{\frac{1}{2}\Sigma_{i=1}^{3}\left(c_{aq,i} - \overline{c_{aq}}\right)} \tag{9.11}$$